1

Thermal Science and Engineering

EnPress Publisher

2025 Volume 8 Issue 1
ISSN: 2578–1782 (Online)

https://systems.enpress-publisher.com/index.php/TSE

Volume 8 Issue 1 • 2025

Thermal Science and Engineering

EnPress Publisher

2025 | Volume 8 | Issue 1

Thermal Science and Engineering

https://systems.enpress-publisher.com/index.php/TSE

Contents

Articles

Thermal Science and Engineering 2025, 8(1), 9781.
https://doi.org/10.24294/tse9781

Article

An enthalpy method for heat conduction in tube containing phase change material

G. A. Evangelakis[1,2], I. E. Lagaris[3,*], D. G. Papageorgiou[3], C. Prouskas[3]

[1] Department of Physics, University of Ioannina, Ioannina 45110, Greece
[2] Institute of Materials Science and Computing, Ioannina 45110, Greece
[3] Department of Computer Science and Engineering, University of Ioannina, Ioannina 45110, Greece
*** Corresponding author:** I. E. Lagaris, lagaris@uoi.gr

CITATION

Evangelakis GA, Lagaris IE, Papageorgiou DG, Prouskas C. An enthalpy method for heat conduction in tube containing phase change material. Thermal Science and Engineering. 2025; 8(1): 9781. https://doi.org/10.24294/tse9781

ARTICLE INFO

Received: 31 October 2024
Accepted: 20 December 2024
Available online: 2 January 2025

Abstract: We present an innovative enthalpy method for determining the thermal properties of phase change materials (PCM). The enthalpy-temperature relation in the "mushy" zone is modelled by means of a fifth order Obreshkov polynomial with continuous first and second order derivatives at the zone boundaries. The partial differential equation (PDE) for the conduction of heat is rewritten so that the enthalpy variable is not explicitly present, rendering the equation nonlinear. The thermal conductivity of the PCM is assumed to be temperature dependent and is modelled by a fifth order Obreshkov polynomial as well. The method has been applied to lauric acid, a standard prototype. The latent heat and the conductivity coefficient, being the model parameters, were retrieved by fitting the measurements obtained through a simple experimental procedure. Therefore, our proposal may be profitably used for the study of materials intended for heat-storage applications.

Keywords: enthalpy; moving boundaries; phase-change materials; nonlinear optimization; thermal conductivity; latent heat

1. Introduction

Phase Change Materials (PCMs), have been widely used in several applications [1–5] that exploit the released (or absorbed) energy during a phase transition. PCMs allow for latent heat utilization and have attracted the keen interest of the heat-storage engineering community. Naturally, the determination of the PCM thermal properties is of major importance for designing effective thermal depositories. Although the heat transfer equation could in principle describe accurately the charging (or discharging) process of a PCM, the temperature activated phase change, renders the problem highly nonlinear and its solution non trivial. This in turn, incommodes the determination of the specific and latent heat as well as of the thermal conductivity, i.e., the crucial parameters for the design of an effective heat-storage system. Indeed, significant effort has been devoted in developing techniques for the reliable determination of PCMs' thermal properties, the most common ones being the Differential Scanning Calorimetry (DSC) [6], the T-History method [7] and its variants [8–12]. Nevertheless, these methods suffer from several problems regarding reproducibility, accuracy and robustness [13], qualities that become even more important in the case of mixed PCMs that are widespread in practical applications. In particular, the determination of PCM's thermal conductivity, in the full operational temperature range, still remains a challenge.

The aim of the present work is to provide a framework facilitating the reliable determination of PCM's thermal properties, by means of simple experiments coupled to an analysis based on a theoretical model.

In the following, we describe the simple experimental setup, the associated heat conduction equation along with the proper boundary and initial conditions, and we detail the employed numerical technique.

2. Description of the approach

The procedure we follow consists of the following steps: *i*) The PCM is initially prepared to be in liquid state at a predefined temperature. Next, it is cooled by immersion in a heat-bath that is maintained at a lower temperature, and standard T-History measurements are performed to obtain the enthalpy—temperature curve within a temperature range where the liquid solidifies and is further cooled down to the heat-bath's temperature. From this curve we determine the liquid and solid regions, and using simple energy considerations (described by Yinping et al. and Hong et al. [7,8]), we obtain the corresponding specific heats for each region, c_p^l and c_p^s, by fitting the theoretical predictions to the experimental curves, provided that the corresponding densities are known. ii) From the obtained temperature versus time curves in the liquid and solid regions, and using the determined specific heats, we deduce the corresponding thermal conductivities, k_l and k_s. iii) The latent heat is calculated using the proposed models that are described below.

2.1. Thermal conductivity model, and latent heat enthalpy-based model

We consider a system of a long glass-tube containing a Phase Change Material (PCM). The tube's inner and outer radii are respectively denoted by R_1 and R_2 in **Figure 1**. Let T_l and T_s be the PCM's liquidation and solidification temperatures. The system is brought initially at a temperature $T_0 > T_l$, so that the PCM is in liquid state, and subsequently is immersed in a heat bath maintained at a constant temperature $T_1 < T_s$.

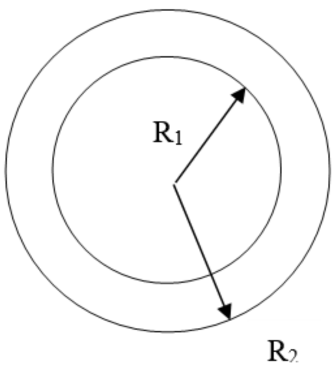

Figure 1. Geometrical representation of the model system.

The temperature "zone" $T \in [T_s, T_l]$, is referred to as the "mushy" zone, where the material is in a "mixed" state, and it is in fact the temperature region where the latent heat is released upon cooling, and therefore, it will be used for its determination. The temperature depends on both time and position. The position is measured from the tube's axis, and is denoted by r. Due to cylindrical symmetry there is no angular dependence, and since the tube is long compared to its radial extent, z-dependence may be neglected.

At $r = R_2$, the temperature is known to be $J(t), \forall t > 0$. Let the subscripts p and g refer to PCM and glass quantities correspondingly. Then, the governing equations for heat conduction may be written as:

$$\rho_p \frac{\partial H_p(r,t)}{\partial t} = k_p(T)\left(\frac{\partial^2 T(r,t)}{\partial r^2} + \frac{1}{r}\frac{\partial T(r,t)}{\partial r}\right) + \frac{dk_p(T)}{dT}\left(\frac{\partial T(r,t)}{\partial r}\right)^2, \quad \mathrm{r} \in [0, R_1] \tag{1}$$

$$\rho_g c_g \frac{\partial T(r,t)}{\partial r} = k_g\left(\frac{\partial^2 T(r,t)}{\partial r^2} + \frac{1}{r}\frac{\partial T(r,t)}{\partial r}\right), \quad \mathrm{r} \in [R_1, R_2] \tag{2}$$

where $H_p(r,t)$ is the enthalpy function of the PCM. Let the quantities c_p^s, c_p^l, L denote its specific heats in the solid and liquid phases and the latent heat per unit mass.

As the apparatus is immersed in the heat-bath, consisting of a tank filled with water, the temperature on the outer glass surface of the tube is not constant for a considerable amount of time. Hence this temperature $T(R_2,t)$ is measured and recorded. Also the temperature at the tube's axis, $T(0,t)$ is measured and recorded as well. Since analytical solutions for such a system do not exist, we will resort to numerical approximate solutions.

Heat conduction through PCMs is a highly nonlinear "moving boundary" problem. The boundary that is moving is the interface between the solid and liquid phase and on which special conditions must be satisfied.

"Front-tracking" methods, monitor the motion of the solid-liquid interface and require the satisfaction of the associated conditions on this moving boundary. A discretization grid is employed, and since the interface position will not always fall on a grid point, either interpolation, or a variable time step, or even a time-dependent grid is employed to accommodate this requirement. These approaches are complicated, have accuracy issues, and their implementation is quite cumbersome if feasible at all.

"Front-fixing" methods apply a variable transformation to immobilize the interface in the new coordinate system. However, the arising equations are even more complicated.

The enthalpy method is a "fixed-domain" method based on a reformulation of the heat conduction equation adopting a model for the enthalpy-temperature relationship. In this approach the solid-liquid interface does not explicitly appear and hence the difficulties due to the moving boundary are avoided. Based on this idea a variety of similar methods have been developed. We have chosen the enthalpy approach because it simplifies the numerical work and provides a direct modelling interpretation. The purpose of this study is to explore the possibility to reliably deduce PCM's properties (i.e., latent heat, thermal conductivity, specific heat, critical temperature, etc.) from the available measurements alone.

The enthalpy may be modelled as:

$$H_p(T) = \begin{cases} c_p^s T, & if\ T < T_s \\ \mathcal{H}_p(T), & if\ T_s \le T \le T_l \\ c_p^l(T - T_l) + c_p^s T_s + \mathrm{L}, & if\ T > T_l \end{cases} \tag{3}$$

where $H_p(T)$ is a fifth order polynomial in T [14], so as to match the enthalpy and its first and second derivatives at the endpoints of the mushy zone: $T \in [T_s, T_l]$.

$$H_p(T) = c_p^s T + A_3\left(\frac{T - T_s}{T_l - T_s}\right)^3 + A_4\left(\frac{T - T_s}{T_l - T_s}\right)^4 + A_5\left(\frac{T - T_s}{T_l - T_s}\right)^5 \tag{4}$$

Letting $\Delta = T_l - T_s$, one obtains:

$$A_3 = 10L - \Delta\left(6c_p^s + 4c_p^l\right) \tag{5}$$

$$A_4 = -15L + \Delta\left(8c_p^s + 7c_p^l\right) \tag{6}$$

$$A_5 = 6L - 3\Delta\left(c_p^s + c_p^l\right) \tag{7}$$

The derivative of the model function is given by:

$$Q_p(T) \equiv \frac{dH_p(T)}{dT} = \begin{cases} c_p^s, & if\ T < T_s \\ \dfrac{d\mathcal{H}_p(T)}{dT}, & if\ T_s \le T \le T_l \\ c_p^l, & if\ T > T_l \end{cases} \tag{8}$$

Note that in Equation (1) we can substitute: $\frac{\partial H_p(r,t)}{\partial t} = \frac{dH_p(T)}{dT}\frac{\partial T(r,t())}{\partial t}$

Therefore Equation (1) may be rewritten as:

$$\rho_p \frac{\partial T(r,\mathrm{t})}{\partial t} = \frac{k_p(T)}{Q_p(\mathrm{T})}\left(\frac{\partial^2 T(r,\mathrm{t})}{\partial t^2} + \frac{1}{r}\frac{\partial T(r,\mathrm{t})}{\partial r}\right) + \frac{1}{Q_p(T)}\frac{dk_p(T)}{\mathrm{dT}}\left(\frac{\partial T(r,\mathrm{t})}{\partial r}\right)^2, \forall r \in [0, R_1] \tag{9}$$

Now for the conductivity as a function of the temperature we use a fifth order polynomial for $T \in (T_s, T_l)$ that is continuous at the mushy zone endpoints along with its first and second derivatives. Namely:

$$k_p(T) = \begin{cases} k_p^s, ifT < T_s \\ K_p(T), ifT_s \le T \le T_l \\ k_p^l, ifT > T_l \end{cases} \tag{10}$$

With

$$K_p(T) = k_p^s + \left(k_p^l - k_p^s\right)\left[10\left(\frac{T - T_s}{T_l - T_s}\right)^3 - 15\left(\frac{T - T_s}{T_l - T_s}\right)^4 + 6\left(\frac{T - T_s}{T_l - T_s}\right)^5\right] \tag{11}$$

Adopting the following definitions:

$$f(T) \equiv \frac{k_p(T)}{\rho_p Q_p(T)} and g(T) \equiv \frac{dk_p(T)}{dT}\frac{1}{\rho_p Q_p(T)} \tag{12}$$

Equation (9) may be rewritten as:

$$\frac{\partial T(r,\mathrm{t})}{\partial t} = f(T)\left(\frac{\partial^2 T(r,\mathrm{t})}{\partial r^2} + \frac{1}{r}\frac{\partial T(r,\mathrm{t})}{\partial r}\right) + g(T)\left(\frac{\partial T(r,\mathrm{t})}{\partial r}\right)^2, \forall r \in [0, R_1] \quad (13)$$

2.2. Initial, boundary, and interface conditions

At the origin, due to azimuthal symmetry, the following Neumann condition holds:

$$\frac{\partial T(r,t())}{\partial r}|_{r=0}\Big| \quad (14)$$

At the PCM-glass interface, continuity of temperature and heat-flux requires that:

$$T(R_1 - \varepsilon, t) = T(R_1 + \varepsilon, t) \quad (15)$$

$$k_p(T)\frac{\partial T(r,t())}{\partial r}|_{r=R_1-\varepsilon}\, k_g(T)\frac{\partial T(r,t())}{\partial r}|_{r=R_1+\varepsilon}\Big\|\quad (16)$$

At the outer tube boundary, we have:

$$T(R_2, t) = J(t) \quad (17)$$

And initially, i.e., at t = 0:

$$T(r,0) = \theta_0, \forall \in [0, \mathrm{R}_2] \quad (18)$$

2.3. Discretization

Let $n+1$ points $r_i, i = 0,1,\ldots,n$ be the grid for $r \in [0, R_1]$ which is the space filled by the PCM, and let $m+1$ points $r_{n+j}, j = 0,1,\ldots,m$ be the grid over the glass part, i.e., for $r \in [R_1, \mathrm{R}_2]$.

$$r_i = ih \equiv \frac{i}{n}R_1, \forall i = 0,1,\ldots,n \quad (19)$$

$$r_{n+j} = R_1 + j\delta \equiv R_1 + \frac{j}{m}(R_2 - R_1), \forall j = 0,1,\ldots,m \quad (20)$$

Space derivatives are estimated by central differences as:

$$\frac{\partial T(r,t)}{\partial r} \approx \frac{T(r+s,t) - T(r-s,t)}{2s} \quad (21)$$

$$\frac{\partial^2 T(r,t)}{\partial r^2} \approx \frac{T(r+s,t) + T(r-s,t) - 2T(r,t)}{s^2} \quad (22)$$

And the time derivative by forward differences as:

$$\frac{\partial T(r,t)}{\partial t} \approx \frac{T(r,t+\tau) - T(r,t)}{\tau} \quad (23)$$

In order to solve Equations (2) and (9), we have chosen the implicit and unconditionally stable Crank-Nicolson scheme. We use the following notation:

$$T_i^j = T(r_i, j\tau), f_i^j = f\left(T_i^j\right), g_i^j = g\left(T_i^j\right), \text{ and } a_g = \frac{k_g}{\rho_g c_g}$$

At $r \to 0, \frac{\partial^2 T(r,t)}{\partial r^2} + \frac{1}{r}\frac{\partial T(r,t)}{\partial r} = \frac{4}{h^2}\Big(T\big((h,t) - T(0,t)\big)\Big) = \frac{4}{h^2}\left(T_1^j - T_0^j\right)$ for $t = j\tau$

The Crank-Nicolson scheme yields [15,16]:

$$\begin{aligned} T_i^{j+1} = T_i^j &+ \frac{\tau}{2}\left[f\left(T_i^{j+1}\right)\nabla^2 T_i^{j+1} + f\left(T_i^j\right)\nabla T_i^j\right] \\ &+ \frac{\tau}{2}\left[g\left(T_i^{j+1}\right)\left(\frac{\partial T_i^{j+1}}{\partial r}\right)^2 + g\left(T_i^{j+1}\right)\left(\frac{\partial T_i^{j+1}}{\partial r}\right)^2\right], \forall i \in [0, n] \end{aligned} \tag{24}$$

$$T_i^{j+1} = T_i^j + \frac{\tau a_g}{2}\left[\nabla^2 T_i^{j+1} + \nabla^2 T_i^j\right], \forall i \in [n, n+m] \tag{25}$$

For $i = 0$ Equation (24) may be rewritten as:

$$T_0^{j+1} - \frac{2\tau}{h^2} f_0^{j+1}\left(T_1^{j+1} - T_0^{j+1}\right) = T_0^j + \frac{2\tau}{h^2} f_0^j\left(T_1^j - T_0^j\right) \tag{26}$$

For $i = 1, 2, \ldots, n-1$ Equation (24) takes the form:

$$\begin{aligned} &\left(1 + \frac{\tau}{h^2} f_i^{j+1}\right) T_i^{j+1} - \frac{\tau}{2h^2} f_i^{j+1}\left(\left(1 + \frac{1}{2i}\right) T_{i+1}^{j+1} + \left(1 - \frac{1}{2i}\right) T_{i-1}^{j+1}\right) \\ &\qquad - \frac{\tau}{8h^2} g_i^{j+1}\left(T_{i+1}^{j+1} - T_{i-1}^{j+1}\right)^2 \\ &\qquad = \left(1 - \frac{\tau}{h^2} f_i^j\right) T_i^j + \frac{\tau}{2h^2} f_i^j\left(\left(1 + \frac{1}{2i}\right) T_{i+1}^j + \left(1 - \frac{1}{2i}\right) T_{i-1}^j\right) \\ &\qquad + \frac{\tau}{8h^2} g_i^j\left(T_{i+1}^j - T_{i-1}^j\right)^2 \end{aligned} \tag{27}$$

For $i = n$ using the interface conditions (15,16) we obtain the relation:

$$k_p\left(T_n^{j+1}\right)\frac{T_n^{j+1} - T_{n-1}^{j+1}}{h} - k_g\frac{T_{n+1}^{j+1} - T_n^{j+1}}{\delta} = 0 \tag{28}$$

For $i = n+1, n+2, \ldots, n+m-1$ and with $x_i = i - n + \frac{R_1}{\delta}$

$$\begin{aligned} &\left(1 + \frac{\tau a_g}{\delta^2}\right) T_i^{j+1} - \frac{\tau a_g}{2\delta^2}\left(\left(1 + \frac{1}{2x_i}\right) T_{i+1}^{j+1} + \left(1 - \frac{1}{2x_i}\right) T_{i-1}^{j+1}\right) \\ &\qquad = \left(1 - \frac{\tau a_g}{\delta^2}\right) T_i^j + \frac{\tau a_g}{2\delta^2}\left(\left(1 + \frac{1}{2x_i}\right) T_{i+1}^j + \left(1 - \frac{1}{2x_i}\right) T_{i-1}^j\right) \end{aligned} \tag{29}$$

And finally for $i = n+m$ we have from the boundary condition Equation (17)

$$T_{n+m}^{j+1} = J\big((j+1)\tau\big) \tag{30}$$

So at each time step, we face a system of $n + m + 1$ nonlinear Equations (26)–(30), for the $n + m + 1$ unknowns, $T_{i=0,n+m}^{j+1}$. The solution procedure is based on nonlinear optimization and minimizes the sum of the squared residuals [17–21].

3. Results

Lauric acid is a well-studied PCM, and we have used it as a benchmark to test the proposed methodology. We have used the presented experimental setup to obtain the necessary measurements (**Figure 2**) and subsequently performed the suggested analysis to estimate the relevant Lauric acid properties.

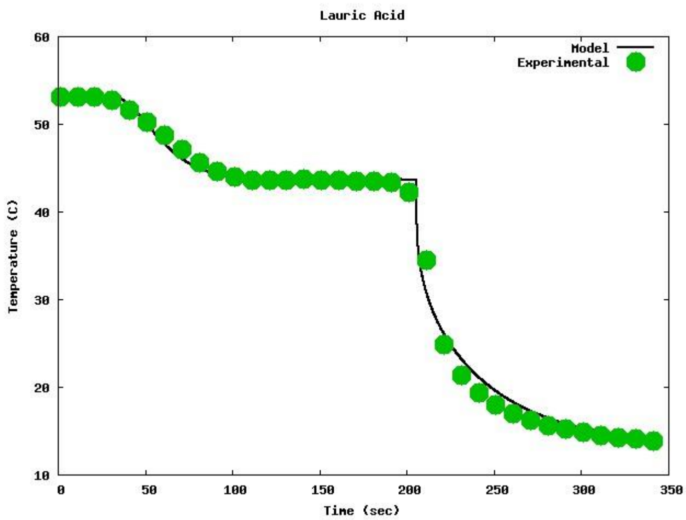

Figure 2. Application of the proposed method for the benchmark case of Lauric acid.

As it can be seen the solution reproduces satisfactorily the experimental data. Once this solution is achieved, Latent Heat, specific Heats and thermal conductivities in the three regions (Liquid, Mushy zone and Solid) are deduced. Our results are summarized in **Table 1**, and are compared to estimates from the relevant literature.

Table 1. Comparison of Lauric acid properties by our model, to values from the literature.

Latent Heat	**Specific Heat Solid Phase**	**Specific Heat Liquid Phase**	**Thermal Conductivity Solid Phase**	**Reference**
$L\ (KJ/Kg)$	$c_p^s\ (KJ/Kg\ K)$	$c_p^l\ (KJ/Kg\ K)$	$k^s\ (W/mK)$	
180 ± 7	2.14 ± 0.11	2.02 ± 0.08	0.23 ± 0.02	Present work
160	-	1.75	0.17	Ref. [7]
186 ± 10	2.81 ± 0.60	2.14 ± 0.46	-	Ref. [8]

4. Conclusions

We have presented a novel enthalpy-based method that provides a holistic description of the temperature evolution of a PCM upon cooling or heating, while the determination of their thermal properties can be deduced by performing two simple experiments. Note that as result, the thermal conductivity coefficients can be evaluated in the three temperature ranges of interest corresponding to liquid, solid and intermediate (mushy) phases. The method has been successfully applied to the Lauric acid prototype, estimating its thermal properties within reasonable error, and consequently it could be useful for the analysis and design of heat storage PCM-based systems.

Highlights

1) PCM thermal properties via simple measurements, coupled to an enthalpy model.
2) Non-linear heat conduction PDE, solved by optimization.
3) Test case: Lauric acid. Determination of thermal conductivity, latent & specific heats.

Author contributions: Conceptualization, GAE and IEL; methodology, IEL; software, IEL and DGP; validation, GAE and CP; formal analysis, IEL; investigation, GAE and CP; data curation, CP; writing—original draft preparation, GAE and IEL; writing—review and editing, GAE and IEL; supervision, GAE; project administration, GAE; funding acquisition, GAE. All authors have read and agreed to the published version of the manuscript.

Conflict of interest: The authors declare no conflict of interest.

Nomenclature

PCM	Phase Change Material
DSC	Differential Scanning Calorimetry
c_p^l	Specific heat of liquid
c_p^s	Specific heat of solid
k_l	Thermal conductivity of liquid
k_s	Thermal conductivity of solid
R_1	Inner radius of the glass tube
R_2	Outer radius of the glass tube
T_l	Liquidation temperature
T_s	Solidification temperature
T_0	Initial temperature
H_p	The enthalpy function of the PCM
L	Latent heat per unit mass
$T(R_2,t)$	Tube temperature at the outer surface at time t
T(R1,t)	Tube temperature at the inner surface at time t
$T(R_0,t)$	Tube temperature at the central axis at time t

References

1. Zhang X, Wu JY, Niu J. PCM-in-water emulsion for solar thermal applications: The effects of emulsifiers and emulsification conditions on thermal performance, stability and rheology characteristics. Solar Energy Materials and Solar Cells. 2016; 147: 211-224. doi: 10.1016/j.solmat.2015.12.022
2. Selvnes H, Allouche Y, Manescu RI, et al. Review on cold thermal energy storage applied to refrigeration systems using phase change materials. Thermal Science and Engineering Progress. 2021; 22: 100807. doi: 10.1016/j.tsep.2020.100807
3. Reji Kumar R, Samykano M, Pandey AK, et al. Phase change materials and nano-enhanced phase change materials for thermal energy storage in photovoltaic thermal systems: A futuristic approach and its technical challenges. Renewable and Sustainable Energy Reviews. 2020; 133: 110341. doi: 10.1016/j.rser.2020.110341
4. D'Oliveira EJ, Pereira SCC, Groulx D, et al. Thermophysical properties of Nano-enhanced phase change materials for domestic heating applications. Journal of Energy Storage. 2022; 46: 103794. doi: 10.1016/j.est.2021.103794

5. Shao J, Darkwa J, Kokogiannakis G. Review of phase change emulsions (PCMEs) and their applications in HVAC systems. Energy and Buildings. 2015; 94: 200-217. doi: 10.1016/j.enbuild.2015.03.003
6. Fatahi H, Claverie J, Poncet S. Thermal Characterization of Phase Change Materials by Differential Scanning Calorimetry: A Review. Applied Sciences. 2022; 12(23): 12019. doi: 10.3390/app122312019
7. Yinping Z, Yi J, Yi J. A simple method, the -history method, of determining the heat of fusion, specific heat and thermal conductivity of phase-change materials. Measurement Science and Technology. 1999; 10(3): 201-205. doi: 10.1088/0957-0233/10/3/015
8. Hong H, Kim SK, Kim YS. Accuracy improvement of T-history method for measuring heat of fusion of various materials. International Journal of Refrigeration. 2004; 27(4): 360-366. doi: 10.1016/j.ijrefrig.2003.12.006
9. Mar n JM, Zalba BN, Cabeza LF, et al. Determination of enthalpy temperature curves of phase change materials with the temperature-history method: improvement to temperature dependent properties. Measurement Science and Technology. 2003; 14(2): 184-189. doi: 10.1088/0957-0233/14/2/305
10. Gopinathan A, Jerz J, Kováčik J, et al. Implementation of T-history method to determine the thermophysical properties of the phase change materials. Thermochimica Acta. 2023; 723: 179485. doi: 10.1016/j.tca.2023.179485
11. Jansone D, Dzikevics M, Veidenbergs I. Determination of thermophysical properties of phase change materials using T-History method. Energy Procedia. 2018; 147: 488-494. doi: 10.1016/j.egypro.2018.07.057
12. Miyagi S. Measurement method for T-h properties of phase change material. Journal of Asian Architecture and Building Engineering. 2022; 22(4): 2376-2391. doi: 10.1080/13467581.2022.2153062
13. Ye WB, Arıcı M. Redefined interface error, 2D verification and validation for pure solid-gallium phase change modeling by enthalpy-porosity methodology. International Communications in Heat and Mass Transfer. 2023; 147: 106952. doi: 10.1016/j.icheatmasstransfer.2023.106952
14. Obreshkov N. On the Mechanical Quadratures. J. Bulgar. Acad. Sci. and Arts LXV-8. 1942; 191-289.
15. Crank J. Free and Moving Boundary Problems. Oxford Science Publications; 1988.
16. Alexiades V, Solomon AD, Lunardini VJ. Mathematical Modeling of Melting and Freezing Processes. Journal of Solar Energy Engineering. 1993; 115(2): 121-121. doi: 10.1115/1.2930032
17. Hu H, Argyropoulos SA. Mathematical modelling of solidification and melting: a review. Modelling and Simulation in Materials Science and Engineering. 1996; 4(4): 371-396. doi: 10.1088/0965-0393/4/4/004
18. Voller VR, Swaminathan CR, Thomas BG. Fixed grid techniques for phase change problems: A review. International Journal for Numerical Methods in Engineering. 1990; 30(4): 875-898. doi: 10.1002/nme.1620300419
19. Date AW. A strong enthalpy formulation for the Stefan problem. Int. J. Heat mass Transfer. 1991; 34(1991): 2231-2235. doi: 10.1016/0017-9310(91)90049-K
20. Caldwell J, Chan CC. Numerical solutions of Stefan problem in annuli by enthalpy method and heat balance integral method. Communications in Numerical Methods in Engineering. 2001; 17(6): 395-405. doi: 10.1002/cnm.415
21. Idelsohn SR, Storti MA, Crivelli LA. Numerical methods in phase-change problems. Archives of Computational Methods in Engineering. 1994; 1(1): 49-74. doi: 10.1007/bf0273618

Thermal Science and Engineering 2025, 8(1), 9883.
https://doi.org/10.24294/tse9883

Article

Numerical analysis of closed loop pulsating heat pipe with varying condenser temperatures

Sriram Chidambaranathan

College of Engineering Guindy, Anna University, Chennai 600025, India; sriraamc86@gmail.com

CITATION

Chidambaranathan S. Numerical analysis of closed loop pulsating heat pipe with varying condenser temperatures. Thermal Science and Engineering. 2025; 8(1): 9883. https://doi.org/10.24294/tse9883

ARTICLE INFO

Received: 25 October 2024
Accepted: 19 December 2024
Available online: 2 January 2025

Abstract: A numerical investigation utilizing water as the working fluid was conducted on a 2D closed loop pulsating heat pipe (CLPHP) using the CFD software AnsysFluent19.0. This computational fluid dynamics (CFD) investigation explores three instances where there is a consistent input of heat flux in the evaporator region, but the temperatures in the condenser region differ across the cases. In each case, the condenser temperatures are set at 10 °C, 20 °C, and 30 °C respectively. The transient simulation is conducted with uniform time steps of 10 s. Generally, the heat rejection medium operated at a lower temperature performs better than at a higher temperature. In this CFD study the thermal resistances gets decreased with the decreasing value of condenser temperatures and the deviation of 35.31% of thermal resistance gets decreased with the condenser region operated at the temperature of 10 °C.

Keywords: closed loop pulsating heat pipe; boiling and condensation; slug and plug flow; thermal resistance; Nusselt number

1. Introduction

With the rapid development of electronic components miniaturization, heat dissipation in the electronic components also proliferated. The performance of the electronic components is affected not only by the heat generated inside the components but also by temperature, which plays a major role. Therefore, proper thermal management is necessary to provide a stable operation in the electronic components. The heat pipe is mainly used to carry out the heat dissipation in the electronic components. The heat pipe is a passive heat exchanger device that transports heat with high thermal conductivity and low resistance. Out of the several types of heat pipes, a commonly used passive heat-exchanging device called a pulsating heat pipe is studied in this research work. The Closed-loop pulsating heat pipe is a two-phase heat transfer device that operates between the evaporator and condenser medium. According to Akachi [1], a pulsating heat pipe is a long metallic capillary tube with an internal dimension small enough to enable compressed two-phase working fluid, which is sealed inside the metallic capillary tube. Wu et al. [2] investigated experimentally and numerically refrigerant flow boiling in horizontal serpentine tubes, and they concluded that the stratification flow exists in the horizontal tube and the buoyancy force is dominant against gravity. Rudresha et al. [3] study deals with the experimental as well as numerical investigation of the thermal performance of CLPHP charged with DI water and Nanofluids such as SiO_2/DI Water and Al_2O_3/DI Water, and he found that the heat transfer coefficient gets increased with Nanofluids than DI Water. Erfan et al. [4] made a comparison of a four-turn aluminum flat plate PHP and an additional branch on the evaporator section on the same. The authors investigated different filling ratios and heat inputs, which showed that the thermal resistance decreased by up to 11%–20% by using an additional branch on the evaporator section on the four-turn PHP. Pramod et al. [5] did experimental work on two turn copper closed loop pulsating heat pipe with a single component fluid such as water, ethanol, methanol, and acetone and also with binary mixtures such as water-ethanol, water-methanol, and water-acetone. The authors validated the experimental results numerically, and his results show that thermal performance was increased with the use of working fluid as a binary mixture of water-acetone. Anwar et al. [6] study deals with an investigation of seven-turn CLPHP with water as a working fluid in which the evaporator section is heated employing hot air with different velocities such as 0.5, 1, and 1.5 m/s, and proposed that the thermal resistance was found low with high heat input. He also compared the experimental investigation with a CFD study of maximum heat input of 107.75 W and with the minimum heat input of 13.75 W corresponding to the air inlet temperature. Karthikeyan et al. [7] investigated eight-turn copper pulsating heat pipes with water as a working fluid, and the wall temperatures were measured employing high-resolution infrared thermography, in which the authors studied the flow behavior inside the CLPHP also concluded that the thermal resistance was found lower with the heat input increased from 30 W to 500 W. Duy-Tan et al. [8] investigated experimentally and numerically with eight-turn PHP using working fluid as R123, and they found that the CFD analysis work matches the experimental work with the use of the k-ε turbulence model. Przemyslaw et al. [9] validated the numerical model with the experimental data on a three three-turn PHP with ethanol as a working fluid and stated that the relative error was obtained at a 10% level. Nick et al. [10] investigated the effect of condenser temperatures in a PHP, and they concluded that lower thermal resistance was obtained by increasing condenser temperatures. Jiaqiang et al. [11] did a numerical investigation on single-turn and two-turn CLPHP by considering the VOF model. He found that the double-turn CLPHP has higher heat transfer capability than the single-turn CLPHP. Jiansheng et al. [12] analyzed numerically a CLPHP with a partial horizontal structure (Evaporator and Condenser Sections are horizontal) by varying filling ratios and heat flux, and in which the author's results reveal that when the height difference between the evaporator and condenser section is more the thermal performance gets increased. Qingfeng et al. [13] numerical work deals with the anti-dry out in the evaporator section of the CLPHP with the use of micro-encapsulated phase change material, and his study proves that the start-up time, circulation of flow, and heat transfer performance were improved significantly with the use of phase change material compared with water. Kalpak et al. [14] conducted a 2D simulation of CLPHP with liquid Nitrogen as a working fluid. It was tested with ground level, low gravity, and milli-gravity conditions with different filling ratios. The authors concluded that more stable flow patterns and heat transfer performance were observed in low-gravity conditions when compared with ground-level conditions. Fubo et al. [15] investigated numerically a single-turn CLPHP with two different evaporator geometries, such as a round end and a right-angled end with different heat inputs and in which he proposed a result of later geometry shows rarely the stop-over phenomenon and an increased heat transfer performance. Zirong et al. [16] work deals with the miniature oscillating pulsating heat pipes in which the authors used the

VOF approach with different models in the numerical work; in addition to that, the authors worked on changing the heating source length, internal diameter, and heat input power and the authors concluded that the internal diameter of the OPHP plays a vital role. Hyung et al. [17] made a one-dimensional model assuming liquid slug/vapor plug flow by considering the phase interactions between the solid wall and the liquid film. They also validated the experimental data which is available in the literature. Finally, the authors concluded that by choosing the high merit number (criterion for selecting working fluids), the thermal performance of the CLPHP is maximized. Zufar et al. [18] made 2D simulations on CLPHP with water-based Nano fluids such as Diamond, Silver, and Silica Oxide. The authors studied numerically with constant heat flux and filling ratio and came up with the outcome of diamond-based nanofluids performing better with lower thermal resistance. Jongwook et al. [19] investigated a 2D CLPHP numerically with ethanol as the working fluid in a multi-turn geometry with symmetric and asymmetric modes. The authors predicted that the starting time of the CLPHP with an asymmetric shape is earlier than with a symmetric shape. Also, he found that in the case of zero gravity, the fluid gets dried out in the case of 5 and 10 turns, whereas the fluid remains in the evaporator section in the case of 15 and 20 turns, respectively. Jiansheng et al. [20] research work deals with the simulation of 2D single loop CLPHP with varying.

Heat input from 10 W to 40 W and varying filling ratios from 30% to 60%, respectively, and the authors found that the thermal resistance decreased with the high heat input and also with the same filling ratio and input power also the authors varied the condenser length of the CLPHP in which he observed that the start-up time gets accelerated. Ayad et al. [21] analyzed wickless heat pipe using a commercial CFD package, and the flow behavior, heat transfer features, and boiling regimes were studied using their inbuilt user-defined functions. Also, the wickless heat pipe was investigated with different filling ratios, inclination angles, and heat added. Jiansheng et al. [22] performed a 3D simulation in comparison with deionized water and a surfactant called hexadecyl trimethyl ammonium chloride by changing the initial pressure and heat input. The authors suggested that by using surfactant as a working fluid under high initial pressure, the performance of CLPHP was not good. With low initial pressure, its performance also increases, and the heat transfer performance of CLPHP increases with high heat inputs; thereby, the use of surfactants prevents the drying out of the evaporator section. The above-discussed literature shows that the CFD analysis was carried out with fixed evaporator heat input and constant condenser temperatures. This research work entails a numerical investigation focusing on fixed evaporator heat flux boundary conditions while examining the relatively underexplored aspect of varying condenser temperatures. A 2D computational fluid dynamics (CFD) analysis is conducted using water as the working fluid, with the condenser temperatures manipulated to be below ambient temperature.

2. Research methodology

The current research methodology encompasses several key steps, including geometry creation, meshing, and solver setup. This involves selecting appropriate models, patching, probe setup, and determining the precise time step size. This present numerical work focuses on the literature [10] and it can be validated to some extent The following section provides a brief overview of the aforementioned research

2.1. Geometry of CLPHP

A thorough literature survey has been carried out, and based on the literature, [23] the following geometry as shown in the **Figure 1** has been selected for the numerical work. The geometry is set as two turns with equal dimensions of the evaporator, adiabatic, and condenser sections, and the internal diameter is 2 mm throughout the pipe.

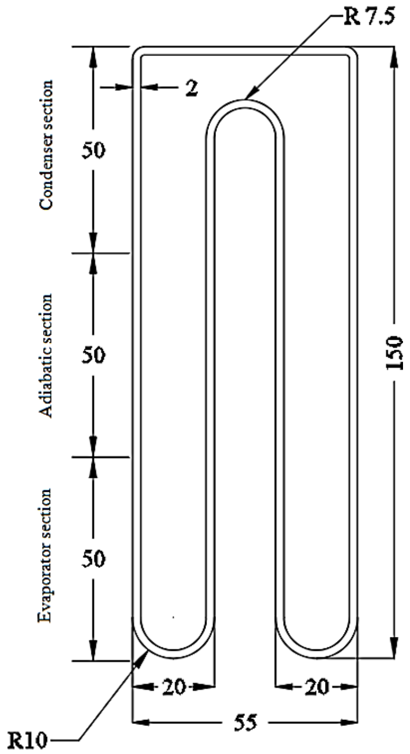

Figure 1. Geometry of CLPHP.

Note: All dimensions in 'mm'.

2.2. Meshing

Meshing is done by using Hypermesh Software and Quadrilateral elements are used for meshing. **Figures 2** and **3** describes the meshing of the CLPHP. The details of the mesh are described below in **Table 1**.

Table 1. 2D mesh description.

Total Nodes	Total elements	Size of the Elements	Type of mesh
23,661 nodes	21,032 elements	0.25 mm	Quadrilateral mesh

Figure 2. 2D meshing of CLPHP.

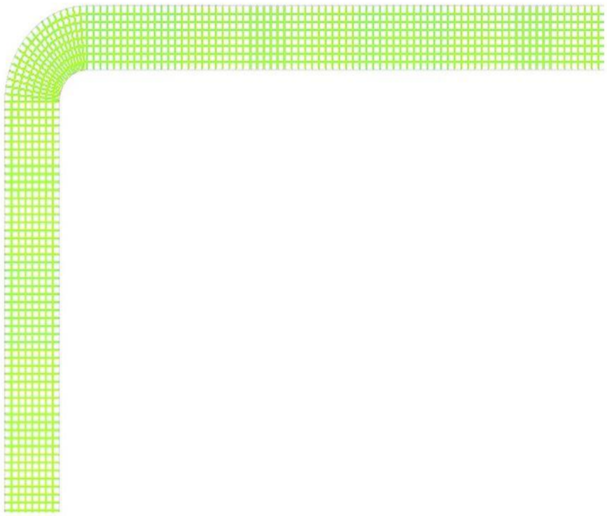

Figure 3. Cut section of 2D mesh of CLPHP.

2.3. Multiphase flow analysis (VOF)

The problem is based on multiphase flow; the VOF model is chosen, and 3 phases have been selected in the GUI. The 3 phases include water liquid, water vapor, and air. We know that all CFD simulations have a set of governing equations: continuity or mass, momentum, and energy equations. Here, the VOF model is based on multiphase flow. It has a separate equation that includes phase fraction, which has to be solved for both liquid and vapor phases. The VOF governing equations are discussed below.

2.4. Governing equations

The flow inside the CLPHP consists of liquid slugs and vapor plugs, which are immiscible fluids. To track the immiscible fluids (liquid-gas), the VOF approach is generally used, and the phase fraction (α) is used to calculate the distinct phases. The condition for the phase fraction (α) was revisited and rephrased for accuracy and clarity. Specifically, the definition now explicitly states that α represents the local volumetric fraction of the liquid or vapor phase and satisfies the condition $0 \leq \alpha \leq 1$. There exists a condition for phase fraction (α), which is given by:

When $\alpha_q = 0$, the cell is empty (No fluids present), $\alpha_q = 1$, the cell is filled with fluid (Full fluid is present), and $0 < \alpha_q < 1$, the cell has a mixture of two or three fluids.

2.5. Mass equation

In CLPHP the evaporation and condensation phenomenon takes place, the liquid-vapor mass transfer is governed by the vapor transport Equation (1) and it is given by:

$$\frac{\partial(\alpha_v \rho_v)}{\partial t} + \nabla.(\alpha_v \rho_v v_v) = \dot{m}_{lv} - \dot{m}_{vl} \tag{1}$$

In the case of evaporation, $T_l > T_{sat}$

$$\dot{m}_{lv} = r_{lv}.\alpha_l \rho_l \frac{(T_l - T_{sat})}{T_{sat}} \tag{2}$$

In the case of condensation, $T_v < T_{sat}$

$$\dot{m}_{vl} = r_{vl}.\alpha_v \rho_v \frac{(T_{sat} - T_v)}{T_{sat}} \tag{3}$$

2.6. Momentum equation

A single set of momentum Equation (4) is solved throughout the domain, which is given by:

$$\frac{\partial(\rho\vec{v})}{\partial t} + \nabla.(\rho\vec{v}\vec{v}) = -\nabla P + \nabla.[\mu(\nabla\vec{v} + \nabla\vec{v}^T)] + \rho\vec{g} + \vec{F}_{vol} \tag{4}$$

The surface tension arises because of the cohesive force of the molecules, and it creates a surface force that is added to the source term in the momentum equation. This force in the surface is called volume force, and it is given by:

$$F_{vol} = \sigma_{lv} \frac{\alpha_l \rho_l k_v \nabla\alpha_v + \alpha_v \rho_v k_l \nabla\alpha_l}{\frac{1}{2}(\rho_l + \rho_v)} \tag{5}$$

where the curvature is expressed as

$$k_l = \frac{\Delta\alpha_l}{\nabla\alpha_v} \text{ and } k_v = \frac{\Delta\alpha_v}{\nabla\alpha_l}$$

2.7. Energy equation

The energy shared by the phases Equation (6) is given by the equation:

$$\frac{\partial(\rho E)}{\partial t} + \nabla.(\vec{v}(\rho E + P)) = \nabla.(K.\nabla T) + S_h \tag{6}$$

where S_h is the source term caused by the phase change obtained by multiplying the mass transfer rate by the latent heat.

The expressions for energy shared by the two phases are given by:

$$E = \frac{\alpha_l \rho_l E_l + \alpha_v \rho_v E_v}{\alpha_l \rho_l + \alpha_v \rho_v} \tag{7}$$

where the specific heat of the phases is given by:

$$E_l = C_{v,l}(T - T_{sat}) \tag{8}$$

$$E_v = C_{v,v}(T - T_{sat}) \tag{9}$$

The properties like ρ, K, and μ shared by the phases are given by:

$$\rho = \alpha_l \rho_l + \alpha_v \rho_v \tag{10}$$

$$K = \alpha_l K_l + \alpha_v K_v \tag{11}$$

$$\mu = \alpha_l \mu_l + \alpha_v \mu_v \tag{12}$$

2.8. Setting the probe

The temperature in the evaporator, adiabatic, and condenser sections has to be monitored till the given time steps so that the analytical calculations can be made easily. As the geometry is 2D and the CLPHP is made in two loops, the temperature in each loop of the evaporator section, adiabatic section, and condenser section must be monitored to take the average values. In total, six probes have to be set in the 2D geometry, of which two probes monitor the temperature in the evaporator section, two probes monitor the temperature in the adiabatic section, and two probes monitor the temperature in the condenser section, respectively. From the 2D geometry, the probes are set in the monitor tab in the GUI of fluent, in which points are created in the locations of the evaporator, adiabatic, and condenser sections. In total, six points are designed and created by measuring the X and Y coordinates of the geometry. These created points are then renamed so the data extracted can be easily identified. The probes in the evaporator section are renamed as Te1 and Te2, the probes in the adiabatic section are renamed as Ta1 and Ta2, and the probes in the condenser section are renamed as Tc1 and Tc2, respectively. The suffix indicates the location in the first and second loops of the CLPHP. After renaming the probes under the monitor option in the GUI report, a plot is selected for the selected probes so that the temperature in each section is extracted for the given number of time steps while running the simulation and saved in a separate text file. These temperature data in the evaporator, adiabatic, and condenser sections are then used analytically to calculate thermal resistance and heat transfer coefficient. The below **Figure 4** shows the probes which has been set in the CLPHP.

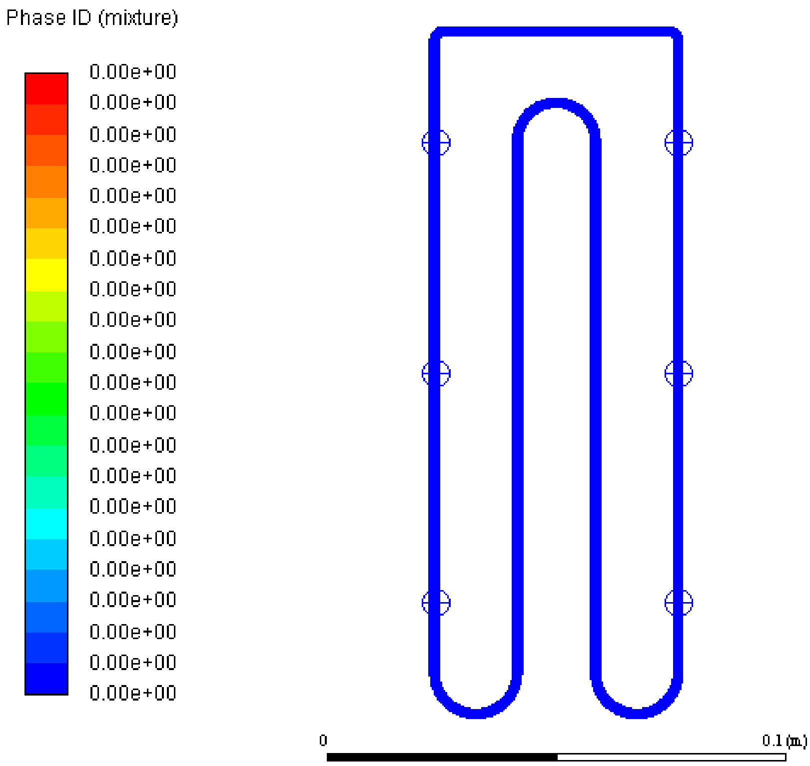

Figure 4. Probes representation in the CLPHP.

2.9. Initializing and patching

The solution is initialized first in the solution initialization option present in the GUI, and the standard initialization iteration method is selected in this simulation. The temperature in the fluid domain is initialized as 303 K, as the simulation has been done for three different condenser wall temperatures of 10 °C, 20 °C, and 30 °C, and the liquid volume fraction and air volume fraction is set as '0' because the next step is to fill the liquid water and air inside the CLPHP. Patching is filling the fluid inside the CLPHP with a suitable proportion. Liquid water and air are patched inside the CLPHP, considering liquid water is patched to 50% of the total volume, and the remaining 50% constitutes the air volume. We can notice from the geometry that the evaporator is at the bottom, and heat flux is applied to it, so the water has to be patched from the bottom of the geometry.

The geometry is created with a total height of 150 mm; as we know, the evaporator, adiabatic, and condenser sections comprise 50 mm each, half of the total height, i.e., 75 mm from the bottom has to be patched with the liquid water and the remaining volume is patched as air. To create a patch for the liquid water in the CLPHP, an option called mark is there in the region where the coordinates are given for patching the liquid water, and then the volume fraction is set to '1'. The same procedure is done for patching the air in the remaining portion of the CLPHP. After patching the liquid water and air in the CLPHP, the new data is created, which indicates the initial time step, i.e., at 0 s, from which the simulation was started. The **Figure 5** below shows the liquid water and air volume fractions created in the CLPHP.

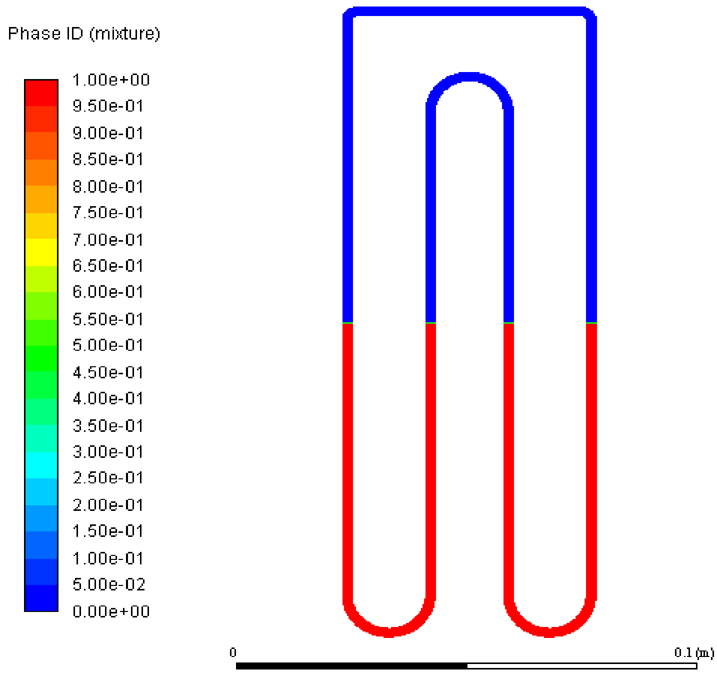

Figure 5. Liquid patch representation on CLPHP.

2.10. Case setting in fluent

In the general tab, the following setting is done. They are as follows:

a) Type of Solver—Pressure based solver is used in this current work and as the working fluid used is incompressible water, the analysis has to be carried out on the same.

b) Time—Transient is used. In the multiphase analysis, the phase fraction has to be calculated in each time step, and generally, PHP works in an unsteady state. Therefore, the transient state is selected.

c) Gravity—The orientation of the CLPHP is vertical (i.e. 90°). The acceleration due to gravity is taken in the negative Y axis, given as −9.81 m/s^2.

2.11. Viscous model

In order to find whether the flow is laminar or turbulent, it is necessary to calculate the Reynolds number. The Reynolds number (13) is given by,

$$\mathrm{Re} = \frac{\rho \times v \times d}{\mu} \tag{13}$$

where the density (ρ) and kinematic viscosity (μ) are taken from the saturation pressure and temperature, as we know that the PHP is operated under vacuum, the operating pressure is taken as 4000 pascals, [24] which is studied from the literature. The saturation pressure is found to be 0.04 bar, from which the saturation temperature must be calculated. The saturation temperature is calculated from the Antoine equation, which is given below.

In general, the Antoine Equation (14) is given as:

$$\log_{10}(P) = A - \frac{B}{T + C} \tag{14}$$

where *A*, *B*, and *C* are constants.

$$\log_{10}(0.04) = 5.31384 - \frac{1690.864}{T - 51.804} \tag{15}$$

$$-1.39794 + \frac{1690.864}{T - 51.804} = 5.31384 \tag{16}$$

$$\frac{1690.864}{T - 51.804} = 5.31384 + 1.39794 \tag{17}$$

$$6.71178T - 347.69705 = 1690.864 \tag{18}$$

$$6.71178T = 2038.56105 \tag{19}$$

$$T = 303.72 \text{ K} \tag{20}$$

$$T = 30\ ℃ \tag{21}$$

Thus, the saturation temperature is 30 ℃, corresponding to the saturation pressure of 4000 Pa or 0.04 bar.

With the above data of saturation temperature and pressure, the properties of water liquid, water vapor, and air can be taken from the available resources. The following **Table 2** shows the properties of water liquid, water vapor, and air at a saturation temperature of 30 ℃ and saturation pressure of 0.04 bar.

Table 2. Properties of water at a saturation temperature of 30 ℃.

Fluid	**Density (ρ) (kg/m^3)**	**Dynamic Viscosity (μ) (kg/ms)**	**Specific Heat (C_p) (kj/kgK)**	**Thermal Conductivity (K) (W/mK)**	**Surface Tension (σ) (N/m)**
Water (liquid)	995.91	0.00081	4.180	0.613	0.07
Water (Vapor)	0.0287	0.000009	1.916	0.018	
Air	0.0461	0.000018	1004.83	0.027	

Now, the Reynolds number calculated based on Equation (13) is 2213.13.

We know that when the Re < 2300, the flow is said to be laminar. Therefore, a laminar viscous model is chosen to simulate the fluid flow in the CLPHP.

2.12. Phase definition and phase interactions

This work has three phases: liquid, vapor, and air. In the VOF approach, all three phases have to be defined. The phase descriptions are as follows.

1) Water vapor—Primary phase;
2) Water liquid—Secondary phase;
3) Air—Secondary phase.

In addition to the phase definitions, the phase interactions must also be defined. Phase interactions are nothing but mass transfer and surface tension. Mass transfer occurs in the CLPHP due to its evaporation and condensation, and as the pipe diameter is so slight, surface tension plays an important role. It also has to be adequately defined. At saturation temperature, the liquid turns to vapor, and the vapor turns liquid. So, the evaporation–condensation mechanism is defined as the mass interaction from the vapor to the liquid phase. The Continuum surface force (CSF) model modeled the surface tension force, and the constant value of 0.07 N/m is given as input to the surface tension coefficient.

2.13. Boundary conditions

The CLPHP geometry is divided into three zones: evaporator in the bottom, adiabatic zone in the middle, and condenser in the top. All three sections are equally divided with a height of 50 mm, each having an inner diameter of 2 mm. As we discussed before, the liquid water is patched to 50% of the total volume of the CLPHP, and the remaining portion is filled with air. Generally, the boundary conditions are given at the walls of the sections,

and here, they are given at the evaporator, adiabatic, and condenser sections. The heat flux given at the walls of the evaporator gives rise to the temperature, and the heat gets rejected at the condenser, producing a pulsation effect. Zero heat flux is given at the adiabatic zone so that no heat transfer occurs in this zone. In this work, the evaporator and adiabatic zone wall conditions are fixed, and the condenser wall temperature is changed in all three cases to investigate the effect of the thermal performance of CLPHP. The boundary conditions used in this analysis in all three cases are discussed below:

a) Evaporator—constant heat flux of 10,000 w/m^2 [25] having a wall thickness of 0.005 m (Neumann).
b) Adiabatic—constant heat flux of 0 w/m^2 having a wall thickness of 0.005 m (Neumann).
c) Condenser—Temperature of 10 ℃, 20 ℃, and 30 ℃ (Dirichlet).

3. Numerical analysis results

The probes fixed in the each section of the CLPHP reads the temperature values in each time step size and the evaporator and condenser temperature values are taken into consideration for analyzing the results of all 3 cases.

3.1. Temperature vs. time plot

The following plots discuss the temperature monitored from the evaporator and condenser section for time steps of 10 s. In two-turn CLPHP, two probes are fixed in the evaporator, adiabatic, and condenser sections in each loop, respectively. Therefore, an average of evaporator temperature (Te) and condenser temperature (Tc) are calculated, and the graph is plotted against time.

Figure 6 represents the plot between the average evaporator and condenser temperature against time for the condenser temperature fixed at 10 ℃. Due to high heat flux, the evaporator temperature is increased to a maximum value. The non-linear trend in the evaporator temperature is due to the probes fixed in the surface of the 2D CLPHP geometry measures the liquid slug temperature as well as the vapor plug temperature. We know that as the vapor plug density is lower compared to the liquid slug, the temperature in the vapor plug is higher than the temperature in the liquid slug. During the simulation for a total timestep, when the vapor plug comes into contact with the probes fixed in any one turn of the evaporator section the temperature is drastically increased compared to the liquid slug temperature. Therefore, a sharp rise in the average evaporator temperature was observed during the analytical calculations. As the wall of the condenser temperature was fixed as 283 K it shows a linear variation throughout the timesteps found to be decreased slighter.

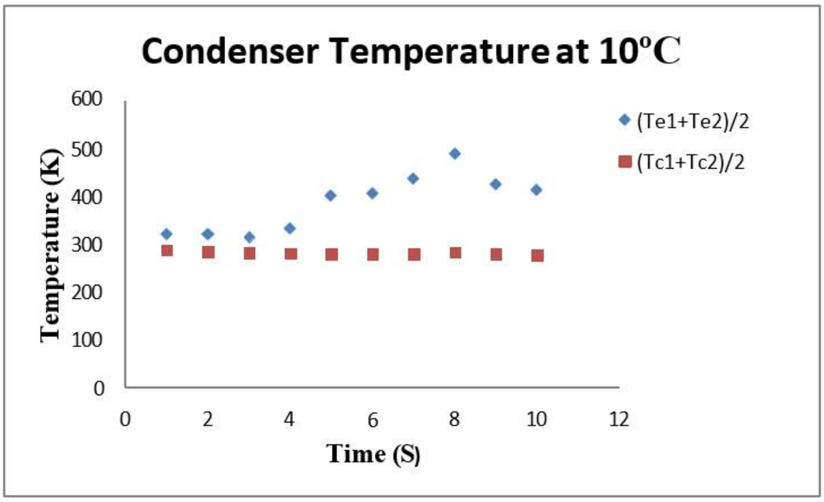

Figure 6. Temperature versus time for the condenser temperature at 10 ℃.

Figure 7 shows the average temperature variation of evaporator and condenser section over time when the condenser wall temperatures are fixed at 20 ℃. Similar observation was found in the average condenser temperature whereas the average evaporator temperature was found to be increasing non-linearly.

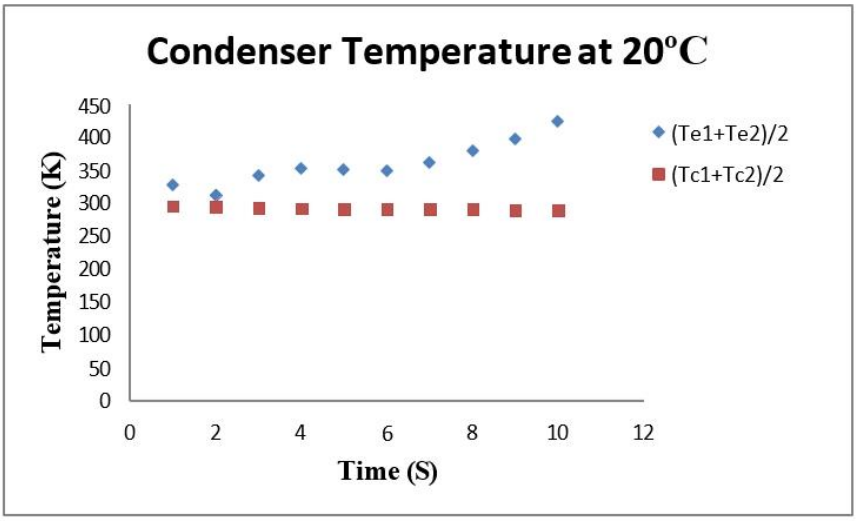

Figure 7. Temperature versus time for the condenser temperature at 20 ℃.

Figure 8 shows the temperature against time of average evaporator and condenser sections, when the condenser walls are prescribed at ambient temperature i.e 30 ℃. Similar observations were found as in the above 2 cases, the only difference observed is that the average evaporator temperature is found increased.

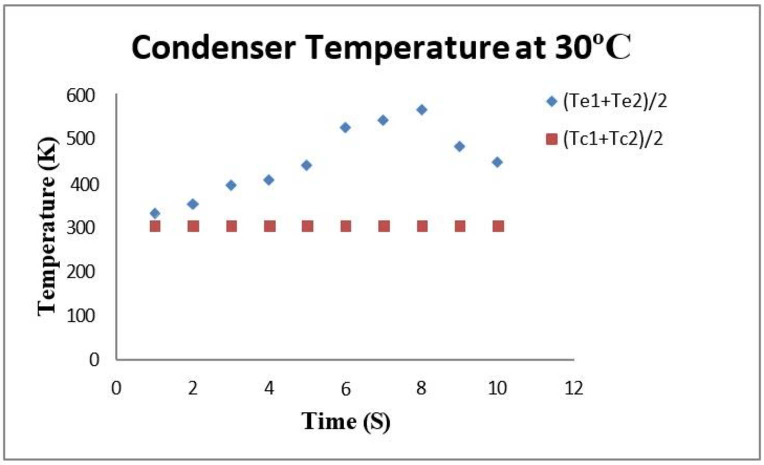

Figure 8. Temperature versus time for the condenser temperature at 30 ℃.

We clearly observe that when the condenser walls are maintained at 10 ℃ it absorbs more heat compared to other 2 cases and the temperature difference of evaporator and condenser sections are found low compared with condenser walls are fixed at 20 ℃ and 30 ℃. As we know that with the input heat flux, when the temperature difference of evaporator and condenser sections are low then the thermal resistance gets decreased and the heat transfer coefficient also found to be increased. From this numerical analysis it is clearly observed that the thermal performance of the 2D CLPHP is increased when the condenser temperature is fixed at 10 ℃. Due to the limited computational resources the simulations were performed only for the time steps of 10 s. If the simulations were carried out for more number of time steps then the temperature difference of evaporator and condenser section was found too low and the thermal performances can be compared well for all the 3 cases.

3.2. Contours of CLPHP

The distinct phases like liquid and vapor are visualized after simulating for the given time steps and are shown below.

The above **Figure 9** represents the contour of the phase mixture i.e the liquid and vapor phases can be observed clearly. This contour shows the liquid slug and vapor plug oscillation takes place inside the CLPHP.

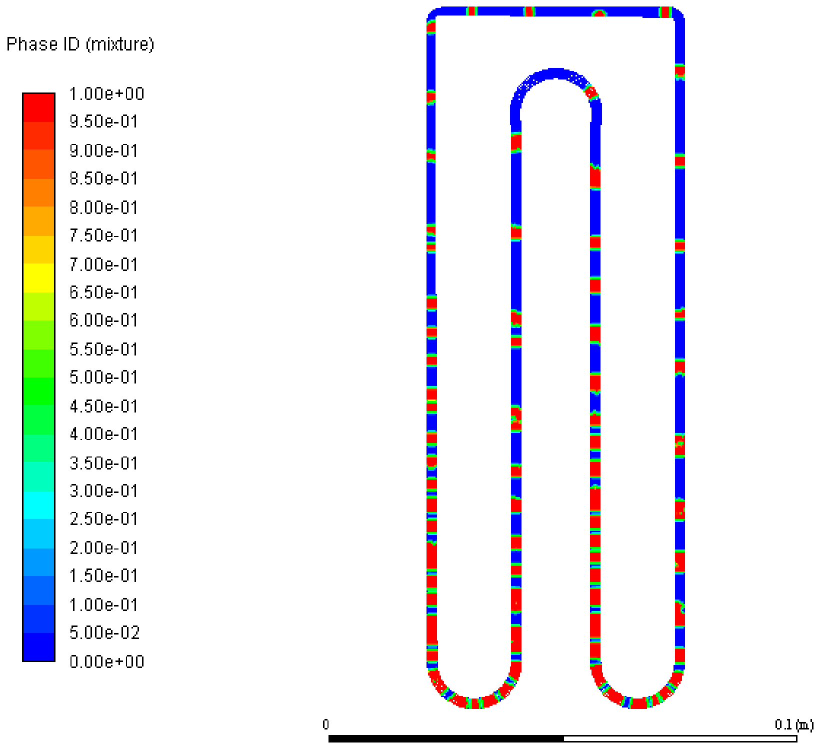

Figure 9. Contour for the phase mixture in the CLPHP.

The above **Figure 10** shows the volume fraction of the vapor phase exist inside the CLPHP for certain time steps. It is noted that the liquid and vapor phase can be observed throughout the CLPHP.

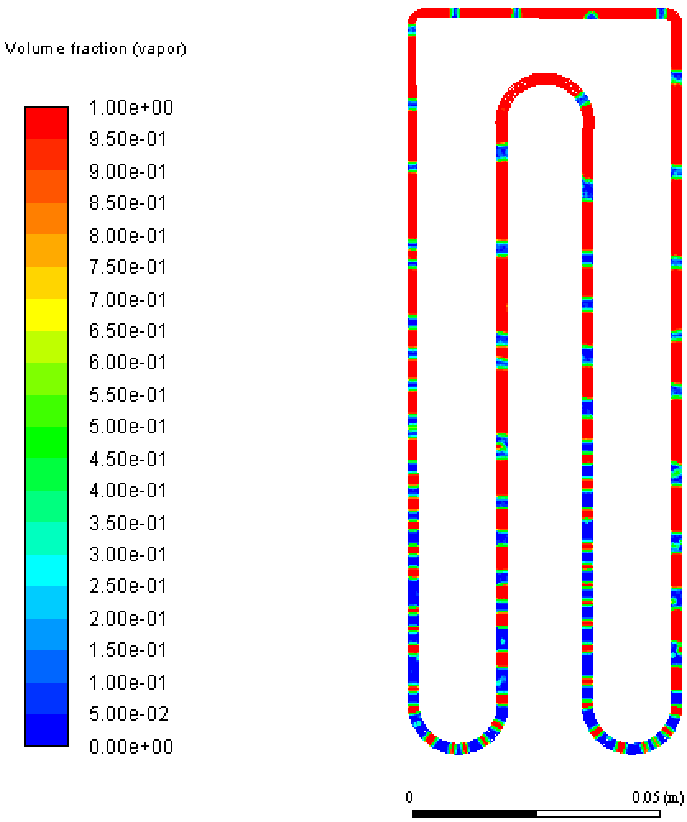

Figure 10. Contour for the volume fraction in the CLPHP.

3.3. Nusselt number calculation

In general, Nusselt number (Nu) is the ratio of convective heat transfer to the conductive heat transfer in a fluid. It is a dimensionless number and it indicates the heat transfer takes place in a fluid medium is by conduction or convection.

The Nusselt number is given by:

$$\mathrm{Nu} = \frac{hL}{K}$$

The Nusselt number range represents the heat transfer characteristics in a fluid flow and it is given as:

If Nu = 0, Pure conductive heat transfer;

If 0 < Nu < 10, Slug flow or laminar flow;

If 100 < Nu < 1000, High convective heat transfer or Turbulent flow.

In this present numerical work the Nusselt number was calculated for all the 3 cases from the temperature datas measured with the help of probes. The Nusselt number was calculated analytically and it is found to be within 1 in all the 3 cases which is shown above in **Table 3**. The highest Nusselt number was obtained from the case of condenser temperature fixed at 10 ℃. The Nusselt number range in the present simulation indicates the slug flow or laminar flow which can be observed from the available contours.

Table 3. Nusselt number values for different condenser temperatures.

Temperature (℃)	**10**	**20**	**30**
Nusselt Number	0.9311	0.8807	0.8576

4. Conclusion

In the case of CFD analysis water is used as a working fluid and the analysis work was carried out with 2D CLPHP geometry. As discussed about the geometry creation, meshing and the solver setting in the above section brief conclusions are made which are discussed below. They are as follows.

- With constant heat flux at the evaporator and by varying the temperatures of the condenser sections of about 10 ℃, 20 ℃ and 30 ℃ the CLPHP shows a better performance with the condenser temperature of 10 ℃.
- In this analysis for all the 3 cases a constant time of up to 10 s has been calculated for the transient analysis and the results plotted above was only for up to 10 s.
- The contours of phase fraction shows the liquid slug and vapor plug inside the CLPHP and with the further time steps better results can be obtained.
- The Nusselt number calculation from all the 3 cases shows the slug flow or laminar flow.

Conflict of interest: The author declares no conflict of interest.

Nomenclature

PHP	Pulsating Heat Pipe
DI	De-ionized Water
C_v	specific heat, J/kg K
P	pressure, bar
E	internal energy, KJ/kg
g	acceleration due to gravity, m/s^2
T	temperature, K
v	velocity, m/s
D	diameter, mm
h	heat transfer coefficient, w/m^{2}K
L	characteristic length, m

Greek symbols

α	volume fraction
μ	dynamic viscosity
ρ	density
σ	surface tension

Subscripts

a	adiabatic section
c	condenser section
e	evaporator section
l	liquid
SAT	saturation
V	vapor

References

1. Akachi H. Structure of Heat Pipe. U.S. Patent Application No. 5,219,020. 1990.
2. Wu HL, Peng, XF, Ye P, Eric Gong, Y, Simulation of Refrigerant Flow Boiling in Serpentine Tubes. International Journal of Heat and Mass Transfer. 2007; 50(5–6): 1186–1195. doi: 10.1016/j.ijheatmasstransfer.2006.10.013
3. Kumar V, Rudresha S. CFD Analysis and Experimental Investigation on Thermal Performance of Closed Loop Pulsating Heat Pipe Using Different Nanofluids. International Journal of Advanced Research. 2014; 2(8): 753–760.
4. Sedighi E, Amarloo A, Shafii B. Numerical and Experimental Investigation of Flat-Plate Pulsating Heat Pipes with Extra Branches in the Evaporator Section. International Journal of Heat and Mass Transfer. 2018; 126: 431–441. doi: 10.1016/j.ijheatmasstransfer.2018.05.047
5. Pachghare PR, Mahalle AM. Thermo-Hydrodynamics of Closed Loop Pulsating Heat Pipe: An Experimental Study. Journal of Mechanical Science and Technology. 2014; 28(8): 3387–3394. doi: 10.1007/s12206-014-0751-9
6. Barrak AS, Saleh AAM, Naji ZH. Experimental and Numerical Simulation for Thermal Investigation of Oscillating Heat Pipe Using VOF Model. Engineering and Technology Journal. 2020; 38: 88–104.
7. Karthikeyan VK, Khandekar S, Pillai BC, et al. Infrared Thermography of a Pulsating Heat Pipe: Flow Regimes and Multiple Steady States. Applied Thermal Engineering. 2014; 62(2): 470–480. doi: 10.1016/j.applthermaleng.2013.09.041
8. Vo DT, Kim HT, Ko J, et al. An Experiment and Three-Dimensional Numerical Simulation of Pulsating Heat Pipes. International Journal of Heat and Mass Transfer. 2020; 150: 119317. doi: 10.1016/j.ijheatmasstransfer.2020.119317

9. Błasiak P, Opalski M, Parmar P, et al. The Thermal—flow Processes and Flow Pattern in a Pulsating Heat Pipe—numerical Modelling and Experimental Validation. Energies. 2021; 14(18). doi: 10.3390/en14185952
10. Hansen N, Versteeg J, Michna GJ. Effect of Condenser Temperature on Pulsating Heat Pipe Performance. In: Proceedings of the ASME 2013 Heat Transfer Summer Conf; 14–19 July 2013; Minneapolis, MN, USA. pp. 1–6.
11. Jiaqiang E, Zhu R, Zuo H, et al. Simulation and Analysis on Heat Transfer Performance of Oscillating Heat Pipe with Single and Double Passageway. Advanced Materials Research. 2012; 516–517: 433–37. doi: 10.4028/www.scientific.net/AMR.516-517.433
12. Wang J, Bai X. The Features of CLPHP with Partial Horizontal Structure. Applied Thermal Engineering. 2018; 133: 682–89. doi: 10.1016/j.applthermaleng.2018.01.058
13. Li Q, Wang Y, Lian C, et al. Effect of Micro Encapsulated Phase Change Material on the Anti-Dry-out Ability of Pulsating Heat Pipes. Applied Thermal Engineering. 2019; 159: 113–854. doi: 10.1016/j.applthermaleng
14. Kalpak RS, Naik HB, Mehta HB. CFD Analysis of Cryogenic Pulsating Heat Pipe with Near Critical Diameter under Varying Gravity Conditions. Theoretical Foundations of Chemical Engineering. 2020; 54(1): 64–76. doi: 10.1134/S0040579520010212
15. Xie F, Li X, Qian P, et al. Effects of Geometry and Multisource Heat Input on Flow and Heat Transfer in Single Closed-Loop Pulsating Heat Pipe. Applied Thermal Engineering. 2019; 168: 114856. doi: 10.1016/j.applthermaleng.2019.114856
16. Lin Z, Wang S, Shirakashi R, et al. Simulation of a Miniature Oscillating Heat Pipe in Bottom Heating Mode Using CFD with Unsteady Modeling. International Journal of Heat and Mass Transfer. 2013; 57(2): 642–656. doi: 10.1016/j.ijheatmasstransfer.2012.09.007,
17. Noh HY, Kim SJ. Numerical Simulation of Pulsating Heat Pipes: Parametric Investigation and Thermal Optimization. Energy Conversion and Management. 2020; 203: 112237. doi: 10.1016/j.enconman.2019.112237
18. Zufar M, Gunnasegaran P, Ching Ng K. Numerical Study on the Effects of using Nanofluids in Pulsating Heat Pipe. International Journal of Engineering & Technology. 2018; 7(4): 6.
19. Choi J, Zhang Y. Numerical Simulation of Oscillatory Flow and Heat Transfer in Pulsating Heat Pipes with Multi-Turns Using OpenFOAM. Numerical Heat Transfer; PartA: Applications. 2020; 77(8): 761–781. doi: 10.1080/10407782.2020.1717202
20. Wang J, Ma H, Zhu Q. Effects of the Evaporator and Condenser Length on the Performance of Pulsating Heat Pipes. Applied Thermal Engineering. 2015; 91: 1018–1025. doi: 10.1016/j.applthermaleng.2015.08.106
21. Al Jubori AM, Jawad QA. Computational Evaluation of Thermal Behavior of a Wickless Heat Pipe under Various Conditions. Case Studies in Thermal Engineering. 2020; 22: 100767. doi: 10.1016/j.csite.2020.100767
22. Wang J, Xie J, Liu X. Investigation on the Performance of Closed-Loop Pulsating Heat Pipe with Surfactant. Applied Thermal Engineering. 2019; 160: 113998. doi: 10.1016/j.applthermaleng.2019.113998
23. Chidambaranathan S, Rangaswamy SM. Experimental Investigation of Higher Alcohols as Self-Rewetting Fluids in Closed Loop Pulsating Heat Pipes. Thermal Science. 2021; 25: 781–790. doi: 10.2298/TSCI200509347C
24. Sedighi E, Amarloo A, Shafii B. Numerical and experimental investigation of flat-plate pulsating heat pipes with extra branches in the evaporator section. International Journal of Heat and Mass Transfer. 2018; 126: 431–441. doi: 10.1016/j.ijheatmasstransfer.2018.05.047
25. Costa Bitencourt, Umberto. (2016). CFD simulation of a Pulsating Heat Pipe using ANSYS FLUENT. Available online: https://www.researchgate.net/publication/305608515 (accessed on 15 November 2024).

Thermal Science and Engineering 2025, 8(1), 8601.
https://doi.org/10.24294/tse8601

Article

Fabrication and analysis of solar operated vapour absorption refrigeration system using methanol water

Furqan Ahmad[1], Saqlain Abbas[1,*], Taha Ejaz[1], Zulkarnain Abbas[2], Zahid Hussain[1], Muhammad Rizwan[1]

[1] Department of Mechanical Engineering, University of Engineering and Technology Lahore (Narowal Campus), Narowal 51600, Pakistan
[2] Department of Mechanical Engineering, National Fertilizer Cooperation (NFC), Institute of Engineering and Technology (IET), Multan 59000, Pakistan
*** Corresponding author:** Saqlain Abbas, saqlain.abbas@uet.edu.pk

CITATION

Ahmad F, Abbas S, Ejaz T, et al. Fabrication and analysis of solar operated vapour absorption refrigeration system using methanol water. Thermal Science and Engineering. 2025; 8(1): 8601. https://doi.org/10.24294/tse8601

ARTICLE INFO

Received: 14 November 2024
Accepted: 26 December 2024
Available online: 14 January 2025

Abstract: This study investigates the performance assessment of methanol and water as working fluid in a solar-powered vapour absorption refrigeration system. This research clarifies the system's performance across a spectrum of operating conditions. Furthermore, the HAP software was utilized to determine and scrutinize the cooling load, facilitating a comparative analysis between software-based results and theoretical calculations. To empirically substantiate the findings, this research investigates methanol-water as a superior refrigerant compared to traditional ammonia- water and LiBr-water systems. Through experimental analysis and its comparison with previous research, the methanol-water refrigeration system demonstrated higher cooling efficiency and better environmental compatibility. The system's performance was evaluated under varying conditions, showing that methanol-water has a 1% higher coefficient of performance (COP) compared to ammonia-water systems, proving its superior effectiveness in solar-powered applications. This empirical model acts as a pivotal tool for understanding the dynamic relationship between methanol concentration (40%, 50%, 60%) and system performance. The results show that temperature of the evaporator (5–15 ℃), condenser (30 ℃–50 ℃), and absorber (25 ℃–50 ℃) are constant, the coefficient of performance (COP) increases with increase in generator temperature. Furthermore, increasing the evaporator temperature while keeping constant temperatures for the generator (70 ℃–100 ℃), condenser, and absorber improves the COP. The resulting data provides profound insights into optimizing refrigerant concentrations for improved efficiency.

Keywords: renewable energy; solar energy; environmental sustainability; methanol-water; VARs

1. Introduction

Worldwide, the vapour compression refrigeration process in the air-cooling system utilizes 70%–75% of domestic power, necessitating the use of more fossil fuels to generate the required electricity from fossil fuel power plants. The combustion of fuel in such structures leads to the disintegration of additional greenhouse gases (CO_2), negatively impacting the world's atmosphere. Therefore, it is imperative to establish a substitute refrigeration process that utilizes electricity from renewable energy sources in order to alleviate the detrimental effects of fossil fuel powerplants on the global environment [1,2].

The extensive use of sustainable energy resources for driving air conditioning cycles, especially solar energy, has been a current priority due to its readily available nature [3]. Solar-powered refrigeration systems are ideal for use in fields such as agriculture and medicine because they are not dependent on outside energy sources or the electric grid, and they are compatible with environmental conditions of Narowal, Pakistan.

When considering absorption refrigeration cycles, it is crucial to choose an appropriate absorbent-refrigerant combination based on scientific parameters. For a liquid to be an efficient refrigerant, it must possess the following properties: it must have a boiling temperature, a vaporization pressure that is lower than atmospheric pressure, a high heat of vaporization, non-flammable and non-explosive features, and be beneficial to the atmosphere and ozone [4]. A couple of literary masterpieces were offered. One of the suggested approaches was the transformation of refrigerant vapour to liquid phase using an adequate absorbent to absorb the refrigerant vapour. The mixing propensity between the components was enhanced by the close association between the absorbent and the refrigerant molecules. This was done using the same low-pressure method [5].

The scientists' primary goal was to improve the COP values of the absorption-refrigeration system. Multiple subjects were studied in the earlier research through the number of experiments. Sierra developed solar bonding to boost the discontinuous absorption of refrigeration using NH_3-H_2O solution. It has been demonstrated that a significant generation value of 73 ℃ while preserving a vaporization value of −2 °C can be attained. The variation of the calculated COP outcomes was from 0.24 to 0.28 [6]. Porumb examined the influence of operational factors like solar heated water, chilled water, and cold-water temperature on the coefficient of performance of the LiBr-H_2O absorption refrigerator, and the outcomes proved that the computational model is capable of estimating the suitable operational circumstances of the refrigeration system while assuming crystallization [7].

Jasim designed a digital model to imitate three separate working fluids: ammonia-water, ammonia-lithium nitride, and ammonia-sodium thiocyanate. Equations based on polynomials were included in the simulation to compute the heating and cooling characteristics. The variance in temperatures among all three process and the generator, evaporator and condenser demonstrates that the ammonia-water process has worse efficiency than the remaining two cycles [8]. The inspection, design and manufacturing of a green, advantageous VARs for unit output was done by Bajpai, utilizing ammonia and water as the solution pair. The system was designed and evaluated under different operating situations utilizing hot water as a power source and a planar solar collector; the obtained COP for this arrangement was 0.58. Moreno utilized a CPC device in Mexico with a tripartite mixture (NH_3/$LiNO_3$/H_2O). The COP was 0.098, which reached an evaporator temperature of −11°C. He discovered that the time of cooling is 8 h, and the COP goes up by 24% greater than the binaries combination (NH_3/$LiNO_3$) in the CPC device [9]. Agrouaz conducted energy evaluations to determine the effectiveness of using solar refrigeration systems under Moroccan meteorological conditions. The findings indicated that variety of factors, such as the inclination of solar energy collector, collector surface field, and evaporator and generator circulation rates, play a vital role in boosting the overall functionality [10]. Applying a methanol-water combination a solar-powered absorption cooling system was built and tested Nabeel A. Ghyadh, having every single factor computed separately. The components of the parabolic trough collector are a 2.1 m^2 aperture stainless steel reflector and an illuminated evacuated tube containing a black-painted helical copper tube receiver (12.7 mm in diameter and 1 mm in thickness). Convection inefficiencies and radiation are reduced by the glass cover [11].

There are actually two proactive liquids utilized in VARs, which include water-LiBr and NH_3-water solutions because of their high coefficient of performance. Both substances have restrictions. The framework becomes more complicated due to necessity for an analyser and rectifier due to the difference in boiling temperatures between the two parts of NH_3-water system. Water-LiBr shows challenges with crystallization, and in both scenarios, the components electrolytic character could lead to corrosion occurrence. Consequently, there has been a significant amount of research into the recognition of different functioning fluid opportunities, such as deep eutectic solvents and organic and ionic liquids. Developments have been pointed out in working VARs, like the COP and percentage concentration [12].

The main objective of this research is to utilize a methanol-water combination to figure out the system's COP and to make a comparison study between refrigerants like ammonia-water. A VARs may allow us to achieve excellent energy efficiency, especially when surplus heat or low- quality sources of energy i.e., solar, are present. The solution of methanol and water meets all the specifications for an appropriate refrigerant; as it does not produce crystallization and does not need any additional components. The methanol-water combination has advantageous thermodynamic characteristics that allow it operate across a broad temperature spectrum. Its low price and accessibility make it an environment friendly for cooling needs.

2. Research methodology

The research methodology of this research is divided into three portions: mathematical modelling in which different governing equations are discussed to calculate COP and Cooling load, simulation analysis to validate theoretical cooling load and experimental setup and all these are explained below.

2.1. Mathematical modelling

There are two main parts of mathematical modelling in this research: first is for calculating the coefficient of performance of VARs and second is for calculating the cooling load of the system.

The coefficient of performance is a dimensionless ratio that evaluates the efficiency of heat pumps, refrigeration systems, and other heat-transfer apparatuses. It is defined as the ratio of the intended output to the necessary input energy. A higher COP implies a more effective system since it transmits more heat per unit of energy unit. The parameters required to calculate coefficient of performance is shown in **Table 1.**

Table 1. Parametric values to calculate COP.

Parameter	Expression	Units	Value
Generator temperature	T_g	℃	90
Condenser temperature	T_c	℃	30
Absorber temperature	T_a	℃	26

Table 1. (*Continued*).

Parameter	Expression	Units	Value
Evaporator temperature	T_e	℃	5
Heat input	Q_{in}	W	30
Concentration at Absorber exit	X_{abs}	-	0.35
Concentration at Generator exit	X_{gen}	-	0.45
Enthalpy at evaporator exit	h_{fge}	kJ/kg	2434.6
Enthalpy at condenser exit	h_{fgc}	kJ/kg	115.6
Enthalpy at generator exit	h_{sg}	kJ/kg	2401.3
Enthalpy at absorber exit	h_{sa}	kJ/kg	44.0

The volume of refrigerant that moves via a particular location in the system in unit time is called the mass flow rate (m_r) in arefrigeration system.

$$m_r = \frac{Q_{in}}{hfg_e} \tag{1}$$

An important parameter in VARs is mass flow rate of strong solution and is given by;

$$m_s = m_r \times \frac{X_{gen} - X_{abs}}{X_{abs} - X_{gen}} \tag{2}$$

The mass of a solute (weak solution) flowing through a specific site in a unit time is usually expressed as the mass flow rate of the weak solution.

$$m_w = m_s + m_r \tag{3}$$

First of all, we'll calculate heat transfer rate at evaporator i.e., Q_e

$$Q_e = m_r \times \mathrm{hfg}_e \tag{4}$$

Now, we'll calculate the heat transfer at condenser so the equation required to find the heat transfer rate at condenser Q_c is;

$$Q_c = m_r \times \mathrm{hfg}_c \tag{5}$$

Now, we'll calculate the heat transfer at absorber so the equation required to find the heat transfer rate at absorber Q_{abs} is;

$$Q_{abs} = m_s \times (\mathrm{hs}_g - \mathrm{hs}_a) \tag{6}$$

Now, we'll calculate the heat transfer at generator so the equation required to find the heat transfer rate at generator Q_{gen} is;

$$Q_{gen} = Q_e + Q_{abs} + Q_c \tag{7}$$

Finally, now we'll calculate coefficient of performance COP for methanol-water solution so;

$$\mathrm{COP} = \frac{Q_e}{Q_{gen}} \tag{8}$$

Finding the vapor absorption refrigeration system's theoretical cooling load is the main goal of the experiment's first phase. To determine the quantity of heat needs to be removed from the assigned space in order to maintain the required temperature, extensive calculations must be performed. Theoretical calculations consider various parameters, including ambient conditions, heat transfer characteristics, and refrigeration system specific requirements. Parameters to calculate cooling load and air properties of air at 20 ℃ is shown in **Tables 2** and **3** respectively.

Table 2. Parameters to calculate cooling load.

Parameter	Expression	Units	Value
Area	A	m²	0.577
Material	-	-	Iron (darkgrey surface)
Sunlight	-	-	Very lessor none
Doors/Windows	-	-	None Extra
Extra Heat Devices	-	-	None
Ambient Temperature	TA	°C	30
Required Temperature	Td	°C	20
Iron emissivity	ε	-	0.31
Stefan-Boltzmann constant	σ	W/m^2K^4	5.67×10^{-8}

Table 3. Properties of air at 20 ℃.

Property	Expression	Units	Value
Volumetric thermal expansion coefficient	β	1/K	3.43×10^{-3}
Kinematic viscosity	v	m^2/s	2.02×10^{-5}
Thermal diffusivity	α	m^2/s	2.17×10^{-5}
Thermal conductivity	k	W/mK	0.025

Natural convection can be useful in a number of system parts in a vapor absorption refrigeration system, especially the absorber and the generator.

$$Q_{\text{natural}} = (\mathrm{h})(\mathrm{A})(\mathrm{Tamb} - \mathrm{Tdesired}) \tag{10}$$

Now we will find out the forced convection and its value is 0 because no door and window are included.

Hence, total convection is the sum of natural convection and forced convection and is given as;

$$Q_{\text{convection}} = Q_{\text{natural}} + Q_{\text{forced}} \tag{11}$$

Now we will find out the cooling load

$$Q_{\text{total}} = Q_{\text{radiation}} + Q_{\text{convection}} \tag{12}$$

2.2. Simulation analysis

HAP 4.9 software is employed to estimate the cooling load of a chamber having dimensions 3 by 3ft. HAP has given us the different graphical on the basis of parameters given to it according the Narowal's geographical considerations. **Figure 1** is a bar graph of yearly cooling load that illustrates the cumulative cooling for each day of the year. As heating load is not required and our main focus is cooling load so the graph shows the cooling load The U-value taken for the system is 0.397(BTU/(hr-ft^2-°F)). The value for zone flow is fixed 4.4 but the value of sensible load from hour to hour and has a minimum value 41.0 BTU/hr. and maximum value 61.8 BTU/hr. and these values are set according to condition of Narowal, Pakistan.

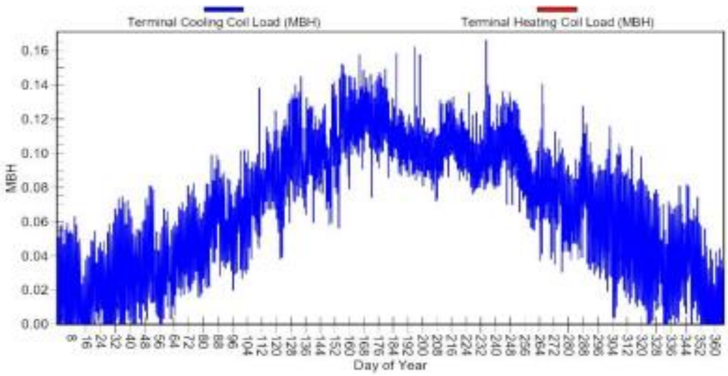

Figure 1. Yearly cooling load.

2.3. Experimental setup

To complete the experimental setup, the following key components were used;

- Evacuated Tube Solar Collector
- Absorber
- Condenser
- Evaporator
- Generator

2.3.1. Solar collector

Solar Collectors are heat exchangers that collect solar radiation and transform it into thermal energy. In VARs, thermal energy s utilized to fuel the generation process, which entails boiling a methanol and water solution. The reinsulating methanol vapour travels to a condenser, where it discharges heat before condensing back into a liquid. The liquid methanol is then sent to absorber, where it combines with water vapour from the evaporator. This absorption process releases heat, which is absorbed by the chilling water. Solar collector is shown in **Figure 2**.

Figure 2. Solar collector.

2.3.2. Absorber

In a vapour absorption refrigeration system, the absorber performs an important function. Imagine a sponge absorbing water—that's what the absorber does, but rather than water, it absorbs refrigerant vapour. This refrigerant vapour comes from the evaporator, where it's been transformed from liquid due to low pressure and is ready to be absorbed. The absorber contains a liquid absorbent, often water in methanol-water system. As the refrigerant vapour gets absorbed by the absorbent, it produces a richer solution. This absorption process is exothermic, mean it releases heat. The enriched solution is then circulated to another part of the system for regeneration. The absorber is shown is **Figure 3**.

Figure 3. Absorber.

2.3.3. Condenser

The condenser is a heat transfer mechanism, usually a tube-and-fin design. Hot, high-pressure refrigerant vapour goes into the condenser. This vapour emanates from the generator, where it was distilled out of a mild methanol-water solution. Outside the condenser tubes, chilling water or air circulates. As the heated methanol vapour encounters the colder walls of the condenser, it condenses back into the liquid. This process releases the heat accumulated in the generator, and that's what ultimately provides the chilling effect. Now liquid methanol, at a lower temperature, then departs the condenser, heading to the expansion valve for the next stage of the cycle. The colder liquid conveying the relinquished heat is then drawn away from the condenser.

The condenser functions as a radiator, dispersing the heat extracted from the space to be chilled to the surrounding environment through the chilling water or air. This enables the low-pressure methanol to return to the evaporator, ready to absorb heat and repeat the cycle. It also functions like a heat disposal mechanism, removing the energy accumulated by the coolant and dispersing it to the surroundings. This enables the system to operate on a consistent refrigeration cycle. The condenser is shown in **Figure 4**.

Figure 4. Condenser.

2.3.4. Evaporator

The evaporator functions as a heat absorber in a refrigerator that absorbs methanol and water vapour. The refrigerant's vaporization point is substantially reduced as a result of the low pressure. The heat is readily transferred from the heated object to the refrigerant when it comes into contact with these channels. The refrigerant undergoes a phase change, transitioning from a liquid to a low-pressure vapour as it absorbs this heat. This phase transition is essential. The refrigerant achieves the desired chilling effect by absorbing heat and vaporizing, thereby removing thermal energy from its surrounding and resulting in a decrease in temperature. This low-pressure methanol absorbs heat from the object that needs to be cool, such as air or water. The methanol becomes vapour as it heats up, leaving the water solution behind to absorb additional heat and maintain a mild temperature. In a vapour absorption refrigeration system, the evaporator functions as a heat sink, absorbing heat from its surrounding through the process of refrigerant evaporation, which creates a revitalizing and cold atmosphere. The evaporator is shown in **Figure 5**.

Figure 5. Evaporator.

3. Complete experimental setup

In this research, a solar powered VARs was fabricated and tested. Methanol-water was used as solution pair in which methanol worked as refrigerant and water as absorbent. The design, working and testing of the system was carried out at University of Engineering and Technology Lahore, Narowal Campus, Narowal city, Punjab province, Pakistan, under the outdoor conditions of Narowal. The complete experimental setup of solar powered VARs is shown in **Figure 6**.

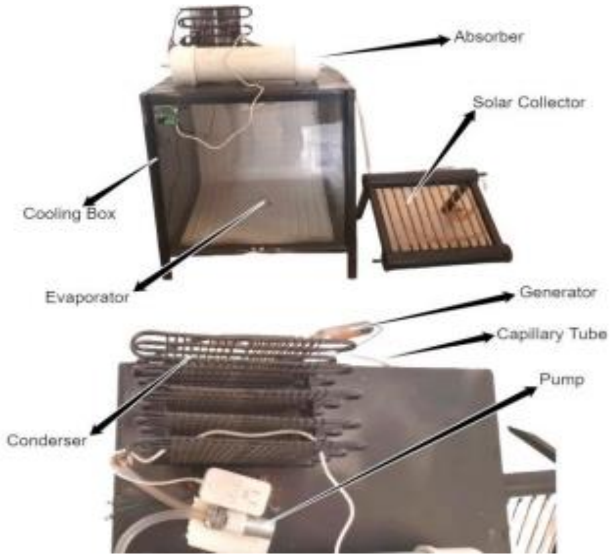

Figure 6. Complete experimental setup.

In vapour absorption refrigeration system low pressure methanol vapors enters the absorber from the evaporator. The methanol vapour dissolve within the absorber into cold water, forming a concentrated methanol solution. The energy discharged during methanol ingestion is dispersed by flowing chilly water through tubes within the absorber. The extremely strong methanol solution is delivered to the generator via a heating element. In the heating element, the highly concentrated methanol solution is warmed due to the blisteringly weak solution coming from the generator to the absorber. The tepid solution is heated more inside the generator, enabling methanol vapors to emerge from the solution. Methanol's boiling temperature is lower than that of water. The excess feeble solution from the generator flows back to the absorber. The precisely purified methanol vapour then moves forward towards the condenser. In the condenser, the unused energy of methanol vapour is given off to the chilled water, resulting in methanol vapour condensing into liquid state. The elevated pressure of methanol causes a decrease in temperature, resulting in incomplete vaporization. This slightly vaporized liquid travels to the evaporator. Inside the evaporator, the liquid methanol thoroughly vaporizes. The unused energy of evaporation is taken in from additional substances being chilled, like air or water. The low-temperature methanol vapour departing the evaporator comes back to the absorber, completing the cycle. **Figure 7** represents the process diagram of proposed system.

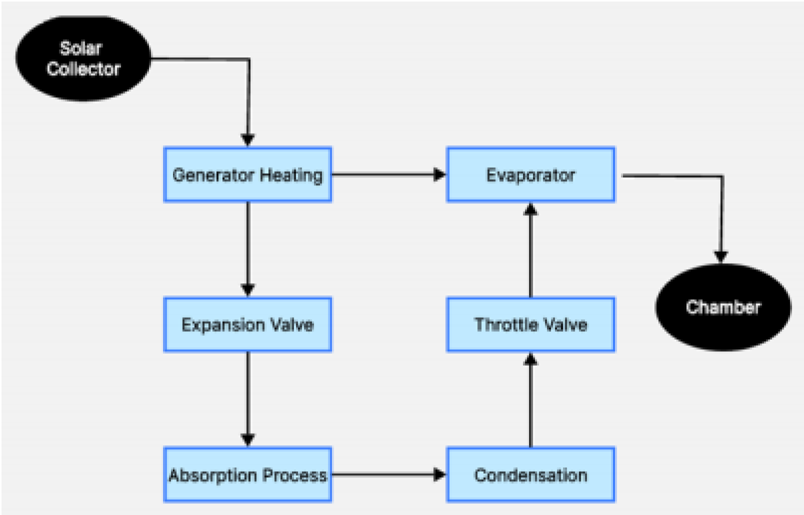

Figure 7. Schematic diagram of the system.

4. Results and discussions

Figure 8 elaborates the comparison of cooling load using mathematical model and simulation result. The comparison has been made for the month of June. Mathematical model shows a maximum value of 42.7 W and simulation result has shown 41.03 W cooling load in the month of June. The graph shows that value of cooling load is maximum in day time 12 pm–17 pm, after that graph start decreasing again.

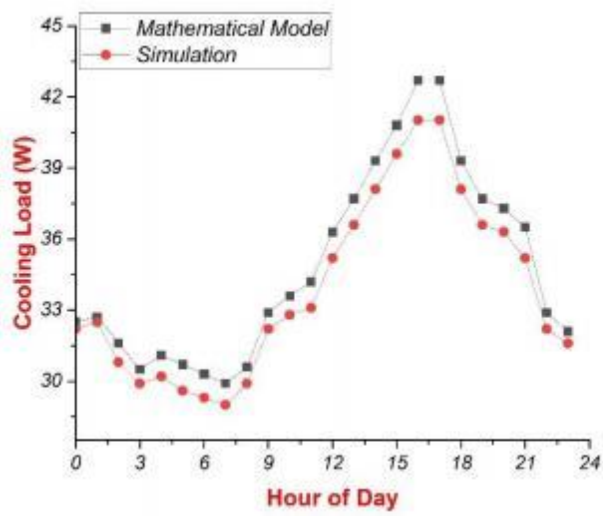

Figure 8. Comparison of mathematical model and HAP simulation for cooling load.

The comparative analysis of coefficient of performance (COP) from both the current research and existing literature is shown in **Figure 9**. The graph clearly illustrates that the COP of the methanol-water system exceeds that of the ammonia-water solution pair. In particular, the maximum COP for the methanol-water solution pair at the condenser temperature (T_c) of 30 °C and an evaporator temperature (T_e) of 5 °C is 0.42. Conversely, the ammonia-water solution pair attains a maximum COP of 0.41 under identical conditions. It has also been noted that the coefficient of performance in both systems increases as the generator temperature increases.

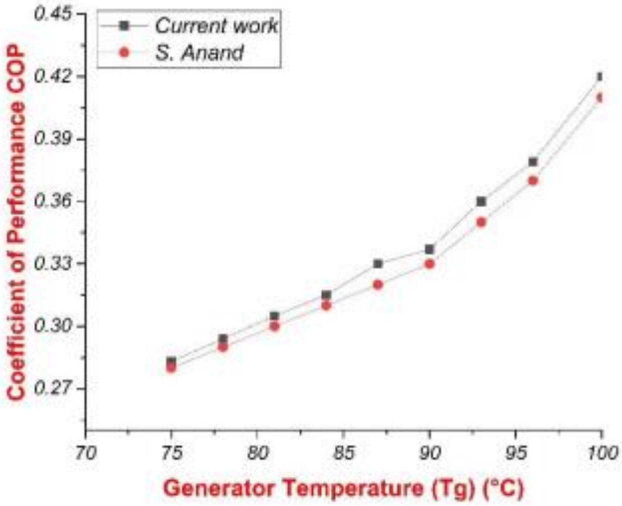

Figure 9. Comparison of COP of current work with the work of Anand [13].

The coefficient of performance (COP) of the refrigeration system is illustrated in **Figure 10**, which highlights the impact of varying evaporator and generator temperatures (T_e = 5 °C, 10 °C, and 15 °C). It is evident from the graph that the highest COP is attained at the maximum evaporator temperature, T_e = 15 °C, as the generator temperature increases. This discovery underscores the significance of refining evaporator temperatures to enhance the efficiency of refrigeration system, particularly when the generator temperatures fluctuate significantly. The advantage of operating at high evaporator temperature is illustrated by the relationship between higher generator temperatures and enhanced COP at higher evaporator temperature.

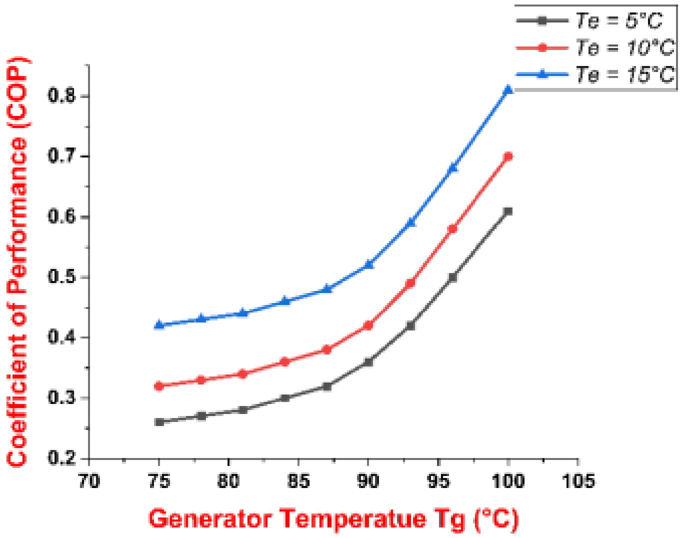

Figure 10. Variation of COP with generator temperature at different evaporator temperatures (T_c = 30 °C).

Impact of variations in the generator temperature on the coefficient of performance (COP), including the influence of varying condenser temperature is shown in **Figure 11**. It is evident that the COP reaches its maximum at a reduced condenser temperature, T_c = 10 °C, as the generator temperature increases. This underscores a critical insight: in order to achieve maximum system efficiency, the generator temperature should be maximized while simultaneously maintaining the condenser temperature at the lowest feasible level. The significance of precision control of temperatures in order to optimize the cycle's performance in underscore by the intricate interplay between these temperature variables.

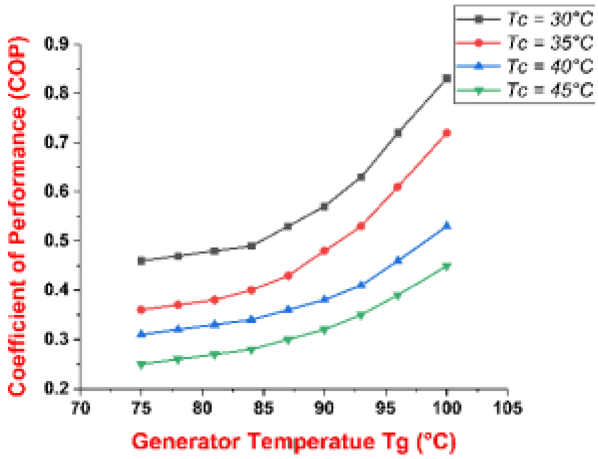

Figure 11. Variation of COP with generator temperature at different condenser temperatures (T_e = 5 °C).

The temperature drop fluctuation in the evaporator at 40%, 50%, and 60% solution concentrations is depicted in **Figure 12**. It has been noted that the largest concentration of methanol vapor produced in the evaporator results in the maximum temperature reduction. The evaporator has a temperature drop range of 7.8 °C–16.3 °C. High concentration was employed, resulting in increased methanol vapor emission and a significant variation in pressure across the evaporator and condenser.

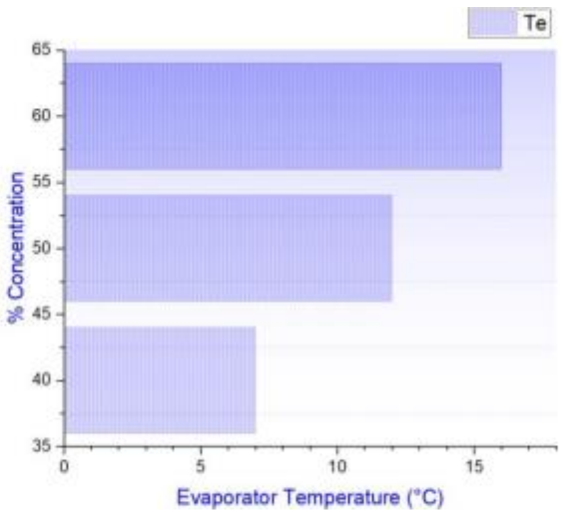

Figure 12. Variation of maximum temperature drop of evaporator.

The impact of solution concentration on the system's COP is displayed in **Figure 13**. This graph demonstrates how raising the concentrations raises the COP. It has been shown that high concentrations yield great performance since they produce a lot of methanol vapor. COP ranges from 0.35 to 0.62. Since the refrigeration system's coefficient of performance rises with increasing pressure variation between the condenser and evaporator (or generator), the high concentration results in both more released methanol and a greater pressure fluctuation between the two components.

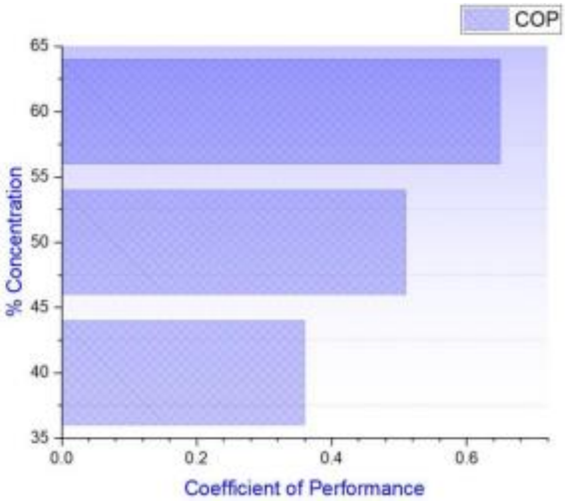

Figure 13. Maximum variable COP with variable concentration.

5. Conclusion

An experimental investigation was conducted in the present work using methanol as a refrigerant in an absorption-refrigeration cooling system at University of Engineering and Technology Lahore, Narowal Campus. It can be concluded that the investigated system is viable practically and ecologically, where the approach is more effective as an outcome of using a renewable energy source and does not harm the ozone layer, resulting in a smaller adverse effect on global warming. Physically, a higher temperature drop could be attained by the studied system at higher concentrations as an outcome of generating a higher amount of refrigerator vapor, where the drop ranged from 7.8 °C to 16.3 °C, concluding that the system is more efficient thermally. Additionally, as generator temperature increases, COP increases as a consequence when the maximal generator temperature reaches 100 °C. The COP of Methanol- Water solution is 6% higher than the COP of Ammonia-Water solution in the refrigeration system (VARS), i.e., 0.42, for Methanol-Water and 0.41, for Ammonia-Water. The theoretical cooling load is 42.7 watts, and by conducting analysis, the value of the cooling load is 0.14 MBU, i.e., 41.03 watts. The principal implementation of this undertaking is its use at the domestic level. Cost effectiveness and improved efficiency by using methanol as a refrigerant are the potential uses of a solar-operated refrigeration system. Non-renewable energy sources are scarce and could cease to be available to us by the next century, which makes it more crucial than ever for us to make use of all forms of renewable energy, such as solar. Despite challenges and limitations, solar-operated vapor absorption refrigeration systems using methanol water offer a promising and sustainable option for domestic cooling.

Author contributions: Conceptualization, FA and SA; methodology, FA, TE and ZA; software, FA; validation, SA, MR and FA; formal analysis, FA and ZH. All the authors agreed to the published version of the manuscript.

Acknowledgments: The authors are thankful to UET Lahore, Pakistan and other supporting institutes for providing the opportunity to finish this research work.

Conflict of interest: The authors declare no conflict of interest.

Nomenclature

COP	Co-efficient of performance
mr	mass flow rate
Qin	heat input
mw	mass flow rate of weak solution
Xabs	Concentration at Absorber exit
ms	mass flow rate of strong solution
Qgen	heat transfer rate at generator
A	area
Tamb	Ambient Temperature
Xgen	Concentration at Generator exit

References

1. Rajendra Kumar S. Design and Analysis of Absorption Refrigeration System Using H_2O+[EMIM][TFA] [PhD thesis]. National Institute of Technology, Rourkela; 2015.
2. Guo Y, Ding Y, Li J, et al. The performance of [Emim]Br/H2O as a working pair in the absorption refrigeration system. Next Energy. 2024; 2: 100038. doi: 10.1016/j.nxener.2023.100038
3. Franchini G, Notarbartolo E, Padovan LE, et al. Modeling, Design and Construction of a Micro-scale Absorption Chiller. Energy Procedia. 2015; 82: 577-583. doi: 10.1016/j.egypro.2015.11.874
4. Aman S, Devesh Shukla AM, Chauhan K. COP derivation and thermodynamic calculation of ammonia-water vapor absorption refrigeration system. International journal of mechanical engineering and technology. 2015.
5. Razmi A, Soltani M, M. Kashkooli F, et al. Energy and exergy analysis of an environmentally-friendly hybrid absorption/recompression refrigeration system. Energy Conversion and Management. 2018; 164: 59-69. doi: 10.1016/j.enconman.2018.02.084
6. Sierra FZ, Best R, Holland FA. Experiments on an absorption refrigeration system powered by a solar pond. Heat Recovery Systems and CHP; 1993.
7. Porumb R, Porumb B, Balan M. Numerical Investigation on Solar Absorption Chiller with LiBr-H 2 O Operating Conditions and Performances. Energy Procedia. 2017; 112: 108-117. doi: 10.1016/j.egypro.2017.03.1071
8. Abdulateef JM, Sopian K, Alghoul MA, et al. Solar Absorption Refrigeration System Using New Working Fluid Pairs. The ACM Digital Library; 2008.
9. Moreno-Quintanar G, Rivera W, Best R. Comparison of the experimental evaluation of a solar intermittent refrigeration system for ice production operating with the mixtures NH3/LiNO3 and NH3/LiNO3/H2O. Renewable Energy. 2012; 38(1): 62-68. doi: 10.1016/j.renene.2011.07.009
10. Agrouaz Y, Bouhal T, Allouhi A, et al. Energy and parametric analysis of solar absorption cooling systems in various Moroccan climates. Case Studies in Thermal Engineering. 2017; 9: 28-39. doi: 10.1016/j.csite.2016.11.002
11. Ghyadh NA, Hammadi SH, Shahad HAK. Using solar collector unit in a methanol-water vapor absorption cooling system under iraqi environmental conditions. Case Studies in Thermal Engineering. 2020; 22: 100749. doi: 10.1016/j.csite.2020.100749
12. Jain V, Singhal A, Sachdeva G, et al. Advanced exergy analysis and risk estimation of novel NH3-H2O and H2O-LiBr integrated vapor absorption refrigeration system. Energy Conversion and Management. 2020; 224: 113348. doi: 10.1016/j.enconman.2020.113348
13. Anand S, Gupta A, Anand Y, et al. Use of process steam in vapor absorption refrigeration system for cooling and heating applications: An exergy analysis. Cogent Engineering. 2016; 3(1): 1160639. doi: 10.1080/23311916.2016.1160639

Thermal Science and Engineering 2025, 8(1), 9275.
https://doi.org/10.24294/tse9275

Article

Mixed convection from an isothermal rough plate

Aubrey Jaffer[1,*], Martin Jaffer[2]

[1] Independent Researcher, Waltham, MA 02452, USA
[2] Independent Researcher, Atlanta, GA 30318, USA
* **Corresponding author:** Aubrey Jaffer, agj@alum.mit.edu

CITATION

Jaffer A, Jaffer M. Mixed convection from an isothermal rough plate. Thermal Science and Engineering. 2025; 8(1): 9275. https://doi.org/10.24294/tse9275

ARTICLE INFO

Received: 4 September 2024
Accepted: 16 December 2024
Available online: 23 January 2025

Abstract: This investigation derives formulas to predict the mixed convective surface conductance of a flat isotropic surface roughness having a convex perimeter in a Newtonian fluid with a steady forced flow in the plane of that roughness. Heat transfer measurements of a 30.5 cm square rough plate with forced air velocities between 0.1 m/s and 2.5 m/s were made by the present apparatus in two inclined and all five orthogonal orientations. The present work's formulas are compared with 104 measurements in twelve data-sets. The twelve data-sets have root-mean-square relative error (RMSRE) values between 1.3% and 4% relative to the present theory. The present work's formulas are also compared with 78 measurements in 28 data-sets on five vertical rough surfaces in horizontal flow from prior work. The five stucco data-sets have RMSRE values between 2.5% and 6.5%; the other data-sets have RMSRE values between 0.2% and 5%.

Keywords: heat transfer; surface roughness; natural convection; forced flow

1. Introduction

Natural convection is the flow caused by nonuniform density in a fluid under the influence of gravity. Forced convection is the heat or solute transfer to or from a surface induced by forced fluid flow parallel to that surface. Mixed convection is the heat or solute transfer when both processes are operating simultaneously.

Modeling mixed convection from the exterior faces of walls and roofs is essential to predicting the thermal performance of buildings and determining their heating and cooling requirements. This investigation derives and tests mixed convection formulas for a rough, flat exterior face at any inclination, subjected to forced flow in the plane of the surface.

Three modes of forced flow of a Newtonian fluid along a (flat) surface are laminar flow, turbulent flow, and rough flow. Flow along flat, smooth plates gradually transitions from laminar to turbulent in a continuous boundary-layer[1] [1].

Surface roughness repeatedly disrupts the boundary-layer in rough flow, which occurs along rough surfaces [2].

Forced convection fluid flow is parallel to the surface. In natural convection the temperature difference between the fluid and surface creates an upward or downward fluid flow, which is not necessarily parallel to the surface. Along a vertical plate, "aiding" has natural and forced flows in the same direction; "opposing" flows are in opposite directions.

Natural convection is sensitive to plate inclination, while forced convection is not. Forced convection has different formulas for laminar, turbulent, and rough flows, while a single formula governs both laminar and turbulent natural convection [3–5].

There is a symmetry in external natural convection; a cooled plate induces downward flow instead of upward flow. Flow from a cooled upper face is the mirror image of flow from a heated lower face. Flow from a cooled lower face is the mirror image of flow from a heated upper face.

The rest of this investigation assumes a surface warmer than the fluid.

1.1. Fluid mechanics

In engineering, heat transfer rates for both natural and forced convection are expressed using the average surface conductance $\overline{h}$ with units $\mathrm{W/(m^2 \cdot K)}$.

In fluid mechanics, the convective heat transfer rate is represented by the dimensionless average Nusselt number ($\overline{Nu} \equiv \overline{h}\, L/k$), where k is the fluid's thermal conductivity with units $\mathrm{W/(m \cdot K)}$, and L is the system's characteristic length (m).

The Reynolds number Re is dimensionless and proportional to fluid velocity. The Rayleigh number Ra is the impetus for fluid flow due to temperature difference and gravity. A fluid's Prandtl number Pr is its momentum diffusivity per thermal diffusivity ratio. The system's characteristic length L scales both $\overline{Nu}$ and Re; Ra is scaled by L^3; both $\overline{h}$ and Pr are independent of L.

1.2. Combining transfer processes

Equation (1) is an unnamed form for combining functions which appears frequently in heat transfer formulas:

$$F^p = F_1^p + F_2^p \tag{1}$$

Churchill and Usagi [6] stated that such formulas are "remarkably successful in correlating rates of transfer for processes which vary uniformly between these limiting cases." Convection transfers heat (or solute) between the plate and fluid.

1.3. The ℓ^p-norm

When $F_1 \geq 0$ and $F_2 \geq 0$, taking the pth root of both sides of Equation (1) yields a vector-space functional form known as the ℓ^p-norm, which is notated $\|F_1\ ,\ F_2\|_p$:

$$\|F_1\ ,\ F_2\|_p \equiv [\ |F_1|^p + |F_2|^p]^{1/p} \tag{2}$$

Norms generalize the notion of distance. Formally, a vector-space norm obeys the triangle inequality: $\|F_1, F_2\|_p \leq |F_1| + |F_2|$, which holds only for $p \geq 1$. However, $p < 1$ is also useful.

- When $p > 1$, the processes modeled by F_1 and F_2 compete and $\|F_1, F_2\|_p \geq \max(|F_1|, |F_2|)$; the most competitive case is $\|F_1, F_2\|_{+\infty} \equiv \max(|F_1|, |F_2|)$.
  - Equation (25) uses the ℓ^3-norm.
  - Equation (26) uses the $\ell^{\sqrt{3}}$-norm.
- The ℓ^2-norm is equivalent to root-sum-squared; it models perpendicular competitive processes.
  - Equations (21) and (23) use the ℓ^2-norm.
- The ℓ^1-norm models independent processes; $\|F_1, F_2\|_1 \equiv |F_1| + |F_2|$.
- When $0 < p < 1$, the processes cooperate and $\|F_1, F_2\|_p \geq |F_1| + |F_2|$.
  - Cooperation between conduction and flow-induced heat transfer manifests as the $\ell^{1/2}$-norm in natural convection Equation (7).
- When $p < 0$, $\|F_1, F_2\|_p \leq \min(|F_1|, |F_2|)$, with the transition sharpness controlled by p; the extreme case is $\|F_1, F_2\|_{-\infty} \equiv \min(|F_1|, |F_2|)$. Negative p can model a single flow through serial processes; the most restrictive process limits the flow.
  - Equation (18) uses the ℓ^{-4}-norm.
  - Equation (A4) uses the $\ell^{-\sqrt{1/3}}$-norm.

1.4. Roughness

The present theory treats surface roughness as an elevation function $z(x, y)$ defined on an area A having a convex perimeter. Function $z(x, y)$ has only one value at each (x, y) coordinate; thus surfaces with tunnels and overhangs are disqualified, as are porous surfaces. The mean elevation $\overline{z}$ and root-mean-squared (RMS) height-of-roughness $\varepsilon \ll L$ are:

$$\overline{z} = \int_A z\,\mathrm{d}A \Big/ \int_A \mathrm{d}A \tag{3}$$

$$\varepsilon = \sqrt{\int_A |z - \overline{z}|^2\,\mathrm{d}A \Big/ \int_A \mathrm{d}A} \tag{4}$$

1.5. Prior work

Nearly all of the experimental prior works [7–13] concern smooth plates. The exception is Rowley et al. [14], the 1930 result of cooperative research between the University of Minnesota and the American Society of Heating and Ventilation Engineers. They measured mixed convection of 0.305 m square vertical plates in horizontal flow in a wind tunnel. They tested common rough exterior surfaces, specifically concrete, brick, stucco, and rough and smooth plaster.

Mixed convection measurements from the graphs in Rowley et al. [14] were captured by measuring the distance from each point to its graph's axes, then scaling to the graph's units using the "Engauge" software (version 12.1). **Table 1** lists the data-sets to be compared with the present theory, where θ is the angle of the plate from vertical and ψ is the angle of the forced flow from the zenith; $\psi = 90°$ is horizontal.

1.6. Approaches

Rowley et al. [14] provided graphs for engineering use which cover both laminar and turbulent flows. It applies only to forced horizontal flow in the plane of a vertical plate. It lacked a roughness metric which would have allowed application to other types of rough surfaces. Unfortunately, forced convection from rough plates does not scale simply, being inversely proportional to $\log^2(L/\varepsilon)$.

The present work is primarily theoretical, combining the system-wide heat transfer derivations of natural and forced convections from Jaffer [5] and Jaffer [2], respectively. It applies to convex flat surfaces at any inclination having isotropic roughness with $0 < \varepsilon \ll L$ and forced flow parallel to the surface.

1.7. Not empirical

Empirical theories derive their coefficients from measurements, inheriting the uncertainties from those measurements. Theories developed from first principles derive their coefficients mathematically. For example, Incropera et al. [15] (p. 210) gives the thermal conductance of one face of a diameter D disk into a stationary, uniform medium having thermal conductivity k as exactly $8\,k/[\pi\,D]$ (units $\mathrm{W/(m^2 \cdot K)}$). The present theory derives from first principles; it is not empirical. Each formula is tied to aspects of the plate geometry and orientation, fluid, and flow.

Table 1. Rowley et al. mixed convection data-sets.

Surface	θ	ψ	$Ra \geq$	$Ra \leq$	$Re \geq$	$Re \leq$	Count
smooth-plaster	0.0°	90.0°	2.8×10^6	1.1×10^7	7.9×10^4	8.3×10^4	2
smooth-plaster	0.0°	90.0°	3.1×10^6	1.1×10^7	6.7×10^4	7.1×10^4	2
smooth-plaster	0.0°	90.0°	3.2×10^6	1.1×10^7	5.6×10^4	5.9×10^4	2
smooth-plaster	0.0°	90.0°	3.7×10^6	1.1×10^7	4.5×10^4	4.7×10^4	2
smooth-plaster	0.0°	90.0°	4.1×10^6	1.2×10^7	3.4×10^4	3.5×10^4	2
smooth-plaster	0.0°	90.0°	5.0×10^6	1.2×10^7	2.2×10^4	2.3×10^4	2
concrete	0.0°	90.0°	1.1×10^7	1.1×10^7	7.9×10^4	7.9×10^4	1
concrete	0.0°	90.0°	7.9×10^6	1.1×10^7	6.7×10^4	6.9×10^4	3
concrete	0.0°	90.0°	2.9×10^6	1.1×10^7	5.6×10^4	5.9×10^4	7
concrete	0.0°	90.0°	3.1×10^6	1.1×10^7	4.5×10^4	4.7×10^4	2
concrete	0.0°	90.0°	3.9×10^6	1.1×10^7	3.4×10^4	3.5×10^4	2
concrete	0.0°	90.0°	4.3×10^6	1.2×10^7	2.2×10^4	2.4×10^4	2
brick	0.0°	90.0°	2.0×10^6	1.1×10^7	6.4×10^4	6.7×10^4	6
brick	0.0°	90.0°	3.4×10^6	1.1×10^7	5.5×10^4	5.8×10^4	4
brick	0.0°	90.0°	2.7×10^6	1.1×10^7	4.5×10^4	4.7×10^4	3
brick	0.0°	90.0°	3.1×10^6	1.1×10^7	4.0×10^4	4.2×10^4	5
brick	0.0°	90.0°	4.3×10^6	1.1×10^7	3.0×10^4	3.2×10^4	4
brick	0.0°	90.0°	5.3×10^6	1.1×10^7	1.7×10^4	1.8×10^4	4
rough-plaster	0.0°	90.0°	1.1×10^7	1.1×10^7	6.7×10^4	6.7×10^4	1
rough-plaster	0.0°	90.0°	3.6×10^6	1.1×10^7	5.6×10^4	5.9×10^4	2
rough-plaster	0.0°	90.0°	3.7×10^6	1.1×10^7	4.5×10^4	4.7×10^4	2
rough-plaster	0.0°	90.0°	4.0×10^6	1.2×10^7	3.4×10^4	3.5×10^4	3
rough-plaster	0.0°	90.0°	4.8×10^6	1.2×10^7	2.2×10^4	2.4×10^4	2
stucco	0.0°	90.0°	1.1×10^6	1.1×10^7	6.7×10^4	7.1×10^4	2
stucco	0.0°	90.0°	6.9×10^5	1.1×10^7	5.6×10^4	6.0×10^4	3
stucco	0.0°	90.0°	1.2×10^6	1.1×10^7	4.5×10^4	4.8×10^4	3
stucco	0.0°	90.0°	1.5×10^6	1.1×10^7	3.4×10^4	3.6×10^4	3
stucco	0.0°	90.0°	2.1×10^6	1.1×10^7	2.2×10^4	2.4×10^4	2

1.8. RMS relative error

Root-mean-squared (RMS) relative error (RMSRE) provides an objective, quantitative evaluation of experimental data versus theory. It gauges the fit of measurements $g(Re_j)$ to function $f(Re_j)$, giving each of the n samples equal weight in Equation (5). Along with presenting RMSRE, charts in the present work split RMSRE into the bias and scatter components defined in Equation (6). The root-sum-squared of bias and scatter is RMSRE.

$$\text{RMSRE} = \sqrt{\frac{1}{n}\sum_{j=1}^{n}\left|\frac{g(Re_j)}{f(Re_j)} - 1\right|^2} \tag{5}$$

$$\text{bias} = \frac{1}{n}\sum_{j=1}^{n}\left\{\frac{g(Re_j)}{f(Re_j)} - 1\right\} \qquad \text{scatter} = \sqrt{\frac{1}{n}\sum_{j=1}^{n}\left|\frac{g(Re_j)}{f(Re_j)} - 1 - \text{bias}\right|^2} \tag{6}$$

2. Natural convection

Jaffer [5] derived a natural convection formula for external flat plates (with convex perimeter) in any orientation from its analyses of horizontal and vertical plates. This investigation uses the same approach.

Figure 1a–c show the induced fluid flows around heated vertical and horizontal surfaces.

For a horizontal plate with heated upper face, streamlines photographs in Fujii and Imura [3] show natural convection pulling fluid horizontally from above the plate's perimeter into a rising central plume. **Figure 1b** is a diagram of this upward-facing convection. Horizontal flow is nearly absent at the elevation of the dashed line.

The streamlines photograph of a vertical plate in Fujii and Imura [3] shows fluid being pulled horizontally before rising into a plume along the vertical plate. **Figure 1a** is its diagram.

Modeled on a streamlines photograph in Aihara et al. [16], **Figure 1c** is a flow diagram for a horizontal plate with heated lower face. Unheated fluid below the plate flows horizontally inward. It rises a short distance, flows outward closely below the plate, and flows upward upon reaching the plate edge. The edge flows self-organize so that they are at the opposing edges of the plate which are nearest to each other.

Horizontal flow in **Figure 1b** is radial, but not radial in **Figure 1c**.

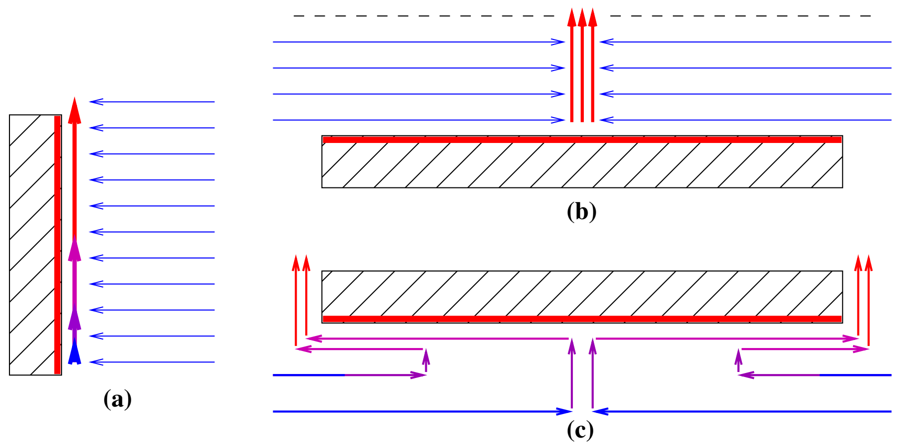

Figure 1. (a) Vertical plate, **(b)** flow above a heated plate, and **(c)** flow below a heated plate.

An important aspect of all three flow topologies is that fluid is pulled horizontally before being heated by the plate. Pulling horizontally expends less energy than pulling vertically because the latter does work against the gravitational force. Inadequate horizontal (or vertical) clearance around a plate can obstruct flow and reduce convection and heat transfer; such a plate is not "external".

From thermodynamic constraints, Jaffer [5] derives generalized natural convection Equation (7) with the parameters specified in **Table 2**:

- θ is the angle of the plate from vertical;
- L is the characteristic length of a flat plate with convex perimeter:
  - face up L^* is the area-to-perimeter ratio;
  - vertical L' is the harmonic mean of the perimeter vertical spans (the height of a level rectangle);
  - face down L_R is the harmonic mean of the perimeter distances to that bisector which is perpendicular to the shortest bisector (1/2 of the shorter side of a rectangle);
- Nu_0 is the conduction into the fluid when not moving (static);

- Ra' is computed with vertical L'; $Ra^* = Ra'\,[L^*/L']^3$; $Ra_R = Ra'\,[L_R/L']^3$.
  Pr does not affect upward-facing heat transfer because the heated fluid flows directly upward, as does conducted heat. When heated fluid must flow along vertical and downward-facing plates, its heat transfer potential is reduced by dividing Ra by Ξ from Equation (8).
- E is the count of $90°$ changes in direction of fluid flow;
- B is the sum of the mean lengths of flows parallel to the plate divided by L;
- C is the plate area fraction responsible for flow induced heat transfer;
- D is the effective length of heat transfer contact with the plate divided by L;
- The ℓ^p-norm combines the static conduction and induced convective heat flows.

$$\overline{Nu} = \left\| Nu_0 \left[1 - C\right],\ \sqrt[2+E]{\left[C\,D\,Nu_0\right]^{3+E} \frac{2}{B}\,Ra} \right\|_p \tag{7}$$

$$\Xi = \left\| 1\ ,\ \frac{0.5}{Pr} \right\|_{\sqrt{1/3}} \qquad Nu_0^* = \frac{2}{\pi} \qquad Nu_0' = \frac{2^4}{\sqrt[4]{2}\,\pi^2} \tag{8}$$

Table 2. Natural convection parameters.

Face	θ	L	$\overline{Nu}$	Nu_0	Ra	E	B	C	D	p
up	$-90°$	L^*	$\overline{Nu^*}$	Nu_0^*	Ra^*	1	2	$1/\sqrt{8}$	1	$1/2$
vertical	$0°$	L'	$\overline{Nu'}$	Nu_0'	Ra'/Ξ	1	$1/2$	$1/2$	$1/4$	$1/2$
down	$+90°$	L_R	$\overline{Nu_R}$	$Nu_0'/2$	Ra_R/Ξ	3	4	$1/2$	2	1

2.1. Effective vertical reynolds number

From the derivation in Jaffer [5] with $Ra'/\Xi \gg 1$, $\overline{Nu} \approx C\,D\,Nu_0\,Re$. Heat transfer $\overline{Nu'}$ is reduced by the self-obstruction factor $1/\sqrt[3]{\Xi}$, which grows with Pr. However, heat transfer is not the same as fluid flow, which increases with decreasing Pr. The Ξ^3 factor in Equation (9) makes Re_N increase with decreasing Pr. Proposed is Equation (9) as the Reynolds number associated with the natural convective flow from a vertical plate.

$$Re_N \approx \frac{\overline{Nu}\,\Xi^{2+E}}{Nu_0\,C\,D} = \frac{8\,\overline{Nu'}\,\Xi^3}{Nu_0'} \qquad \overline{Nu'} \gg Nu_0' \tag{9}$$

2.2. Natural convection from an inclined plate

Ra is proportional to gravitational acceleration. Following the approach of Fujii and Imura [3], the Ra argument to $\overline{h'}(Ra) \equiv k\,\overline{Nu'}(Ra)/L'$ is scaled by $|\cos\theta|$, modeling the reduced convection of a tilted plate as a reduction in gravitational acceleration. Similarly, the Ra arguments to $\overline{h^*}$ and $\overline{h_R}$ are scaled by $|\sin\theta|$. An unobstructed plate induces a single steady-state mode of natural convection (face up, down, or vertical). The instances of max() in Equation (10) choose the largest surface conductance among these modes.

$$\overline{h} = \begin{cases} \max\left(\overline{h'}(|\cos\theta|\,Ra'/\Xi),\ \overline{h^*}(|\sin\theta|\,Ra^*)\right) & \sin\theta < 0 \\ \max\left(\overline{h'}(|\cos\theta|\,Ra'/\Xi),\ \overline{h_R}\left(|\sin\theta|\,Ra_R/\Xi\right)\right) & \sin\theta \geq 0 \end{cases} \tag{10}$$

In reality, the θ transition is more gradual using the ℓ^{16}-norm in Equation (11):

$$\overline{h} = \begin{cases} \left\|\overline{h'}(|\cos\theta|\,Ra'/\Xi),\ \overline{h^*}(|\sin\theta|\,Ra^*)\right\|_{16} & \sin\theta < 0 \\ \left\|\overline{h'}(|\cos\theta|\,Ra'/\Xi),\ \overline{h_R}\,(|\sin\theta|\,Ra_R/\Xi)\right\|_{16} & \sin\theta \ge 0 \end{cases} \tag{11}$$

2.3. Rough natural convection

The agreement of rough plate measurements with theory over the $\pm 90°$ range in **Figure 2** indicates that Equation (11) governs plates with RMS height-of-roughness $0 \le \varepsilon \ll L$.

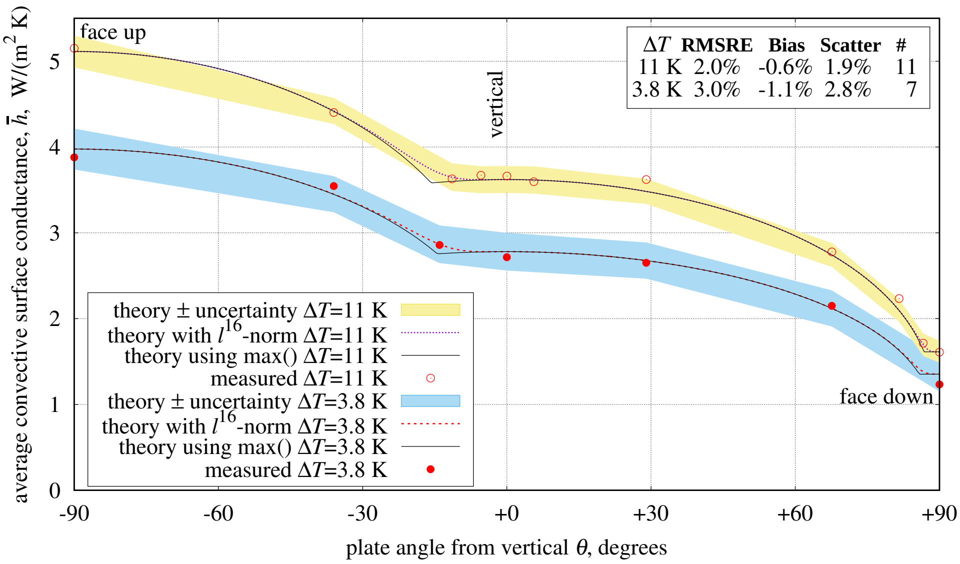

Figure 2. Rough $\varepsilon = 3.0$ mm natural convection versus angle.

3. Forced convection

Forced convection $\overline{Nu}$ is the heat transfer caused by forced flow along (and parallel to) a heated plate. The surface conductance $\overline{h_F} \equiv \overline{Nu}\,k/L$ grows with Re_F, Pr, and k. Its characteristic length L is the length of the plate in the direction of forced flow.

3.1. Rough convection

Jaffer [2] derives the forced convection $\overline{Nu_\rho}$ of rough flow from isotropic, periodic roughness:

$$\overline{Nu_\rho}(Re_F) = \frac{Re_F\,Pr_\infty^{1/3}\,w}{6\,[\ln(L/\varepsilon)]^2} \qquad Re_F > \left[\frac{0.664}{\varepsilon}\right]^2 L_P\,L \tag{12}$$

$$w = \|1, \varepsilon/L_W\|_{\sqrt{1/2}} \tag{13}$$

- $\varepsilon \ll L$ is the root-mean-squared (RMS) height of roughness.
- $L_P \ll L$ is the isotropic period of the roughness [2].
- L_W is the width of the plate (perpendicular to L).
- Pr_∞ is the bulk fluid's Prandtl number (far from the plate).

If the roughness extends to the plate's rim, then it increases the effective width of the rough face by more than $2\,\varepsilon$ because, in addition to the fluid adjacent to plate's face and rim, the fluid near the edge between them is affected. Thus ε and plate width L_W cooperate weakly, leading to an effective width of $\|L_W, \varepsilon\|_{\sqrt{1/2}}$. Dividing by L_W, Equation (13) is the edge roughness correction factor w. **Figure 3** graphs w as a function of ε.

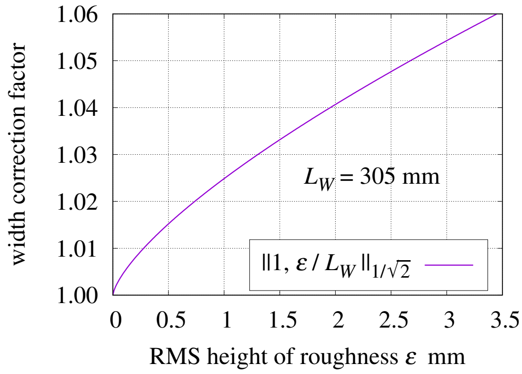

Figure 3. Edge roughness correction factor.

3.2. Plateau roughness

There are isotropic, periodic roughnesses whose convective heat transfer differs from Equation (12).

- Informally, a "plateau roughness" is an isotropic, periodic roughness with most of its area at its peak elevation. A quantitative definition is given in Jaffer [2].
- A "plateau wells roughness" is an array of co-planar wells dropping below a flat surface.
- A "plateau islands roughness" is an array of co-planar islands.

  The present apparatus plate has plateau islands roughness.

For a given Re_F, a plateau roughness may contain areas transferring heat per Equation (12), and separate areas transferring heat as turbulent flow along a smooth plate, but with characteristic length L_P.

3.3. Turbulent forced convection

Jaffer [2] derives the average surface conductance, $\overline{h_F} \equiv \overline{Nu_\tau}\, k/L$, of turbulent flow along an isothermal plate as Equation (14).

$$\overline{Nu_\tau} = \frac{Nu_0\, Re_F\, \overline{f_\tau}}{\sqrt{3}} \sqrt{\frac{Pr/\sqrt{162}+1}{\sqrt{162}\, Pr\, \overline{f_\tau}+1}} \sqrt[3]{\frac{Pr/\Xi}{\|1, 1/Pr\|_3}} \qquad \sqrt{162} \equiv 9\sqrt{2} \tag{14}$$

$$\overline{f_\tau} = \frac{2^{-5/4}}{\left[\mathrm{W}_0\left(Re_F/\sqrt{3}\right)-1\right]^2} \qquad \Xi = \left\|1, \frac{0.5}{Pr}\right\|_{\sqrt{1/3}} \qquad Nu_0 = \frac{2^4}{\pi^2\, \sqrt[4]{2}} \tag{15}$$

- The fluid's effective Prandtl number $Pr = Pr_W^{1/4}\, Pr_\infty^{3/4}$ (from Žukauskas and Šlančiauskas [17]).

  Pr_W is the Prandtl number of fluid at wall (plate) temperature.

  Pr_∞ is the Prandtl number of fluid at the bulk flow temperature.
- W_0 is the principal branch of the Lambert W function, defined as $\mathrm{W}_0(\varphi \exp\varphi) = \varphi$ when $\varphi \geq 0$.
- In Equation (15), $2^{-5/4}$ replaces the $\sqrt[3]{2}/3$ coefficient from Jaffer [2], a $+0.11\%$ correction.
- Plateau islands roughness can shed rough and turbulent flow simultaneously.

3.4. Plateau islands roughness

The plateau islands roughness described in Appendix C has $\overline{Nu_\rho}$ Equation (12) rough convection in the leading Re_I/Re_F portion of the plate, and $\overline{Nu_I}$ Equation (16) turbulent convection in the rest of the plate. Equation (17) Re_I separates the regions, where $L^\bullet$ is the ratio of each (convex) island's area to its perimeter.

$$\overline{Nu_I} = \left\{1 - \Omega + \left\| \frac{\Omega}{2}, \frac{2\,\varepsilon\,[4\,L^\bullet]}{L_P^2} \right\|_2 \right\} \frac{L}{L_P}\, \overline{Nu_\tau}\left(\frac{Re_F\,L_P}{L}\right) \tag{16}$$

$$Re_I = \frac{3^3\,\varepsilon^2\,L^2}{L^\bullet\,L_P^3}\ \ln \frac{3^3\,\varepsilon^2\,L^2}{\sqrt{3}\,L^\bullet\,L_P^3} \tag{17}$$

$$\overline{Nu_\iota} = \overline{Nu_I}(Re_F) + \overline{Nu_\rho}\,(\|Re_F, Re_I\|_{-4}) - \overline{Nu_I}\,(\|Re_F, Re_I\|_{-4}) \tag{18}$$

"Openness" $0 < \Omega < 1$ is the non-plateau area per cell area ratio. Given a $w \times w$ matrix of elevations $S_{s,t}$:

$$\Omega \approx \frac{1}{w^2} \sum_{t=0}^{w-1} \sum_{s=0}^{w-1} \begin{cases} 1, & S_{s,t} < \max(S) - \varepsilon^2/L_P \\ 0, & \text{otherwise} \end{cases} \tag{19}$$

In the log-log plots in **Figure 4a,b**, the effective Re_F exponent is the slope of its line. For example, the "$Re_F/200$" and "$Re_F/333$" lines have slope 1; thus they are proportional to ${Re_F}^1 \equiv Re_F$. In each plot, the "bi-level" trace is $\overline{Nu_\iota}$ Equation (18). The "turbulent part" trace is Equation (20), which is the turbulent component of $\overline{Nu_\iota}$ Equation (18):

$$\overline{Nu_I}(Re_F) - \overline{Nu_I}\,(\|Re_F, Re_I\|_{-4}) \tag{20}$$

In both **Figure 4a,b**, the slope of the Equation (20) "turbulent part" trace is close to 1 through more than an order of magnitude of Re_F. The discrepancy at larger Re_F is unimportant because the heat transfer is dominated by forced convection in that range.

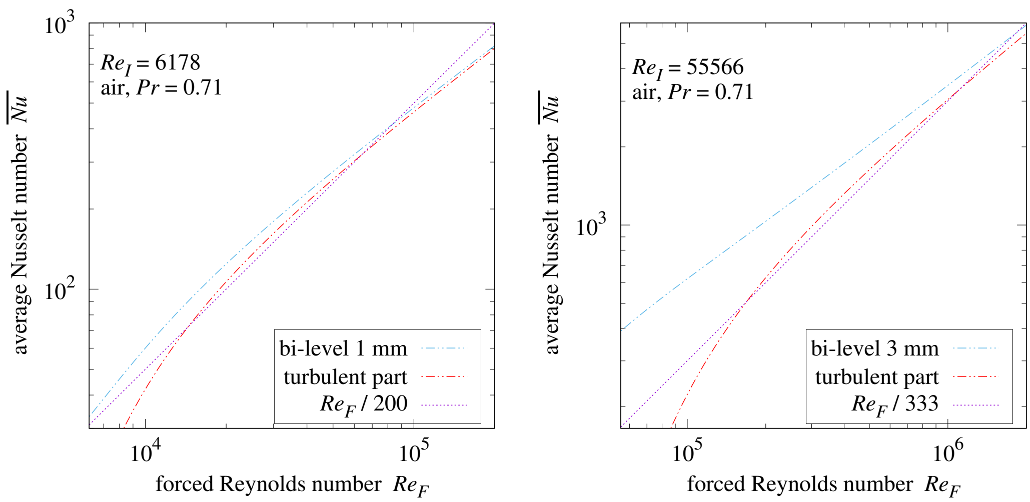

(a) **(b)**

Figure 4. (a) Forced convection $Re_I = 6178$ and **(b)** Forced convection $Re_I = 55,566$.

4. Mixing natural and forced convections

The previous sections established that:

- The effective natural Reynolds number Re_N is proportional to $\overline{Nu_N}$ when $\overline{Nu_N} \gg Nu_0$.
- Forced rough convection $\overline{Nu_\rho}$ is proportional to Re_F in Equation (12).
- And forced turbulent Equation (20) is nearly proportional to Re_F when $Re_F > Re_I$.

On that basis, this investigation proposes:

- Surface conductances $\overline{h_N}$ and $\overline{h_F}$ both being proportional to Reynolds numbers indicates that they are commensurate; they can be combined using symmetrical functions such as the ℓ^p-norm.

One approach to predicting mixed convection would be to compute $\overline{Nu}$ from a function of Re_F and Re_N. However, choosing a single $\overline{Nu}$ formula is problematic; while Re and $\overline{Nu}$ are nearly proportional in all three cases, their coefficients are very different. Also, rough convection $\overline{Nu_\rho}$ is strongly dependent on height-of-roughness ε, but Section 2 found that natural convection is insensitive to roughness $\varepsilon \ll L$.

- This investigation combines a natural surface conductance $\overline{h_N}$ (specifically $\overline{h^*}$, $\overline{h'}$, or $\overline{h_R}$) with the forced surface conductance $\overline{h_F}$ using the ℓ^p-norm (where p depends on plate and flow orientations). Surface conductance $\overline{h}$ is used instead of $\overline{Nu}$ in order to avoid characteristic-length mismatch between $\overline{Nu}$ formulas.

This approach departs from prior works (all of which concerned smooth plates), which compute $\overline{Nu}$ from a ratio of powers of Re_F and the Grashof number $Gr = Ra/Pr$.

4.1. Theory and measurements

Figures which follow plot $\overline{Nu}$ at $L = L'$ measurements and theoretical curves versus $10^3 < Re_F < 10^5$ using logarithmic scales on both axes. Logarithmic scales do not include 0; the following figures plot the natural convection measurement ($Re_F = 0$) at $Re_F = 10^3$.

θ is the angle of the plate from vertical; $-90°$ is face up; $+90°$ is face down.

ψ is the angle of the forced flow from the zenith; $\psi = 90°$ is horizontal flow; $\psi = 0°$ is upward. In this investigation, forced flow is always parallel to the plate; hence, horizontal plates have $\psi = 90°$.

RMSRE is calculated from the measurements between the vertical lines, $1950 < Re_F < 5 \times 10^4$.

The $\varepsilon = 3$ mm plate sheds only rough flow at $1950 < Re_F < 5 \times 10^4$; its graphs are captioned "rough". The $\varepsilon = 1.04$ mm plate sheds rough flow at $Re_F < Re_I = 6178$ and turbulent flow otherwise. Hence it sheds mostly turbulent flow at $1950 < Re_F < 5 \times 10^4$; its graphs are captioned "turbulent".

5. Horizontal forced flow

5.1. Vertical plate with horizontal forced flow

Figure 1a shows that fluid is drawn horizontally towards the heated surface, then rising. The forced and natural heat flows are thus perpendicular, suggesting the ℓ^2-norm for combining $\overline{h_F}$ and vertical $\overline{h'}$:

$$\overline{h} = \left\| \overline{h_F}, \overline{h'} \right\|_2 \tag{21}$$

5.2. American society of heating and ventilation engineers

Rowley et al. [14] measured mixed convection of 0.305 m square vertical plates in horizontal flow in a wind tunnel. Their graphs report surface conductance of the plate versus T_m, the mean of the plate and airflow (Fahrenheit) temperatures. The Rayleigh numbers used by natural convection formulas have the temperature difference as a factor. Through trial and error it was found that taking $1.05\,T_m$ as the (Fahrenheit) plate temperature and $0.95\,T_m$ as the fluid temperature kept RMSRE values less than 10%, which fixed temperature offsets did not. Using coefficients of 1.1 and 0.9 or 1.2 and 0.8 did not strongly affect RMSRE values.

Figures 5 and **6** compare ($\overline{Nu} \equiv \overline{h}\,L/k$) Equation (21) with measurements of vertical plates in horizontal flow shedding turbulent and rough flow, respectively.

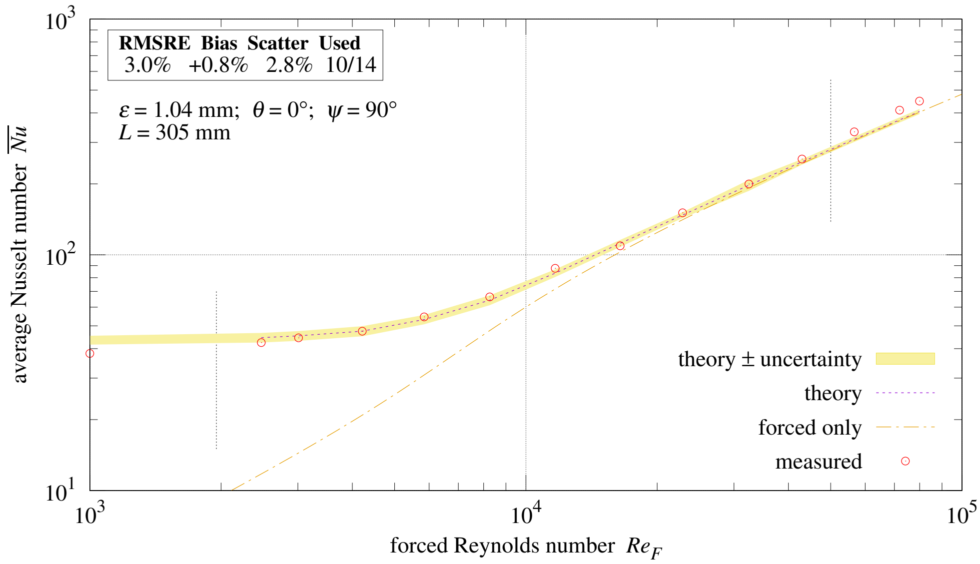

Figure 5. Vertical plate in horizontal forced turbulent flow.

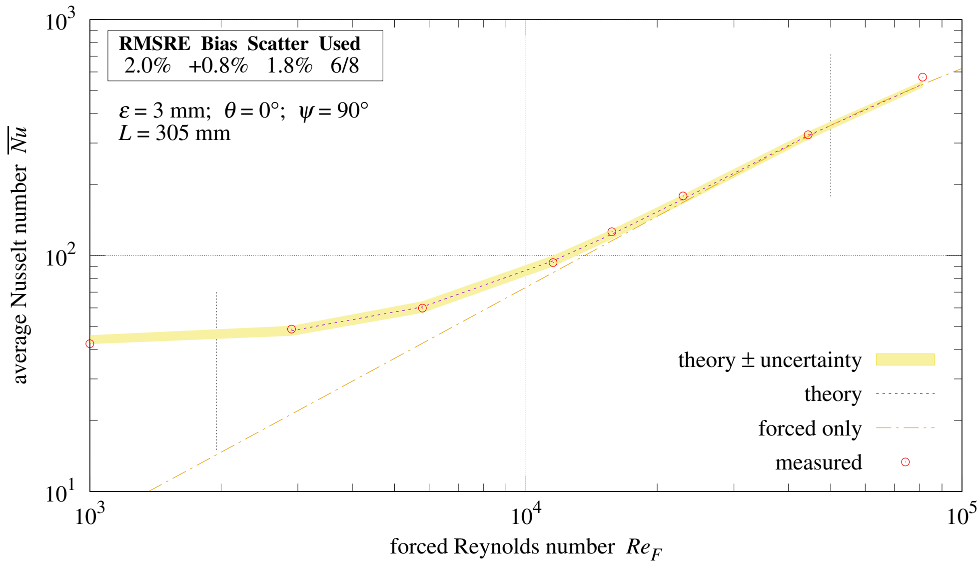

Figure 6. Vertical plate in horizontal forced rough flow.

At a constant rate of airflow, increasing fluid temperature causes kinematic viscosity ν to grow and h_F to shrink because $Re_F = V\,L/\nu$. However, the traces in the graphs from Rowley et al. [14] show increasing convective conductance with temperature. Rowley et al. [14] reports the airspeed measured at the center of the duct (of which the rough plate replaces one side). However, V is defined as the average velocity inside a duct. Let $V_\odot$ be the velocity at the center of the duct.

The velocity is 0 at the duct wall, so some velocity near the wall must be used as the effective velocity V at the test plate. The velocity profile across the duct develops from flat at the duct entrance to the Hagen-Poiseuille parabolic velocity profile for a "fully developed" flow [18] (p. 356). The dimensionless development length is $L_D/D = 25.625$, where $L_D = 5.207$ m is the duct length between the fan and the leading edge of the plate and $D = 203.2$ mm is the hydraulic-diameter of the duct.

$V = V_\odot$ when $L_D = 0$; otherwise $V < V_\odot$. Dimensional analysis finds that V must depend on $V_\odot$, L_D/D, ν, and a viscosity parameter which is independent of temperature. For a gas, let ν_0 be the viscosity at its boiling point.

Dry air is composed of 78.084% N_2, 20.946% O_2, and 0.934% Argon. N_2 has kinematic viscosity $\nu_0 = 1.15 \times 10^{-6}$ m^2/s at its 77.355 K boiling point. O_2 has $\nu_0 = 1.58 \times 10^{-6}$ m^2/s at its 90.188 K boiling point; Argon gas has 1.4223×10^{-6} m^2/s at 100 K. Combining these per the air percentages yields $\overline{\nu_0} = 1.2422 \times 10^{-6}$ m^2/s. Equation (22) is the effective V at the plate.

$$V = V_\odot \Big/ \left[1 + \sqrt{2}\,\frac{L_D}{D}\,\frac{\overline{\nu_0}}{\nu}\right] \qquad \overline{\nu_0} \approx 1.2422 \times 10^{-6}\ \frac{\mathrm{m}^2}{\mathrm{s}} \tag{22}$$

Rowley et al. [14] did not characterize the roughnesses other than to note that the forced convection component was greatest from stucco, followed by brick and rough-plaster, followed by concrete, and the least from smooth-plaster. This investigation has assigned the RMS height-of-roughness (ε) parameters shown in **Table 3**.

Table 3. Assigned parameters.

Figure	**Surface**	ϵ	ε
Figure 7	stucco	0.91	1.47 mm
Figure 8a	rough-plaster	0.91	0.75 mm
Figure 8b	brick	0.93	0.75 mm
Figure 9a	concrete	0.94	0.55 mm
Figure 9b	smooth-plaster	0.91	0.20 mm

Rowley et al. [14] did not address thermal radiative transfers except to state "In order to obtain average radiation conditions, the inside surface of the test duct was painted a dull gray, and all the pipe outside of the refrigerator was covered with a one-inch thick blanket of insulating material." **Table 3** shows common values for the surface emissivity ϵ of each rough material tested. Experimenting with its value, an effective inside surface emissivity of $\epsilon = 0.70$ keeps all non-stucco RMSRE values less than 5%. Unexpectedly small for paint, $\epsilon = 0.70$ would compensate for the wind-tunnel walls being warmer than the forced airflow.

Figure 7 shows the mixed convective conductance curves for stucco, the roughest surface Rowley et al. [14] tested. The derivation in Jaffer [2] of rough convection Equation (12) assumes isotropic roughness. Stucco being non-uniform in its application, it has larger RMSRE than the other surfaces.

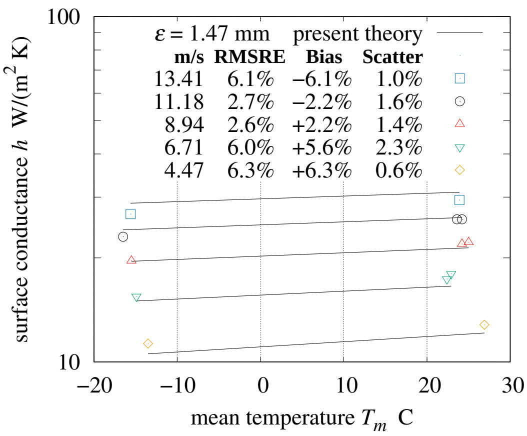

Figure 7. Stucco.

Figures 8a,b and **9a,b** compare the present theory with measurements from rough plaster, brick, concrete, and smooth plaster, respectively[2]. Closer to the isotropic ideal, they have RMSRE values smaller than 5%.

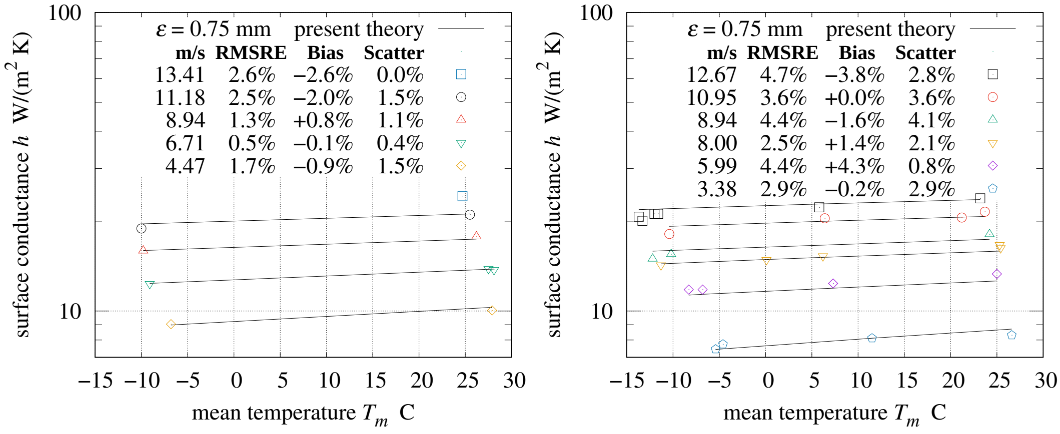

(a) **(b)**

Figure 8. (a) Rough Plaster and **(b)** Brick.

Lacking the actual RMS height-of-roughness and emissivities of the original apparatus, while these results lend support to the present theory, they are not conclusive.

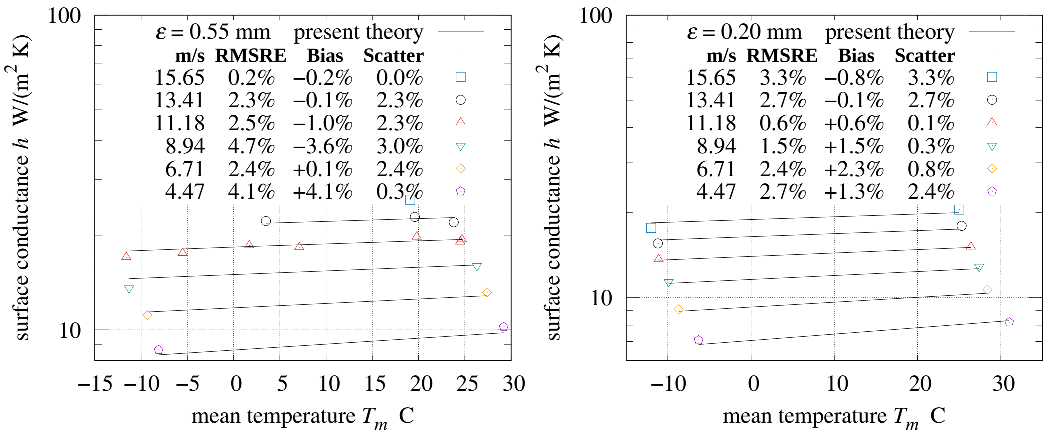

(a) **(b)**

Figure 9. (a) Concrete and **(b)** Smooth plaster.

5.3. Upward facing plate

Figure 1b shows that flow is inward above the heated surface. Forced flow parallel to the surface is thus compatible with upward natural convection $\overline{h^*}$. Their heat flows are perpendicular, suggesting the ℓ^2-norm for combining $\overline{h^*}$ and $\overline{h_F}$:

$$\overline{h} = \left\|\overline{h_F}, \overline{h^*}\right\|_2 \tag{23}$$

Figures 10 and **11** compare Equation (23) with measurements of upward-facing plates shedding turbulent or rough flow, respectively.

5.4. Downward facing plate

Figure 1c shows that flow is outward immediately beneath the heated surface. Forced flow parallel to this surface is thus incompatible with downward natural convection $\overline{h_R}$. These two fluid flows will compete for surface area. **Table 2** shows that $\overline{Nu_R}$ is asymptotically proportional to $\sqrt[5]{Ra_R}$. The ℓ^5-norm combines Ra_R with ${Re_F}^5$, manifesting the fragility of

$\overline{h_R}$ flow because moderate Re_F values can overpower the $\overline{h_R}$ term:

$$\overline{h} = \left\| \overline{h_F}, \overline{h_R} \right\|_5 \tag{24}$$

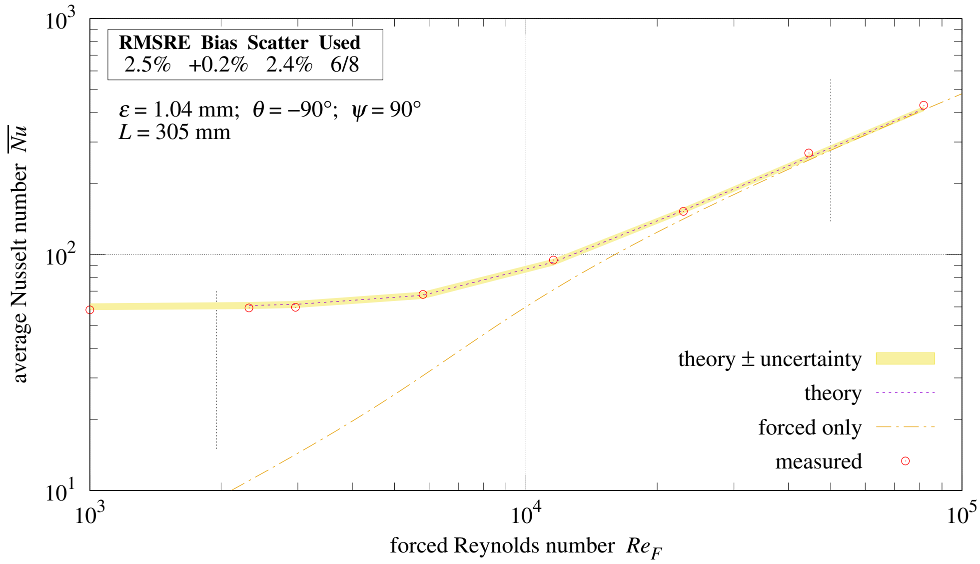

Figure 10. Upward facing plate in horizontal forced turbulent flow.

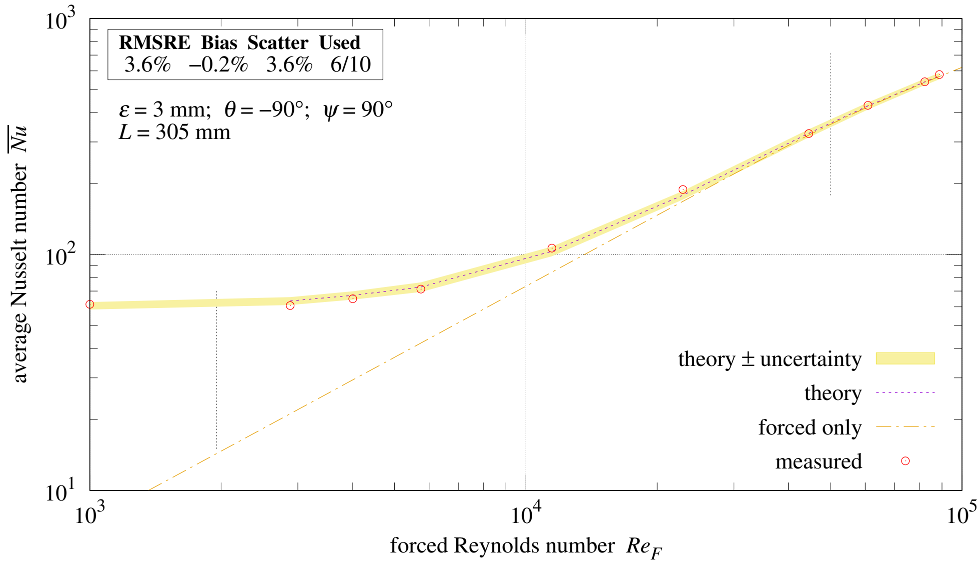

Figure 11. Upward facing plate in horizontal forced rough flow.

Figures 12 and **13** compare Equation (24) with measurements of downward-facing plates shedding turbulent or rough flow, respectively.

6. Vertical plate with vertical forced flow

A vertical plate with vertical forced flow requires a more thorough analysis.

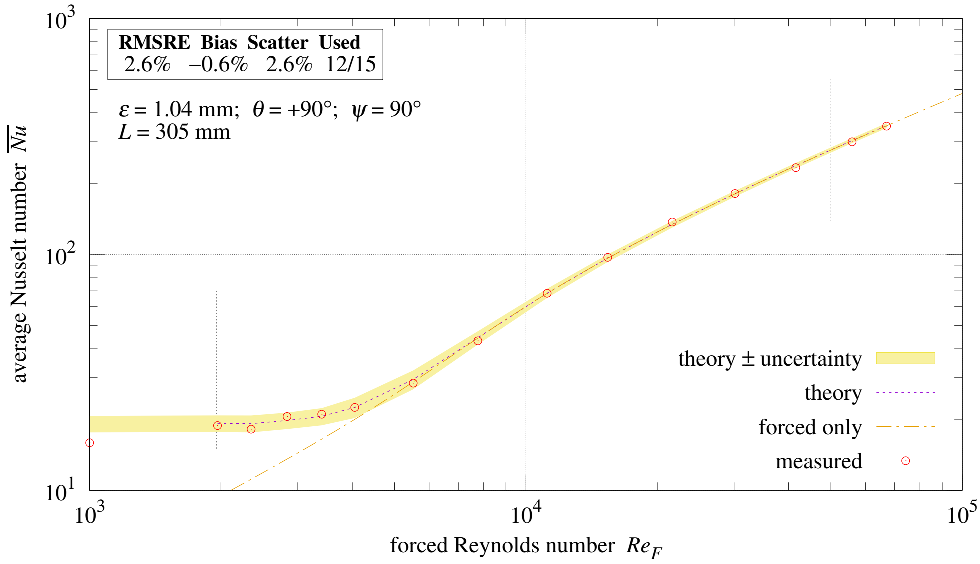

Figure 12. Downward facing plate in horizontal forced turbulent flow.

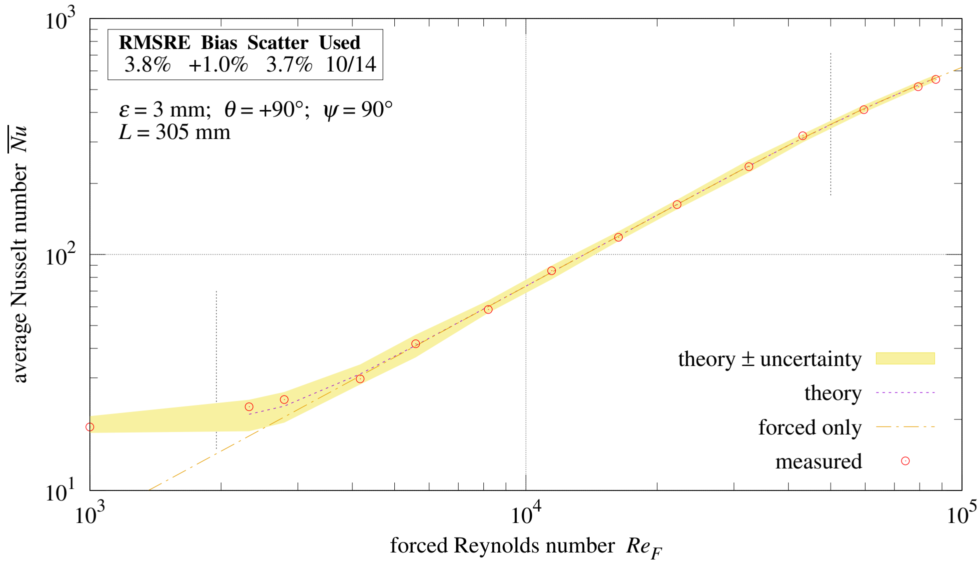

Figure 13. Downward facing plate in horizontal forced rough flow.

6.1. Velocity profiles

The velocity profile function $u(y)$ is the velocity at $x = L/2$ and distance $0 < y < \delta$ from the plate, where δ is the boundary layer thickness at $x = L/2$. Positive $u(y)$ is in the direction of forced flow. The upper plot in **Figure 14** shows the velocity profiles of forced turbulent and natural convection adjacent to a vertical 30.5 cm square plate per the theory in Appendix A, as well as their sum and difference profiles.

The widest y span of constant $u(y)$ occurs in opposing vertical flows when $Re_F = Re_N$. Because of the laminar sublayer of turbulent flows, this cancellation occurs around $u = 0.065$ m/s, not $u = 0$.

The lower plot in **Figure 14** shows the theoretical velocity profiles of forced turbulent flow, and that flow combined with laminar natural flow. The forced Re_F values are double and half of natural Re_N.

In the opposing flow cases, the "forced − natural" and "forced − natural 21,600" traces both have two inflection points near the plate. These indicate that the boundary layer is split, with laminar flow at $0 < y < 5$ mm and turbulent flow at $5 < y < 15$ mm.

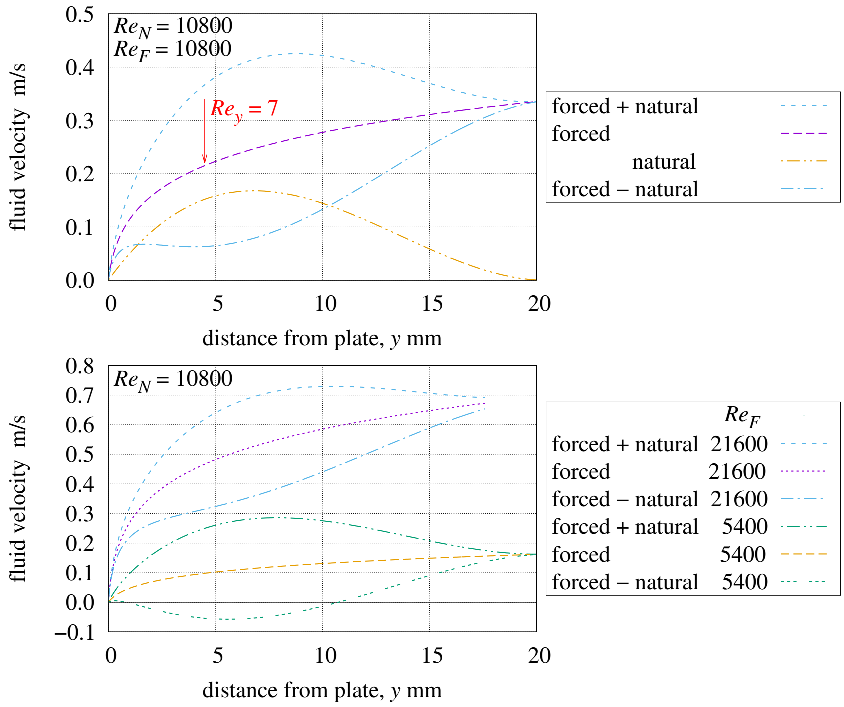

Figure 14. Velocity profiles.

6.2. Vertical plate with forced downward flow

Because the net velocity of the "forced – natural 5400" curve goes negative near the plate, these opposing fluid flows compete for plate area. $\overline{Nu'}$ is asymptotically proportional to $\sqrt[3]{Ra'}$ in **Table 2**; the ℓ^3-norm combines Ra' with ${Re_F}^3$ (which is more robust than the ℓ^5-norm):

$$\overline{h} = \left\|\overline{h_F}, \overline{h'}\right\|_3 \tag{25}$$

The "forced – natural 21,600" trace indicates that its boundary layer is split with laminar natural flow near the plate and forced turbulent flow away. This serves to increase heat transport through the boundary layer (compared with pure laminar), exceeding the ℓ^2-norm, but less than the $\ell^{\sqrt{2}}$-norm. The "mixed $\ell^{\sqrt{3}}$-norm" curve, Equation (26), is close to the upper measurements in **Figures 15** and **16**.

$$\overline{h} = \left\|\overline{h_F}, \overline{h'}\right\|_{\sqrt{3}} \tag{26}$$

Both the 1 mm and 3 mm plates had plateau islands roughness, as described in Section 3. The Re_I arrow marks the transition from rough to turbulent flow along the plateau islands roughness.

The Re_N arrow indicates the position of natural convection's effective Reynolds number calculated by Equation (9). "$Re_N\,\chi_I$" is Re_N scaled by the roughness correction ($\chi_I \geq 1$) detailed in Appendix B; it marks the Re_F lower-bound of the transition between $p = 3$ and $p = \sqrt{3}$.

When the whole plate is shedding turbulent flow, $\chi_I = 1$. When the whole plate is shedding rough flow, $\chi_I = \chi$, which is derived in Appendix A. The close spacing between the arrows in **Figure 15** indicates that nearly all of the plate is shedding turbulent flow.

Figures 15 and **16** show the theory curve and the measurements switching from the "mixed ℓ^3-norm" to the "mixed $\ell^{\sqrt{3}}$-norm" at $Re_F > Re_N\,\chi_I$.

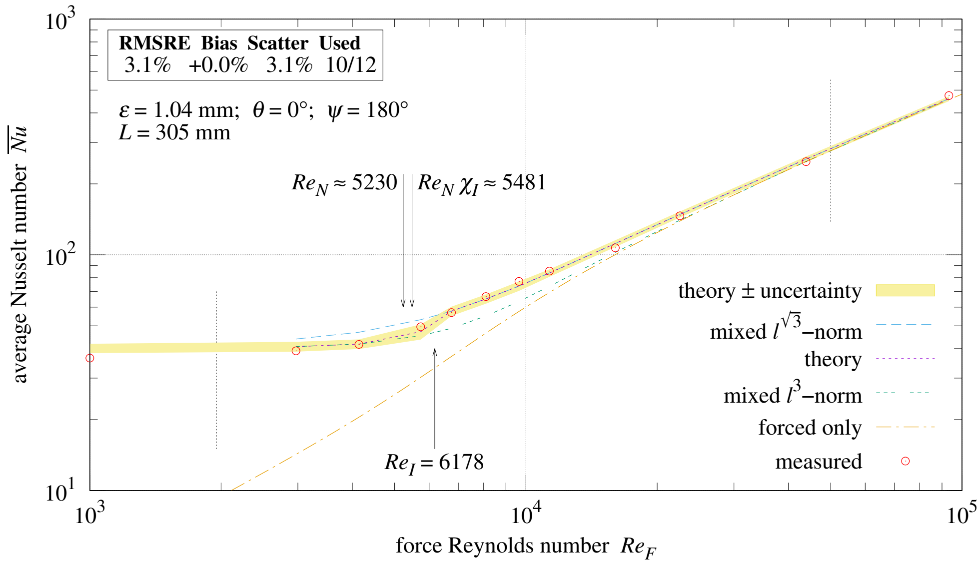

Figure 15. Vertical plate in opposing forced turbulent flow.

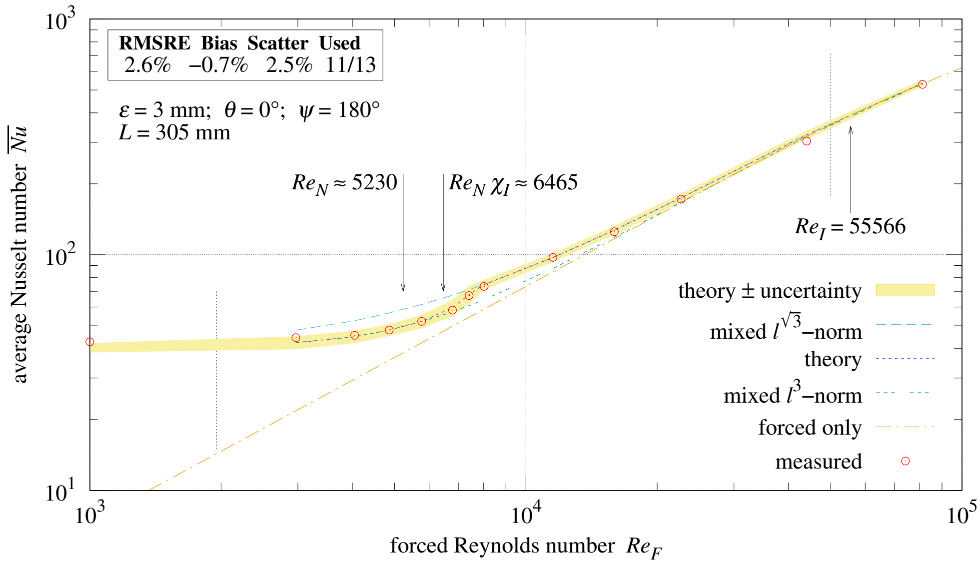

Figure 16. Vertical plate in opposing forced rough flow.

6.3. Vertical plate with forced upward flow

At low speeds, the wide separation between the "forced + natural 5400" and "forced 5400" traces in **Figure 14** indicates the boundary layer is split, with laminar natural flow near the plate and forced turbulent flow away, leading to $\overline{h} = \left\| \overline{h_F}, \overline{h'} \right\|_{\sqrt{3}}$.

The steep slope of the "forced + natural 21,600" and "forced 21,600" traces near the plate indicates that both flows are close to the plate, competing for plate area and leading to $\overline{h} = \left\| \overline{h_F}, \overline{h'} \right\|_3$.

Figures 17 and **18** show the theory curve and the measurements switching from the "mixed ℓ^3-norm" to the "mixed $\ell^{\sqrt{3}}$-norm" at Re_F smaller than $Re_N\,\chi_I$.

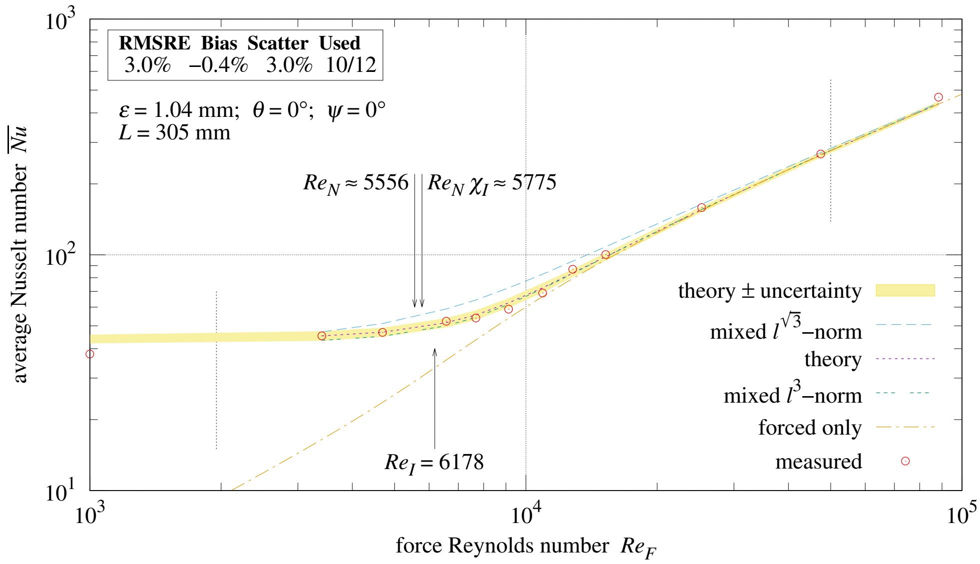

Figure 17. Vertical plate in aiding forced turbulent flow.

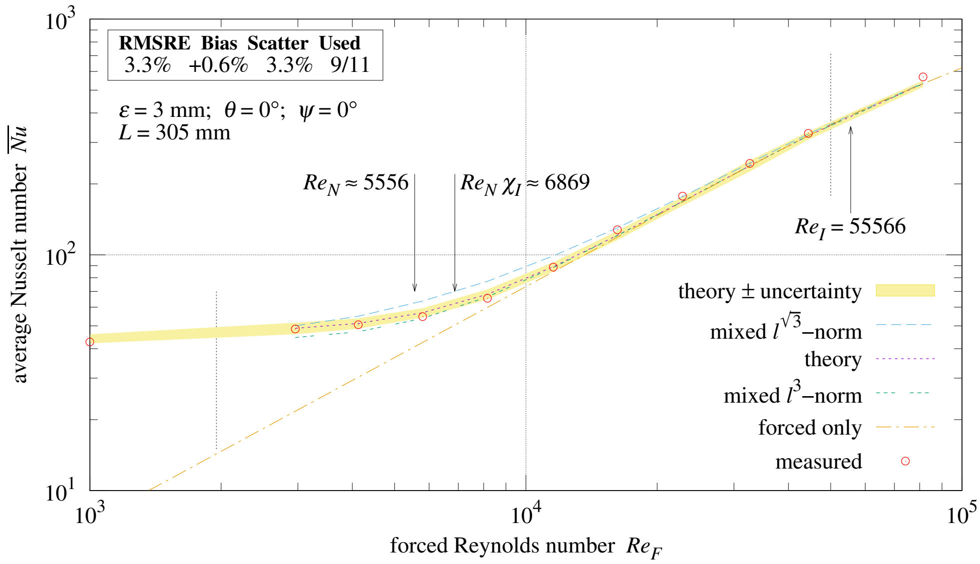

Figure 18. Vertical plate in aiding forced rough flow.

7. Vertical plate with forced flows at any angle

All vertical cases examined so far combine $\overline{h'}$ and $\overline{h_F}$ using the ℓ^p-norm with $\sqrt{3} \le p \le 3$. However, p is a function of Re_F in the vertical aiding and opposing cases. Needed is a function of Re_F which varies smoothly between asymptotes $\sqrt{3}$ and 3. This suggests raising 3 to an exponent between 1/2 and 1. With $\zeta > 1$ and $\eta > 0$, the expression η^ζ/ζ varies between 0 and ∞, and $\exp_\zeta\left(-\eta^\zeta/\zeta\right)$ varies between 0 and 1. Equation (27) varies between $p = 3$ and $p = \sqrt{3}$, with the transition slope controlled by ζ.

The aiding flow transition is gradual with $\zeta = 2$ and $\eta = Re_N\,\chi_I/Re_F$. The opposing flow transition is abrupt with $\zeta = 16$ and $\eta = Re_F/[Re_N\,\chi_I]$. Note that $\eta = Re_N\,\chi_I/Re_F$ differs from $\eta = Re_F/[Re_N\,\chi_I]$.

$$p(\zeta,\eta) = \exp_3\left(1/2 + \exp_\zeta\left(-\eta^\zeta/\zeta\right)/2\right) \tag{27}$$

Introduced in Section 4, ψ is the angle between the forced flow and the zenith. **Figure 19a,b** plot p at $\zeta = 2$ and $\zeta = 16$, used with $\cos\psi > 0$ and $\cos\psi < 0$, respectively.

Table 4 lists p for horizontal and vertical plate and flows.

The theory curve and error statistics in **Figures 15–18** employ p Equation (27).

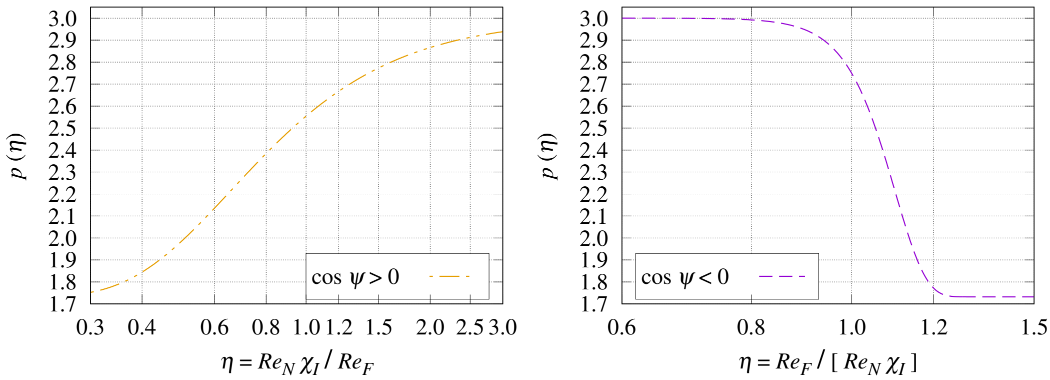

(a) **(b)**

Figure 19. (a) Vertical aiding plate p and **(b)** Vertical opposing plate p.

Table 4. Corner cases p.

Description	$\boldsymbol{\theta}$	$\boldsymbol{\psi}$	$\boldsymbol{p}$
upward facing plate	-90°	90°	2
aiding vertical plate	$+0^\circ$	0°	$\exp_3\left(1/2+\exp_2\left(-[Re_N\,\chi_I/Re_F]^2/2\right)/2\right)$
vertical plate, level flow	$+0^\circ$	90°	2
opposing vertical plate	$+0^\circ$	180°	$\exp_3\left(1/2+\exp_{16}\left(-[Re_F/[Re_N\,\chi_I]]^{16}/16\right)/2\right)$
downward facing plate	$+90^\circ$	90°	5

At $\psi = 0^\circ$, the forced and natural flows align. As ψ tilts toward horizontal ($\pm 90^\circ$), the forced flow can be split into components aligned and perpendicular to the natural upward flow. The coefficients of these components are trigonometric functions of ψ. Tilting to the left or right of $\psi = 0^\circ$ by equal angles must transfer the same amount of heat. Thus, the trigonometric coefficients must be "even" functions of ψ, that is, $F(\psi) = F(-\psi)$. Equation (28) coefficients $[\sin\psi]^2$, $[\cos\psi]^2$, $[\sin\psi]^4$, and $[\cos\psi]^4$ are even functions of ψ.

Downward tilted flow requires a steeper transition slope around $\psi = 180^\circ$; this is implemented using $[\sin\psi]^4$ and $[\cos\psi]^4$ as the coefficients in the second line of Equation (28).

$$\overline{h_\theta} = \begin{cases} [\sin\psi]^2 \left\|\overline{h_F}, \overline{h'_\theta}\right\|_2 + [\cos\psi]^2 \left\|\overline{h_F}, \overline{h'_\theta}\right\|_{p(2,Re_N\,\chi_I/Re_F)} & 0 \le \cos\psi; \\ [\sin\psi]^4 \left\|\overline{h_F}, \overline{h'_\theta}\right\|_2 + [\cos\psi]^4 \left\|\overline{h_F}, \overline{h'_\theta}\right\|_{p(16,Re_F/[Re_N\,\chi_I])} & \cos\psi \le 0 \end{cases} \tag{28}$$

The vertical natural convection component is independent of ψ:

$$\overline{h'_\theta} = \overline{h'}(|\cos\theta|\,Ra'/\Xi) \tag{29}$$

8. Mixed convection from an inclined plate

To compute mixed convection from an inclined plate, Equation (30) replaces conductance functions $\overline{h'}$, $\overline{h^*}$, and $\overline{h_R}$ in Equation (11) with ℓ^p-norms mixing each function with $\overline{h_F}$.

$$\overline{h} = \begin{cases} \left\|\overline{h_\theta}, \left\|\overline{h_F}, \overline{h^*}(|\sin\theta|\,Ra^*)\right\|_2\right\|_{16} & 0 \le \sin\theta \\ \left\|\overline{h_\theta}, \left\|\overline{h_F}, \overline{h_R}(|\sin\theta|\,Ra_R/\Xi)\right\|_5\right\|_{16} & \sin\theta \le 0 \end{cases} \tag{30}$$

Figure 20 shows forced flow opposing natural convection at $\theta = +82$ with $\psi = 98°$. **Figure 21** shows forced flow aiding natural convection at $\theta = \psi = +82°$. The $\theta = \psi = +90°$ curve is shown for comparison.

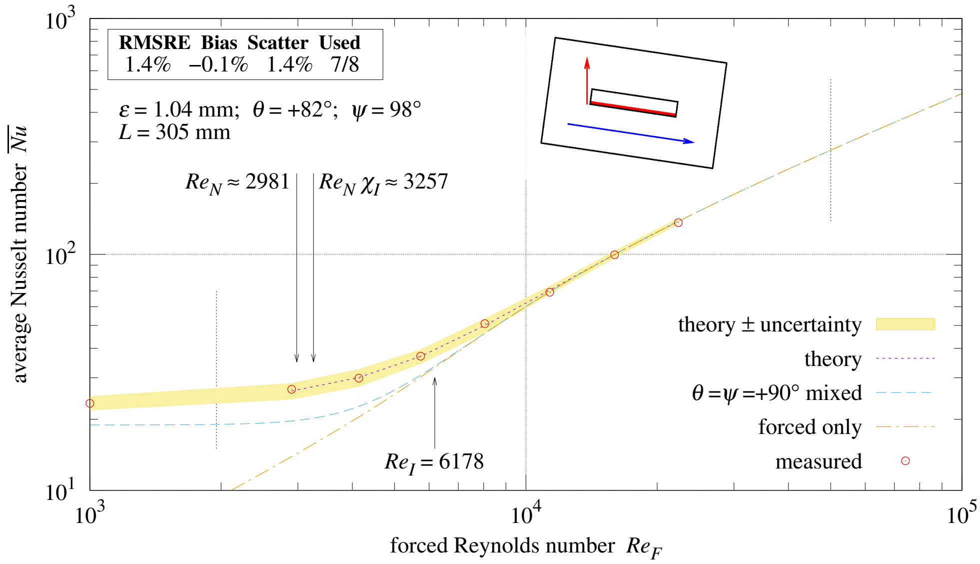

Figure 20. Inclined plate, $\theta = +82°$, opposing forced turbulent flow.

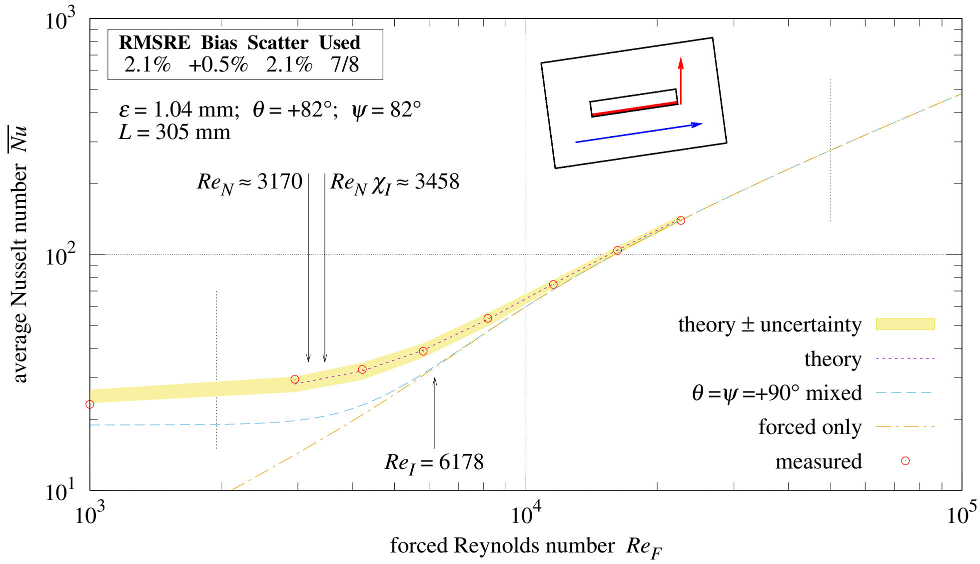

Figure 21. Inclined plate, $\theta = +82°$, aiding forced turbulent flow.

With $\overline{h_F} = 0$, mixed Equation (30) simplifies to natural Equation (11).

When θ and ψ are multiples of 90°, Equation (30) simplifies to $\left\|\overline{h_F}, \overline{h_N}\right\|_p$, with p from **Table 4**.

9. Practice

The natural convection heat transfer formulas for $\overline{h^*}$, $\overline{h'}$, and $\overline{h_R}$ were presented in Section 2. The formulas for forced convection heat transfer $\overline{h_F}$ were presented in Section 3. These are combined using the ℓ^p-norm:

$$\|F_1, F_2\|_p \equiv [\,|F_1|^p + |F_2|^p]^{1/p} \tag{31}$$

θ is the angle of the plate from vertical; $-90°$ is face up; $+90°$ is face down. Coefficient $|\sin\theta|$ scales Ra^* and Ra_R to model the effect of the plate's inclination as a reduction in the gravitational acceleration.

$$\overline{h} = \begin{cases} \left\|\overline{h_\theta},\ \left\|\overline{h_F}, \overline{h^*}(|\sin\theta|\, Ra^*)\right\|_2\right\|_{16} & 0 \le \sin\theta \\ \left\|\overline{h_\theta},\ \left\|\overline{h_F}, \overline{h_R}\,(|\sin\theta|\, Ra_R/\Xi)\right\|_5\right\|_{16} & \sin\theta \le 0 \end{cases} \tag{32}$$

ψ is the angle of the forced flow from the zenith; $\psi = 0°$ is upward flow; $\psi = 90°$ is horizontal flow; $\psi = 180°$ is downward flow. The forced flow is always parallel to the plate.

$$\overline{h_\theta} = \begin{cases} [\sin\psi]^2 \left\|\overline{h_F}, \overline{h'_\theta}\right\|_2 + [\cos\psi]^2 \left\|\overline{h_F}, \overline{h'_\theta}\right\|_{p(2, Re_N\,\chi_I/Re_F)} & 0 \le \cos\psi; \\ [\sin\psi]^4 \left\|\overline{h_F}, \overline{h'_\theta}\right\|_2 + [\cos\psi]^4 \left\|\overline{h_F}, \overline{h'_\theta}\right\|_{p(16, Re_F/[Re_N\,\chi_I])} & \cos\psi \le 0 \end{cases} \tag{33}$$

The vertical natural convection component $\overline{h'_\theta}$ is independent of ψ:

$$\overline{h'_\theta} = \overline{h'}(|\cos\theta|\, Ra'/\Xi) \tag{34}$$

However, its combination with $\overline{h_F}$ depends on function $p(\zeta, \eta)$, specifically $p(2, Re_N\,\chi_I/Re_F)$ when $\cos\psi \ge 0$, and $p(16, Re_F/[Re_N\,\chi_I])$ when $\cos\psi \le 0$:

$$p(\zeta, \eta) = \exp_3\left(1/2 + \exp_\zeta\left(-\eta^\zeta/\zeta\right)/2\right) \qquad \exp_b(\varphi) \equiv b^\varphi \tag{35}$$

The χ_I factor models the longer path which forced flow takes along plateau islands roughness. The χ factor models the longer path which forced flow takes along non-plateau roughness. Re_I Equation (17) is in Section 3. Use $Re_I = +\infty$ (which implies $\chi_I = \chi$) for non-plateau roughness.

$$\chi = 1 - 3\sqrt{3}\,\frac{\varepsilon}{L}\,\ln\frac{\varepsilon}{L} \qquad \chi_I = \exp_\chi\left(\exp_4\left(-\,[Re_F/Re_I]^4\right)\right) \tag{36}$$

Re_N is the effective Reynolds number of vertical natural convection:

$$Re_N \approx \frac{8\,\overline{Nu'}\,\Xi^3}{Nu'_0} \qquad \Xi \equiv \left\|1\ ,\ \frac{0.5}{Pr}\right\|_{\sqrt{1/3}} \qquad \overline{Nu'} \equiv \frac{\overline{h'}\,L}{k} \qquad Nu'_0 \equiv \frac{2^4}{\sqrt[4]{2}\,\pi^2} \tag{37}$$

10. Results

Table 5 shows the combinations of flow types and orthogonal orientations.

Configurations measured by the present apparatus with its 0.305 m square plates are marked with •.

Configurations having turbulent natural convection are marked with ◯. These would require either a larger plate and wind-tunnel or higher plate temperatures than the present apparatus supports.

Table 5. Mixed convective modes.

Natural	**Forced**	**Vertical**	**Up**	**Down**	**Opposing**	**Aiding**
laminar	turbulent	•**Figure 5**	•**Figure 10**	•**Figure 12**	•**Figure 15**	•**Figure 17**
laminar	rough	•**Figure 6**	•**Figure 11**	•**Figure 13**	•**Figure 16**	•**Figure 18**
turbulent	turbulent	◯	◯	◯	◯	◯
turbulent	rough	◯	◯	◯	◯	◯

Tables 6 and **7** summarize the present theory's conformance with 104 measurements in twelve data-sets from the present apparatus's two plates.

The "ε" column identifies the 30.5 cm square plate used. The 3.00 mm plate had rough flow over the $1950 < Re_F < 5 \times 10^4$ range. The 1.04 mm plate had turbulent flow over nearly all of the same range. The "Used" column is the count of measurements having $1950 < Re_F < 5 \times 10^4$ out of the count of measurements. Measurements at $Re_F > 5 \times 10^4$ were practically unaffected by mixing.

The $\varepsilon = 3.00$ mm data-sets have RMSRE values between 2.0% and 3.8%.

The $\varepsilon = 1.04$ mm data-sets have RMSRE values between 1.3% and 3.1%.

Table 6. Convection measurements versus present theory, forced rough flow.

Description	ε	θ	ψ	RMSRE	Bias	Scatter	Used
downward facing plate	3.00 mm	$+90.0°$	$90.0°$	3.8%	$+1.0\%$	3.7%	10/14
upward facing plate	3.00 mm	$-90.0°$	$90.0°$	3.6%	-0.2%	3.6%	6/10
vertical plate, level flow	3.00 mm	$+0.0°$	$90.0°$	2.0%	$+0.8\%$	1.8%	6/8
opposing vertical plate	3.00 mm	$+0.0°$	$180.0°$	2.6%	-0.7%	2.5%	11/13
aiding vertical plate	3.00 mm	$+0.0°$	$0.0°$	3.3%	$+0.6\%$	3.3%	9/11

Table 7. Convection measurements versus present theory, forced turbulent flow.

Description	ε	θ	ψ	RMSRE	Bias	Scatter	Used
downward facing plate	1.04 mm	$+90.0°$	$90.0°$	2.6%	-0.6%	2.6%	12/15
upward facing plate	1.04 mm	$-90.0°$	$90.0°$	2.5%	$+0.2\%$	2.4%	6/8
vertical plate, level flow	1.04 mm	$+0.0°$	$90.0°$	3.0%	$+0.8\%$	2.8%	10/14
opposing vertical plate	1.04 mm	$+0.0°$	$180.0°$	3.1%	$+0.0\%$	3.1%	10/12
aiding vertical plate	1.04 mm	$+0.0°$	$0.0°$	3.0%	-0.4%	3.0%	10/12
opposing inclined plate	1.04 mm	$+82.0°$	$98.0°$	1.4%	-0.1%	1.4%	7/8
aiding inclined plate	1.04 mm	$+82.0°$	$82.0°$	2.1%	$+0.5\%$	2.1%	7/8

Table 8 summarizes the present theory's conformance with 78 measurements in 28 data-sets on five vertical rough surfaces in horizontal flow from Rowley et al. [14]. The five stucco data-sets have RMSRE values between 2.5% and 6.5%; the other data-sets have RMSRE values between 0.2% and 5%.

11. Discussion

Developing this theory was difficult due to the lack of photographs of mixed convection streamlines along rough surfaces. Analysis of the measurements made clear that mixed convection from rough plates was different from that of smooth plates. The flow patterns had to be inferred from these measurements and knowledge of natural and forced convections.

Many theories were tried and discarded concerning the forced vertical flow cases. Examination of hypothetical velocity profiles sparked the present theory, which explains the aiding and opposing flow cases both having $\ell^{\sqrt{3}}$-norm and ℓ^3-norm asymptotes.

11.1. Heat transfer bounds

All of the ℓ^p-norms combining natural and forced heat transfer have $\sqrt{3} \le p \le 5$. The mixed heat transfer is thus bounded between $\|\overline{h_F}, \overline{h_N}\|_5$ and $\|\overline{h_F}, \overline{h_N}\|_{\sqrt{3}}$.

Table 8. Rowley et al. mixed convection measurements.

Surface	ϵ	ε	V	**RMSRE**	**Bias**	**Scatter**	**Count**
smooth-plaster	0.910	0.200 mm	15.65 m/s	3.3%	−0.8%	3.3%	2
smooth-plaster	0.910	0.200 mm	13.41 m/s	2.7%	−0.1%	2.7%	2
smooth-plaster	0.910	0.200 mm	11.18 m/s	0.6%	+0.6%	0.1%	2
smooth-plaster	0.910	0.200 mm	8.94 m/s	1.5%	+1.5%	0.3%	2
smooth-plaster	0.910	0.200 mm	6.71 m/s	2.4%	+2.3%	0.8%	2
smooth-plaster	0.910	0.200 mm	4.47 m/s	2.7%	+1.3%	2.4%	2
concrete	0.940	0.550 mm	15.65 m/s	0.2%	−0.2%	0.0%	1
concrete	0.940	0.550 mm	13.41 m/s	2.3%	−0.1%	2.3%	3
concrete	0.940	0.550 mm	11.18 m/s	2.5%	−1.0%	2.3%	7
concrete	0.940	0.550 mm	8.94 m/s	4.7%	−3.6%	3.0%	2
concrete	0.940	0.550 mm	6.71 m/s	2.4%	+0.1%	2.4%	2
concrete	0.940	0.550 mm	4.47 m/s	4.1%	+4.1%	0.3%	2
brick	0.930	0.750 mm	12.67 m/s	4.7%	−3.8%	2.8%	6
brick	0.930	0.750 mm	10.95 m/s	3.6%	+0.0%	3.6%	4
brick	0.930	0.750 mm	8.94 m/s	4.4%	−1.6%	4.1%	3
brick	0.930	0.750 mm	8.00 m/s	2.5%	+1.4%	2.1%	5
brick	0.930	0.750 mm	5.99 m/s	4.4%	+4.3%	0.8%	4
brick	0.930	0.750 mm	3.38 m/s	2.9%	−0.2%	2.9%	4
rough-plaster	0.910	0.750 mm	13.41 m/s	2.6%	−2.6%	0.0%	1
rough-plaster	0.910	0.750 mm	11.18 m/s	2.5%	−2.0%	1.5%	2
rough-plaster	0.910	0.750 mm	8.94 m/s	1.3%	+0.8%	1.1%	2
rough-plaster	0.910	0.750 mm	6.71 m/s	0.5%	−0.1%	0.4%	3
rough-plaster	0.910	0.750 mm	4.47 m/s	1.7%	−0.9%	1.5%	2
stucco	0.910	1.500 mm	13.41 m/s	6.8%	−6.7%	1.0%	2
stucco	0.910	1.500 mm	11.18 m/s	3.3%	−2.9%	1.6%	3
stucco	0.910	1.500 mm	8.94 m/s	2.1%	+1.5%	1.4%	3
stucco	0.910	1.500 mm	6.71 m/s	5.4%	+4.9%	2.3%	3
stucco	0.910	1.500 mm	4.47 m/s	5.7%	+5.7%	0.6%	2

11.2. Horizontal flow obstruction

The fan pulling air through the chamber is sufficient to counter the effect of the wind-tunnel's obstructions to horizontal flow, except in the case of the vertical plate with opposing flow. In order to draw some air upward at slow (downward) fan speeds, the air's momentum must be reversed. This is modeled by increasing parameter B of **Table 2** by twice the vertical distance from the plate to the test chamber upper edge, normalized by L and the ratio of the upper edge perimeter to the plate width. This same correction applies to still air in the vertical tunnel.

11.3. Effective vertical reynolds number

Aiding and opposing vertical plate measurements in a fluid other than air are needed to further test the effective vertical Reynolds number, Re_N Equation (9).

11.4. Rough velocity profiles

The hypothetical forced flows in the Section 6 velocity profiles were turbulent flows. Measurements of both vertical plates in vertical flow conforming to the present theory suggests that the rough and turbulent velocity profiles are similar.

11.5. Duct velocity profile

The aggregate boiling point kinematic viscosity $\overline{\nu_0}$ in Equation (22) may be useful in developing formulas for pipe and duct velocity profiles as a function of duct length.

12. Conclusions

Formulas were presented for predicting the mixed convective surface conductance of a flat isotropic surface roughness having a convex perimeter in a Newtonian fluid with a steady forced flow in the plane of that roughness.

The prerequisites are the RMS height-of-roughness $0 < \varepsilon$, angle θ of the surface from vertical, angle ψ of the forced flow from the zenith, Ra/L^3 and Pr of the fluid, and the characteristic-length $L > 0$ and $Re > 0$ of the forced flow.

- RMS height-of-roughness ε is the correct metric for predicting forced convective surface conductance.
- Roughness $\varepsilon \ll L$ does not affect the natural component of mixed convection.
- Plate inclination does not affect the forced component of mixed convection.
- When $Re = 0$, the mixed convection is the same as its natural component.

The present work's formulas were compared with 104 measurements in twelve data-sets from the present apparatus in two inclined and all five corner case orientations. The twelve data-sets had RMSRE values between 1.3% and 4% relative to the present theory.

The present work's formulas were compared with 78 measurements in 28 data-sets on five vertical rough surfaces in horizontal airflow from Rowley et al. [14]. The five stucco data-sets had RMSRE values between 2.5% and 6.5%; the other data-sets had RMSRE values between 0.2% and 5%.

Supplementary materials: A zip archive of PDF files of graphs and estimated measurement uncertainties of each 102-min time-series producing a convection measurement can be downloaded from: `http://people.csail.mit.edu/jaffer/convect`. A zip archive of the aggregate measurements is also available from the site.

Author contributions: Conceptualization, AJ and MJ; methodology, AJ; software, AJ; validation, AJ; formal analysis, AJ; investigation, AJ and MJ; resources, AJ; data curation, AJ; writing–original draft preparation, AJ; writing–review and editing, MJ; visualization, MJ and AJ; supervision, AJ; project administration, AJ; funding acquisition, AJ. All authors have read and agreed to the published version of the manuscript.

Acknowledgments: Thanks to John Cox (1957–2022) and Doug Ruuska for machining the bi-level plate. Thanks to Roberta Jaffer for assistance and problem-solving suggestions. Thanks to anonymous reviewers for their useful suggestions.

Conflict of interest: The authors declare no conflict of interest.

Nomenclature

Latin letters

A	surface area (m^2)
Gr	Grashof number
$\overline{h}$	average convective surface conductance ($\mathrm{W}/(\mathrm{m}^2 \cdot \mathrm{K})$)
$\overline{h_F}$	forced convective surface conductance ($\mathrm{W}/(\mathrm{m}^2 \cdot \mathrm{K})$)
$\overline{h_N}$	natural convective surface conductance ($\mathrm{W}/(\mathrm{m}^2 \cdot \mathrm{K})$)
$\overline{h^*}$	upward natural convective surface conductance ($\mathrm{W}/(\mathrm{m}^2 \cdot \mathrm{K})$)
$\overline{h'}$	vertical plate natural convective surface conductance ($\mathrm{W}/(\mathrm{m}^2 \cdot \mathrm{K})$)
$\overline{h_\theta}$	vertical mode of inclined natural convective surface conductance ($\mathrm{W}/(\mathrm{m}^2 \cdot \mathrm{K})$)
$\overline{h'_\theta}$	vertical component of $\overline{h_\theta}$ ($\mathrm{W}/(\mathrm{m}^2 \cdot \mathrm{K})$)
$\overline{h_R}$	downward natural convective surface conductance ($\mathrm{W}/(\mathrm{m}^2 \cdot \mathrm{K})$)
k	fluid thermal conductivity ($\mathrm{W}/(\mathrm{m} \cdot \mathrm{K})$)
L	characteristic length (m)
L_P	roughness spatial period (m)
L^*	ratio of plate area to its perimeter (m)
$L^\bullet$	ratio of island area to its perimeter (m)
L_W	width of plate (m)
$\overline{Nu}$	average Nusselt number
$\overline{Nu_N}$	average Nusselt number of natural convection
$\overline{Nu'}$	average Nusselt number of vertical plate natural convection
Nu'_0	Nusselt number of vertical plate conduction
p	exponent in ℓ^p-norm: $\{\lvert F_1\rvert^p + \lvert F_2\rvert^p\}^{1/p}$
Pr	Prandtl number of the fluid
Ra	Rayleigh number
Ra'	vertical plate Rayleigh number
Ra^*	upward Rayleigh number
Ra_R	downward Rayleigh number
Re_F	Reynolds number of the forced flow parallel to the plate
Re_I	Reynolds number of rough turbulent transition to forced turbulent flow
Re_N	effective Reynolds number of vertical natural convection
Re_y	friction Reynolds number
$u(y)$	velocity at $x = L/2$ and distance y from the plate (m/s)
u_N	effective natural flow speed $= \nu\, Re_N/L$ (m/s)
u^*	friction velocity (m/s)
W_0	principal branch of the Lambert W function
y	distance from plate (m)
$\overline{z}$	average roughness elevation (m)

Greek symbols

δ	boundary layer thickness (m)
δ_λ	laminar boundary layer thickness (m)
δ_τ	turbulent boundary layer thickness (m)
ϵ	surface emissivity
ε	surface RMS height-of-roughness (m)
η	ratio of Re_N and Re_F (either order)
κ	von Kármán constant ≈ 0.41
Ω	ratio of non-plateau area to cell area ($\mathrm{m}^2/\mathrm{m}^2$)
ν	fluid kinematic viscosity (m^2/s)
ν_0	gas kinematic viscosity (m^2/s) at boiling point
ψ	angle between the forced flow and the zenith; $0°$ is aiding flow; $180°$ is opposing flow
θ	angle of the plate surface from vertical; face up is $-90°$; face down is $+90°$
Ξ	natural convection self-obstruction factor
χ	roughness velocity correction factor for forced flow
χ_I	plateau islands roughness correction factor

Notes

[1] Schlichting [19] describes a boundary-layer: "In that thin layer the velocity of the fluid increases from zero at the wall (no slip) to its full value which corresponds to external frictionless flow."

[2] One outlying measurement for brick at $V = 15.65$ m/s was omitted.

References

1. Lienhard JH. Heat Transfer in Flat-Plate Boundary Layers: A Correlation for Laminar, Transitional, and Turbulent Flow. Journal of Heat Transfer. 2020; 142(6): 04.
2. Jaffer A. Skin-friction and forced convection from rough and smooth plates. Thermo. 2023; 3(4): 711–775. doi: 10.3390/thermo3040040
3. Fujii T, Imura H. Natural-convection heat transfer from a plate with arbitrary inclination. International Journal of Heat and Mass Transfer. 1972; 15(4): 755–764. doi: 10.1016/0017-9310(72)90118-4
4. Churchill SW, Chu HHS. Correlating equations for laminar and turbulent free convection from a vertical plate. International Journal of Heat and Mass Transfer. 1975; 18(11): 1323–1329. doi: 10.1016/0017-9310(75)90243-4.
5. Jaffer A. Natural convection heat transfer from an isothermal plate. Thermo. 2023; 3(1): 148–175. doi: 10.3390/thermo3010010
6. Churchill SW, Usagi R. A general expression for the correlation of rates of transfer and other phenomena. AIChE Journal. 1972; 18(6): 1121–1128. doi:10.1002/aic.690180606
7. Hieber CA. Mixed convection above a heated horizontal surface. International Journal of Heat and Mass Transfer. 1973; 16(4): 769–785. doi: 10.1016/0017-9310(73)90090-2
8. Wang XA. An experimental study of mixed, forced, and free convection heat transfer from a horizontal flat plate to air. Journal of Heat Transfer. 1982; 104(1): 139–144. doi: 10.1115/1.3245040
9. Siebers DL, Schwind RG, Moffat RJ. Experimental mixed-convection heat transfer from a large, vertical surface in a horizontal flow. Technical report, Sandia National Lab; 1983.
10. Ramachandran N, Armaly BF, Chen TS. Measurements and Predictions of Laminar Mixed Convection Flow Adjacent to a Vertical Surface. Journal of Heat Transfer. 1985; 107(3): 636–641. doi: 10.1115/1.3247471
11. Lin HT, Yu WS, Chen CC. Comprehensive correlations for laminar mixed convection on vertical and horizontal flat plates. Wärme-und Stoffübertragung. 1990; 25(6): 353–359.
12. Kobus CJ, Wedekind JL. An experimental investigation into forced, natural and combined forced and natural convective heat transfer from stationary isothermal circular disks. International Journal of Heat and Mass Transfer. 1995; 38(18): 3329–3339. doi: 10.1016/0017-9310(95)00096-R

13. Kobus CJ, Wedekind JL. An experimental investigation into natural convection heat transfer from horizontal isothermal circular disks. International Journal of Heat and Mass Transfer. 2001; 44(17): 3381–3384. doi: 10.1016/S0017-9310(00)00330-6
14. Rowley FB, Algren AB, Blackshaw JL. Surface conductances as affected by air velocity, temperature and character of surface. ASHVE Trans. 1930; 36: 429–446.
15. Incropera FP, DeWitt DP, Bergman TL, Lavine AS. Fundamentals of Heat and Mass Transfer. Wiley; 2007.
16. Aihara T, Yamada Y, Endö S. Free convection along the downward-facing surface of a heated horizontal plate. International Journal of Heat and Mass Transfer. 1972;15(12): 2535–2549. doi: 10.1016/0017-9310(72)90145-7
17. Žukauskas A, Šlančiauskas A. Heat Transfer in Turbulent Fluid Flows. Hemisphere Publishing Corp; 1987.
18. Lienhard IV JH, Lienhard VA JH. Heat Transfer Textbook. Phlogiston Press; 2020.
19. Schlichting H. Boundary-Layer Theory. McGraw Hill; 2014.
20. Rice RW. Emittance factors for infrared thermometers used for wood products. Wood and Fiber Science. 2004; 36: 520–526.
21. Barreira E, Almeida RMSF, Simões ML. Emissivity of building materials for infrared measurements. Sensors. 2021; 21(6). doi: 10.3390/s21061961
22. Abernethy RB, Benedict RP, Dowdell RB. Asme measurement uncertainty. ASME. J. Fluids Eng. 1985; 107(2): 161–164. doi: 10.1115/1.3242450

Appendix A

I. Velocity profiles

This investigation assumes that the laminar natural boundary layer thickness δ_λ is the same as the forced laminar thickness calculated using the effective vertical Re_N. Formulas from Lienhard and Lienhard [18] lead to natural convection velocity profile $u(y)$ Equation (A1), where y is the horizontal distance from the mid-line of the vertical plate, ν is the fluid's kinematic viscosity, and $u_N = \nu\, Re_N/L$ is the effective natural flow speed.

$$u(y) \approx 4\, u_N \, \frac{y}{\delta_\lambda} \left[1 - \frac{y}{\delta_\lambda}\right]^2 \qquad 0 < y < \delta_\lambda \approx \frac{4.92\, L}{\sqrt{Re_N}} \tag{A1}$$

In forced turbulent flow along a smooth plate, let friction velocity $u^* \approx u_\infty \sqrt{\overline{f_\tau}/2}$, and $Re_y = u^*\, y/\nu$, with $\overline{f_\tau}$ from Equation (15). Lienhard and Lienhard [18] gives the viscous sublayer velocity profile as Equation (A2), and the log-layer velocity profile as Equation (A3). The von Kármán constant $\kappa \approx 0.41$.

$$\frac{u(y)}{u^*} \approx Re_y \qquad Re_y < 7 \tag{A2}$$

$$\frac{u(y)}{u^*} \approx \left[\frac{1}{\kappa}\ \ln\left(Re_y\right) + 5.5\right] \qquad Re_y > 30 \tag{A3}$$

Lienhard and Lienhard [18] does not tell how to interpolate these two formulas. The $7 < Re_y < 30$ range to be interpolated is large, and the transition must be gradual. Adapting the staged-transition formula from Jaffer [2] by using the $\ell^{-\sqrt{1/3}}$-norm instead of the ℓ^{-4}-norm in Re_Y Equation (A4) yields Equation (A5).

$$Re_Y = \|7, Re_y\|_{-\sqrt{1/3}} \qquad y < \delta_\tau \approx \frac{0.37\, L}{\sqrt[5]{Re}} \tag{A4}$$

$$\frac{u(y)}{u^*} = \left[5.5 + \frac{\ln\left(Re_y\right)}{\kappa}\right] + \frac{Re_Y}{Re_y}\left[Re_Y - 5.5 - \frac{\ln\left(Re_Y\right)}{\kappa}\right] \tag{A5}$$

Equation (A6) is a proposed alternative to Equation (A5) based on the Lambert W_0 function.

$$\frac{u(y)}{u^*} = \frac{8}{\sqrt{3}}\, \mathrm{W}_0(\sqrt{3}\, Re_y) \tag{A6}$$

The "interpolated" Equation (A5) and Equation (A6) curves are nearly identical in **Figure A1**. It is not surprising that a formula for turbulent flow involves the Lambert W_0 function. Equation (A6) uses $\mathrm{W}_0(\sqrt{3}\, Re_y)$ while $\overline{f_\tau}$ Equation (15) uses $\mathrm{W}_0(Re_F/\sqrt{3})$.

While interesting, these curves are employed only for estimating the net vertical flow near the plate. None of the convective surface conductance formulas quantitatively depend on them.

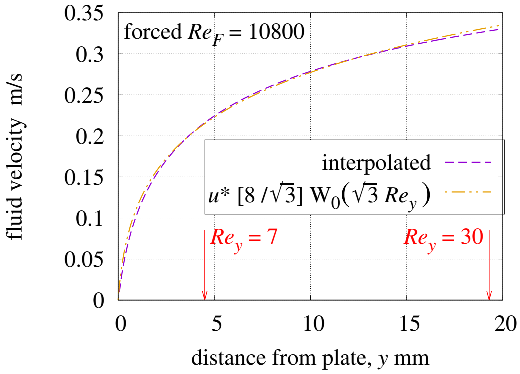

Figure A1. Forced convection velocity profile.

II. Rough plates

Because roughness $\varepsilon \ll L$ has negligible effect on natural convection, u_N should be the same from smooth and rough plates. Hence, their $Re_N \equiv u_N\,\varepsilon/\nu$ should also be equal.

Forced flow along a rough surface traverses a path longer than L. The effective Re_N/Re_F ratio of a rough surface should be increased by a function of the "roughness Reynolds number" Re_ε Equation (A7).

$$Re_\varepsilon = \frac{u^*\,\varepsilon}{\nu} = \frac{Re}{\sqrt{3}\,[L/\varepsilon]\;\ln(L/\varepsilon)} \tag{A7}$$

Proposed is Re_N/Re scale factor χ Equation (A8), where Re is the solution of Equation (A7) combined with $Re_\varepsilon = 3\,[\varepsilon/L]^2$. **Figure A2a** graphs χ as a function of ε.

$$\chi = \frac{Re_F + Re}{Re_F} = 1 - 3\,\sqrt{3}\,\frac{\varepsilon}{L}\;\ln\frac{\varepsilon}{L} \tag{A8}$$

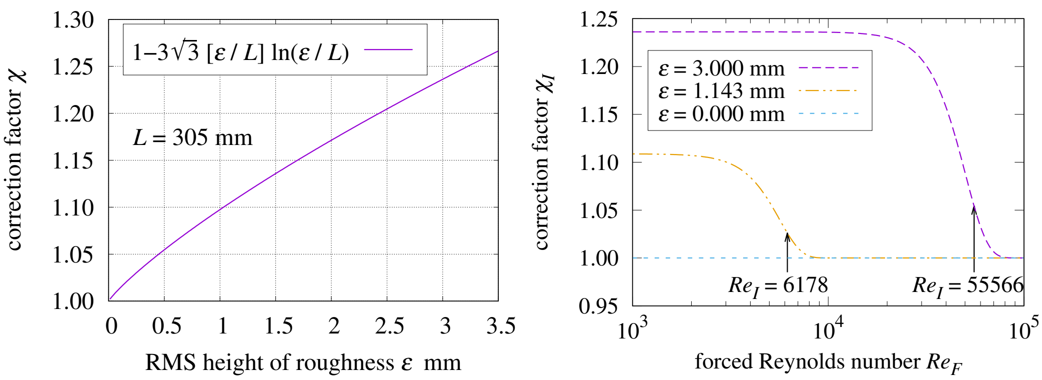

(a) **(b)**

Figure A2. **(a)** χ versus ε and **(b)** Re_N correction factor χ_I.

Appendix B

Plateau islands roughness correction

Plates shedding only turbulent flow have $\chi_I = 1$. Plates shedding only rough flow have $\chi_I = \chi$ from Equation (A8).

Plateau roughness (forced) convection transitions from rough flow to turbulent flow as the ℓ^{-4}-norm in Equation (18). The scale factor χ_I should vary between 1 and χ as a function of Re_F. Expression $\exp_4\left(-[Re_F/Re_I]^4\right)$ varies between 0 and 1. Proposed is χ_I, the Re_N/Re_F scale factor:

$$\chi_I = \exp_\chi\!\left(\exp_4\left(-[Re_F/Re_I]^4\right)\right) \tag{B1}$$

Note the similarity of Equation (B1) and Equation (27) with $\zeta = 4$.

Figure A2b plots χ_I with $\varepsilon = 3$ mm, $\varepsilon = 1.143$ mm, and $\varepsilon = 0$.

Appendix C

I. Apparatus and measurement methodology

The original goal of the present apparatus was to measure forced convection heat transfer from a precisely rough plate over the widest practical span of airflow velocities. To minimize natural convection, it measured downward natural convection mixed with horizontal forced flow. Its measurements are presented in Jaffer [2].

Although more complicated to analyze, the plate was suspended, not embedded, in the wind-tunnel. The measurements from prior investigations which embedded the plate in a wind-tunnel wall were largely incompatible with the present theory because their flows were not isobaric.

The small size of the wind-tunnel chassis (1.3 m $\times$ 0.61 m $\times$ 0.65 m) afforded an opportunity to characterize mixed convection at other orientations of the plate and flow.

II. The plate

Figure C1a shows the rough surface of the test plate; it was milled from a slab of MIC-6 aluminum (Al) to have (676 of) square $8.33\,\text{mm} \times 8.33\,\text{mm} \times 6\,\text{mm}$ posts spaced on 11.7 mm centers over the 30.5 cm $\times$ 30.5 cm plate. The area of the top of each post was $0.694\,\text{cm}^2$, which was 50.4% of its $1.38\,\text{cm}^2$ cell. The RMS height-of-roughness $\varepsilon = 3.00$ mm. Openness $\Omega \approx 49.6\%$. Embedded in the plate are 9 electronic resistors as heating elements and a Texas Instruments LM35 Precision Centigrade Temperature Sensor. 2.54 cm of thermal insulating foam separates the back of the plate from a 0.32 mm thick sheet of aluminum with an LM35 at its center. **Figure C1b** is a cross-section illustration of the plate assembly.

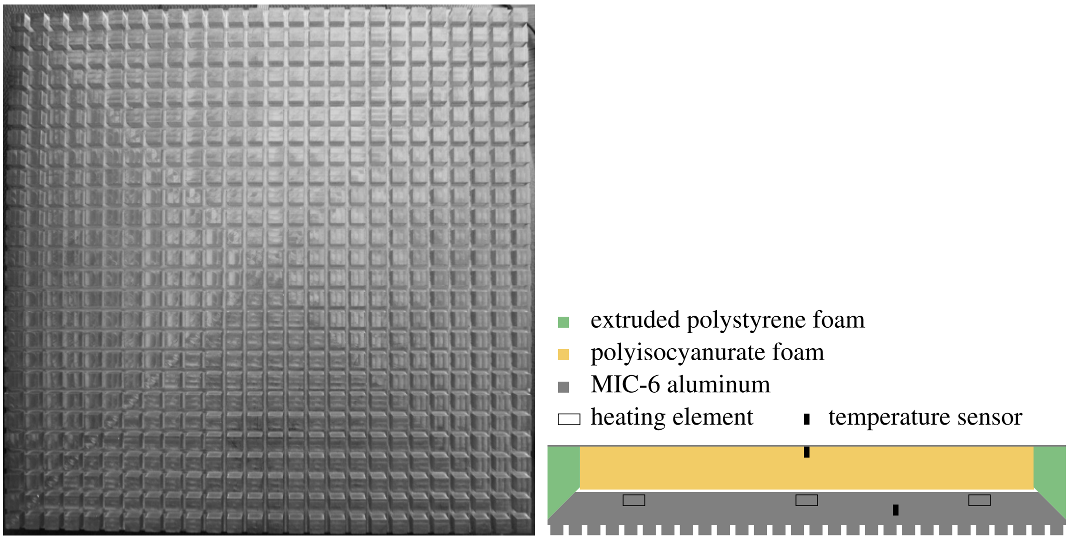

(a) **(b)**

Figure C1. **(a)** Rough surface of plate and **(b)** Plate assembly cross-section.

III. Wind tunnel

The fan pulls air from the test chamber's open intake through the test chamber. The fan blows directly into a diffuser made of folded plastic mesh to disrupt vortexes generated by the fan. In a sufficiently large room, the disrupted vortexes dissipate before being drawn into the open intake.

To guarantee isobaric (no pressure drop) flow, the wind-tunnel must be sufficiently large that its test chamber and plate assembly boundary-layers do not interact at fan-capable airspeeds.

The wind-tunnel test chamber in **Figure C2a** has a 61 cm $\times$ 35.6 cm cross-section and a 61 cm depth. This allows the plate assembly to be centered in the wind-tunnel with 15 cm of space on all sides. The fan pulling air through the test chamber produces a maximum airspeed of 4.65 m/s ($Re \approx 9.2 \times 10^4$ along the 30.5 cm square plate). Its minimum nonzero airspeed is 0.12 m/s ($Re \approx 2300$).

Test chamber laminar and turbulent 99% boundary-layer thicknesses ([19]) are:

$$\delta_\lambda = 4.92\sqrt{\frac{x\nu}{u}} \qquad \delta_\tau = 0.37\,x^{4/5}\left[\frac{\nu}{u}\right]^{1/5} \tag{C1}$$

Figure C2b shows that the 15 cm clearance between the plate and the test chamber walls is sufficient to prevent their boundary-layers from interacting at airspeeds within the fan's capabilities.

The plate assembly (face down in **Figures C1b** and **C2a** is suspended by six lengths of 0.38 mm-diameter steel piano wire terminated at twelve zither tuning pins in wooden blocks fastened to the exterior of the test chamber. With the plate assembly in the test chamber, the airspeed increases in proportion to the reduction of test chamber aperture A_e by the plate's cross-sectional area $A_\times$:

$$\frac{u_\times}{u} = \frac{A_e}{A_e - A_\times} \approx 107.6\% \tag{C2}$$

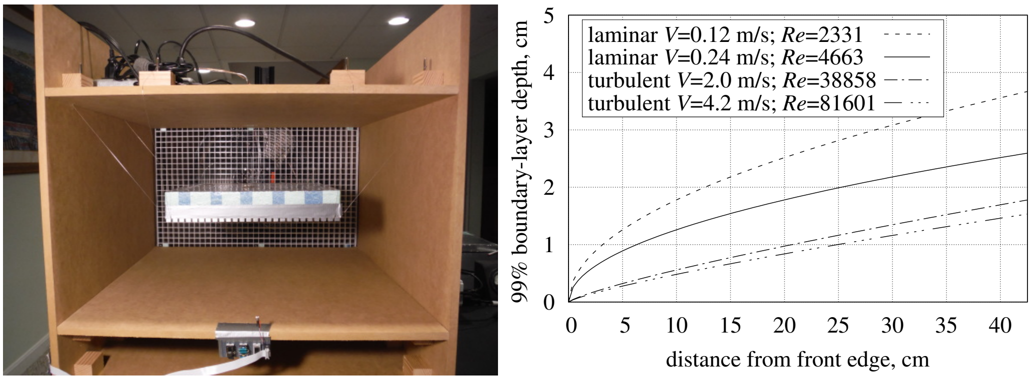

(a) **(b)**

Figure C2. (a) $\varepsilon = 3$ mm plate in wind-tunnel and **(b)** Wind-tunnel boundary-layers.

IV. Automation

Data capture and control of convection experiments are performed by an "STM32F3 Discovery 32-Bit ARM M4 72MHz" development board. The program written for the STM32F3 captures readings and writes them to the microprocessor's non-volatile RAM, controls the plate heating, servos the fan speed, and later uploads its data to a computer through a USB cable.

Once per second during an experiment, the program calibrates and reads each on-chip 12 bit analog-to-digital converter 16 times, summing the sixteen 12 bit readings to create a 16 bit reading per converter.

Rotations of the fan are sensed when a fan blade interrupts an infrared beam. The microprocessor controls a solid-state relay (supplying power to the fan) to maintain a fan rotation rate, ω, which is dialed into switches. At $\omega \le 210$ r/min, the microprocessor pulses power to the fan to phase-lock the beam interruption signal to an internal clock. At $\omega > 210$ r/min, the microprocessor servos the duty cycle of a 7.5 Hz square-wave gating power to the fan. This system operates at $32\ \mathrm{r/min} < \omega < 1400\ \mathrm{r/min}$.

V. Calibration

The correspondence between fan rotation rate ω and test chamber airspeed u was determined using an "Ambient Weather WM-2", which specifies an accuracy of $\pm3\%$ of reading. After 2017 an "ABM-200 Airflow & Environmental Meter" specifying an accuracy of $\pm0.5\%$ of reading between 2.2 m/s and 62.5 m/s, was used.

The "UtiliTech 20 inch 3-Speed High Velocity Floor Fan" has three blades with maximum radius $r = 0.254$ m. Its characteristic length is its hydraulic-diameter, $D_H = 0.550$ m. The velocity of the blade tips is $2\,\pi\,r\,\omega/60$, where ω is the number of rotations per minute. The Reynolds number of the fan is:

$$Re_f = \frac{2\,\pi\,r\,D_H\,\omega/60}{3\,\nu} \tag{C3}$$

The 3 blade tips trace the whole circumference in only 1/3 of a rotation, hence the 3 in the denominator.

Faster fan rotation ω yields diminishing increases of test-chamber airspeed u_t, suggesting Equation (C4), where u_u is the limiting velocity for arbitrarily fast rotation, and coefficient η converts fan Re_f to test-chamber Re_t. **Figure C3** gives the parameters and measurements at $300\ \mathrm{r/min} \le \omega \le 1500\ \mathrm{r/min}$. The "3mm" points are the WM-2 measurements of the 3 mm plate in the original wind-tunnel; The "1mm" points are the ABM-200 measurements of the 1 mm plate in the tunnel with a new diffuser and fan cowling.

$$Re_t = \|\eta\, Re_f,\ D_H\, u_u/\nu\|_{-2} \qquad u_t = \|\pi\,\eta\, r\,\omega/90,\ u_u\|_{-2} \tag{C4}$$

Airspeeds slower than 2 m/s should be nearly proportional to ω. Both anemometers show evidence of dry (bearing) friction in **Figure C3**. The ABM-200 "meter predictions" trace plots $1.125\,u_t - 0.381$; the WM-2 "meter predictions" trace plots $1.477\,u_t - 0.81$ when $u_t < 1.725$ and u_t otherwise. A mistake in the 2016 measurement software under-counted fan rotations at $\omega > 1200$ r/min. It is compensated by replacing ω in Equations (C3, C4) with $[\omega^{-6} - 1750^{-6}]^{-1/6}$ in the WM-2 "meter predictions". The RMSRE and Bias are relative to the "meter predictions". The second "1mm" row includes the point at 400 r/min.

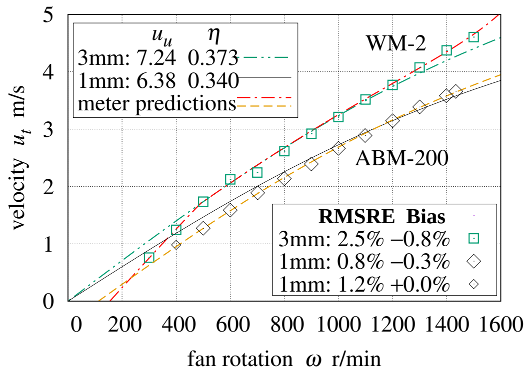

Figure C3. Airspeed versus fan speed.

Figure C4a,b show the fan speed variability in each experiment; these are used in the measurement uncertainty calculations.

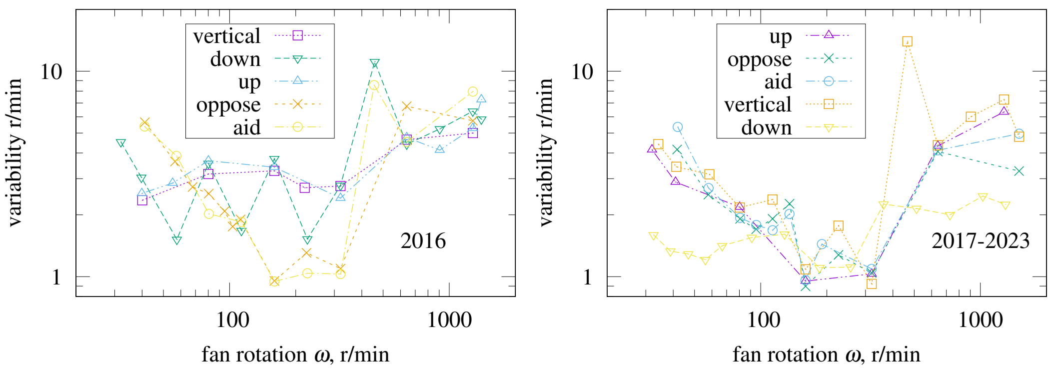

(a) **(b)**

Figure C4. (a) Fan variability 3 mm plate and **(b)** Fan variability 1 mm plate.

VI. Ambient sensing

Figure C5a shows the ambient sensor board which was at the lower edge of the test chamber in **Figure C2a**. It measures the pressure, relative humidity, and air temperature at the wind-tunnel intake. Wrapped in aluminum tape to minimize radiative heat transfer, the LM35 temperature sensor projects into the tunnel. To minimize self-heating, the LM35 is powered only while being sampled.

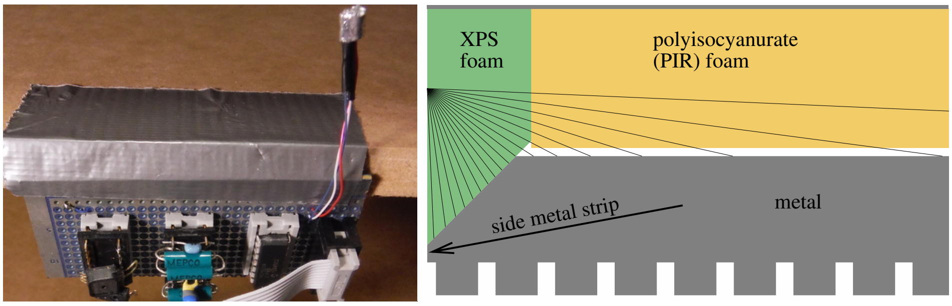

(a) **(b)**

Figure C5. **(a)** Ambient sensors and **(b)** XPS wedge conduction.

VII. Physical parameters

Table C1 lists the static parameters from measurements and specifications.

The effective ϵ_{wt} may differ from the medium-density-fiberboard emissivity given by Rice [20] because the temperatures of the test chamber surfaces may not be uniform. Through the open intake, the plate also exchanges thermal radiation with objects in the room having different temperatures.

Table C1. Physical parameters.

Symbol	**Values**	**Description**
L	0.305 m	length of flow along test-surface
A	0.093 m^2	area of test-surface
ε	3.00 mm 1.04 mm	RMS height-of-roughness
C_{pt}	4691 J/K 4274 J/K	plate thermal capacity
D_{Al}	19.4 mm	metal slab thickness
D_{PIR}	25.4 mm	polyisocyanurate (PIR) foam thickness
D_w	19.05 mm	XPS foam wedge height
k_{PIR}	$0.0222\ \text{W}/(\text{m}\cdot\text{K})$	PIR foam thermal conductivity
k_{XPS}	$0.0285\ \text{W}/(\text{m}\cdot\text{K})$	XPS foam thermal conductivity
U_I	0.075 W/K	front-to-back insulation thermal conductance
ϵ_{Al}	0.04	test-surface (MIC-6 Al) emissivity
ϵ_{XPS}	0.515	XPS foam emissivity (see text)
ϵ_{dt}	0.89	duck tape emissivity
ϵ_{wt}	0.90	test chamber interior emissivity

VIII. The 1 mm roughness plate

When the 6 mm posts were milled down to 2 mm height, the four corner posts were left at their 6 mm height in order to preserve the wire suspension. This resulted in $\varepsilon = 1.04$ mm for the plate as a whole. However, Re_I occurs within the first few rows of posts. $\varepsilon = 1.143$ mm over the first three rows of posts results in $Re_I = 6178$.

IX. Modeling of parasitic heat flows

The plate has six surfaces from which heat can flow. At low airflow velocities, the sides of the insulation behind the test plate can leak more heat than the test-surface transfers, shrinking to 6% at 1300 r/min.

In order to measure natural convection from the (rough) test surface, natural convection and thermal radiation from the four sides (U_S) and back must be deducted from the total heat flow. Heat from the front plate flows through thermal insulating foam to a thin aluminum sheet with a temperature sensor at its center. This heat flow is simply $U_I\,[T_P - T_B]$, the product of the foam's thermal conductance and the temperature difference across it.

X. Forced convection side model

The four sides are not isothermal; a 3.5 mm metal strip (see cross-section **Figure C5** runs the length of the side; and a D_w-tall wedge of extruded polystyrene foam (XPS) insulation fills the metal slab's 27 mm ($= \sqrt{2}\,D_{\mathrm{Al}}$) $45°$ chamfer. The local surface conductance $h_W(z)$ at elevation z (from the wedge point) is found by averaging the reciprocal distance to slab metal with respect to angle θ:

$$\begin{aligned} h_W(z) &= \int_0^{\theta_c} \frac{k_{\mathrm{XPS}}}{\sqrt{2}\,z\,\theta_c} \cos\left(\theta + \frac{\pi}{4}\right) \mathrm{d}\theta + \int_{\theta_w}^{\theta_W} \frac{k_{\mathrm{PIR}}}{z - D_w} \frac{\cos\theta}{\theta_W - \theta_w} \mathrm{d}\theta \\ &= \frac{k_{\mathrm{XPS}}}{\sqrt{2}\,z\,\theta_c} \left[\sin\left(\theta_c + \frac{\pi}{4}\right) - \sin\frac{\pi}{4}\right] + \frac{k_{\mathrm{PIR}}}{z - D_w} \left[\frac{\sin\theta_W - \sin\theta_w}{\theta_W - \theta_w}\right] \\ \theta_c &= \arctan\frac{D_w - z}{D_w} \quad \theta_w = \arctan\frac{D_w}{z - D_w} \quad \theta_W = \max\left(\theta_w,\ \arctan\frac{L - D_w}{z - D_w}\right) \end{aligned} \tag{C5}$$

Forced air flows parallel to the long dimension on two sides, but flows into the windward side and away from the leeward side. Air heated by the windward side reduces heat transfer from the test-surface; air heated by the test-surface suppresses heat transfer from the leeward side. Hence, the model excludes windward and leeward forced convection. The average forced convective conductance of the flow-parallel foam wedges is calculated by integrating $h_W(z)$ in series (reciprocal of the sum of reciprocals, which is also the ℓ^{-1}-norm) with the local surface conductance $k\,Nu_\sigma(Re_x)/L$, where $Nu_\sigma(Re_x)$ is the local pierced-laminar convection from Jaffer [2]:

$$U_W = \int_0^{D_w} \int_0^L \left\| h_W(z), \frac{k\,Nu_\sigma(Re_x)}{L} \right\|_{-1} \mathrm{d}x\,\mathrm{d}z \tag{C6}$$

XI. Other side models

The heat flow through the four sides U_S will be estimated from the plate and ambient temperatures. While the forced convective surface conductance of the sides is modeled by integrating the local forced surface conductance, this is not generally possible for natural convection.

Natural convection formulas are known for some convex surfaces. The plate's side metal surface is not convex.

Instead, the effective side width L_{es} and effective emissivity ϵ_W are introduced into the model. The natural convection of each side is calculated for an $L_{es} \times L_C$ area instead of its actual $L_S \times L_C$ area. The black-body radiation from each side is calculated for its actual $L_S \times L_C$ area with an effective emissivity of ϵ_W.

The schematic drawing **Figure 1b** (modeled on the flow patterns in Fujii and Imura [3] Fig. 14(e) and 14(f)) shows a plume rising from the center of an upward-facing plate fed by flow from the plate's edges. For the test surface, the upward heat flow of 0.467 W/K is more than twice the 0.212 W/K expected from the back and sides. Convective flow from the upward-facing test surface will draw in the air heated by the back and sides, reducing heat transfer from the test surface. In order to avoid double counting the convected heat from the back and sides, they should not be deducted from the plate heat (the thermal radiation is still deducted). The "reuptake" of this convected back and side heat should be nearly complete; its coefficient was set to 1 to avoid introducing another degree-of-freedom into the model.

Not deducting side convection from upward natural convection has an unexpected benefit: the upward convection model is thus insensitive to L_{es}, allowing ϵ_W to be determined from only upward-facing measurements.

XII. Radiative transfer side model

The 3 mm roughness plate had its sides wrapped with duck tape, which has a different emissivity from the foam wedges forming each side surface. Some of the 1 mm roughness plate runs were with tape and some without, requiring different ϵ_W values. For taped sides $\epsilon_W \approx 0.703$; without tape $\epsilon_W \approx 0.515$.

Figure C2a shows duck tape applied to the lower 54% of the plate's side, which corresponds to 50% coverage of the XPS foam wedge. For this partial tape coverage, ϵ_W Equation (C7) is the area proportional mean of the duck tape emissivity and XPS emissivity. Barreira et al. [21] measured ϵ_{dt} emissivities of 0.86 and 0.89 from two brands of "duck tape". The emissivity is largely controlled by the exposed polyethylene film, and increases with oxidation. Hence, the larger value is used for the aged duck tape on the plate sides. As of this writing, published emissivity measurements of XPS foam have not been located.

$$\epsilon_W = 50\%\,\epsilon_{dt} + 50\%\,\epsilon_{\text{XPS}} \tag{C7}$$

Natural convection measurements ($u = 0$) from the plate assembly over the span of inclinations in **Figure 2** have less than 3.3% RMSRE when calculated with $\epsilon_{\text{XPS}} = 0.515$; the RMSRE increases to either side of 0.515. This value is consistent with natural convection measurements of the plate assembly without tape.

XIII. Natural convection side model

With ϵ_W thus determined, L_{es} was the remaining degree of freedom. Trials with vertical and downward plate measurements found that L_{es} had a value near the sum of the aluminum slab thickness 19.4 mm and the effective height of the side face of the roughness $\approx \sqrt{2}\,\varepsilon$. This makes sense for a natural convection dimension; it is used for L_{es}. The 3 mm roughness plate has $L_{es} \approx$ 23.6 mm; 1 mm has $L_{es} \approx$ 21.0 mm.

In the vertical case, 1/2 of the heated air from the bottom side flows along the vertical test surface and would be counted twice. And 1/2 of the air drawn by the top side comes from the vertical test surface and would be counted twice. This vertical reuptake coefficient was set to 1/2; discrepancy from the actual reuptake coefficient will manifest as error in measurements.

Consider the (initially) vertical plate as θ decreases from $0°$. As the bottom side face tilts upward, more (than half of the) heated air will rise toward the test surface. That heat will reduce the convection from the test surface. When tilted downward, the heat from the test surface will reduce the convection from the top side. To handle these cases, Equation (C8) includes a term $2\,\cos\theta\,\sin\theta$ whose minimum of -1 is reached at $\theta = -45°$ and a term $-2\,\cos\theta\,\sin\theta$ whose minimum of -1 is reached at $\theta = +45°$.

XIV. Combining radiative transfer and convection

A side's radiative emissions, U_ϵ, compete with its convective heat transfer. Both increase with side temperature, but both act to lower that side temperature. Competitive heat transfer processes can often be modeled using the ℓ^p-norm with $p > 1$. The value of p was adjusted so that the $\Delta T = 3.8$K and $\Delta T = 11$K data points align with the theory traces in **Figure 2**. The optimal range is between $p = 4/3$ and $p = 3/2$; the geometric mean of those values is $p = \sqrt{2}$. The $\ell^{\sqrt{2}}$-norm appears three times in U_S Equation (C8).

Equation (C8) U_S is an amount which will be deducted from the measured heat flow. For each side, the $\ell^{\sqrt{2}}$-norm of the radiative and convective conductances is paired with the product of the convective conductance and a continuous trigonometric function of θ which goes negative when the natural convection would otherwise be double counted. Because of the triangle inequality, the $\ell^{\sqrt{2}}$-norm will be greater than the convective component; thus, each side's contribution to U_S will be positive.

No more than one reuptake process will be simultaneously active for a side. In Equation (C8) the expressions $\min(0, \sin\theta, -.5\,\cos\theta, 2\,\cos\theta\,\sin\theta)$ and $\min(0, \sin\theta, -.5\,\cos\theta, -2\,\cos\theta\,\sin\theta)$ return the negative of the largest magnitude potential reuptake. **Table C2** describes the natural convection parameters and function.

Note that this analysis applies only to the plate assembly in alignment with the wind-tunnel, and oriented to have at least one horizontal edge. Hence, rotation in plane of plate, ϕ, must be an integer multiple of $90°$. The only effect of ϕ in the equations is to swap arguments L_F and L_W when ϕ is an odd multiple of $90°$.

$$\begin{aligned}
U_S = {} & \|U_\epsilon, U_N(\theta - 90°, L_C, L_{es}, 0°)\|_{\sqrt{2}} \\
& + U_N(\theta - 90°, L_C, L_{es}, 0°)\,\min(0, \sin\theta, -.5\,\cos\theta, -2\,\cos\theta\,\sin\theta) \\
& + \|U_\epsilon, U_N(90° - \theta, L_C, L_{es}, 0°)\|_{\sqrt{2}} \\
& + U_N(90° - \theta, L_C, L_{es}, 0°)\,\min(0, \sin\theta, -.5\,\cos\theta, 2\,\cos\theta\,\sin\theta) \\
& + 2\,\|U_\epsilon, U_N(0°, L_{es}, L_C, \theta)\|_{\sqrt{2}} \\
& + 2\,U_N(0°, L_{es}, L_C, \theta)\,\min(0, \sin\theta)
\end{aligned} \tag{C8}$$

Table C2. Natural convection function and parameters.

Symbol	Description
$U_N(\theta, L_F, L_W, \phi)$	natural convective conductance from Jaffer [5]
θ	surface angle from vertical ($-90°$ is face up)
L_F	plate length
L_W	plate width
ϕ	rotation in plane of plate; integer multiple of 90°
$L_C = 0.305$ m	plate length = side length
$L_S = 45.8$ mm	side width
$L_{es} = 19.4\text{ mm} + \sqrt{2}\,\varepsilon$	effective side width for natural convection
$\epsilon_{wt} = 0.9$	wind-tunnel test chamber emissivity
$\epsilon_W \approx 0.703$ taped; 0.515 bare	effective side emissivity
h_R	black-body radiative surface conductance
$U_\epsilon = L_C\, L_S\, \epsilon_W\, \epsilon_{wt}\, h_R$	radiative emission from a side

U_{B0} is the test surface reuptake conductance from the back. Its $\min(0, \sin\theta)$ term is squared because the heated air from the back must flow around two right-angle edges to reach the test surface.

$$U_{B0} = -U_N(90°, L_C, L_C, 0°)\ \min(0, \sin\theta)^2 \tag{C9}$$

Figures C6–C8 show upward, vertical, and downward convection measurements, respectively. Taken from 3 mm and 1 mm roughness plates over a range of Ra values, these graphs, in combination with **Figure 2** test the natural convection and radiative transfer side models.

The traces labeled "theory" are Equation (7) with the appropriate row of **Table 2**. The difference between $\psi = 0°$ and $\psi = 180°$ in **Figure C7** is explained in Section 11.

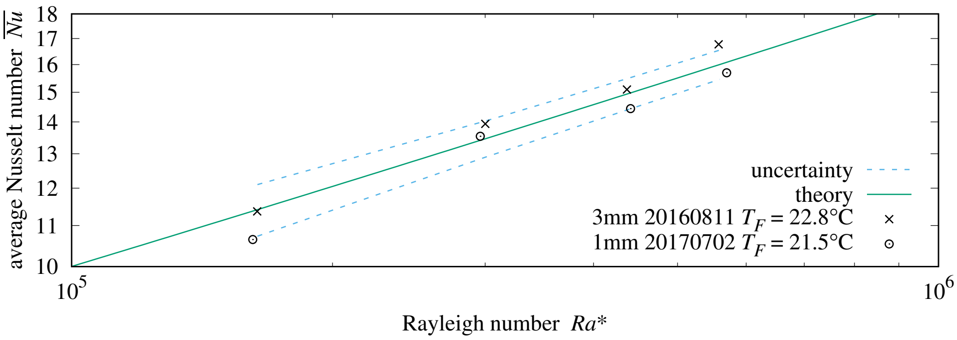

Figure C6. Natural convection from upward-facing surface.

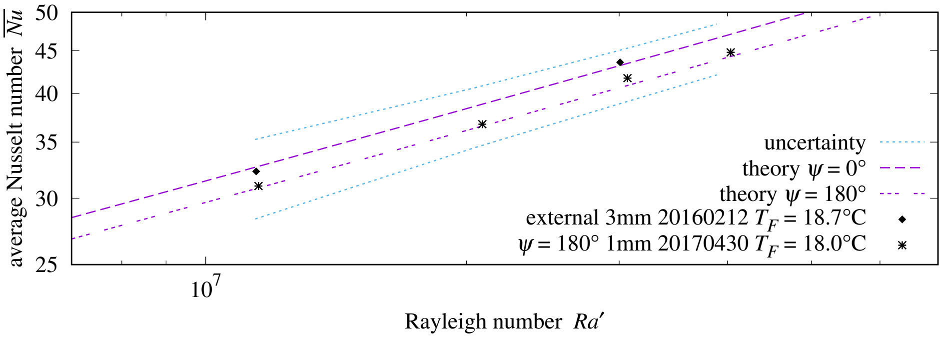

Figure C7. Natural convection from vertical surface.

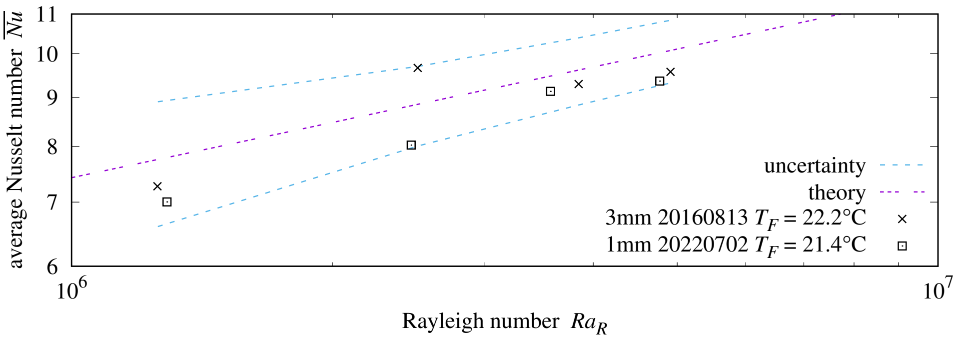

Figure C8. Natural convection from downward-facing surface.

XV. Mixed convection side model

Each $\ell^{\sqrt{2}}$-norm instance of a call to U_N is replaced by a call to U_M, with first argument $U_{fl}(u)$ or $U_{ft}(u)$ **Table C3**. In order to ignore forced convection from the leading and trailing sides, $U_{ft}(u) = 0$ when $\psi = 90°$ (horizontal flow); otherwise, $U_{fl}(u) = 0$. The reuptake instances of $U_N(\theta, L_F, L_W, \phi)$ are changed to the equivalent $U_M(0, \theta, L_F, L_W, \phi, 0°)$.

Table C3. Mixed conductance functions and parameters.

Symbol	Description
$U_{fl}(u)$	level flow side forced thermal conductance
$U_{ft}(u)$	tilted flow side forced thermal conductance
u	bulk flow velocity
$U_M(U_F, \theta, L_F, L_W, \phi, \psi)$	mixed convective conductance
U_F	forced thermal conductance
θ	surface angle from vertical ($-90°$ is face up)
L_F	forced characteristic length
L_W	other plate dimension
ϕ	rotation in plane of plate; integer multiple of 90°
ψ	angle of fluid flow from vertical (0° is upward)

$$
\begin{aligned}
U_S(u) = {} & \|U_\epsilon, U_M(U_{fl}(u), \theta - 90^\circ, L_C, L_{es}, 0^\circ, \psi)\|_{\sqrt{2}} \\
& + U_M(0, \theta - 90^\circ, L_C, L_{es}, 0^\circ, 0^\circ)\ \min(0, \sin\theta, -.5\ \cos\theta, -2\ \cos\theta\ \sin\theta) \\
& + \|U_\epsilon, U_M(U_{fl}(u), 90^\circ - \theta, L_C, L_{es}, 0^\circ, \psi)\|_{\sqrt{2}} \\
& + U_M(0, 90^\circ - \theta, L_C, L_{es}, 0^\circ, 0^\circ)\ \min(0, \sin\theta, -.5\ \cos\theta, 2\ \cos\theta\ \sin\theta) \\
& + 2\ \|U_\epsilon, U_M(U_{ft}(u), 0^\circ, L_{es}, L_C, \theta, \psi)\|_{\sqrt{2}} \\
& + 2\, U_M(0, 0^\circ, L_{es}, L_C, \theta, 0^\circ)\ \min(0, \sin\theta)
\end{aligned}
\tag{C10}
$$

When u is large, $U_S(u)$ approaches the sum of the forced convection conductances. $U_S(0) \equiv U_S$ of Equation (C8).

XVI. Measurement methodology

The measurement methodology employed is unusual. Instead of waiting until the plate reaches thermal equilibrium, the plate is heated to 15 K above ambient, heating stops, the fan runs at the designated speed, and convection cools the plate. All of the sensor readings are captured each second during the 102 min process, **Table C4** lists the dynamic physical quantities measured each second. **Table C5** lists computed quantities. Both $U_S(u)$ and $\{\epsilon_{\mathrm{Al}}\, \epsilon_{wt}\, h_R\, A\}$ are subtracted from the combined heat flow. The mean of $\overline{h}(u,t)$ over the time interval in which ΔT drops by half (or exceeds 6142 s total time) is the result from that experiment.

Table C4. Dynamic quantities.

Symbol	Units	Description
ω	r/min	fan rotation rate
T_F	K	ambient air temperature
T_P	K	plate temperature
T_B	K	back surface temperature
P	Pa	atmospheric pressure
Φ	Pa/Pa	air relative humidity

Table C5. Computed quantities.

Symbol	Units	Description
h_R	$\mathrm{W/(m^2K)}$	radiative surface conductance
$U_S(u)$	W/K	side radiative and convective conductance
$\overline{h}(u,t)$	$\mathrm{W/(m^2K)}$	convective surface conductance

XVII. Heat balance

Collecting into $U_T(u)$ Equation (C11) those terms which have a factor of temperature difference $\overline{T_P} - \overline{T_F}$, Equation (C12) is the heat balance equation of the plate during convective cooling:

$$U_T(u) = U_S(u) + \{\overline{h}(u)\, A\} + \{\epsilon_{\mathrm{Al}}\, \epsilon_{wt}\, h_R\, A\} \tag{C11}$$

$$0 = U_T(u)\ \left[\overline{T_P} - \overline{T_F}\right] + U_I\ \left[\overline{T_P} - \overline{T_B}\right] + C_{pt}\, \frac{\mathrm{d}\overline{T_P}}{\mathrm{d}t} \tag{C12}$$

The plate and ambient temperatures are functions of time t. Determined experimentally during heating, the temperature group-delay through the 2.54 cm block of insulation between the slab and back sheet is 110 s:

$$\overline{T_P}(t) = \frac{U_T(u)\, \overline{T_F}(t) + U_I\, \overline{T_B}(t - 110\ \mathrm{s}) - C_{pt}\, [\mathrm{d}\overline{T_P}(t)/\mathrm{d}t]}{U_T(u) + U_I} \tag{C13}$$

To compute Nusselt number $\overline{Nu} = \overline{h}\, L/k$, Equation (C13) is solved for the $\{\overline{h}(u,t)\, A\}$ term from Equation (C11).

$$\varsigma(t) = -U_I\ \left[\overline{T_P}(t) - \overline{T_B}(t - 110\ \mathrm{s})\right] \tag{C14}$$

$$\{\overline{h}(u,t)\, A\} = \frac{\varsigma(t) - C_{pt}\ \left[\overline{T_P}(t) - \overline{T_P}(t')\right] / [t - t']}{\overline{T_P}(t) - \overline{T_F}(t)} - \{\epsilon_{\mathrm{Al}}\, \epsilon_{wt}\, h_R\, A\} - U_S(u) \tag{C15}$$

where t' is the previous value of t. In Equations (C14) and (C15), $\overline{T_P}(t)$, $\overline{T_F}(t)$, and $\overline{T_B}(t)$ are the 15-element cosine averages of plate and fluid temperatures (centered at time t).

In order to simulate T_P from the other dynamic inputs, (C13) is solved as a finite-difference equation where d$t = t - t' = 1$:

$$T_P(t) = \frac{U_T(u)\, \overline{T_F}(t) + U_I\, \overline{T_B}(t - 110\ \mathrm{s}) + C_{pt}\, T_P(t')}{U_T(u) + U_I + C_{pt}} \tag{C16}$$

In Equation (C16), $T_P(t')$ is the previous simulated value, not a measured value.

XVIII. Measurement uncertainty

Following Abernethy et al. [22], the final steps in processing an experiment's data are:

- Using Equation (C15), calculate the sensitivities of convected power $\overline{h}\, A\, \Delta T$ per each parameter's average over the measurement time-interval;
- multiply the absolute value of each sensitivity by its estimated parameter bias to yield component uncertainties;
- calculate combined bias uncertainty as the root-sum-squared (RSS) of the component uncertainties;
- calculate the RSS combined measurement uncertainty as the RSS of the combined bias uncertainty and twice the product of the rotation rate sensitivity and variability.

Tables C6 and **C7** list the sensitivity, bias, and uncertainty for each component contributing more than 0.20% uncertainty for downward-facing 3 mm and 1 mm roughness plates, respectively. **Figure C9a, b** show the measurements relative to the present theory for rough flow and turbulent flow, respectively.

The supplementary data contains these graphs and tables for each data-set.

Table C6. Estimated measurement uncertainties, bi-level 3mm roughness at $Re = 59,593$.

Symbol	Nominal	Sensitivity	Bias	Uncertainty	Component
ΔT	9.47K	+12.2%/K	0.10K	1.22%	LM35C differential
P	101kPa	+0.0009%/Pa	1.5kPa	1.28%	MPXH6115A6U air pressure
C_{pt}	4.69kJ/K	+0.024%/(J/K)	47J/K	1.13%	plate thermal capacity
η	0.401	+180%	0.014	2.52%	anemometer calibration
ς	6.00mm	+11285%/m	100um	1.13%	post height
				3.49%	combined bias uncertainty
Symbol	**Nominal**	**Sensitivity**	**Variability**	**Uncertainty**	**Component**
ω	905r/min	+0.081%/(r/min)	5.2r/min	0.43%	fan rotation rate
				3.60%	RSS combined uncertainty

Table C7. Estimated measurement uncertainties, bi-level 1mm roughness at $Re = 55,935$.

Symbol	Nominal	Sensitivity	Bias	Uncertainty	Component
ΔT	10.2K	+11.7%/K	0.10K	1.17%	LM35C differential
P	100.0kPa	+0.0008%/Pa	1.5kPa	1.26%	MPXH6115A6U air pressure
C_{pt}	4.24kJ/K	+0.028%/(J/K)	42J/K	1.17%	plate thermal capacity
η	0.340	+195%	0.003	0.66%	anemometer calibration
u_u	6.381	+2.44%	0.100	0.24%	diffuser airflow upper bound
L_T	8.34mm	+9365%/m	100um	0.94%	post length
L_m	3.57mm	+454%/m	500um	0.23%	side metal strip width
ϵ_{rs}	0.040	+20.4%	0.010	0.20%	test-surface emissivity
ϵ_{wt}	0.900	+9.05%	0.025	0.23%	wind-tunnel emissivity
				2.44%	combined bias uncertainty
Symbol	**Nominal**	**Sensitivity**	**Variability**	**Uncertainty**	**Component**
ω	1.03kr/min	+0.065%/(r/min)	2.5r/min	0.16%	fan rotation rate
				2.46%	RSS combined uncertainty

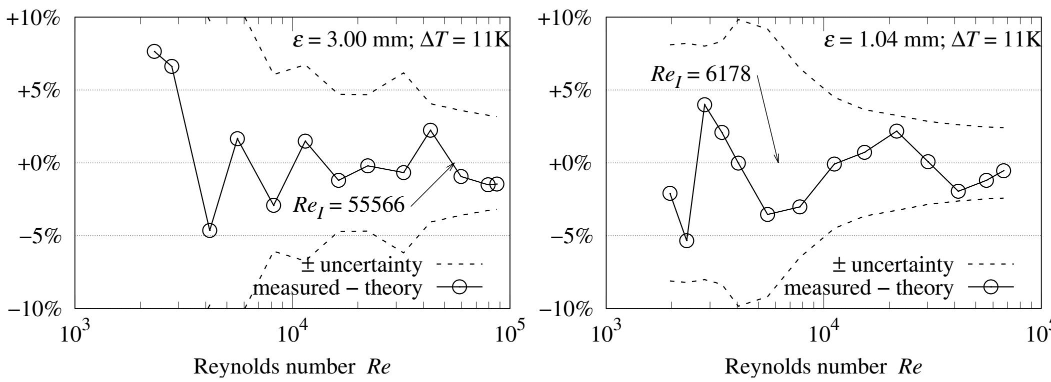

(a) **(b)**

Figure C9. **(a)** Measured versus theory $\varepsilon = 3$ mm and **(b)** Measured versus theory $\varepsilon = 1$ mm.

XIX. Details

Documentation, photographs, electrical schematics, and software source-code for the apparatus, as well as calibration and measurement data are available from: `http://people.csail.mit.edu/jaffer/convect`.

Thermal Science and Engineering 2025, 8(1), 10909.
https://doi.org/10.24294/tse10909

Article

Energy at the boundary of an elastic and thermoelastic mediums under different theories of thermoelasticity

Kamal Kumar[1], Vandana Gupta[2], Manoj Kumar[3], Shruti Goel[1,*]

[1] Department of Physical Sciences (Mathematics), Baba Mastnath University, Rohtak 124021, India
[2] Indira Gandhi National College, Behlolpur 136132, India
[3] Maharishi Markandeshwar University, Mullana 133207, India
*** Corresponding author:** Shruti Goel, shruti1922goel@gmail.com

CITATION

Kumar K, Gupta V, Kumar M, Goel S. Energy at the boundary of an elastic and thermoelastic mediums under different theories of thermoelasticity. Thermal Science and Engineering. 2025; 8(1): 10909. https://doi.org/10.24294/tse10909

ARTICLE INFO

Received: 15 December 2024
Accepted: 22 January 2025
Available online: 13 February 2025

Abstract: The study examines the impact of various theories on the reflection and transmission phenomena caused by obliquely incident longitudinal and transverse waves at the interface between a continuously elastic solid half-space and a thermoelastic half-space, using multiple thermoelastic models. Numerical calculations reveal that the thermoelastic medium supports one transmitted transverse wave and two transmitted longitudinal waves. The modulus of amplitude proportions is analyzed as a function of the angle of incidence, showing distinct variations across the studied models. Energy ratios, derived from wave amplitudes under consistent surface boundary conditions for copper, are computed and compared across angles of incidence. The results demonstrate that the total energy ratio consistently sums to one, validating energy conservation principles. Graphical comparisons of amplitude proportions and energy ratios for SV and P waves across different models illustrate significant differences in wave behavior, emphasizing the influence of thermoelastic properties on wave transmission and reflection.

Keywords: coupled model; two-phase-lag model; G-N model; three-phase-lag model; reflection; transmission; G-L model; amplitude ratio; energy ratio; L-S model

1. Introduction

The study of thermoelasticity focuses on the equilibrium of entities that are considered thermodynamic systems and whose interactions with their environment are limited to work-heat transformation, and outside forces in a given medium. In general, the deformation process itself contributes to the change in body temperature in addition to the internal and external heat sources. Under typical heat exchange conditions, the flux caused by deformation results in uneven heating. The study of thermoelasticity is the flow of heat and its effect on stress and strain when temperature and deformation field coupling take place. The elasticity and heat conduction theories are combined in the thermoelasticity hypothesis. It deals with how heat affects the deformation of an elastic medium and how deformation affects the thermal state of the medium under consideration. Numerous appealing models have been created in recent years by utilizing various theories to examine physical processes, including heat conduction and diffusion.

A study on the plane waves reflected off the surface of a thermoelastic immersed, permeable solid half-space with related surface limit conditions was provided. Using the L-S and G-N theories of generalized thermoelasticity of saturated porous medium by McCarthy [1]. The plane is the focal point of the administering conditions. Three connected longitudinal waves and a shear vertical wave are shown to occur in a generalized thermoelastic saturated porous medium via the plane wave solution of these equations. For every incident plane wave travelling through the medium, there are reflected waves. The right possibilities for occurrence, reflected in a half-space wave present, are created using Snell's equation and meet the requisite boundary conditions. Sharma and Sidhu [2] following the derivation of the secular equation, examined the motion of plane harmonic waves in homogeneous anisotropic summed-up thermoelastic materials. Four dispersive wave modes were discovered to be feasible. The typical modes of linked thermoelasticity are three modes referred to as quasi-elastic (E). With a finite velocity of propagation, the fourth mode, alluded to as semi-warm (T) is diffusive in coupled thermoelasticity, presently looks like a wave. All the modes have been approximated at both high and low frequencies. Banerjee and Pao [3] looked into the propagation of the plane harmonic wave in unbounded anisotropic solids. Three of the four characteristic wave speeds discovered are comparable to isothermal or adiabatic elastic waves. The intensity beats, frequently known as the subsequent sound, correspond to the fourth wave, which is mostly a temperature disturbance. Numerical and graphical results are utilized to assess the velocities, slowness, and wave surfaces of the thermoelastic waves for solid helium crystals and NaF.

Puri [4] looked at plane waves in generalized thermoelasticity. In the framework of generalized thermoelasticity, the characteristics of two dilatational motions are examined. The frequency equation's precise solution is presented, and the real and imaginary wave number components precise values are computed. The behavior of the amplitude ratios for small and big frequencies is studied, along with the ranges of validity and approximate representations of this solution for large and small frequencies. Chadwick and Seet [5] published evidence for the propagation of planar harmonic body waves within a single zinc crystal. Dhaliwal and Sherief [6] expanded the generalized thermoelasticity theory for anisotropic heat-conducting thermoelastic materials. In a thermoelastic half-space, wave propagation was studied by Chandrasekharaiah [7]. The motion of summed-up thermoelastic waves transversed in an isotropic medium was covered by Singh and Sharma [8]. Sharma [9] discovered a connection between the concepts of thermoelasticity and poroelasticity and developed a math-related model for the wave motion in an anisotropic generalized medium of thermoelasticity. It was investigated how inhomogeneous waves propagate in anisotropic piezo-thermoelastic mediums.

Prasad et al. [10] described the movement of planar harmonic waves under thermoelasticity with double-stage slack. Asymptotic expressions of several wave field characterizations, for example, explicit loss, phase speed, adequacy ratios, and penetration profundity, result for both low and high values of frequency. Analytical techniques are used to determine the precise dispersion relations for plane waves. Using the computer tool Mathematica, the mathematical upsides of particular wave fields at moderate frequencies are found. The results are then shown in a number of images to illustrate the analytical findings.

Three-dimensional thermoelastic wave movements under the influence of a buried source were shown in half-space by Lykotrafitis et al. [11]. The propagation of waves in a generic anisotropic poroelastic medium was explored by Sharma [12]. Venkatesan and Ponnusamy [13] depicted the wave engendering in a summed-up thermoelastic strong chamber under different circumstances. Kumar and Kansal [14] were examined transversely isotropic thermoelastic diffusive plates by for the motion of a wave that is called lamb. Yu et al. [15] directed thermoelastic wave proliferation in stacked plates was displayed without energy misfortune. Kumar and Gupta [16] described the reflection and transmission of plane waves at the boundary between a flexible half-space and a portion of a thermoelastic half-space. Youssef and El-Bary [17] studied the theory of hyperbolic two-temperature generalized thermoelasticity. Lata et al. [18] worked on transversely isotropic magneto-thermoelastic rotating materials in the Lord-Shulman model and the thermomechanical interactions resulting from time-harmonic sources. Kumar et al. [19] studied wave interference, by considering the fractional order derivative condition on an elastic and two-temperature generalized thermoelastic half-space. Sherief et al. [20] examined how semiconductor elastic materials behaved when exposed to an external magnetic field. The framework takes into account how thermal, elastic, and plasma waves interact. The thermoelastic behavior of semiconductor materials in plasma is described by a new completely coupled mathematical model. Ding et al. [21] studied nonlocal elasticity captures these microstructural interactions, which are crucial for interpreting the overall behavior of the composite. The mechanical response at each position in the examined composite materials with heterogeneous microstructures is influenced by surrounding inclusions or fibers. Li et al. [22] worked on influence of time-dependent effects and long-range forces on the mechanical behavior of nanoscale objects, such as thin films, nanotubes, and nanowires is well captured by this model. Biological tissues, particularly in polymers and soft materials, where the response to loading varies on both time and previous deformations, the model describes history-dependent behavior for viscoelastic materials that is essential for comprehending stress relaxation and creep. Kumar [23] examined micropolar elasticity is appropriate for capturing the varying rotations and deformations of the fibers and matrix in fiber-reinforced composites. The theory also applies to porous and granular materials, such as powders or soils, where complicated mechanical behavior can result from the rotation of individual grains relative to one another. Furthermore, because classical elasticity is unable to explain the behavior of high-frequency, short-wavelength waves, such as ultrasonic waves, in microstructured materials, micropolar elasticity is essential for comprehending high-frequency wave propagation. Yadav et al. [24] examined the nonlocal elasticity reflection phenomena in a hygrothermal medium. Three integrated plane waves—longitudinal displacement, shear vertical SV wave propagation in the medium, moisture diffusion mD-wave, and thermal diffusion TD-wave—are predicted by the plane wave solution. The hygrothermal medium's P, mD, TD, and SV wave velocities are calculated. For the incidence of a hygrothermal plane wave, expressions for the energy ratio and reflection coefficient are created and shown graphically. Abd-Alla et al. [25] studied the wave motion under the effect of a magnetic field in a vacuum and compared the dual-phase-lag model and Lord-Shulman theory in the absence and presence of a magnetic field. Othman et al. [26] compared the reflection of generalized thermoelastic waves for the different theories (CT, L-S, G-L) in the presence of rotation, magnetic field, initial stress and the two-temperature parameter.

The interesting phenomena at a plane point of interaction between a versatile solid half-space and on the other side of the plane, considering different models are discussed in the current work. Work has been done on different theories given by authors, such as couple theory, Lord and Shulman (L-S) theory, Green and Naghdi (G-N) theory, Green and Lindsay (G-L) theory, and two-phase-lag and three-phase-lag theories of thermoelastic solids in other half-space. The amplitude proportions of various refracted and reflected waves to the wave that approaches the boundary are determined. The expressions of the energy proportions for the incident wave to the different reflected waves along with the refracted waves are further found using the amplitude ratios. These energy ratios are visually shown and comparisons are provided for several ideas. The values of energy ratio can be negative or positive but the overall sum of all energies is the same in both cases. Thus, the total sum of energies in every theory is one. Because of the values being both negative and positive, they affect each other and have a sum of 1 for each incident angle. So, during the interaction, the rule of conservation of energy is confirmed.

2. Governing equations

The equation for thermal conductivity, which incorporates the dilatation term based on the thermodynamics of irreversible processes, was satisfactorily derived by Biot [27]. To resolve the contradiction in the conventional uncoupled theory, which states that elastic changes have no impact on temperature, he developed the idea of coupled thermoelasticity. The coupled theory of thermoelasticity results from the coupling of the temperature and strain fields. Equation of motion given as:

$$(\lambda+\mu)v_{k,ki}+\mu v_{i,kk}-\gamma T_{,i}+\rho F_i=\rho\ddot{v}_i \tag{1}$$

Coupled theory equation of heat conduction is:

$$KT_{,ii}+Q=\rho c\dot{T}+\gamma T_0\dot{e}_{kk} \tag{2}$$

By modifying the law of heat conduction, Lord and Shulman [28] introduced the theory of generalized thermoelasticity with one relaxation time (the isotropic body), which resolves the paradox of infinite speeds of heat and elastic disturbance propagation present in both the coupled and uncoupled theories of thermoelasticity. The theory of heat conduction is as follows:

$$KT_{,ii}=\left(1+\tau_0\frac{\partial}{\partial t}\right)\left(\rho c\dot{T}+\gamma T_0\dot{e}_{kk}-Q\right) \tag{3}$$

The theory of thermoelasticity with two relaxation times or the theory of temperature-rate-dependent thermoelasticity, as presented by Green and Lindsay [29], is a further generalization of the coupled theory of thermoelasticity and is as follows:

The equation of motion and the equation of heat conduction are respectively:

$$(\lambda+\mu)v_{k,ki}+\mu v_{i,kk}-\gamma\left(T+\tau_1\dot{T}\right)_{,i}+\rho F_i=\rho\ddot{v}_i \tag{4}$$

$$KT_{,ii}+Q=\rho c\left(\dot{T}+\tau_0\ddot{T}\right)+\gamma T_0\dot{e}_{kk} \tag{5}$$

For homogeneous and isotropic materials, Green and Naghdi [30,31] suggested three thermoelasticity models. The terms type-I, type-II, and type-III thermoelasticity are used to refer to the three different theories. While the second and third models provide for additional sound effects, the first of these models is identical with coupled thermoelasticity. The Green-Naghdi (Type-III) theory of the heat conduction equation is:

$$\mathrm{K}\mathrm{T}_{,ii}+\mathrm{K}^{*}v_{,ii}+\rho\dot{r}=\rho c\ddot{\mathrm{T}}+\gamma T_0\ddot{e}_{kk} \tag{6}$$

RoyChoudhuri [32] identified the initiative in the three-phase-lag model heat transport equation as:

$$\left(1+\tau_q\frac{\partial}{\partial t}\right)\left(\rho c\dot{T}+\gamma T_0\dot{e}_{kk}-Q\right)=\tau_v^{*}T_{,ii}+K\tau_T\dot{T}_{,ii}+K^{*}\nu_{,ii} \tag{7}$$

We assume that the material parameters satisfy the inequality $0\le\tau_v<\tau_t<\tau_q$. Then the equation states that the temperature gradient and the thermal displacement gradient established across a material volume located at position $P(r)$ at time $t+\tau_t$ and $t+\tau_\nu$ result in heat flux to flow at a different instant of time τ_q. The third delay time τ_ν may be interpreted as the phase lag of the thermal displacement gradient.

Tzou [33] defined the two-phase-lag model heat conduction equation as:

$$K\left(1+\tau_T\frac{\partial}{\partial t}\right)T_{,ii}=\left(1+\tau_q\frac{\partial}{\partial t}+\frac{1}{2}\tau_q^2\frac{\partial^2}{\partial t^2}\right)\left(\rho c\dot{\mathrm{T}}+\gamma T_0\dot{e}_{kk}-Q\right) \tag{8}$$

According to which the temperature gradient at a point P at time $t+\tau_t$ corresponds to the heat flux vector at P at time $t+\tau_q$. The delay time τ_t is interpreted as that caused by the microstructural interactions, such as photon-electron interaction or photon scattering, and is called the phase lag of the temperature gradient. The other delay time τ_q is interpreted as the thermal relaxation time due to the fast transient effect of thermal inertia and is called the phase lag of the heat flux. Without even a trace of an outer intensity source (body forces and heat sources), a minimized type of situation for the displacement and temperature field for the thermoelasticity theories previously described in Equations (1)–(8) is as follows.

The equations of motion:

$$(\lambda+\mu)v_{k,ki}+\mu v_{i,kk}-\gamma\left(1+\tau_1\frac{\partial}{\partial t}\right)T_{,i}=\rho\ddot{v}_i \tag{9}$$

The heat conduction equation:

$$\begin{aligned}&K^{'}\left(n^{*}+t_1\frac{\partial}{\partial t}+t_3\frac{\partial^2}{\partial t^2}\right)T_{,ii}=\\&\rho c\left(n_1\frac{\partial}{\partial t}+\tau_0\frac{\partial^2}{\partial t^2}+t_2\frac{\partial^3}{\partial t^3}+t_4\frac{\partial^4}{\partial t^4}\right)T+T_0\gamma\left(n_1\frac{\partial}{\partial t}+n_0\tau_0\frac{\partial^2}{\partial t^2}+t_2\frac{\partial^3}{\partial t^3}+t_4\frac{\partial^4}{\partial t^4}\right)e_{kk}\end{aligned} \tag{10}$$

where $n^{*},t_1,t_3,n_1,\tau_0,t_2,t_4,n_0$ are parameters. Which are defined below for each case.

The Equations (9) and (10) are reduced to several special cases as follows:

Case 1: Coupled theory condition of thermoelasticity is obtained.

$$n^* = 1, t_1 = 0, n_1 = 1, t_2 = 0, t_3 = 0, \tau_0 = 0, t_4 = 0, \tau_1 = 0.$$

Case 2: The L-S theory of thermoelasticity holds.

$$n^* = 1, n_1 = 1, t_1 = 0, t_2 = 0, \tau_1 = 0, t_3 = 0, n_0 = 1, t_4 = 0, \tau_0 = 0.$$

Case 3: The G-L theory of thermoelasticity follows.

$$n^* = 1, t_1 = 0, n_0 = 0, t_2 = 0, \tau_0 = 1, t_3 = 0, n_1 = 1, t_4 = 0, \tau_1 \geq \tau_0.$$

Case 4: The G-N (Type-III) theory of thermoelasticity is obtained when.

$$n^* > 0, n_1 = 0, t_1 = 1, t_2 = 0, \tau_0 = 1, t_3 = 0, t_4 = 0, n_0 = 1.$$

Case 5: The Three-phase-lag theory of thermoelasticity is obtained when.

$$\tau_0 = 1, n_0 = 1, n_1 = 0, \tau_1 = 0, t_2 = \tau_q, t_1 = 1 + n^*\tau_\nu, t_3 = \tau_T, t_4 = \frac{\tau_q^2}{2}.$$

Case 6: The Two-phase-lag theory of thermoelasticity is as follows:

$$n^* = 1, \tau_0 = \tau_q,\ n_0 = 1, n_1 = 1, \tau_1 = 0, t_1 = \tau_T,\ t_2 = \frac{\tau_q^2}{2}, t_3 = 0,\ t_4 = 0.$$

The temperature-stress-strain relationship is denoted as follows:

$$\sigma_{ij} = 2\mu e_{ij} + \lambda e_{kk}\delta_{ij} - \gamma\left(1 + \tau_1 \frac{\partial}{\partial t}\right) T\delta_{ij} \tag{11}$$

The strain is related to displacement as follows:

$$e_{ij} = \frac{1}{2}\left(v_{i,j} + v_{j,i}\right) \tag{12}$$

where

$T = \theta - T_0$, increase in temperature. T_0, temperature of reference for the object chosen to hold $\left|\frac{T}{T_0}\right| << 1$. θ, temperature which is considered absolute for medium. C_E, specific heat when strain is constant. ρ, represents the density, which is not dependent on time. σ_{ij}, are the stress components. e_{ij}, strain components. e_{kk}, represents dilatation. ν, is the thermal displacement. τ_q, heat flux from phase lag. τ_T , temperature of phase lag. K^*, is the material characteristic. τ_ν, thermal displacement of phase lag. K', coefficient of thermal conductivity. $\gamma = (3\lambda + 2\mu)\alpha_t$; μ, λ are the Lame's constants, α_t is the term used as a thermal linear expansion term. v_i, components in the plane of the displacement vector v.

3. Discussion of problem

We assume a homogeneous isotropic space with an interface along $x_3 = 0$ containing thermoelastic theories in $x_3 > 0$ (Medium II) with x_3 points vertically upward and an isotropic elastic solid in $x_3 < 0$ (Medium I) with x_3 points vertically downward. (x_1, x_2, x_3) to be a coordinate of the Cartesian plane. The wave front of the reflection and transmission issue being studied here is parallel to the x_3 axis and is in the two-dimensional plane $x_1 - x_3$ shown in (**Figure 1**). Let's assume that an incident plane harmonic wave P or SV, travels inside the isotropic upper half-elastic solid space.

To solve the problem related to two-dimensional space, consider the displacement vector in medium II as:

$$v_i = (v_1, 0, v_3) \tag{13}$$

Here, dimensionless quantities are defined as:

$$\begin{aligned} &x_i^{'} = C_0\eta x_i, v_i^{'} = C_0\eta v_i, v^{'e}_i = C_0\eta {v_i}^e, i = 1, 3, \\ &t^{'} = {C_0}^2\eta t, \tau_1^{'} = {C_0}^2\eta\tau_1, T^{'} = \frac{T}{T_0}, \\ &\sigma_{ij}^{'} = \frac{\sigma_{ij}}{\rho C_0^2}, {\sigma_{ij}^{'}}^{e} = \frac{{\sigma_{ij}}^e}{\rho C_0^2}, P^{*e^{'}} = \rho C_0 P^{*e}, P_{ij}^{*^{'}} = \rho C_0 P_{ij}^*, i, j = 1,3 \end{aligned} \tag{14}$$

where

$$ {C_0}^2 = \frac{\lambda+2\mu}{\rho}, \eta = \frac{\rho C_E}{K}.$$

By using the Equations (13) and (14) in Equations (9) and (10), after suppressing the primes, the resulting Equations are (15)–(17) as follows:

$$(\beta^2 - 1)\frac{\partial}{\partial x_1}\left(\frac{\partial v_1}{\partial x_1} + \frac{\partial v_3}{\partial x_3}\right) + \nabla^2 v_1 - b\left(1 + \tau_1\beta^2 a\frac{\partial}{\partial t}\right)\left(\frac{\partial T}{\partial x_1}\right) = \beta^2\frac{\partial^2 v_1}{\partial t^2} \tag{15}$$

$$(\beta^2 - 1)\frac{\partial}{\partial x_3}\left(\frac{\partial v_1}{\partial x_1} + \frac{\partial v_3}{\partial x_3}\right) + \nabla^2 v_3 - b\left(1 + \tau_1\beta^2 a\frac{\partial}{\partial t}\right)\left(\frac{\partial T}{\partial x_3}\right) = \beta^2\frac{\partial^2 v_3}{\partial t^2} \tag{16}$$

$$\begin{aligned} &\left(n^* + t_1 c\frac{\partial}{\partial t} + t_3 c^2\frac{\partial^2}{\partial t^2}\right)\nabla^2 T = \\ &\left(n_1\frac{\partial}{\partial t} + \tau_0 c\frac{\partial^2}{\partial t^2} + t_2 c^2\frac{\partial^3}{\partial t^3} + t_4 c^3\frac{\partial^4}{\partial t^4}\right)T + \in\left(n_1\frac{\partial}{\partial t} + n_0\tau_0 c\frac{\partial^2}{\partial t^2} + t_2 c^2\frac{\partial^3}{\partial t^3} + t_4 c^3\frac{\partial^4}{\partial t^4}\right)\left(\frac{\partial v_1}{\partial x_1} + \frac{\partial v_3}{\partial x_3}\right) \end{aligned} \tag{17}$$

where

$$\in = \frac{\gamma}{\rho C_E}, \beta^2 = \frac{\lambda + 2\mu}{\mu}, b = \frac{\gamma T_0}{\mu}, a = \frac{\mu\eta}{\rho}, c = C_0^2\eta \tag{18}$$

The potential operates as follows in relation to the non-dimensional displacement components v_1, v_3 in Medium II.

$$v_1 = \frac{\partial\phi}{\partial x_1} - \frac{\partial\psi}{\partial x_3}, v_3 = \frac{\partial\phi}{\partial x_3} + \frac{\partial\psi}{\partial x_1} \tag{19}$$

where ψ notation is used for the potential transverse waves, φ notation is used for the potential longitudinal waves. Substituting Equation (19) in the Equations (15)–(17) results in the following equations:

$$\beta^2\left(\nabla^2 - \frac{\partial^2}{\partial t^2}\right)\varphi - b\left(1 + \tau_1\beta^2 a\frac{\partial}{\partial t}\right)T = 0 \tag{20}$$

$$\nabla^2\Psi - \beta^2\frac{\partial^2\Psi}{\partial t^2} = 0 \tag{21}$$

$$\left(n^* + t_1 c \frac{\partial}{\partial t} + t_3 c^2 \frac{\partial^2}{\partial t^2}\right) \nabla^2 T = \left(n_1 \frac{\partial}{\partial t} + \tau_0 c \frac{\partial^2}{\partial t^2} + t_2 c^2 \frac{\partial^3}{\partial t^3} + t_4 c^3 \frac{\partial^4}{\partial t^4}\right) T + \in \left(n_1 \frac{\partial}{\partial t} + n_0 \tau_0 c \frac{\partial^2}{\partial t^2} + t_2 c^2 \frac{\partial^3}{\partial t^3} + t_4 c^3 \frac{\partial^4}{\partial t^4}\right) \nabla^2 \varphi \tag{22}$$

For propagation of harmonic waves in the considered plane as:

$$\{\phi, \psi, T\}(x_1, x_3, t) = \{\bar{\phi}, \bar{\psi}, \bar{T}\} e^{-i\omega t} \tag{23}$$

Here the particle's angular frequency of vibration is ω. After simplifying the Equations (20) and (22) by substituting Equation (23), we obtained Equation (24):

$$[R\nabla^4 + S\nabla^2 + T]\bar{\phi} = 0 \tag{24}$$

where

$$R = \beta^2(n^* - it_1 c\omega - t_3 c^2 \omega^2),$$
$$S = \beta^2(in_1\omega + \tau_0 c\omega^2 + it_2 c^2 \omega^3 - t_4 c^3 \omega^4) + b \in (1 - i\tau_1 \beta^2 a\omega)(in_1\omega + \tau_0 n_0 c\omega^2 + it_2 c^2 \omega^3 - t_4 c^3 \omega^4),$$
$$T = \beta^2 \omega^2 (n^* - i(t_1 c - n_1)\omega - (t_3 - it_2)c^2\omega^2 + \tau_0 c\omega^2 - t_4 c^3 \omega^4).$$

The general form of Equation (24) solution can be considered as:

$$\bar{\phi} = \bar{\phi}_1 + \bar{\phi}_2 \tag{25}$$

Taking $i = 1, 2$ the potentials satisfy the equations of wave, resulting in:

$$\left[\nabla^2 + \frac{\omega^2}{{V_i}^2}\right]\bar{\phi}_i = 0 \tag{26}$$

Characteristic equations whose roots are named V_1, V_2 for the P and T waves respectively, are given below:

$$TV^4 - S\omega^2 V^2 + R\omega^4 = 0 \tag{27}$$

With the help of Equations (21) and (23), we get:

$$\left[\nabla^2 + \frac{\omega^2}{V_3^2}\right]\bar{\psi} = 0 \tag{28}$$

where $V_3 = \frac{1}{\beta}$, velocity of a transverse wave (SV wave) in medium $x_3 > 0$.

Using Equations (22), (23), (25) and (26), we obtain:

$$\{\varphi, T\} = \sum_{i=1}^{2} \{1, m_i\} \varphi_i \tag{29}$$

where

$$m_i = \frac{(in_1\omega + \tau_0 n_0 c\omega^2 + it_2 c^2\omega^3 - t_4 c^3 \omega^4) \in \omega^2}{V_i^2[(n^* - it_1 c\omega - t_3 c^2\omega^2)\nabla^2 + (in_1\omega + \tau_0 c\omega^2 + it_2 c^2 \omega^3 - t_4 c^3 \omega^4)]}, i = 1, 2 \tag{30}$$

The fundamental equation for homogeneous isotropic elastic solids is expressed as:

$$(\lambda^e + \mu^e)\nabla(\nabla {v_i}^e) + \mu \nabla^2 {v_i}^e = \rho^e \ddot{v}_i \tag{31}$$

where μ^e, λ^e are Lame's constants. v_i^e, represents the components in a Cartesian plane having a displacement vector v^e. ρ^e, indicates the density in the medium $x_3 < 0$.

$$e_1^e = \frac{\partial v_1^e}{\partial x_1} + \frac{\partial v_3^e}{\partial x_3}.$$

For a two-dimensional plane $x_1 - x_3$ problem, the components $v_i^e = (v_1^e, 0, v_3^e)$ can be considered as:

$$v_1^e = \frac{\partial \phi^e}{\partial x_1} - \frac{\partial \psi^e}{\partial x_3}, v_3^e = \frac{\partial \phi^e}{\partial x_3} + \frac{\partial \psi^e}{\partial x_1} \tag{32}$$

where potential φ^e corresponds to longitudinal wave and ψ^e corresponds to transversal wave equations from using Equations (31) and (32):

$$\nabla^2 \varphi^e = \frac{1}{\alpha_p^{2e}} \ddot{\varphi}^e \tag{33}$$

$$\nabla^2 \psi^e = \frac{1}{\beta_s^{2e}} \ddot{\psi}^e \tag{34}$$

where

$$\alpha_p^e = \sqrt{\frac{(\lambda^e + 2\mu^e)}{\rho^e}}, \beta_s^e = \sqrt{\frac{\mu^e}{\rho^e}},\ \alpha = \frac{\alpha_p^e}{C_0},\ \beta = \frac{\beta_s^e}{C_0} \tag{35}$$

The isotropic elastic medium's stress tensor and strain tensor are respectively given by:

$$\begin{aligned} \sigma_{ij}^e &= 2\mu^e e_{ij}^e + \lambda^e e_{kk}^e \delta_{ij} \\ e_{ij}^e &= \frac{1}{2}\left(v_{i,j}^e + v_{j,i}^e\right) \end{aligned} \tag{36}$$

where e_{ii}^e is the dilatation.

4. Wave potential functions

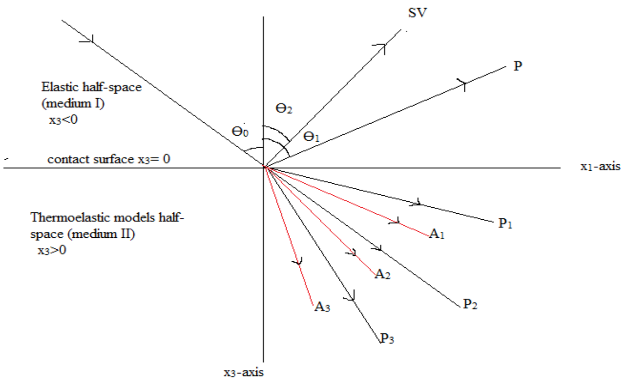

Figure 1. Geometry of the problem.

Consider a harmonic wave (P or SV) striking at the interface $x_3 = 0$ and travelling in medium $x_3 < 0$ and $x_3 > 0$ (**Figure 1**) shown.

In medium $x_3 > 0$, the potential functions satisfying Equations (34) and (33) can be taken as Kumar and Kansal [34]:

$$\phi^e = A'^e_0 \exp\left[i\omega\left\{\left((x_1 \sin\theta_0 + x_3 \cos\theta_0)/\alpha\right) - t\right\}\right] + A'^e_1 \exp\left[i\omega\left\{\left((x_1 \sin\theta_1 - x_3 \cos\theta_1)/\alpha\right) - t\right\}\right] \quad (37)$$

$$\psi^e = B'^e_0 \exp\left[i\omega\left\{\left((x_1 \sin\theta_0 + x_3 \cos\theta_0)/\beta\right) - t\right\}\right] + B'^e_1 \exp\left[i\omega\left\{\left((x_1 \sin\theta_2 - x_3 \cos\theta_2)/\beta\right) - t\right\}\right] \quad (38)$$

ω is the angular frequency, and the coefficients A'^e_0, B'^e_0, A'^e_1 and B'^e_1 are the amplitudes of the incident P (or SV), reflected P and reflected SV waves respectively.

Following Borcherdt [35], the complete structure of the refracted wave's wave field in isotropic thermoelastic solid half-space may be expressed as:

$$\{\phi, T\} = \sum_{i=1}^{2} \{1, m_i\} B'_i\, exp\left(A'_i . r\right) exp\{i(P_i . r - \omega t)\} \quad (39)$$

$$\psi = B'_3\, exp\left(A'_3 . r\right) exp\{i(P_3 . r - \omega t)\} \quad (40)$$

where the coupling constants m_i, $i = 1, 2$ are given in the above Equation (30). $B'_i, i = 1, 2, 3$ be the coefficients taken to represent the amplitudes of refracted P, T and SV waves respectively. The wave motion vector considered $P_i, i = 1, 2, 3$ as well as the attenuation factor $A'_i, i = 1,\ 2,\ 3$ are given by:

$$P_i = \xi_R \hat{x}_1 + dV_{iR} \hat{x}_3,\ \mathrm{A}'_i = -\xi_\mathrm{I} \hat{x}_1 - dV_{iI} \hat{x}_3,\ i = 1, 2, 3 \quad (41)$$

where

$$dV_i = dV_{iR} + i dV_{iI} = p.v.\left(\frac{\omega^2}{{V_i}^2} - \xi^2\right), i = 1, 2 \quad (42)$$

where $\hat{x}_1, \hat{x}_3$ denote the unit vector in the x_1 and x_3 directions, respectively, where p.v. stands for the primary value of the complex quantity generated from the square root. $\xi = \xi_R + i\xi_\mathrm{I}$, where ξ represents the wave number, which is in the form of a complex number, R and I stand for complex numbers having the real and imaginary parts correspondingly. Consider $\xi_R \geq 0$. In the isotropic thermoelastic medium, different models are given by complex numbers:

$$\xi = -i\left|A'_i\right| sin\left(\theta'_i - \gamma'_i\right) + |P_i|\, sin\, \theta'_i,\ i = 1, 2, 3 \quad (43)$$

where θ'_i indicates the refracted angle in Medium II and the angle between the wave propagates and the attenuation vector is taken as γ'_i. If $\left|A'_i\right| \neq 0$, then $\theta'_i = \gamma'_i$, $i =$ 1,2,3, implies that three refracted waves are in the direction of x_3 axis.

5. Surface boundary conditions

The surface boundary conditions with the partition that must be fulfilled $x_3 = 0$ are as follows:

a) Mechanical conditions:

$${\sigma_{33}}^e = \sigma_{33} \quad (44)$$

$$\sigma_{31}{}^{e} = \sigma_{31} \tag{45}$$

b) Displacement conditions:

$$v_1{}^{e} = v_1 \tag{46}$$

$$v_3{}^{e} = v_3 \tag{47}$$

c) Thermal conditions:

$$\frac{\partial T}{\partial x_3} + hT = 0 \tag{48}$$

where

h indicates the coefficient of heat transfer.

$h \rightarrow 0$ is equivalent to a boundary with insulation.

$h \rightarrow \infty$ corresponding to a boundary that is isothermal.

$$\sigma_{31} = \frac{\mu(v_{1,3}+v_{3,1})}{\rho C_0^2}, \sigma_{33} = \frac{[(\lambda^e+2\mu^e)v_{3,3}^e+\lambda^e v_{1,1}^e]}{\rho C_0^2},$$
$$\sigma_{31}^e = \frac{\mu^e(v_{1,3}^e+v_{3,1}^e)}{\rho C_0^2}, \sigma_{33}^e = \frac{[(\lambda^e+2\mu^e)v_{3,3}^e+\lambda^e v_{1,1}^e]}{\rho C_0^2}.$$

Here, construct a system of five equations of non-homogeneous nature in six unknowns by including the potentials provided by Equations (37)–(40) into the earlier boundary conditions Equations (44)–(48).

$$\sum_{k=1}^{5} c_{ik} Z_k = g_i \tag{49}$$

In addition to Snell's law provided by:

$$\xi_R = \frac{\omega \sin\theta_0}{V_0} = \frac{\omega \sin\theta_1}{\alpha} = \frac{\omega \sin\theta_2}{\beta} \tag{50}$$

where $Z_k = |Z_k|e^{i\psi_k^*}$, $|Z_k|$, ψ_k^*, $k = 1, 2, 3, 4, 5$ represents the proportion (ratios) of amplitudes and phase shifts of refracted P, refracted T, refracted SV, reflected P and reflected SV waves with respect to incident waves, c_{ik}, $(i, k = 1, 2, 3, 4, 5)$. Refer to Appendix A.

Also,

$$V_0 = \begin{cases} \alpha, \text{incident P-wave} \\ \beta, \text{incident SV-wave} \end{cases} \tag{51}$$

And,

$$\xi_I = 0.$$

Therefore, in x_3-direction waves are attenuated. The coefficients g_i, $i = 1, 2, 3, 4, 5$ for the right side of the Equation (49) can be written as:

$$g_i = \begin{cases} (-1)^{i+1} c_{i2}, \text{incident SV wave} \\ (-1)^{i} c_{i1}, \text{incident P wave} \end{cases}; i = 1 \cdots 4, \qquad g_i = 0 \quad ; i = 5 \tag{52}$$

According to Achenbach [36], now let's take a look at a unit-sized surface element that sits at the intersection of two media and calculate the amount of energy distributed.

$$P^{*} = \sigma_{lm} l_{m} \dot{v}_{l} \tag{53}$$

The stress tensor is denoted by σ_{lm} and v_i is the component of the particle displacement, I_m the unit normal vector is in the form of a direction cosine, and $\hat{I}$ the normal outward vector is considered part of the area element. Over a period, the time average is denoted by $\langle P^{*}\rangle$.

6. Energy partition

Physically, it is necessary to take into account how the incident wave's energy is distributed among the numerous refracted and reflected waves at the planar contact. According to Achenbach [36], the pace of energy movement per unit region is as follows:

$$\begin{cases} \langle P^{*e}\rangle = \mathrm{Real}\langle\sigma\rangle_{13}^{e}\mathrm{Real}\langle\dot{v}_{1}^{e}\rangle + \mathrm{Real}\langle\sigma\rangle_{33}^{e}\mathrm{Real}\langle\dot{v}_{3}^{e}\rangle(\text{elastic solid medium}) \\ \langle P_{ij}^{*}\rangle = \mathrm{Real}\langle\sigma\rangle_{13}^{(i)}\mathrm{Real}\left\langle\dot{v}_{1}^{(j)}\right\rangle + \mathrm{Real}\langle\sigma\rangle_{33}^{(i)}\mathrm{Real}\left\langle\dot{v}_{3}^{(j)}\right\rangle(\text{thermoelastic solid medium}) \end{cases} \tag{54}$$

By Achenbach [29], consider two complex functions m and n, and we have:

$$\langle\mathrm{Re\,a\,l(m)}\rangle\langle\mathrm{Re\,a\,l(n)}\rangle = \frac{1}{2}\langle\mathrm{Re\,a\,l(m\bar{n})}\rangle \tag{55}$$

The energy ratio E_i used for the reflected SV-waves and reflected P-waves is (Kumar and Kansal [34]):

$$E_{i} = -\frac{\langle P_{i}^{*e}\rangle}{\langle P_{0}^{*e}\rangle}, i = 1,2 \tag{56}$$

$$E_{ij} = \frac{\langle P_{ij}^{*}\rangle}{\langle P_{0}^{*e}\rangle}, i,j = 1,\ 2,\ 3 \tag{57}$$

where E_2, E_1 are the reflected SV and P waves energy ratios respectively. The leading diagonal represents the energy matrix E_{ij} in Equation (57). On the other hand, it represents the P, T and SV waves energy ratios, while the sum of the elements other than the diagonal entries provides the interaction energy share for all refracted waves in Medium-II.

$$E_{RR} = \sum_{i=1}^{3}\left(\sum_{j=1}^{3} E_{ij} - E_{ii}\right) \tag{58}$$

And,

$$\langle P_{1}^{*e}\rangle = \frac{1}{2}\frac{\omega^{4}\rho^{e}c_{0}^{2}}{\alpha}\left|A'^{e}_{1}\right|^{2}\mathrm{Re}(\cos\theta_{1}), \langle P_{2}^{*e}\rangle = \frac{1}{2}\frac{\omega^{4}\rho^{e}c_{0}^{2}}{\beta}\left|B'^{e}_{1}\right|^{2}\mathrm{Re}(\cos\theta_{2}).$$

$$\langle P_0^{*e}\rangle = \begin{cases} \langle P_0^{*e}\rangle = -\dfrac{1}{2}\dfrac{\omega^4\rho^e c_0^2}{\alpha}\left|A'^{e}_{0}\right|\cos\theta_0, (\text{ incident P} - \text{wave}) \\ \langle P_0^{*e}\rangle = -\dfrac{1}{2}\dfrac{\omega^4\rho^e c_0^2}{\beta}\left|B'^{e}_{0}\right|\cos\theta_0, (\text{incident } SV - \text{wave}) \end{cases} \quad (59)$$

$\langle P_{ij}^{*}\rangle$,; i ∈ {1,2,3}, j ∈ {1,2,3}. Refer to Appendix B.

Through the relationship, it is possible to see the incident energy holds the conservation of energy throughout the process for all studied theories.

$$E_{11} + E_{22} + E_{33} + E_1 + E_2 + E_{RR} = 1 \quad (60)$$

7. Numerical results and discussion

Here are some numerical findings for the copper substance (Sherief and Saleh [37]), for which the following physical information is provided:

$C_E = 383.1JKg^{-1}K^{-1},\ K = 0.383\times10^3Wm^{-1}K^{-1}, T_0 = 0293K, h = 0, \alpha_t = 1.78\times10^{-5}K^{-1}$,
$\lambda = 7.76\times10^{10}Kgm^{-1}s^{-2}, \rho = 8.954\times10^3Kgm^{-3}, \mu = 3.86\times10^{10}Kgm^{-1}s^{-2}$.

Bullen [38] provides the numerical values for granite in an elastic medium.

$\alpha^e = 5.27\times10^3ms^{-1}, \rho^e = 2.65\times10^3Kgm^{-3},\ \beta^e = 3.17\times10^3ms^{-1}$.

By considered Cases 1 to 6 defined above. In particular, for G-L theory consider $\tau_0 = 1$, $\tau_1 = 2$, for G-N theory consider $n^* = 2$. The values of energy ratios and an energy matrix defined in the previous section have been calculated using the software MATLAB R2023a for various values of initial falling angle $\theta°$ in interval 0° to 90° and the frequency $\omega = 200\pi$ Hz used for incident P and SV waves. The effect of changes in incident angle with the energy ratios for coupled theory, L-S theory, G-N theory, G-L theory, three-phase-lag theory, and two-phase-lag theory has been shown in **Figures 2–7** (for P wave) and effect of angle on amplitude is observed in **Figures 8–12** (for P) respectively. The effect of angle on energy ratio is observed in **Figures 13–18** (for SV waves) and effect of angle on amplitude is observed in **Figures 19–23** (for SV waves) respectively. In all plotted graph, black, red, blue, pink, green, and navy-blue rectangular strips represent coupled models, the L-S model, the G-L model, the G-N model, the three-phase-lag theory and the two-phase lag theory respectively. 3D graphs are generated to demonstrate the impact of various thermoelasticity theories.

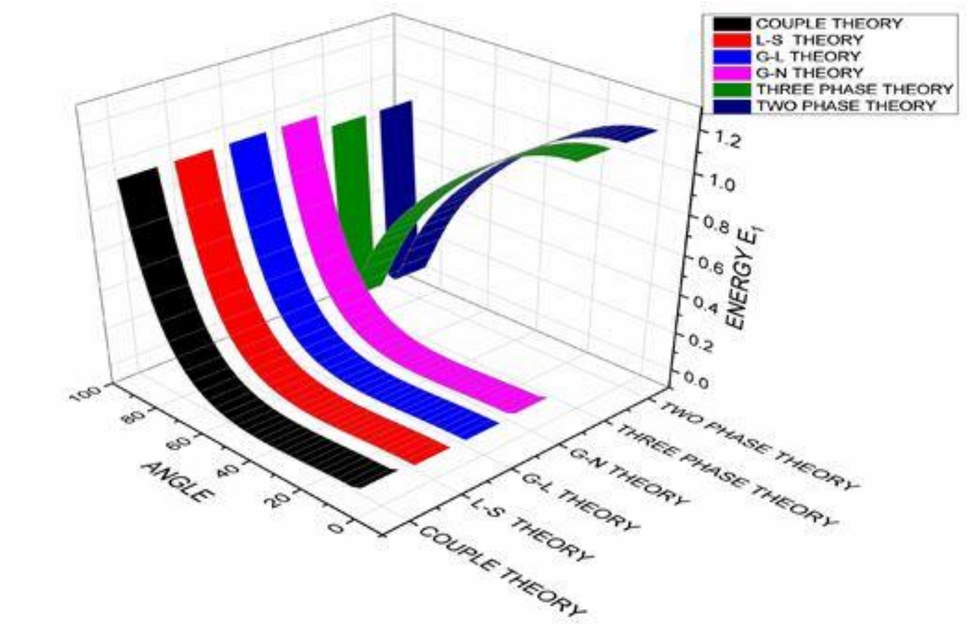

Figure 2. Changes in energy ratio E_1 w.r.t angle for $\theta°$ P wave.

It is observed in **Figure 2** that Coupled, L-S, G-L and G-N model energies show the same behavior the values of energy proportion E_1 increase with the increase in value of angle incidence $0° \leq \theta° \leq 90°$, and three-phase-lag model analysis and two-phase-lag model analysis show the same behavior in which the value of energy decreases as $\theta°$ increases and increases continuously at $\theta° = 86°$.

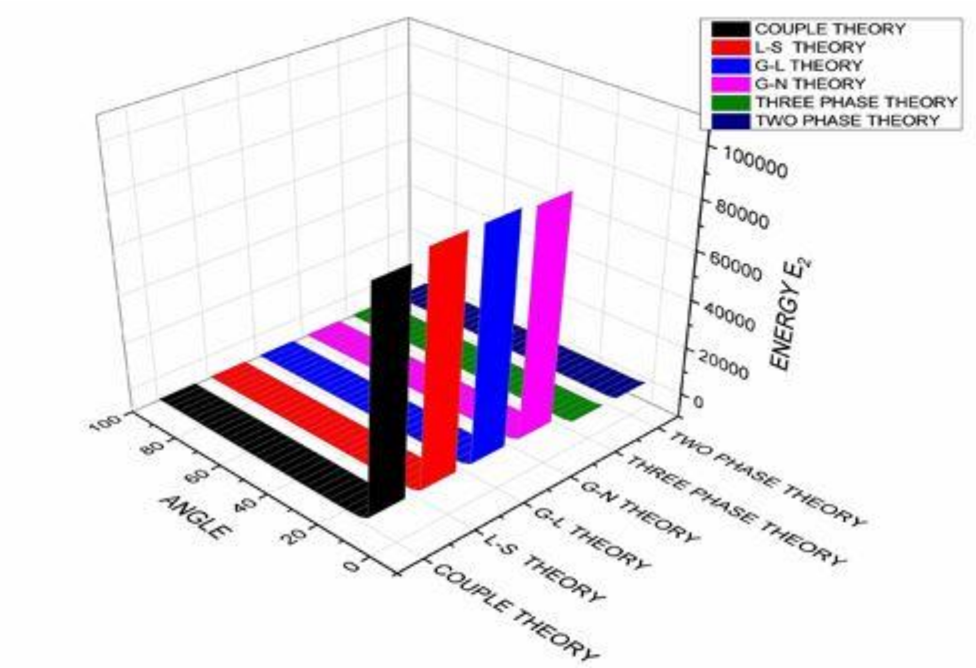

Figure 3. Changes in energy ratio E_2 w.r.t angle $\theta°$ for P wave.

Further, **Figure 3** shows that the values of E_2 decrease as $\theta°$ is in the range $10° \leq \theta° \leq 20°$ and thereafter remain constant as the value of $\theta°$ increases continuously for the Coupled L-S, G-L and G-N models. Three- and two-phase-lag models appear to be constant as their values are above 0 but very small compared to other models.

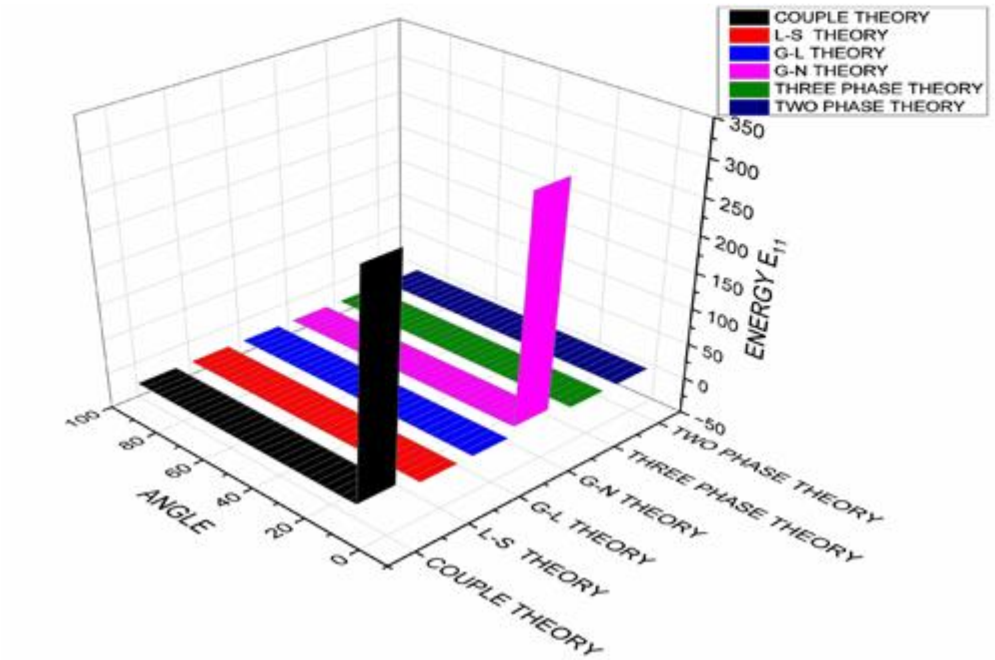

Figure 4. Changes in energy ratio E_{11} w.r.t angle θ° for P wave.

Figure 4 indicates that for L-S, G-L, the three-phase-lag model attains the minimum value of energy as the θ° increases from 0° to 90°. The coupled model and G-N model attain maximum value, decrease continuously, and then attain minimum value in the range 18° ≤ θ° ≤ 90°. The two-phase-lag model attains a comparatively higher value than L-S, G-L and the three-phase-lag model, but there is not much difference as the θ° increases from 0° to 90°.

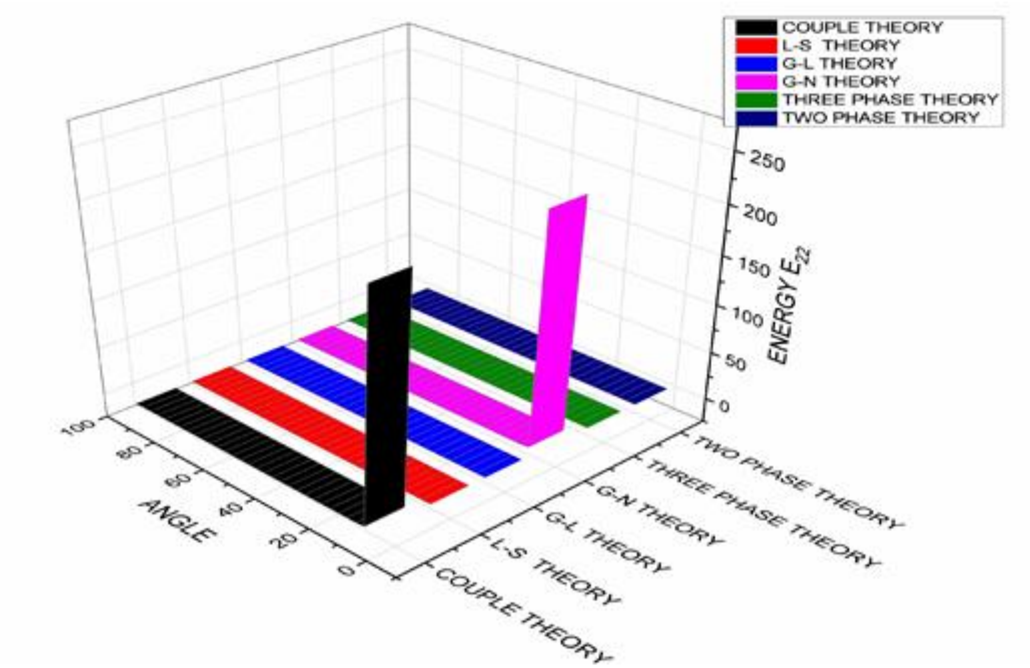

Figure 5. Changes in energy ratio E_{22} w.r.t angle θ° for P wave.

Figure 5 shows that E_{22} has the same behavior and changes as in E_{11}, but the magnitude values are different. For L-S, G-L, two-phase-lag and three-phase-lag model attain the minimum value of energy as the $\theta°$ increases from 0° to 90°. The coupled model and G-N model attain maximum value at $\theta° = 17°$, after which it decreases continuously and then attains minimum value in the range $18° \leq \theta° \leq 90°$. The two-phase-lag model attains a comparatively higher value than L-S, G-L and the three-phase-lag model, but there is not much difference as the $\theta°$ increases from 0° to 90°.

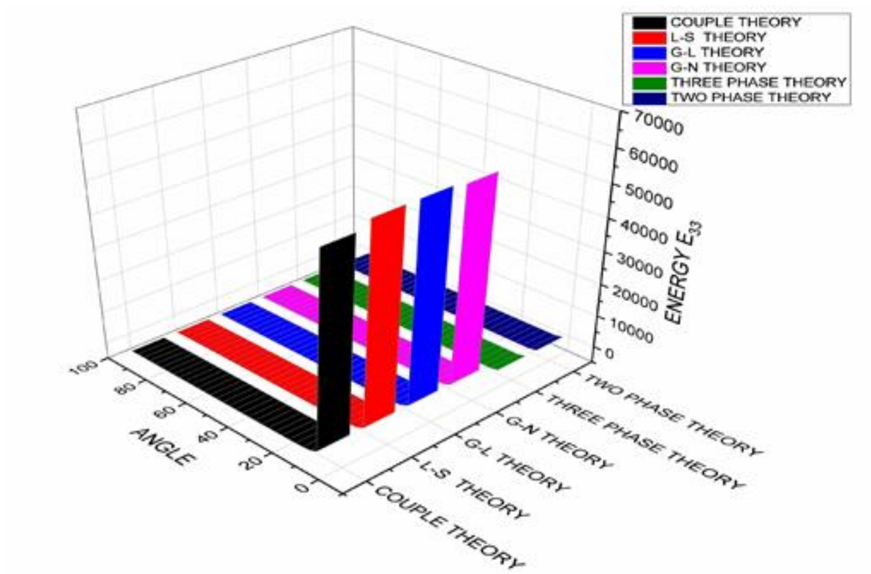

Figure 6. Changes in energy ratio E_{33} w.r.t angle $\theta°$ for P wave.

Figure 6 depicts that the two-phase-lag model and the three-phase-lag model E_{33} attain the minimum value in the range $10° \leq \theta° \leq 90°$ and the maximum value at $\theta° = (0.5°)$. In $0° \leq \theta° \leq 10°$, the value of E_{33} decreases.

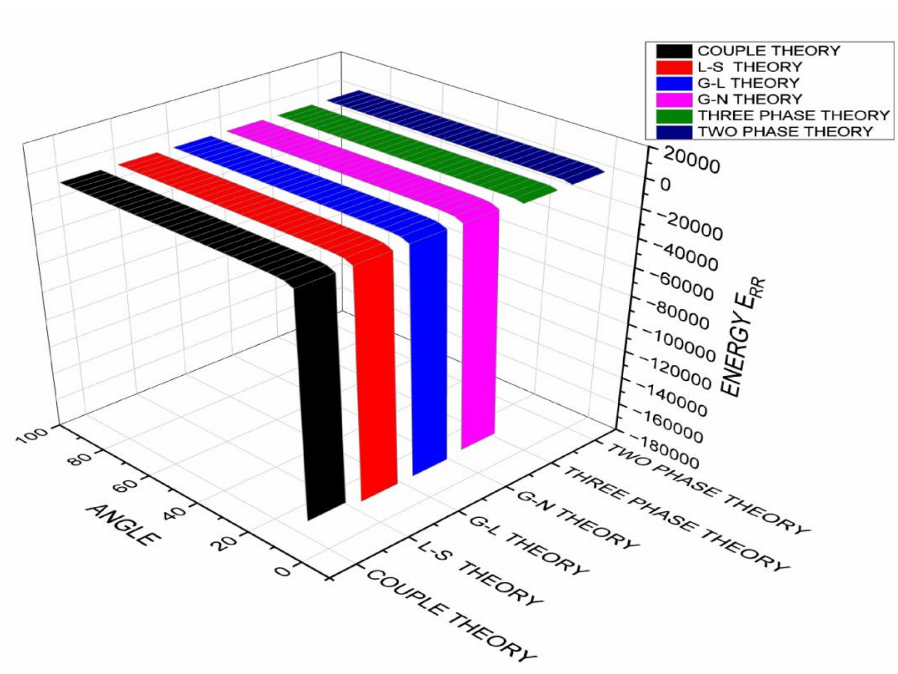

Figure 7. Changes in energy ratio E_{RR} w.r.t angle $\theta°$ for P wave.

Figure 7 depicts that for two-phase-lag and three-phase-lag models, the energy ratio E_{RR} attains a value nearly equal to zero. For coupled L-S, G-L and G-N models the value of E_{RR} attains near zero in the range $10° \leq \theta° \leq 90°$ and outside of this range energy decreases continuously until it attains its minimum value at $\theta° = 7°$.

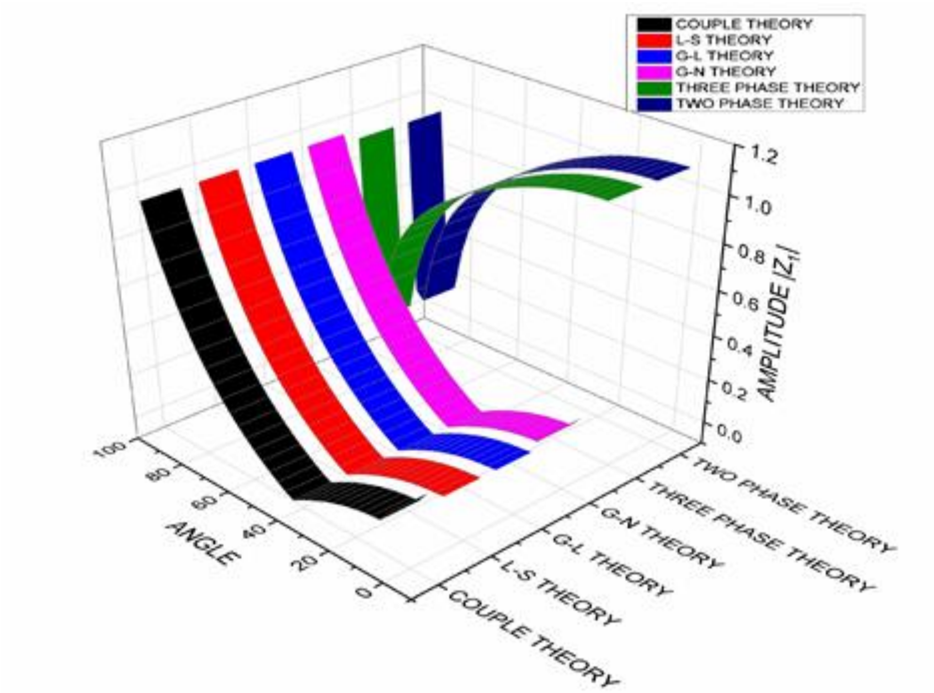

Figure 8. Changes in amplitude ratio $|Z_1|$ w.r.t angle $\theta°$ for P wave.

Figure 8 shows that the values of $|Z_1|$ decrease in the range $20° \leq \theta° \leq 40°$ and after that, they increase continuously with an increase in angle for the coupled L-S, G-N and G-L models. For two-phase-lag and three-phase-lag theories, after attaining the maximum value, the value $|Z_1|$ decreases continuously.

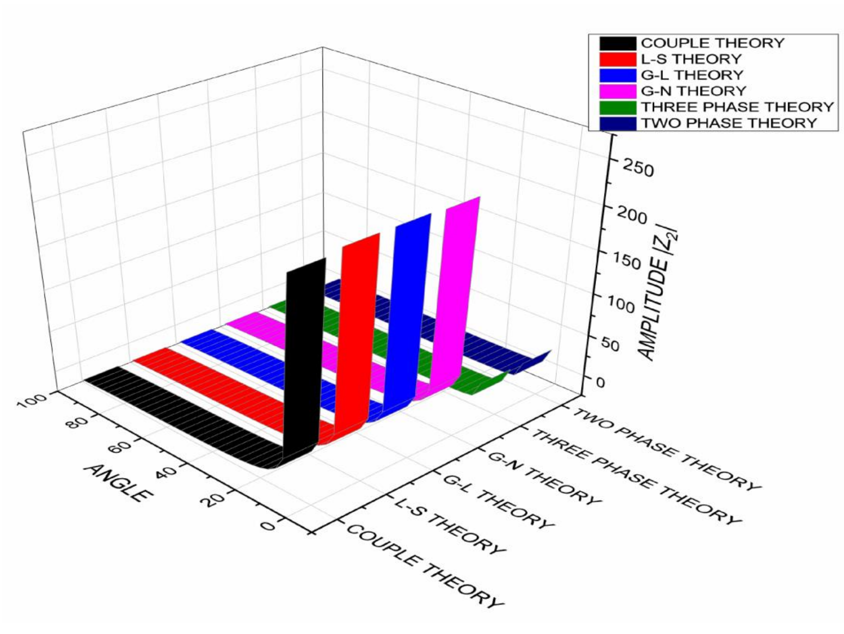

Figure 9. Changes in amplitude ratio $|Z_2|$ w.r.t angle $\theta°$ for P wave.

Figure 9 shows that for the coupled L-S, G-N and G-L models, the value of $|Z_2|$ attains the maximum value at $\theta° = 19°$ after it gives a constant value near to zero. For the other two models, three-phase-lag and two-phase-lag, it remained constant nearing zero when the angle $\theta°$ increases in the range of $0° \leq \theta° \leq 90°$, respectively.

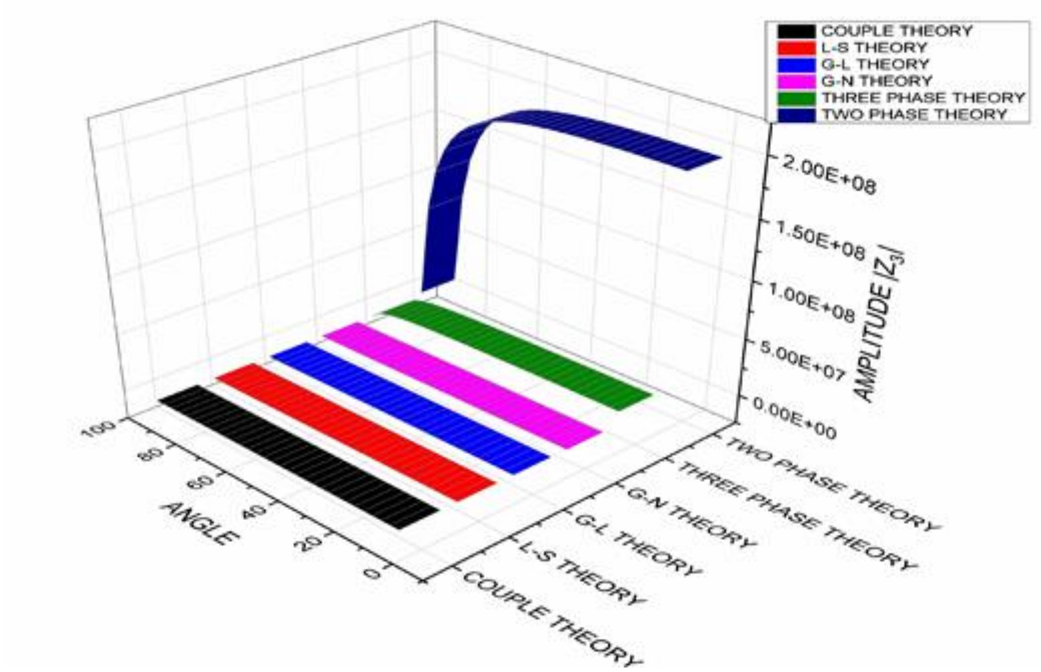

Figure 10. Changes in amplitude ratio $|Z_3|$ w.r.t angle $\theta°$ for P wave.

In **Figure 10**, the value of $|Z_3|$ depicts the same behavior and variations for all the models show values near to zero. For the two-phase-lag model, the value of the amplitude ratio decreases continuously as the $\theta°$ increases in the range $0° \leq \theta° \leq 90°$.

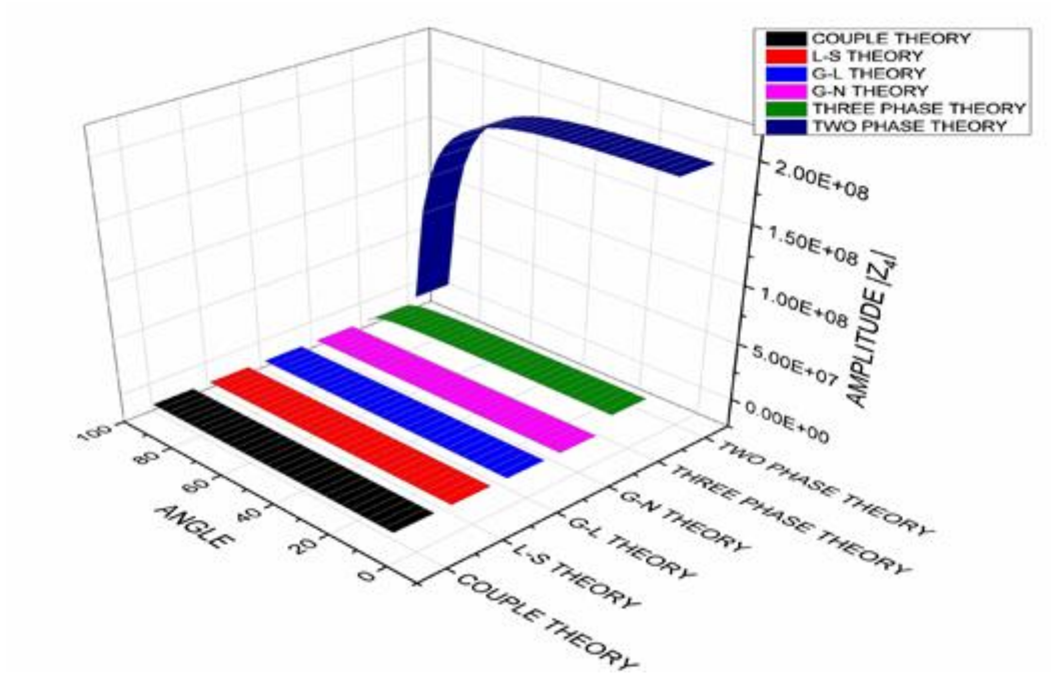

Figure 11. Changes in amplitude ratio $|Z_4|$ w.r.t angle $\theta°$ for P wave.

Figure 11. The values of $|Z_4|$ depict the same behavior and variations for all the models show values near zero for increasing values of incident angle. For the two-phase-lag model, the value of amplitude decreases continuously as $\theta°$ increases in the range of angle $0° \le \theta° \le 90°$.

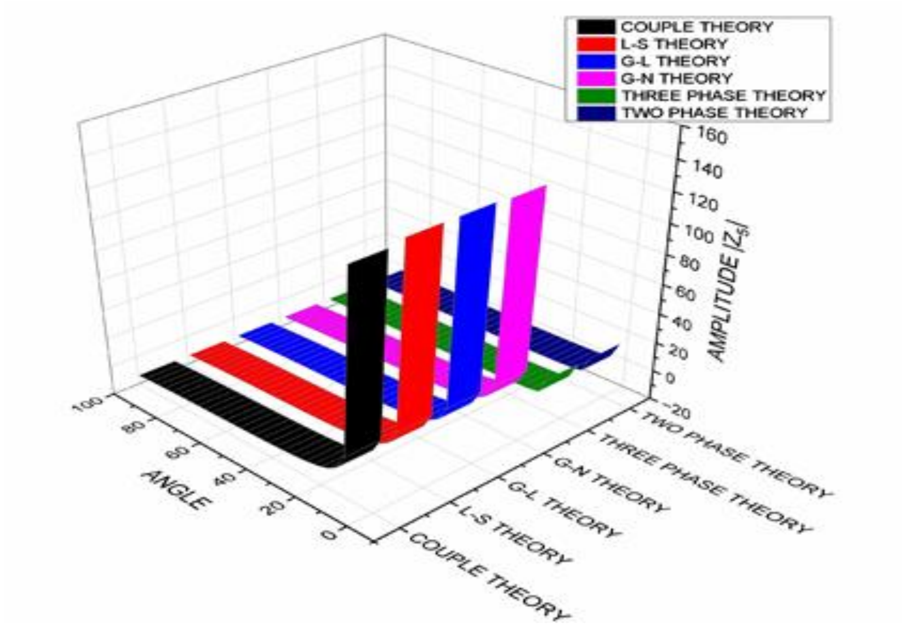

Figure 12. Changes in amplitude ratio $|Z_5|$ w.r.t angle $\theta°$ for P wave.

Figure 12 shows that for the coupled L-S, G-N and G-L models, the values of $|Z_5|$ after attaining the maximum value are constant and near zero. For the other two models, three-phase-lag and two-phase-lag, it remained constant nearing zero as $\theta°$ increases $0° \le \theta° \le 90°$, respectively.

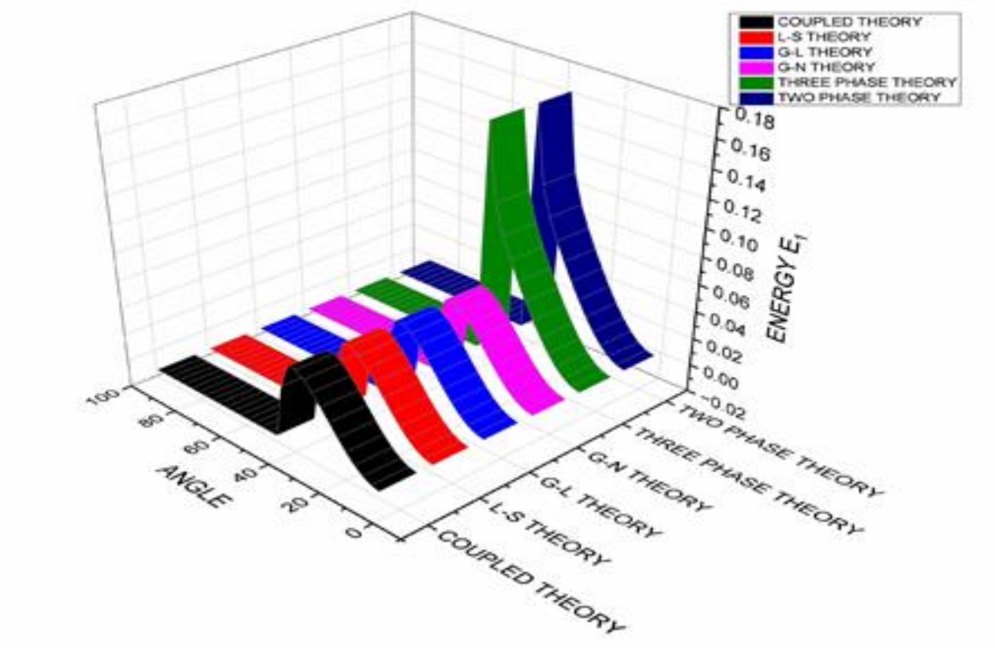

Figure 13. Changes in energy ratio E_1 w.r.t angle $\theta°$ for SV wave.

In **Figure 13**, it is concluded that all models E_1 show an increase in values as the angle increases in $0° \leq \theta° \leq 30°$, attain a maximum at $\theta° = 30°$, decrease rapidly for $30° \leq \theta° \leq 40°$ and thereafter attain a minimum value nearly at zero in the range $50° \leq \theta° \leq 90°$.

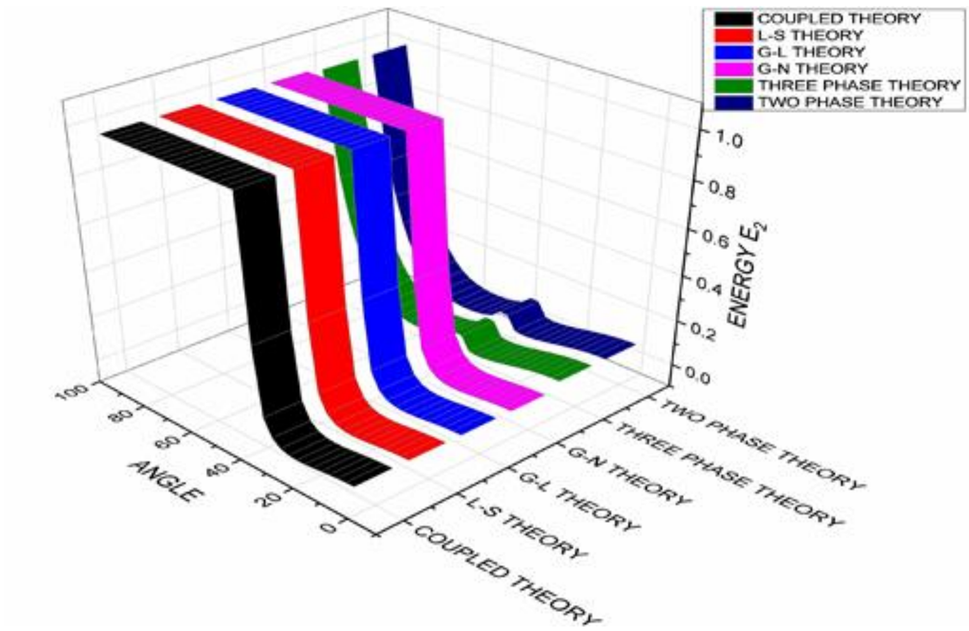

Figure 14. Changes in energy ratio E_2 w.r.t angle $\theta°$ for SV wave.

Figure 14 shows that the behavior of E_2 is opposite to E_1 and has obtained the maximum value of 1 in the interval $40° \leq \theta° \leq 90°$ for Coupled, L-S, G-L and G-N models, but the energy of two-phase-lag and three-phase-lag models increases as $\theta°$ range $40° \leq \theta° \leq 90°$ increases, reaching a maximum at $\theta° = 90°$. For $30° \leq \theta° \leq 40°$, all models show an increase in value with an increase in $\theta°$.

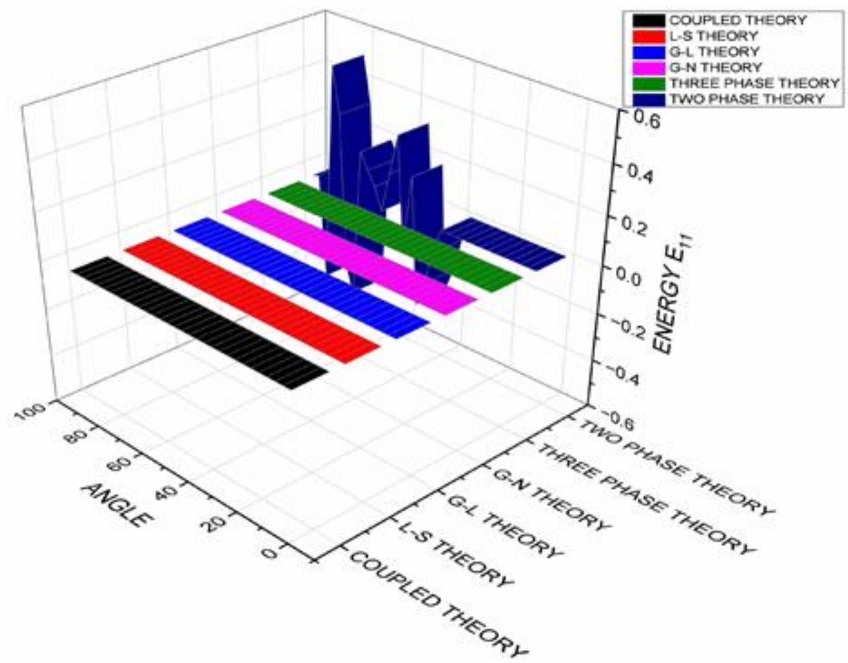

Figure 15. Changes in energy ratio E_{11} w.r.t angle $\theta°$ for SV wave.

In **Figure 15**, it is depicted that E_{11} shows similar behavior and variations for all the models coupled, L-S, G-L, G-N and the three-phase-lag except the two-phase-lag. It attains a value close to zero in the interval $0° \leq \theta° \leq 40°$ and then fluctuates for $40° \leq \theta° \leq 80°$ and finally attains a maximum value in the interval $80° \leq \theta° \leq 90°$.

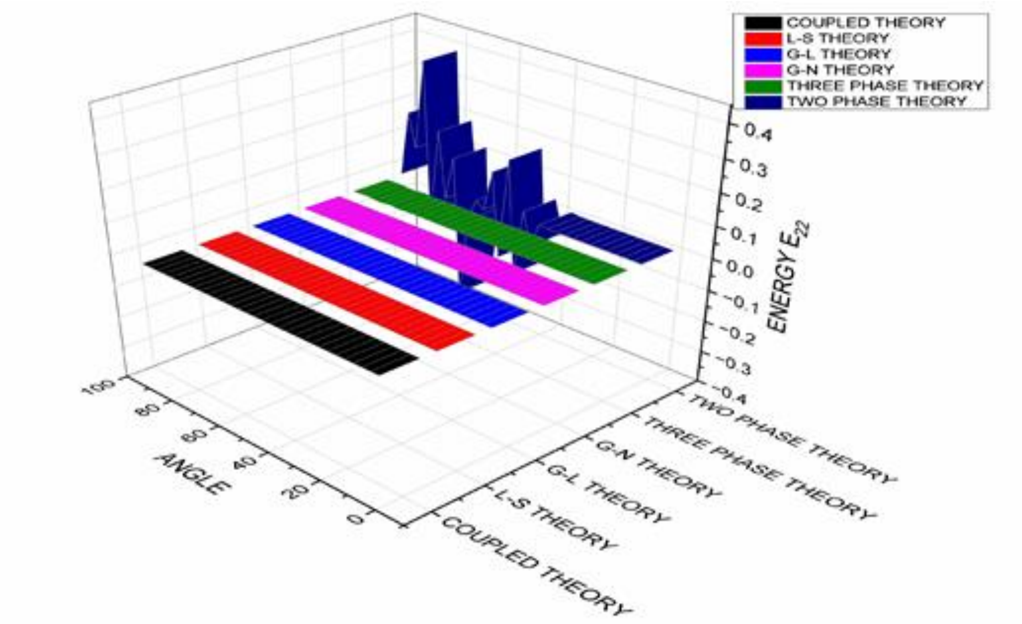

Figure 16. Changes in energy ratio E_{22} w.r.t angle $\theta°$ for SV wave.

Observation in **Figure 16** E_{22} shows similar behavior and variations for all the models except the two-phase-lag model. It attains a value close to zero in the interval $0° \leq \theta° \leq 40°$ and then fluctuates for $40° \leq \theta° \leq 80°$ and finally attains a maximum value in the interval $80° \leq \theta° \leq 90°$.

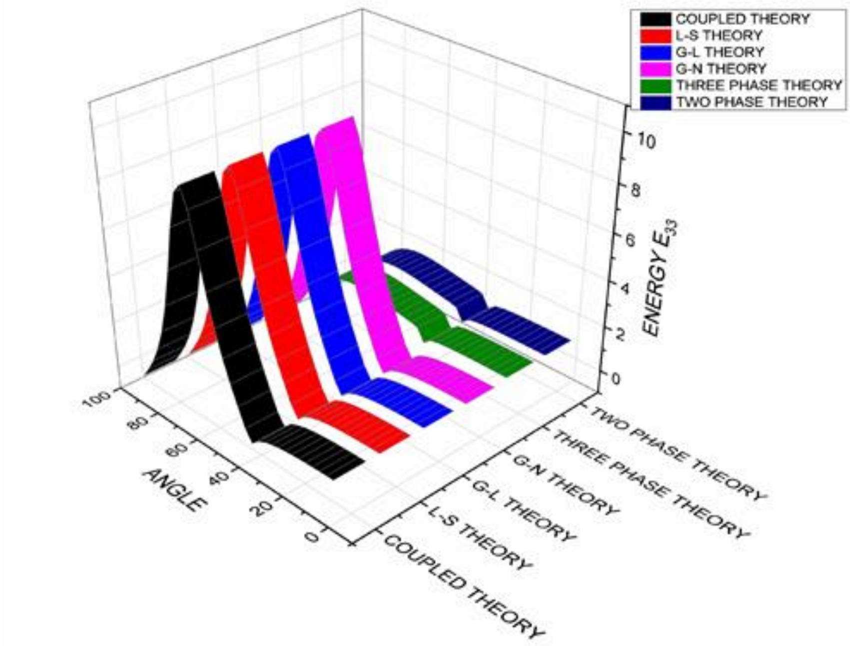

Figure 17. Changes in energy ratio E_{33} w.r.t angle $\theta°$ for SV wave.

Figure 17 indicates that E_{33} attains a value close to zero in the range $0° \leq \theta° \leq 40°$ and then fluctuates at $\theta° = 45°$. Then increases $45° \leq \theta° \leq 80°$ and attains maximum value for Couple, G-L, L-S and G-N models. After that, it decreases and attains its minimum value.

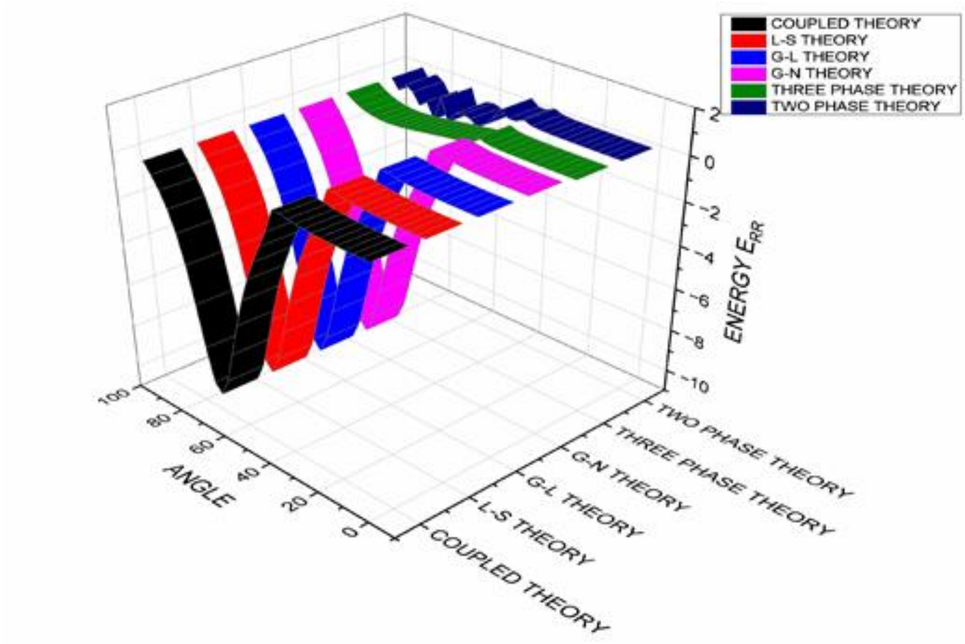

Figure 18. Changes in energy ratio E_{RR} w.r.t angle $\theta°$ for SV wave.

Figure 18 indicates that for all models, values of E_{RR} are nearly zero, decrease smoothly in the range $75° \leq \theta° \leq 80°$, attain the minimum value for $\theta° = 80°$, then increase rapidly in the range $80° \leq \theta° \leq 90°$, and finally take the value 1. But in the case of two-phase-lag and three-phase-lag model behavior, the value is near zero. Both the P and SV waves show the sum of all different energies. This holds for all the theories.

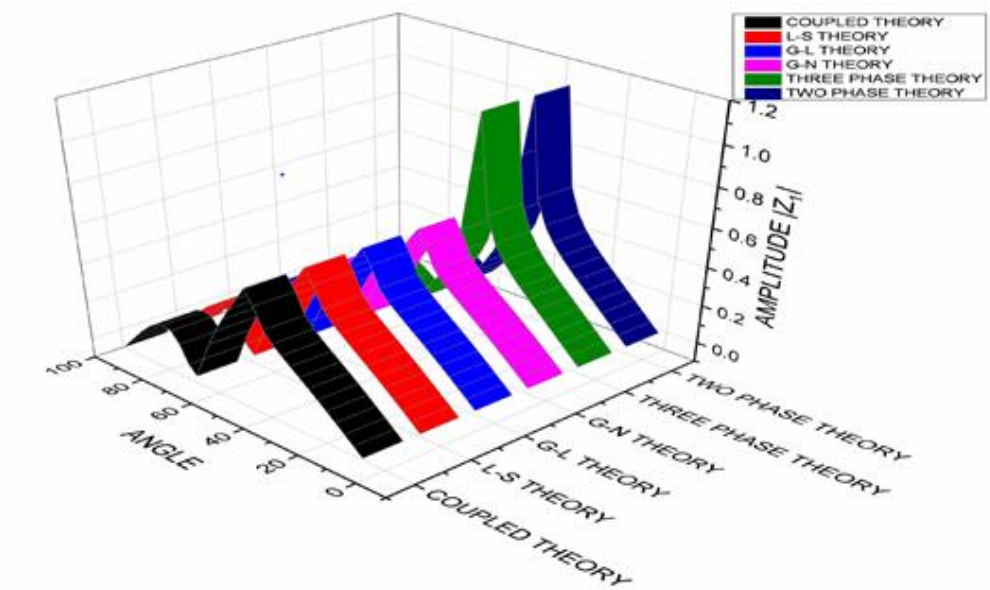

Figure 19. Changes in amplitude ratio $|Z_1|$ w.r.t angle $\theta°$ for SV wave.

From **Figure 19**, it is evident that for all models $|Z_1|$ shows an increase in values as $\theta°$ changes. It increases in the range $0° \leq \theta° \leq 50°$, attains a maximum at $\theta° = 50°$, decreases rapidly for $50° \leq \theta° \leq 75°$ and thereafter increases again after attaining a minimum value nearly to zero in the range $75° \leq \theta° \leq 85°$, then again decreases.

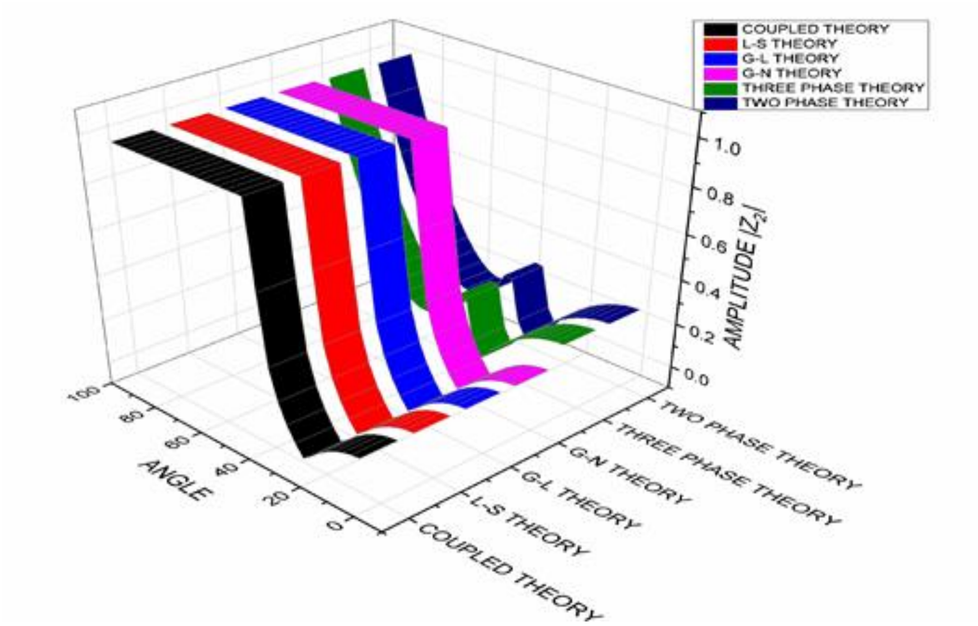

Figure 20. Changes in amplitude ratio $|Z_2|$ w.r.t angle $\theta°$ for SV wave.

Figure 20 shows that the behavior and changes of $|Z_2|$ are opposite to $|Z_1|$ and have a maximum constant amplitude value in the range $40° \leq \theta° \leq 90°$ for the Coupled, L-S, G-N and G-L models. But in two- and three-phase-lag models, fluctuating behavior is shown as $\theta°$ an increase in the range $20° \leq \theta° \leq 90°$.

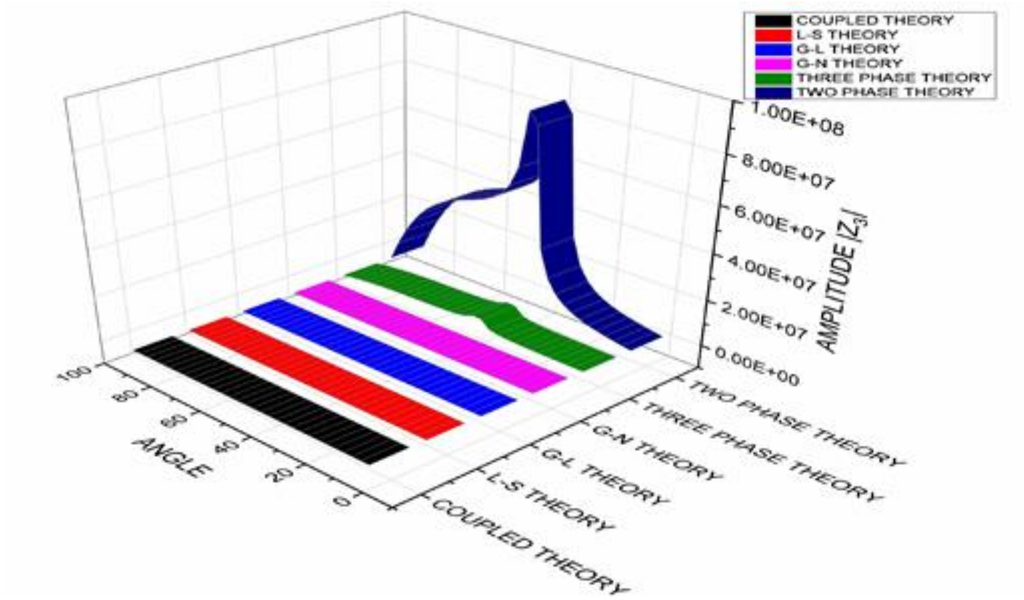

Figure 21. Changes in amplitude ratio $|Z_3|$ w.r.t angle $\theta°$ for SV wave.

In **Figure 21**, it appears that $|Z_3|$ has the same behavior and variations for Coupled, L-S, G-N, G-L and three-phase-lag models. But in the two-phase-lag model, amplitude ratio increases in the interval 0° ≤ θ° ≤ 40° and then decreases in 40° ≤ θ° ≤ 90°.

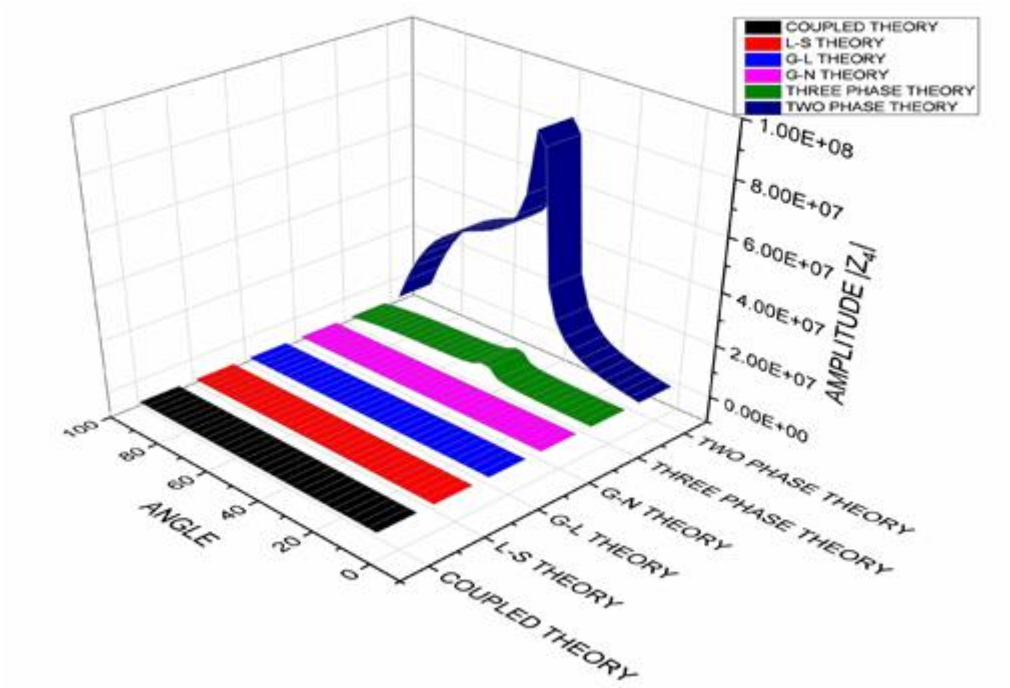

Figure 22. Changes in amplitude ratio $|Z_4|$ w.r.t angle θ° for SV wave.

In **Figure 22**, it appears that $|Z_4|$ has the same behavior and variations for all the models. In the two-phase-lag model, amplitude ratio increases in the interval 0° ≤ θ° ≤ 40° and then decreases in 40° ≤ θ° ≤ 90°.

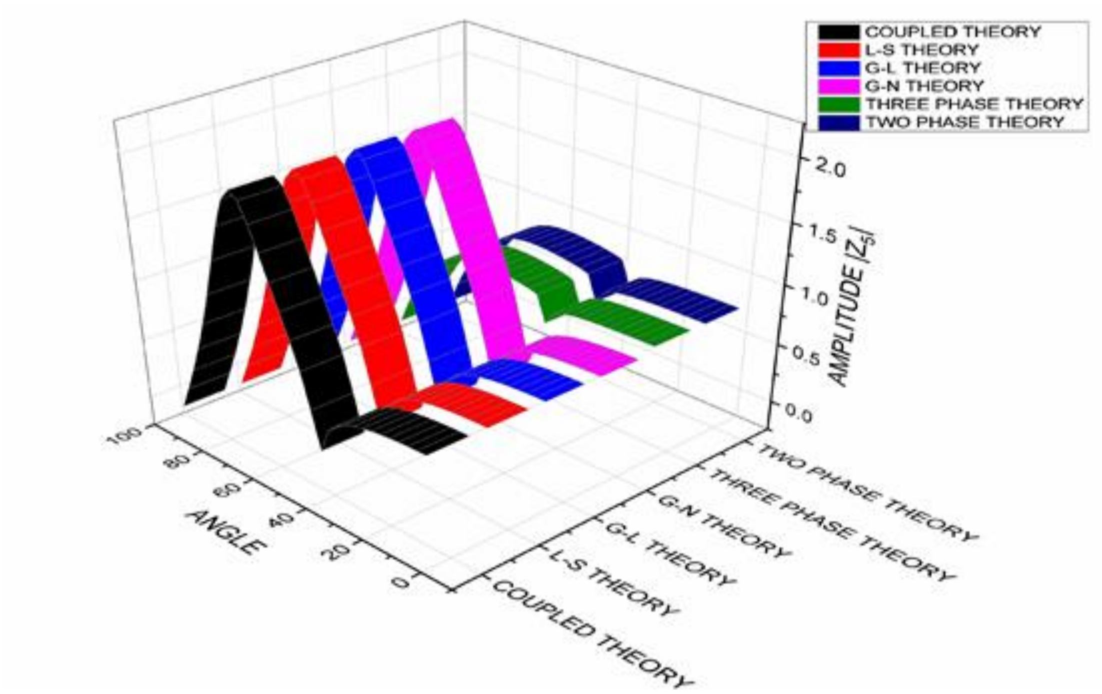

Figure 23. Changes in amplitude ratio $|Z_5|$ w.r.t angle θ° for SV wave.

From **Figure 23**, it is noticed that in the range 40° ≤ θ° ≤ 60°, amplitude $|Z_5|$ shows a constant value for all models. At θ° = 60°, it attained a minimum value and then again increases as angle increases, and 85° ≤ θ° ≤ 90° rapidly decreases.

8. Conclusion

In the current article, the phenomenon of incident elastic waves on the surface $x_3 = 0$ is discussed. Transmission and reflection at the plane between a half-space of elastic solids $x_3 < 0$ and six models in another half-space $x_3 > 0$ of thermoelastic solids (Coupled, L-S, G-N, three-phase-lag, two-phase-lag and G-L theories) has been investigated for isotropic material. Various wave conditions regarding displacement potentials are used to identify and describe the three waves in thermoelastic solid media with different models. With regard to the angle of incidence, the proportions of energies for various refracted and reflected waves with respect to the incident wave are calculated computationally, shown visually and then compared for all six models.

Findings: The analysis of the results permits some concluding remarks:

1) All distributions show a considerable influence from the phase lag effect, which can be seen. The difference between all the thermoelastic models and dual-phase-lag (DPL) thermoelastic model is very clear.
2) Due to differences in phase lags in different thermoelastic models. Differences in energy ratios and amplitude ratios are observed.
3) Graphically, it is observed that values of energy for different angles in P waves achieve the highest and lowest values as compared to SV waves. But still, both acquired the sum of energies as one.
4) We draw the conclusion from numerical results that for all theories of the thermoelastic model, the influence of the angle of incidence on amplitude and energy ratio is substantial.
5) The law of incident energy conservation at the interface is guaranteed by the fact that the total energy ratio of all reflected waves, refracted waves and involvement between refracted waves reliably ends up being unity. It is noticed that the sum of the values of E_1, E_2, E_{11}, E_{33}, E_{22} and E_{RR} energy ratios is found to be unity at each value θ°, which proves the law of conservation of energy in the medium considered.
6) The considered problem has applications in astronautics, earthquake engineering, rocket engineering, and many more engineering areas.

Author contributions: Conceptualization, KK, VG and SG; methodology, KK, VG and SG; software, SG and MK; validation, KK, VG and SG; formal analysis, KK, VG, SG and MK; investigation, KK, VG and SG; data curation, KK, VG and SG; writing—original draft preparation, SG; writing—review and editing, KK, VG and SG; supervision, KK and VG. All authors have read and agreed to the published version of the manuscript.

Conflict of interest: The authors declare no conflict of interest.

References

1. McCarthy MF. Wave propagation in generalized thermoelasticity. International Journal of Engineering Science. 1972; 10(7): 593–602.
2. Sharma JN, Sidhu RS. On the propagation of plane harmonic waves in Anisotropic generalized thermoelasticity. International Journal of Engineering Science. 1986; 24(9): 1511–1516.
3. Banerjee DK, Pao YH. Thermoelastic waves in anisotropic solids. The Journal of the Acoustical Society of America. 1974; 56(5): 1444–1454. doi: 10.1121/1.1903463
4. Puri P. Plane waves in generalized thermoelasticity. International Journal of Engineering Science. 1973; 11(7): 735–744.
5. Chadwick P, Seet LTC. Wave propagation in a transversely isotropic heat-conducting elastic material. Mathematika. 1970; 17(2): 255–274. doi: 10.1112/s002557930000293x
6. Dhaliwal RS, Sherief HH. Generalized thermoelasticity for anisotropic media. Quarterly of Applied Mathematics. 1980; 38(1): 1–8. doi: 10.1090/qam/575828
7. Chandrasekharaiah DS. Wave propagation in a thermoelastic half-space. Indian Journal of Pure and Applied Math. 1981; 12: 226–241.
8. Singh H, Sharma JN. Generalized thermoelastic waves in transversely isotropic media. The Journal of the Acoustical Society of America. 1985; 77(3): 1046–1053. doi: 10.1121/1.392391
9. Sharma MD. Wave Propagation in Anisotropic Generalized Thermoelastic Media. Journal of Thermal Stresses. 2006; 29(7): 629–642. doi: 10.1080/01495730500499100
10. Prasad R, Kumar R, Mukhopadhyay S. Propagation of harmonic plane waves under thermoelasticity with dual-phase-lags. International Journal of Engineering Science. 2010; 48(12): 2028–2043. doi: 10.1016/j.ijengsci.2010.04.011
11. Lykotrafitis G, Georgiadis HG, Brock LM. Three-dimensional thermoelastic wave motions in a half-space under the action of a buried source. International Journal of Solids and Structures. 2001; 38(28–29): 4857–4878.
12. Sharma MD. Wave propagation in a general anisotropic poroelastic medium with anisotropic permeability: phase velocity and attenuation. International Journal of Solids and Structures. 2004; 41(16–17): 4587–4597. doi: 10.1016/j.ijsolstr.2004.02.066
13. Venkatesan M, Ponnusamy P. Wave propagation in a generalized thermoelastic solid cylinder of arbitrary cross-section immersed in a fluid. International Journal of Mechanical Sciences. 2007; 49(6): 741–751. doi: 10.1016/j.ijmecsci.2006.10.003
14. Kumar R, Kansal T. Propagation of Lamb waves in transversely isotropic thermoelastic diffusive plate. International Journal of Solids and Structures. 2008; 45(22–23): 5890–5913. doi: 10.1016/j.ijsolstr.2008.07.005
15. Yu J, Wu B, He C. Guided thermoelastic wave propagation in layered plates without energy dissipation. Acta Mechanica Solida Sinica. 2011; 24: 135–143.
16. Kumar R, Gupta V. Reflection and transmission of plane waves at the interface of an elastic half-space and a fractional order thermoelastic half-space. Archive of Applied Mechanics. 2013; 83(8): 1109–1128. doi: 10.1007/s00419-013-0737-6
17. Youssef HM, El-Bary AA. Theory of hyperbolic two temperature generalized thermoelasticity. Journal of Material Physics and Mechanics. 2018; 40: 158–171.
18. Lata P, Kaur I, Singh K. Thermomechanical interactions due to time harmonic sources in a transversely isotropic magneto thermoelastic rotating solids in Lord-Shulman model. Journal of Material Physics and Mechanics. 2020; 46: 7–26.
19. Kumar R, Bansal P, Gupta V. Reflection and transmission at the interface of an elastic and two-temperature generalized thermoelastic half-space with fractional order derivative. Journal of Material Physics and Mechanics. 2021; 47: 1–19.
20. Sherief H, Anwar MN, El-Latief AA, et al. A fully coupled system of generalized thermoelastic theory for semiconductor medium. Scientific Reports. 2024; 14(1). doi: 10.1038/s41598-024-63554-2
21. Ding W, Patnaik S, Sidhardh S, Semperlotti F. Displacement-driven approach to nonlocal elasticity. Nanomechanics of Structures and Materials. 2024; 277–317. doi: 10.1016/b978-0-443-21949-8.00016-4
22. Li S, Zheng W, Li L. Spatiotemporally nonlocal homogenization method for viscoelastic porous metamaterial structures. International Journal of Mechanical Sciences. 2024; 282: 109572. doi: 10.1016/j.ijmecsci.2024.109572
23. Kumar R, Kaushal S, Kochar A. Analysis of axisymmetric deformation in generalized micropolar thermoelasticity within the framework of Moore-Gibson-Thompson heat equation incorporating non-local and hyperbolic two-temperature effect. The Journal of Strain Analysis for Engineering Design. 2024; 59(3): 153–166. doi: 10.1177/03093247241232180

24. Yadav AK, Carrera E, Marin M, Othman MIA. Reflection of hygrothermal waves in a Nonlocal Theory of coupled thermo-elasticity. Mechanics of Advanced Materials and Structures. 2024; 31(5): 1083–1096. doi: 10.1080/15376494.2022.2130484
25. Abd-Alla AM, Othman MIA, Abo-Dahab SM. Reflection of Plane Waves from Electro-magneto-thermoelastic Half-space with a Dual-Phase-Lag Model. Computers Materials & Continua. 2016; 51(2): 63–79.
26. Othman MIA, Abo-Dahab SM, Alsebaey ONS. Reflection of Plane Waves from a Rotating Magneto-thermoelastic Medium with Two-temperature and Initial Stress under Three Theories. Mechanics and Mechanical Engineering. 2017; 21(2): 217–232.
27. Biot MA. Thermoelasticity and Irreversible Thermodynamics. Journal of Applied Physics. 1956; 27(3): 240–253. doi: 10.1063/1.1722351
28. Lord HW, Shulman Y. A generalized dynamical theory of thermo-elasticity. Journal of Mechanics and Physics of Solids. 1967; 15(5): 299–309.
29. Green AE, Lindsay KA. Thermoelasticity. Journal of Elasticity. 1972; 2(1): 1–7. doi: 10.1007/bf00045689
30. Green AE, Naghdi PM. On undamped heat waves in an elastic solid. Journal of Thermal Stresses. 1992; 15(2): 253–264. doi: 10.1080/01495739208946136
31. Green AE, Naghdi PM. Thermoelasticity without energy dissipation. Journal of Elasticity. 1993; 31(3): 189–208. doi: 10.1007/bf00044969
32. Choudhuri SKR. On a thermoelastic three-phase-lag model. Journal of Thermal Stresses. 2007; 30(3): 231–238. doi: 10.1080/01495730601130919
33. Tzou DY. A unified field approach for heat conduction from macro- to micro-scales. Journal of Heat Transfer. 1995; 117(1): 8–16. doi: 10.1115/1.2822329
34. Kumar R, Kansal T. Reflection and refraction of plane waves at the interface of an elastic solid half-space and a thermoelastic diffusive solid half-space. Archives of Mechanics. 2012; 64: 293–317.
35. Borcherdt RD. Reflection-refraction of general P-and type-I S-waves in elastic and anelastic solids. Geophysical Journal of the Royal Astronomical Society. 1982; 70(3): 621–638. doi: 10.1111/j.1365-246x.1982.tb05976.x
36. Achenbach JD. In: Wave propagation inelastic solids. Elsevier Science Publishers; 1973.
37. Sherief HH, Saleh HA. A half-space problem in the theory of generalized thermoelastic diffusion. International Journal of Solids and Structures. 2005; 42(15): 4484–4493. doi: 10.1016/j.ijsolstr.2005.01.001
38. Bullen KE. In: An introduction to the theory of seismology. Cambridge University Press; 1963.

Appendix A

$$c_{11} = -\lambda^{e}\left(\frac{\xi_R}{\omega}\right)^2 - \rho\alpha^{2e}\left(\frac{dV_\alpha}{\omega}\right)^2, c_{12} = 2\mu^{e}\frac{\xi_R}{\omega}\frac{dV_\beta}{\omega}, c_{15} = 2\mu\frac{\xi_R}{\omega}\frac{dV_3}{\omega}, c_{21} = 2\mu^{e}\frac{\xi_R}{\omega}\frac{dV_\alpha}{\omega}, c_{31} = \frac{\xi_R}{\omega},$$

$$c_{22} = \mu^{e}\left[\left(\frac{dV_\beta}{\omega}\right)^2 - \left(\frac{\xi_R}{\omega}\right)^2\right], c_{25} = \mu\left[\left(\frac{\xi_R}{\omega}\right)^2 - \left(\frac{dV_3}{\omega}\right)^2\right], c_{32} = \frac{dV_\beta}{\omega}, c_{35} = \frac{dV_3}{\omega}, c_{41} = -\frac{dV_\alpha}{\omega},$$

$$c_{42} = \frac{\xi_R}{\omega}, c_{45} = -\frac{\xi_R}{\omega}, c_{51} = c_{52} = c_{55} = 0, c_{1j} = \lambda\left(\frac{\xi_R}{\omega}\right)^2 + \mu\beta^2\left(\frac{dV_j}{\omega}\right)^2 + \gamma n_j(1 - i\omega\tau_1)\frac{T_0}{\omega^2}.$$

$$c_{1j} = \lambda\left(\frac{\xi_R}{\omega}\right)^2 + \mu\beta^2\left(\frac{dV_j}{\omega}\right)^2 + \gamma n_j(1 - i\omega\tau_1)\frac{T_0}{\omega^2}, c_{2j} = 2\mu\frac{\xi_R}{\omega}\frac{dV_j}{\omega}, c_{3j} = -\frac{\xi_R}{\omega}, c_{4j} = -\frac{dV_j}{\omega},$$

$$\frac{dV_\alpha}{\omega} = \left(\frac{1}{\alpha^2} - \left(\frac{\xi_R}{\omega}\right)^2\right)^{\frac{1}{2}} = \left(\frac{1}{\alpha^2} - \frac{\sin^2\theta_0}{V_0{}^2}\right)^{\frac{1}{2}}, c_{5j} = in_j\frac{dV_j}{\omega} + n_j\frac{h}{\omega}, j = 3,4,$$

$$\frac{dV_\beta}{\omega} = \left(\frac{1}{\beta^2} - \frac{\sin^2\theta_0}{V_0{}^2}\right)^{\frac{1}{2}}, \frac{dV_j}{\omega} = p.v.\left(\frac{1}{V_j{}^2} - \frac{\sin^2\theta_0}{V_0{}^2}\right)^{\frac{1}{2}}.$$

Here p.v. is calculated having restriction $j = 1, 2, 3$. $dV_{jI} \geq 0$ to fulfill the decay requirement in a thermal elastic medium.

Appendix B

$$\langle P_{ij}^{*}\rangle = -\frac{\omega^4}{2}\mathrm{Re}\left[\left\{2\mu\frac{dV_i}{\omega}\frac{\xi_R}{\omega}\frac{\bar{\xi}_R}{\omega} + \lambda\left(\frac{\xi_R}{\omega}\right)^2\left(\frac{d\bar{V}_j}{\omega}\right) + \rho c_0^2\left(\frac{dV_i}{\omega}\right)^2\left(\frac{d\bar{V}_j}{\omega}\right) + \frac{\gamma m_i T_0}{\omega^2}\left(\frac{d\bar{V}_j}{\omega}\right)\right\}B_i'\bar{B}_j'\right],$$

$$\langle P_{i3}^{*}\rangle = -\frac{\omega^4}{2}\mathrm{Re}\left[\left\{-2\mu\frac{dV_i}{\omega}\frac{d\bar{V}_3}{\omega}\frac{\xi_R}{\omega} + \lambda\left(\frac{\xi_R}{\omega}\right)^2\left(\frac{\bar{\xi}_R}{\omega}\right) + \rho c_0^2\left(\frac{dV_i}{\omega}\right)^2\left(\frac{\bar{\xi}_R}{\omega}\right) + \frac{\gamma m_i T_0}{\omega^2}\left(\frac{\bar{\xi}_R}{\omega}\right)\right\}B_i'\bar{B}_3'\right],$$

$$\langle P_{3j}^{*}\rangle = -\frac{\omega^4}{2}\mathrm{Re}\left[\left\{\mu\left(\left(\frac{\xi_R}{\omega}\right)^2\frac{\bar{\xi}_R}{\omega} - \frac{\bar{\xi}_R}{\omega}\left(\frac{dV_3}{\omega}\right)^2\right) - \lambda\frac{\xi_R}{\omega}\frac{dV_3}{\omega}\frac{d\bar{V}_j}{\omega} + \rho c_0^2\frac{\xi_R}{\omega}\frac{dV_3}{\omega}\frac{d\bar{V}_j}{\omega}\right\}\bar{B}_j'B_3'\right],$$

$$\langle P_{33}^{*}\rangle = -\frac{\omega^4}{2}\mathrm{Re}\left[\left\{\mu\left(\left(\frac{dV_3}{\omega}\right)^2 - \left(\frac{\xi_R}{\omega}\right)^2\right)\frac{d\bar{V}_3}{\omega} - 2\mu\frac{\xi_R}{\omega}\frac{\bar{\xi}_R}{\omega}\frac{dV_3}{\omega}\right\}B_3'\bar{B}_3'\right],\ i,\mathrm{j} = 1,2.$$

Thermal Science and Engineering 2025, 8(1), 10925.
https://doi.org/10.24294/tse10925

Article

The performance evaluation of monocrystalline PV module by using water-channel cooling technique with forced convection

Ehtsham Ul Haq[1], Zain Ali[1], Muhammad Tuoqeer Anwar[1,*], Muhammad Ahmad Ali[1], Muhammad Rizwan Ameer[1], Naveed Husnain[2], Mohamed Kchaou[3], Tahir Rasheed[4,*], Syed Khawar Hussain Shah[1], Muhammad Salman Nawaz[1]

[1] Department of Mechanical Engineering, COMSATS University Islamabad, Sahiwal 57000, Pakistan
[2] Department of Mechanical Engineering, Faculty of Engineering and Technology, Bahauddin Zakariya University, Multan 60800, Pakistan
[3] Department of Mechanical Engineering, College of Engineering, University of Bisha, Bisha 67714, Saudi Arabia
[4] Interdisciplinary Research Center for Advanced Materials, King Fahd University of Petroleum and Minerals, Dhahran 31261, Saudi Arabia
*** Corresponding authors:** Muhammad Tuoqeer Anwar, engr.tauqeer137@gmail.com; Tahir Rasheed, tahir.rasheed@kfupm.edu.sa

CITATION

Ul Haq E, Ali Z, Anwar MT, et al. The performance evaluation of monocrystalline PV module by using water-channel cooling technique with forced convection. Thermal Science and Engineering. 2025; 8(1): 10925. https://doi.org/10.24294/tse10925

ARTICLE INFO

Received: 16 December 2024
Accepted: 25 January 2025
Available online: 14 February 2025

Abstract: The power and efficiency of the monocrystalline PV module increase by reducing its panel temperature. It depends on the solar irradiance and the operating temperature of the PV module. Due to an increase in the operating temperature of the PV module, the efficiency decreases. As the temperature rises, the power output of the PV module also decreases. To improve the efficiency of the PV module, two different cooling techniques are investigated in this paper, i.e., the water channel cooling technique and the water-channel cooling technique accompanied with forced convection. In the water-channel cooling technique, copper pipes with serpentine and multi-inlet outlet arrangements are utilized at the backside of the mono-crystalline PV module, and the water is passed through pipes, while in water-channel cooling along with forced convection, the copper pipes with serpentine and multi-inlet outlet arrangements along with fans are employed. It is observed that the multi-inlet-outlet arrangement is more efficient as compared to the serpentine arrangement owing to the better heat transfer between the cooling media and the PV module. The experimental results demonstrate an increase in power output and efficiency realized through the reduction in operating temperature of the PV module and thus improving the open circuit voltage.

Keywords: mono-crystalline PV module; back surface cooling; photovoltaic system; forced convection; solar energy

1. Introduction

The advent of solar energy has provided the world with a renewable and sustainable source of energy to address the global energy crisis. Additionally, it is providing solutions to the other environmental issues, such as the provision of fresh water to the distant regions through solar stills. To directly harness solar energy, solar panels are being employed [1–3]. A solar panel is a device that converts solar energy into electricity known as a photovoltaic (PV) cell. This process is carried out with the help of the photovoltaic effect. The photovoltaic effect converts sunlight into voltage or current in a solar cell. In 1839 solar cells were introduced by Edmond Becquerel. In PV modules, the building blocks are solar cells, which are commonly known as solar panels [4].

The photovoltaic effect is such a phenomenon that produces current or voltage in a PV cell when exposed to the sun. This effect is applied to solar cells that convert sunlight into the desired form. The electric field is formed as a result of the formation of a p-n interface in the solar cell, as the n-type and p-type semiconductors form solar cells. In the p-n junction, an electron from the n-type silicon disperses in the p-type. When light is absorbed, free electrons are produced in the form of n, and these free electrons travel through the holes (type p). Electrons from the cathode (type n) to the anode (type p) generate electrical energy. At present, what is produced in this way is a direct current, and with an inverter, it is converted into another variable for home use [5].

The combination of PV cells is called a photovoltaic module; these PV modules form a PV system known as the PV array. Solar panels come in a number of shapes and sizes, each with its own set of characteristics that decide how they are used. These panels generate 100% renewable electricity for free. There are three main types of solar panels, all made of silicon semiconductors, and these are monocrystalline, polycrystalline, and amorphous ones. Nowadays, hybrid solar cells are also produced on a commercial basis. As far as this experimentation is concerned, only the mono-crystalline PV module is discussed [6,7].

In comparison to other panels, monocrystalline solar panels are more efficient. Silicon is used in monocrystalline solar panels. In monocrystalline solar panels, all cells are made up of a single crystal. Silicon is adapted into bars and then cut into wafers in these solar cells. The electron thus generated got more space to travel; that's why monocrystalline solar panels are more efficient. The efficiency is typically around 15%–20% for monocrystalline PV cells [8,9].

The performance parameters of PV modules are affected by environmental factors, geographical factors and the type of PV technology. The major environmental factors that affect the efficiency of photovoltaic modules are dust, wind, orientation, humidity, rain, and temperature. The major geographical factors that affect the efficiency of PV modules are solar intensity, longitude and latitude. Types of PV technology have a major effect on the efficiency of PV modules, offering distinct values.

Siecker et al. reviewed different cooling techniques such as floating concentrating cooling system, thermal and hybrid PV system cooled by water showering, thermoelectric and hybrid PV system cooled by heat submerging, thermal and hybrid PV system cooled by enforced water flow, enhancing the performance of panels by utilizing PCM, cooling by dipping panel in water, PV module cooled by translucent coating, hybrid PV system and thermal system cooled by enforced air flow. They also concluded that actual cooling of PV systems improves electrical, thermal, and overall efficiency, reducing cell degradation and extending the life of the panels. In terms of drawbacks, advantages, and techno-economic and environmental impacts, these various cooling techniques are used to address the unpleasant effect of temperature [10].

Bashir and co-workers reported an experimental analysis to test the efficiency of PV modules in the summer months and in the climate of Taxila near Pakistan's capital. Single junction amorphous silicon, monocrystalline silicon, polycrystalline silicon, were used in the research study. Using an outdoor testing facility, the study centered on measuring module quality, output ratio, and temperature under real operating conditions. The calculated findings are comparable to previously reported data from the same source during the peak winter month. In general, the monocrystalline module had a high average module reliability, while the amorphous silicon module had a higher average output ratio. Furthermore, as the module temperature rises, the efficiency and performance ratio of the modules decreases. It was discovered that during the summer months, modules have a much higher temperature (about 20 ℃ higher) and have a lower efficiency and output ratio than during the peak months. From winter to summer, the average air temperature ranged from 18.1 ℃–38.6 ℃ [11].

In another work, Bashir and his team compared the efficiency of three photovoltaic modules, i.e., monocrystalline, polycrystalline, and single-junction amorphous silicon PV modules in Taxila, Pakistan. During the winter months, the experiment was carried out outside. For each module, the module efficiency, performance ratio and power output were determined. The effects of module temperature and solar irradiance on these parameters were also studied. Module temperature and solar irradiance had a significant influence on module parameters. When the irradiance was strong, monocrystalline and polycrystalline modules performed well; however, when the irradiance was low, performance dropped significantly. Due to its improved light absorption properties, amorphous solar modules have performed well in low irradiance conditions, resulting in a higher overall output ratio. Monocrystalline PV modules showed higher monthly average module performance and were found to be more efficient. With increasing irradiance and photovoltaic cell back surface temperature, module efficiency and performance ratio decreased. With the rise in module temperature from 22 ℃ to 33 ℃, the average module efficiency decreased by around 8.85%, 4.5%, and 26% for c-Si, p-Si, and a-Si modules, respectively. The total PR decrement for the c-Si, p-Si, and a-Si modules was 5.6%, 4.8%, and 25.8%, respectively [12].

Based on the literature review, it is concluded that no study has been carried out employing the back-surface cooling technique accompanied with forced convection. In this study, the authors present a novel approach utilizing a water-channel cooling technique along with forced convection. Two different arrangements of the water channel have been used, i.e., serpentine and multi-inlet-outlet arrangements. The experiments are carried out in the ambient conditions. The performance of the panels is compared with and without the application of back-channel water cooling technique and back-channel water channel cooling technique accompanied with forced convection.

2. Materials and methods

Experimental setup

The tests were carried out in natural conditions on the rooftop of the workshop building of COMSATS University Islamabad (Sahiwal Campus), Punjab, Pakistan (30.6506° N, 73.1158° E). There were no limitations of shadow from bushes or other homes in this area, so it was chosen. Three commercially available 50 W monocrystalline PV modules were used in the research study. The modules were positioned at an attitude of 45° from the roof. Sahiwal is placed in the northern hemisphere, so modules have been faced in the direction of the south [13,14].

$$\text{The angle of inclination (for winter)} = \text{Latitude} + 15° \quad (1)$$

$$\text{Angle of inclination (in winter) for Sahiwal} = 30.6506° + 15° = 45.6506° \quad (2)$$

The back surface cooling technique is the second studied cooling technique for the PV modules [15]. The serpentine-shaped and multi-inlet-outlet copper pipes were used behind the two PV modules, as depicted in **Figure 1**. The same experimentation was performed on two modules for multi-inlet-outlet following experimentation on serpentine-shaped arrangements of PV modules. The copper pipes were fixed tightly with the help of timber sticks for maximum touch. Thermal paste was also used to make contact between copper pipes for both techniques, as it was necessary for maximum conduction of heat. At the back of a panel, a serpentine-shaped copper pipe and 3 fans (12 V) were used to see the effects of the collaboration of two techniques; the same was utilized for the multi-inlet-outlet technique. Forced convection is preferred to avoid uncontrolled and irregular flow of air and leads to an efficiency increase of up to 14% [16,17].

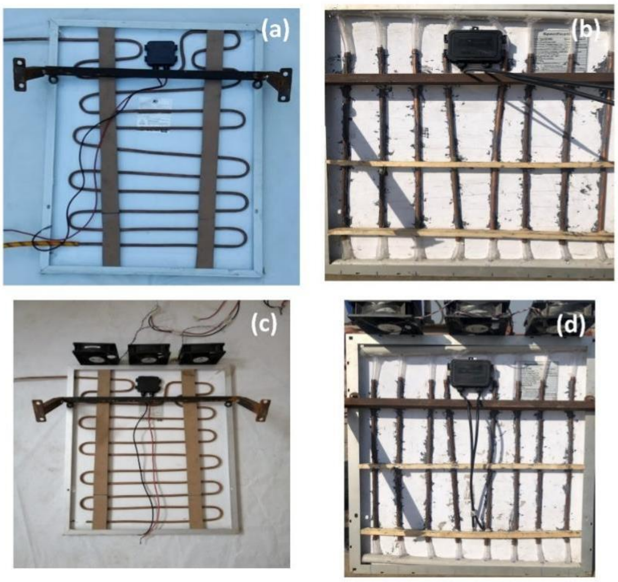

Figure 1. (a) Serpentine-shaped copper pipes on the back surface of PV module; **(b)** multi-inlet-outlet copper pipes, combined cooling techniques; **(c)** fans with serpentine-shaped copper pipes; and **(d)** fans with multi-inlet-outlet copper pipes.

The components and instruments used in the experimentation are sunlight as a source of energy, three photovoltaic modules of mono-crystalline type, panel stands, water drum, tap water as cooling medium, DC fans, DC battery, wooden sticks, PVC pipes, valves, nozzles and water channels of copper pipe (serpentine-shaped and multi-inlet-outlet).

Sunlight was used as a natural source of energy, and it is an abundantly available source of energy all over the world. Water is used for the free convection. Water flows from the back surface cooling channel by gravitational effect, so tap water is used as a cooling medium. For lower back-channel cooling of PV modules, serpentine-shaped and multi-inlet-outlet copper pipes with a 5/16'' (8 mm) outer diameter and a wall thickness of 0.417 mm were used. The experimental arrangement is shown in **Figure 2**.

Figure 2. Experimental setup for simple PV modules and modules with cooling techniques.

Three mono-crystalline PV modules of 50 W were installed on the rooftop. One module was without any cooling technique for the comparison of results, while a back surface cooling channel was placed on the second module. On the third module, the back surface cooling channel and DC fans for the forced convection were placed. The specifications of the PV module, thermocouple thermometer, PV module analyzer, and solar surveyor are provided in **Tables 1–4**.

Table 1. Technical specifications of the PV module.

Module Model	**BS-M50**
Maximum power voltage (Vmaxp)	17.8 V
Open circuit voltage (Voc)	21.64 V
Test conditions (STC)	1000 W/m^2, AM 1.5, 25 ℃
Maximum power (Pmax)	50 W
Maximum power current (Imaxp)	2.80 A
Short circuit current (Isc)	3.32 A
Tolerance	± 3%
Maximum fuse rating	8 A
Maximum system voltage	1000 VDC
Wind resistance	2400 Pa
Weight	3.8 kg
Dimension	635 × 541 × 30 mm
Application Class	A
Operating Temperature	−40 ℃–85 ℃

Table 2. Technical specifications of thermocouple thermometer TYPE-K DM6801A+.

General Specifications		
Display	1/2 digit large LCD, Max. display 1999	
Sampling rate	2.5 times/s	
Over range display	"1" or "−1"	
Working environment	−10 °C–50 °C, relative humidity < 80%	
Store environment	−20 °C–60 °C, relative humidity < 80%	
Battery	9 V battery	
Size	130 mm (length) × 95 mm (width) × 28 mm (height)	
Weight	Approx. 240 g (including battery)	
Accessories	Manual, Case, TP01 probe, 9V battery	
Technical Parameters		
Resolution	**Range**	**Accuracy**
0.1 °C	−50 °C to 199.9 °C	−50 °C to 199.9 °C ± (0.3% + 1 °C)
0.1 °F	−50 °F to 199.9 °F	−50 °F to 199.9 °F ± (0.3% + 1 °F)
1 °C	−50 °C to 1300 °C	−50 °C to 1000 °C ± (0.3% + 2 °C) 1000 °C to 1300 °C ± (0.6% + 2 °C)
1 °F	−50 °F to 1999 °F	−50 °F to 1000 °F ± (0.3% + 2 °F) 1000 °F to 1999 °F ± (0.6% + 2 °F)

Table 3. Technical specifications of PROVA 210 A PV module analyzer.

General Specifications		
Weight:	1160 g/40.9 oz (batteries are included)	
Dimensions:	257 (Length) × 155 (Width) × 57 (Height) mm, 10.1 inch (Length) × 6.1 inch (Width) × 2.2 inch (Height)	
AC-Adaptor:	AC 100 V to 240 V Input, DC 15 V/1 to 3 A Output	
Environment Storage:	−20 °C to 60 °C, 75% RH	
Environment Operation:	5 °C to 50 °C, 85% RH	
Data logging memory size	100 number of records	
Accessories:	User manual, AC Adaptor, USB Optical Cable, 3400 mAh Lithium Rechargeable Battery, CD Software, Manual Software, Carrying Bag, Kelvin Clips, 4 wire connectors.	
Measurement DC Current		
Range	**Resolution**	**Accuracy**
10 to 12 A	10 mA	±1% ± (1% of Ishort ± 0.09 A)
0.01 to 10 A	1 mA	±1% ± (1% of Ishort ± 9 mA)
Simulation DC Current		
Range	**Resolution**	**Accuracy**
10 to 12 A	10 mA	±1% ± 0.09 A
0.01 to 10 A	1 mA	±1% ± 9 mA

Table 4. Technical and general specifications of Solar Survey 200R.

General Specification	
Memory Onboard	Datasets 5000 (Survey 200R only)
Dimensions	14.8 × 8 × 3.3 cm/5.8 × 3.2 × 1.3”
Connectivity	PC USB download (Free data logger-online available) Connections wireless to PV150/PV200/PV210/Solar Utility-Pro (range c. 30 m/100 ft.) Frequency 433 MHz (Rest of World)/915 MHz (US)
Auto Power Down	Unless in transmit mode (After 2 min)
Sample Rate	1 to 60 min (user definable)
Weight	0.25 kg/0.6 lb
Technical Specifications	
Irradiance	
Resolution	1 W/m^2 or 1 Btu/hr-ft^2
Measurement	100 to 1250 W/m^2 or 30 to 400 Btu/hr-ft^2
Display	100 to 1500 W/m^2 or 30 to 500 Btu/hr-ft^2
Temperature	
Resolution	1°
Measurement	−30 ℃ up to +125 ℃
Display	−30 ℃ up to +125 ℃
Compass Bearing	
Resolution	1°
Measurement	0° up to 360°
Display	0° up to 360°
Inclinometer	
Resolution	1°
Measurement	0° up to 90°
Display	0° up to 90°

3. Results and discussion

As far as the results of the research study are concerned, two readings at 12 PM and 1 PM are taken into account, keeping in view the fact that maximum irradiance is observed for these timings. It has been reported that almost 70% of the power falling upon the PV module is transformed into heat; however, the application of the hybrid cooling technique led to the increase in the power output [18]. The power output can be calculated from the product of output voltage and current. The maximum power output of the PV module increased as shown in **Figures 3** and **4,** as well as efficiency also increased as shown in **Figures 5** and **6** after the application of the cooling technique. At 12 PM the maximum power is 42.78 W (**Figure 3**) on day 2, and the maximum efficiency is 14.84% (**Figure 5**) on day 6. Similarly, at 1 PM the maximum power is 39.1 W (**Figure 4**) on day 2, and maximum efficiency is 15.76% (**Figure 6**) on day 2. The better performances are attributed to the fact that effective heat transfer takes place between the cooling media and the PV module, improving the overall performance.

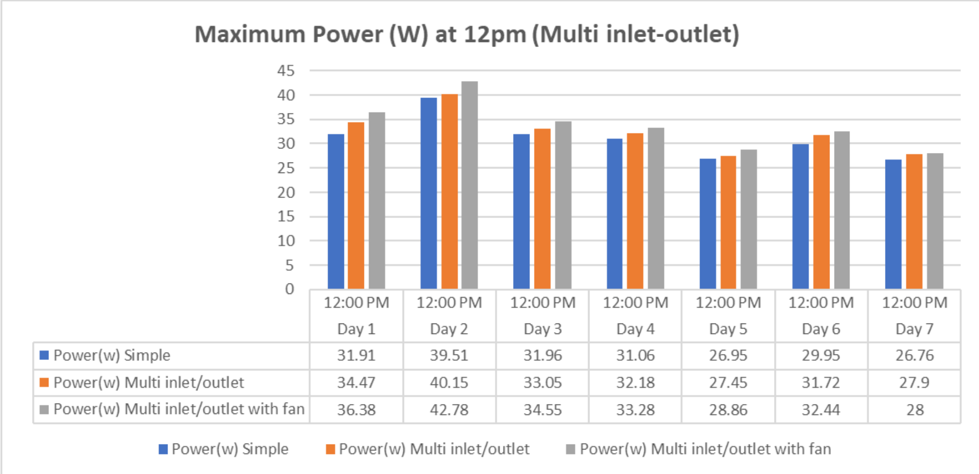

Figure 3. Maximum power comparison for multi-inlet-outlet at 12 PM.

Maximum power is 39.1 W at 1 PM on day 2 as shown in **Figure 4**.

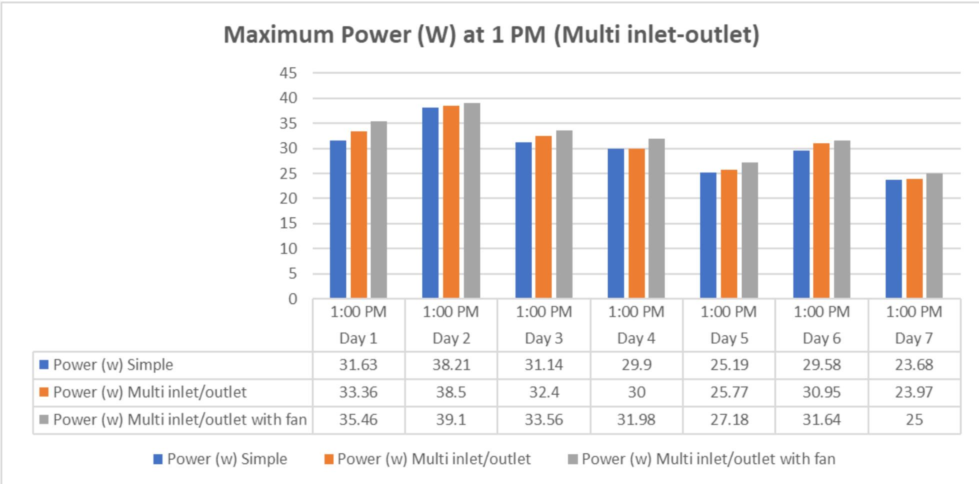

Figure 4. Maximum power comparison for multi-inlet-outlet at 1 PM.

Maximum efficiency is 14.84% at 12 PM on day 6 as shown in **Figure 5**.

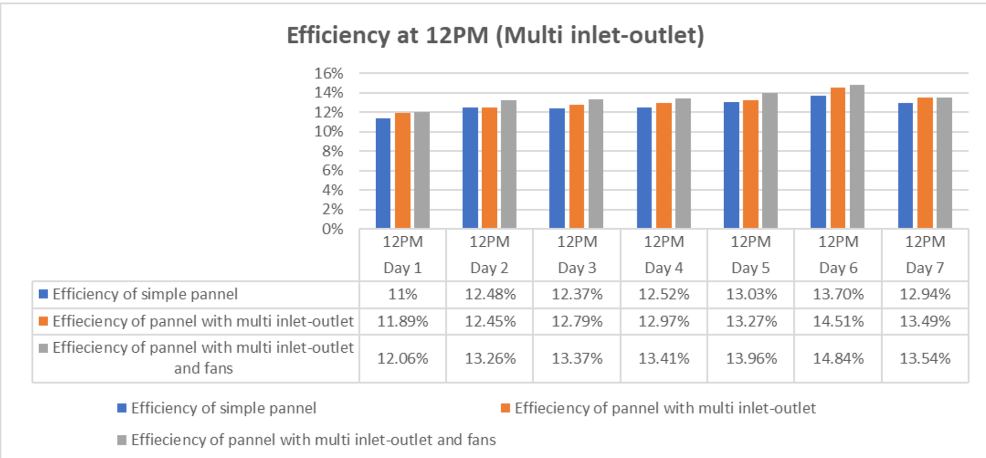

Figure 5. Efficiency comparison for multi-inlet-outlet at 12 PM.

Maximum efficiency is 15.76% at 1 PM on day 2 as shown in **Figure 6**.

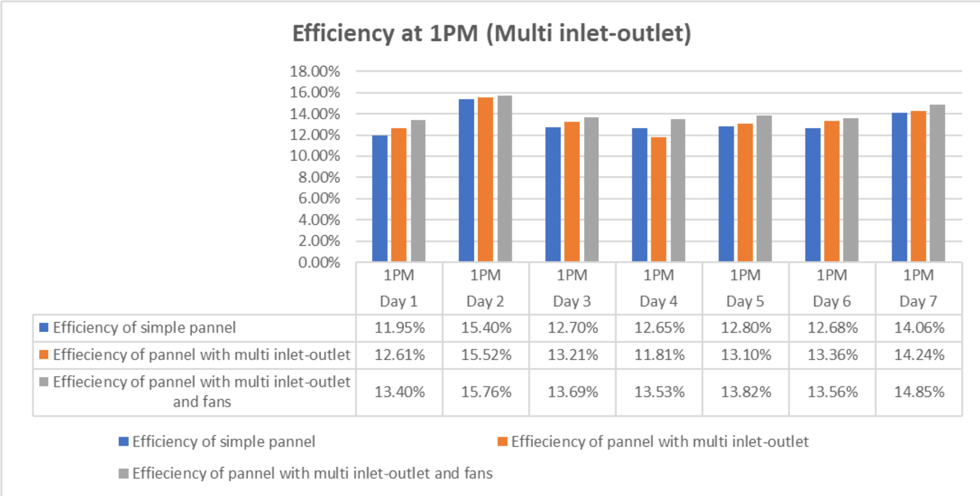

Figure 6. Efficiency comparison for multi-inlet-outlet at 1 PM.

The variation in panel temperature and irradiance is depicted in **Figures 7–11**. It can be observed that there was interference of the clouds during the study that led to the variation of irradiance and consequently to the change in panel temperatures. It can be clearly observed that the application of the cooling technique significantly decreased the panel temperatures. The maximum temperature is 44.9 °C at 12 PM on day 4 as depicted in **Figure 7**.

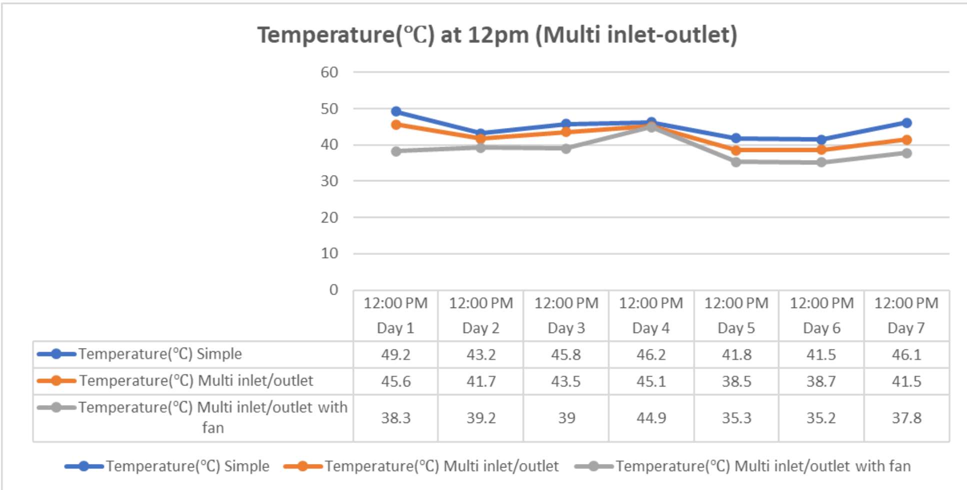

Figure 7. Panel temperature comparison for multi-inlet-outlet at 12 PM.

The maximum temperature is 43.3 °C at 1 PM on day 1 as exhibited in **Figure 8**.

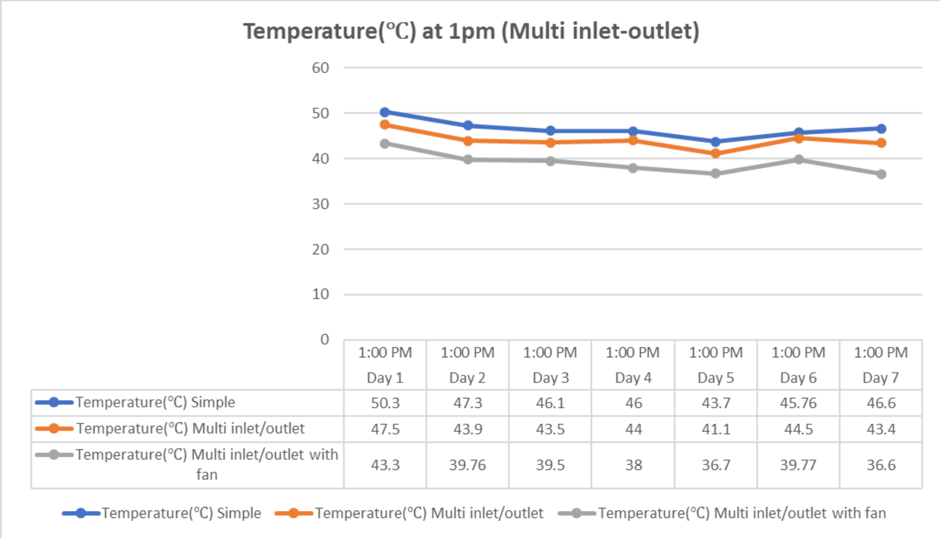

Figure 8. Panel temperature comparison for multi-inlet-outlet at 1 PM.

Maximum irradiance is 1092 W/m^2 at 12 PM on day 2 as demonstrated in **Figure 9**.

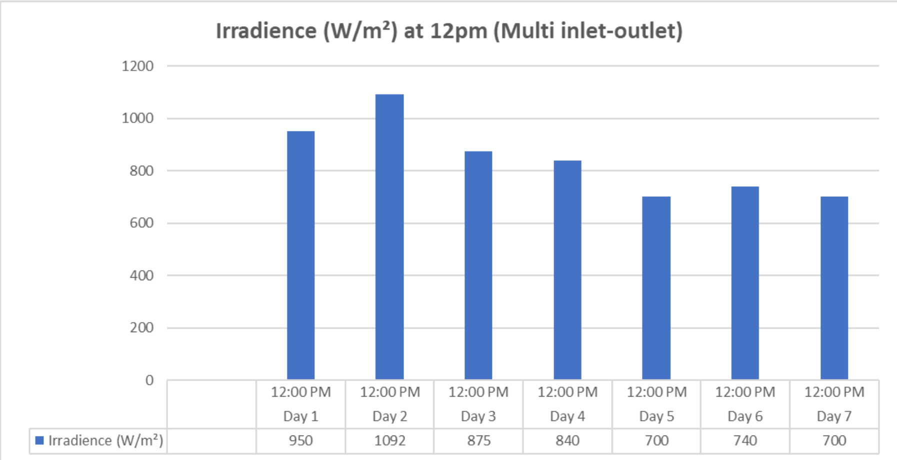

Figure 9. Irradiance comparison for multi-inlet-outlet at 12 PM.

Maximum irradiance is 896 W/m^2 at 1 PM on day 1 as shown in **Figure 10**.

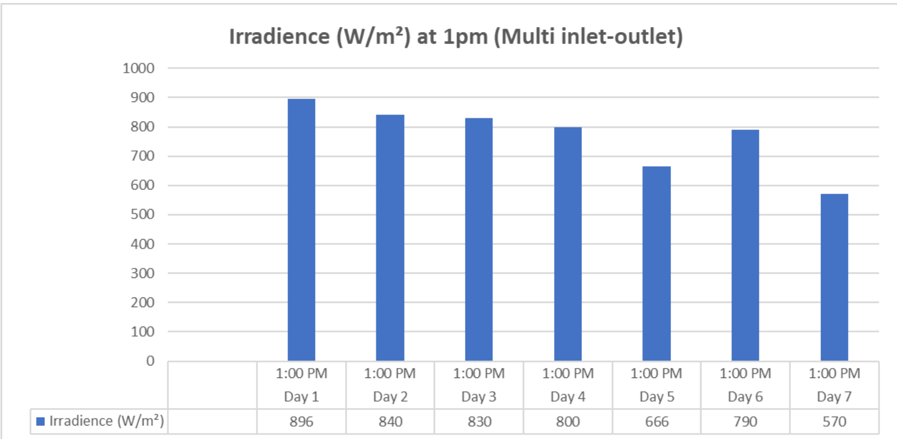

Figure 10. Irradiance comparison for multi-inlet-outlet at 1 PM.

The variation in the temperature of the panel also causes the change in open circuit voltage as depicted in **Figures 11** and **12**. This can be ascribed to the dependence of the properties of semiconductor on the temperature. The rise in temperature leads to the higher saturation current which ultimately affects the open circuit voltage by reducing it [19]. Maximum open circuit voltage is 20.89 V at 12 PM on day 2 as shown in **Figure 11**.

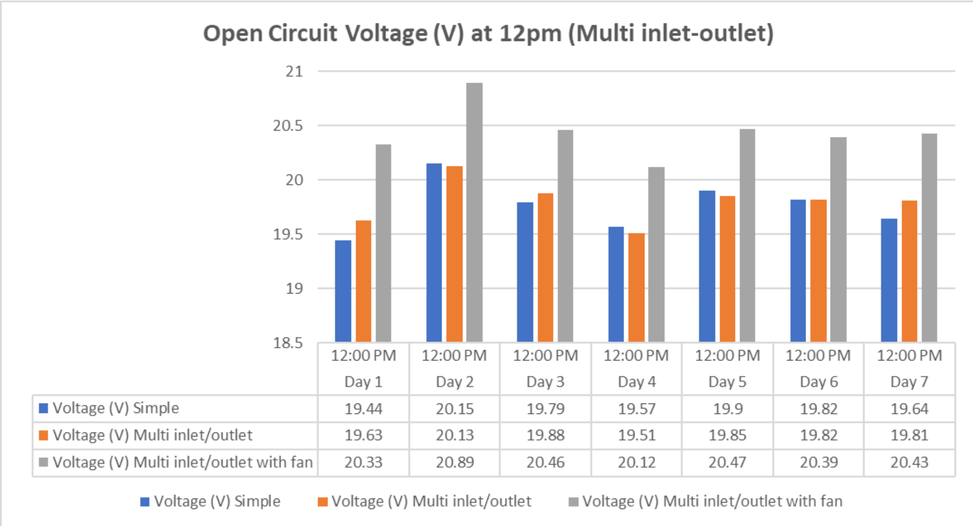

Figure 11. Open circuit voltage comparison for multi-inlet-outlet at 12 PM.

Maximum open circuit voltage is 21.1 V at 1 PM on day 2 as observed in **Figure 12**.

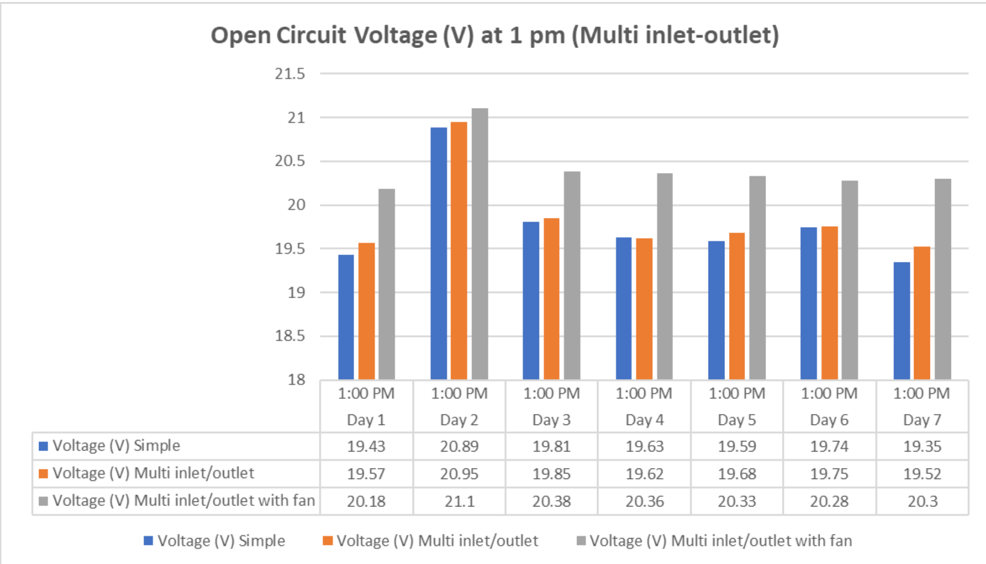

Figure 12. Open circuit voltage comparison for multi-inlet-outlet at 1 PM.

The same set of parameters is investigated for serpentine arrangement as discussed above. The maximum power output of the PV module increased as shown in **Figures 13** and **14,** and efficiency also increased, as shown in **Figures 15** and **16,** owing to the application of the cooling technique. At 12 PM, the maximum power is 40.09 W on day 3, and maximum efficiency is 14.23% on day 2. Similarly, at 1 PM the maximum power is 35.38 W on day 4 and maximum efficiency is 14.09% on day 1. Maximum power at 12 PM is 40.09 W on day 3, as shown in **Figure 13**.

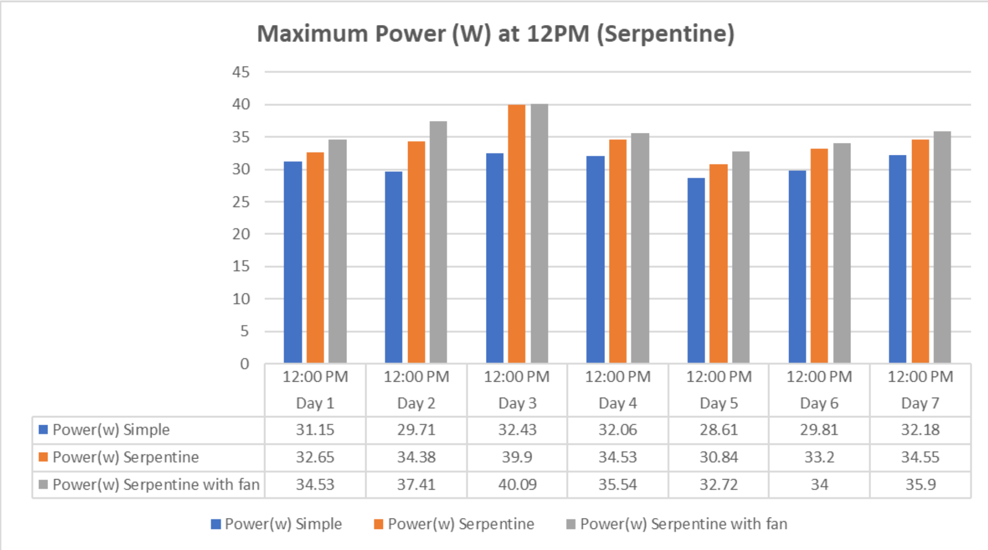

	12:00 PM Day 1	12:00 PM Day 2	12:00 PM Day 3	12:00 PM Day 4	12:00 PM Day 5	12:00 PM Day 6	12:00 PM Day 7
Power(w) Simple	31.15	29.71	32.43	32.06	28.61	29.81	32.18
Power(w) Serpentine	32.65	34.38	39.9	34.53	30.84	33.2	34.55
Power(w) Serpentine with fan	34.53	37.41	40.09	35.54	32.72	34	35.9

Figure 13. Maximum power comparison for serpentine at 12 PM.

Maximum power is 35.38 W on day 4 at 1 PM as shown in **Figure 14**.

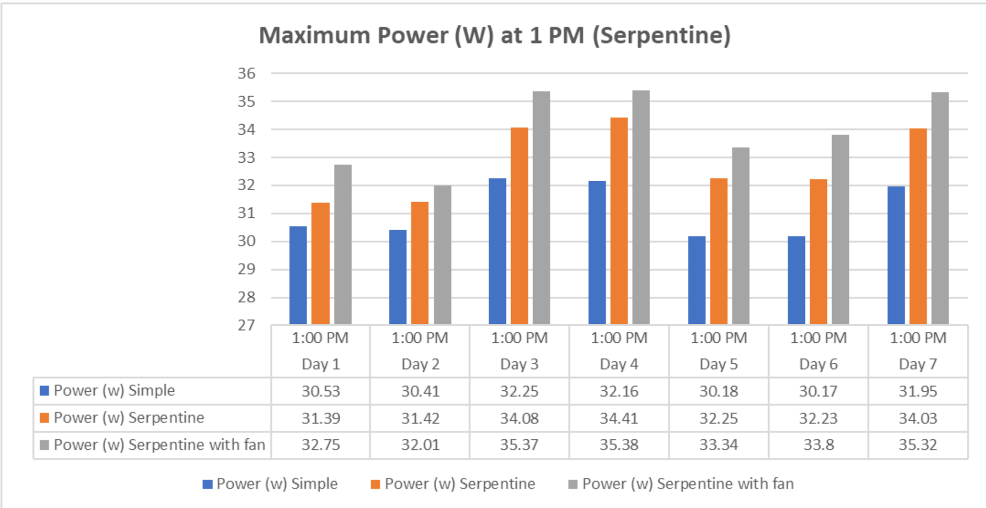

	1:00 PM Day 1	1:00 PM Day 2	1:00 PM Day 3	1:00 PM Day 4	1:00 PM Day 5	1:00 PM Day 6	1:00 PM Day 7
Power (w) Simple	30.53	30.41	32.25	32.16	30.18	30.17	31.95
Power (w) Serpentine	31.39	31.42	34.08	34.41	32.25	32.23	34.03
Power (w) Serpentine with fan	32.75	32.01	35.37	35.38	33.34	33.8	35.32

Figure 14. Maximum power comparison for serpentine at 1 PM.

Maximum efficiency is 14.23% at 12 PM on day 2 as shown in **Figure 15**.

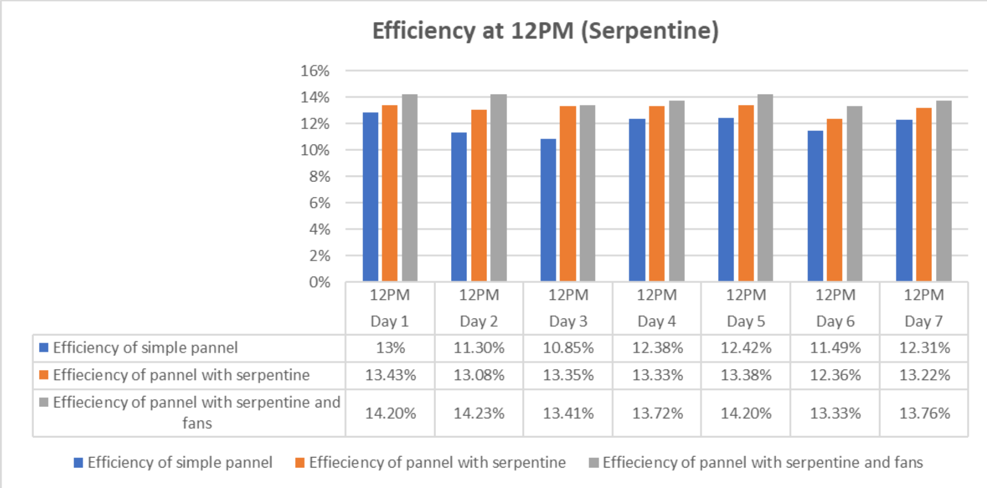

Figure 15. Efficiency comparison for serpentine at 12 PM.

Maximum efficiency is 14.09% at 1 PM on day 1 as shown in **Figure 16**.

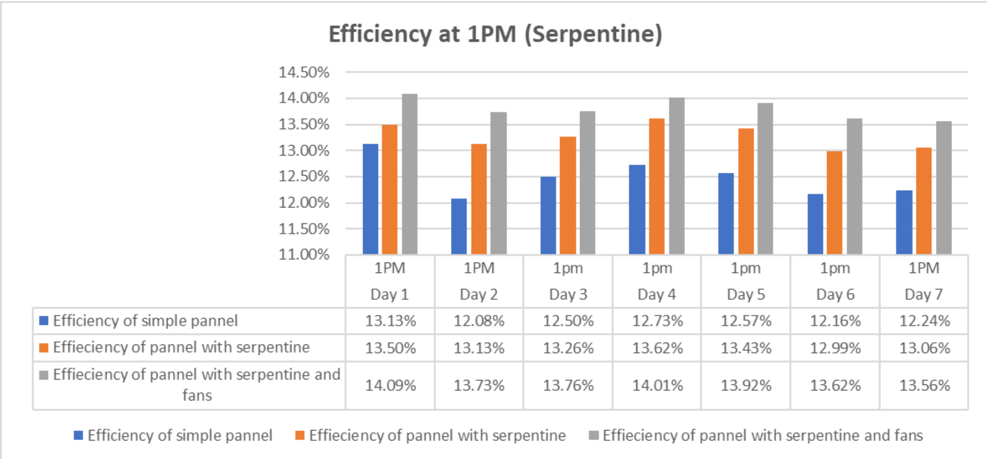

Figure 16. Efficiency comparison for serpentine at 1 PM.

The minimum temperature is 28.8 °C at 12 PM on day 3 as demonstrated in **Figure 17**.

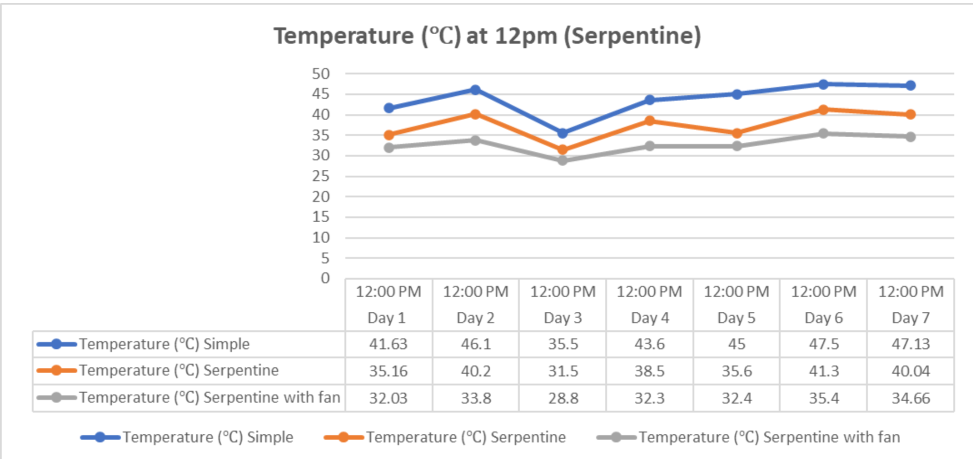

Figure 17. Panel temperature comparison for serpentine at 12 PM.

The minimum temperature is 32.3 °C at 1 PM on day 1 as depicted in **Figure 18**.

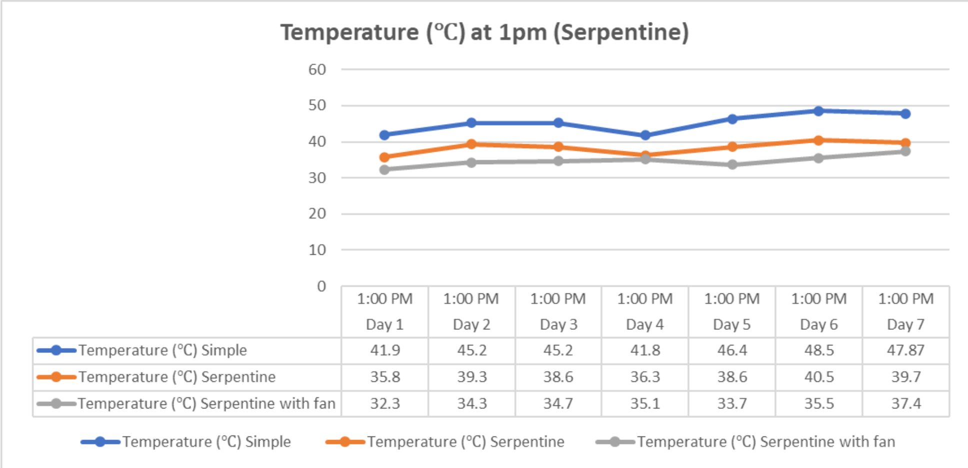

Figure 18. Panel temperature comparison for serpentine at 1 PM.

Maximum irradiance is 1012 W/m^2 at 12 PM on day 3 as observed in **Figure 19**.

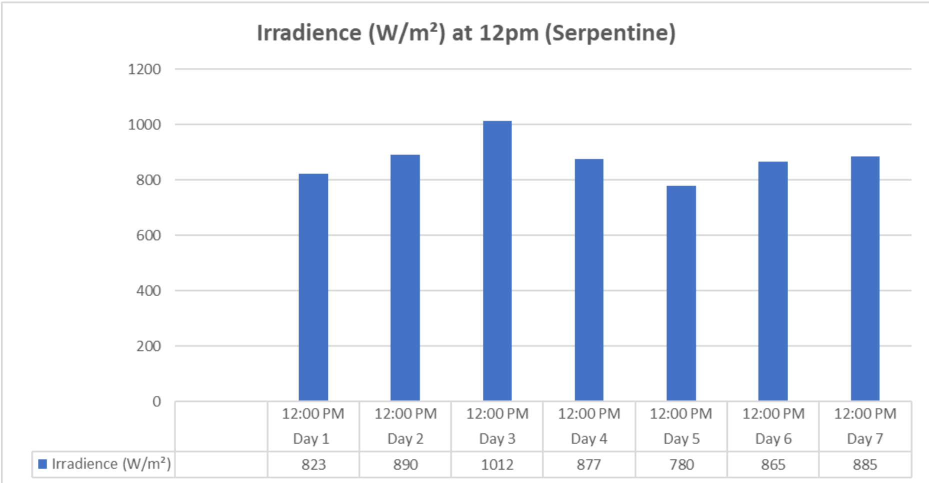

Figure 19. Irradiance comparison for serpentine at 12 PM.

Maximum irradiance is 882 W/m^2 at 1 PM on day 7 as shown in **Figure 20**.

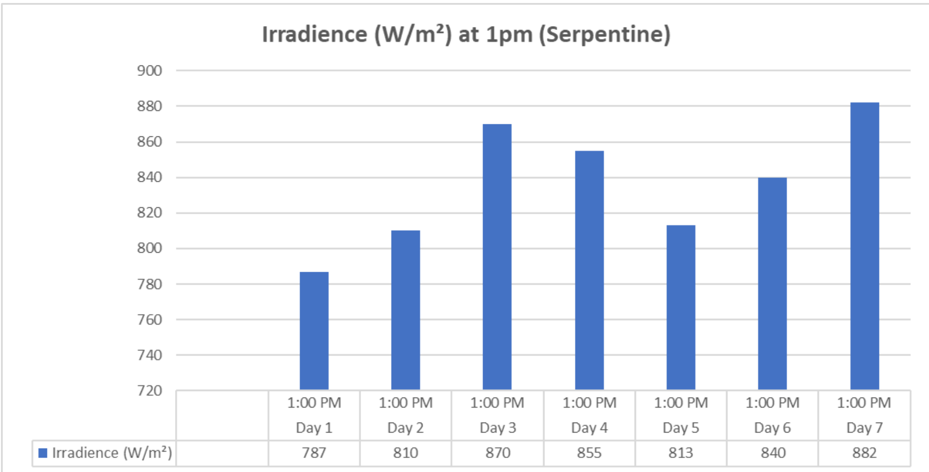

Figure 20. Irradiance comparison for serpentine at 1 PM.

Maximum open circuit voltage is 21.7 V at 12 PM on day 6 as shown in **Figure 21**.

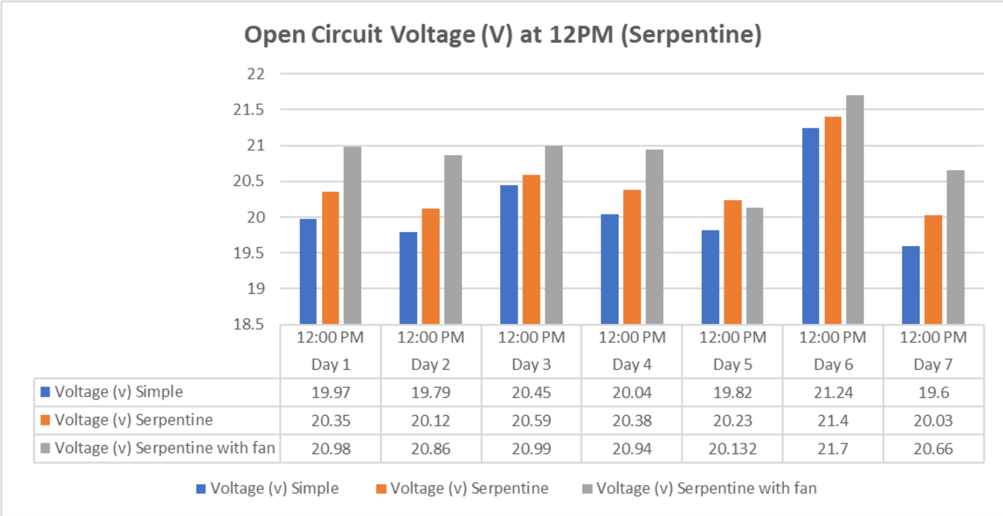

Figure 21. Open circuit voltage comparison for serpentine at 12 PM.

Maximum open circuit voltage is 20.92 V at 1 PM on day 1 as depicted in **Figure 22**.

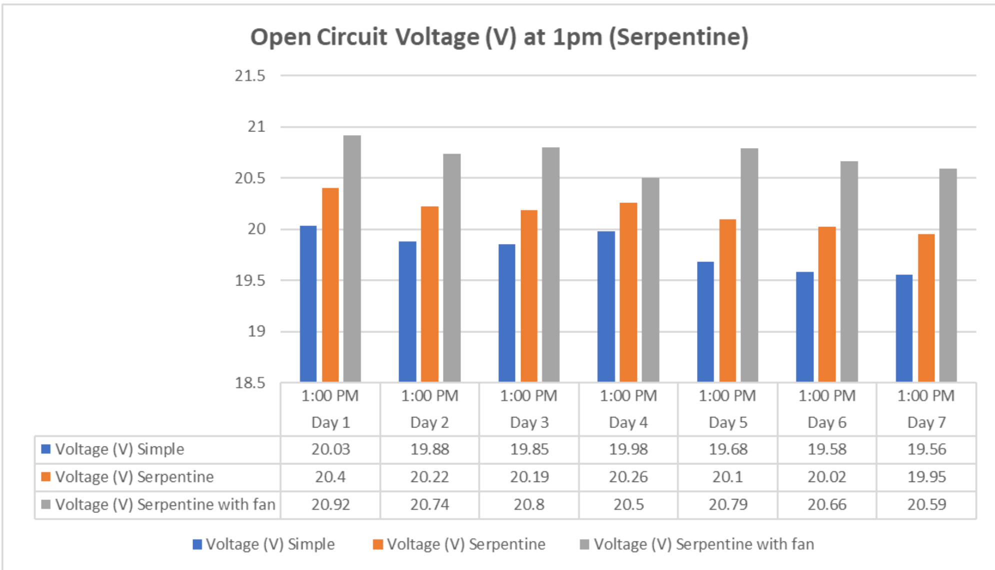

Figure 22. Open circuit voltage comparison for serpentine at 1 PM.

The nature of the solar irradiance is stochastic and undergoes changes. In this backdrop, it is difficult to perform multiple measurements for different arrangements. When measurements are performed, uncertainty affects the experimental results. The independent parameters for the study include current, solar irradiance, voltage, and panel temperature. Different instruments are employed to measure these parameters. It can be noticed that the uncertainty values are quite close for each arrangement. This is ascribed to the measurements taken by the same instrument. The uncertainty analysis is provided in **Table 5** for the instruments used in this experimental study.

Table 5. Overall average fractional uncertainty.

Parameter	Unit	Serpentine	Multi Inlet	Overall Average Fractional Uncertainty
Solar Irradiance	W/m^2	0.001	0.001	0.001
Panel Temperature	C	0.003	0.003	0.003
Improvement in short circuit current	mA	0.055	0.029	0.042
Improvement in open circuit voltage	V	0.022	0.029	0.025
Improvement in fill factor	%	0.411	0.420	0.415
Improvement in power	%W	0.224	0.228	0.226

4. Conclusion

The effect of temperature increase on the performance of the monocrystalline photovoltaic module was investigated. Three mono-crystalline PV modules were placed on the rooftop workshop, mechanical department, COMSATS Sahiwal, Punjab, Pakistan, for 14 consecutive days. Two different techniques, water-channel cooling and water-channel cooling along with forced convection, were employed.

- The results demonstrate that water-channel cooling along with the forced convection technique exhibited higher maximum output power and efficiency as compared to simple and water-channel cooling techniques.
- For serpentine shape, the maximum power output of the simple module is 29.71 W, 34.38 W for the water-channel cooling technique, and 37.41 W for the water-channel cooling technique with forced convection, respectively, is observed on day 2. This is ascribed to the effectiveness of the combined cooling techniques.
- For the multi-inlet-outlet shape, the maximum power output of the simple module is 39.51 W, 40.15 W for the water-channel cooling technique, and 42.78 W is noted for the water-channel cooling technique with forced convection.
- After applying cooling techniques, panel temperature decreases up to 15 ℃, open circuit voltage increases up to 2 V, and efficiency increases up to 4%–5%. By comparison, it is concluded that the multi-inlet-outlet water channel cooling technique is better than the serpentine-shaped water channel cooling technique because maximum power is obtained by that technique. In the future, the incorporation of nanoparticles in the cooling media can be investigated.

Author contributions: Conceptualization, MTA; methodology, TR; software, MAA; validation, NH; writing—review and editing, MK; formal analysis, MSN; investigation, MRA; data curation, ZA; writing—original draft preparation, EUH; writing—review and editing, SKHS; supervision, MTA; project administration, MTA. All authors have read and agreed to the published version of the manuscript.

Conflict of interest: The authors declare no conflict of interest.

References

1. El-Sebaey MS, Ellman A, Hegazy A, et al. Experimental study with thermal and economical analysis for some modifications on cylindrical sector and double slope, single basin solar still. Case Studies in Thermal Engineering. 2023; 49. doi: 10.1016/j.csite.2023.103310

2. El-Sebaey MS, Ellman A, Hegazy A, et al. Experimental analysis and CFD modeling for conventional basin-type solar still. Energies. 2020; 13(21). doi: 10.3390/en13215734
3. Sathyamurthy R, Ali HM, Said Z, et al. Enhancing solar still thermal performance: The role of surface coating and thermal energy storage in repurposed soda cans. Journal of Energy Storage. 2024; 77. doi: 10.1016/j.est.2023.109807
4. Nag SK, Gangopadhyay TK, Paserba J. Solar Photovoltaics: A Brief History of Technologies [History]. IEEE Power and Energy Magazine. 2022; 20(3): 77–85. doi: 10.1109/MPE.2022.3150814
5. Wilson GM, Al-Jassim M, Metzger WK, et al. The 2020 photovoltaic technologies roadmap. Journal of Physics D: Applied Physics. 2020; 53: 493001. doi: 10.1088/1361-6463/ab9c6a
6. Dambhare MV, Butey B, Moharil SV. Solar photovoltaic technology: A review of different types of solar cells and its future trends. Journal of Physics: Conference Series. 2021; 1913: 12053. doi: 10.1088/1742-6596/1913/1/012053
7. Al-Ezzi AS, Ansari MNM. Photovoltaic Solar Cells: A Review. Applied System Innovation. 2022; 5. doi: 10.3390/asi5040067
8. Enaganti PK, Dwivedi PK, Srivastava AK, et al. Study of solar irradiance and performance analysis of submerged monocrystalline and polycrystalline solar cells. Progress in Photovoltaics: Research and Applications. 2020; 28(7): 725–735. doi: 10.1002/pip.3264
9. Jiang L, Cui S, Sun P, et al. Comparison of Monocrystalline and Polycrystalline Solar Modules. In: Proceedings of the 2020 IEEE 5th Information Technology and Mechatronics Engineering Conference (ITOEC); 12–14 June 2020; Chongqing, China. pp. 341–344.
10. Siecker J, Kusakana K, Numbi BP. A review of solar photovoltaic systems cooling technologies. Renewable and Sustainable Energy Reviews. 2017; 79: 192–203. doi: 10.1016/j.rser.2017.05.053
11. Bashir MA, Ali HM, Amber KP, et al. Performance investigation of photovoltaic modules by back surface water cooling. Thermal Science. 2018; 22(6): 2401–2411. doi: 10.2298/TSCI160215290B
12. Bashir MA, Ali HM, Khalil S, et al. Comparison of Performance Measurements of Photovoltaic Modules during Winter Months in Taxila, Pakistan. International Journal of Photoenergy. 2014; 2014: 898414. doi: 10.1155/2014/898414
13. Adar M, Najih Y, Gouskir M, et al. Three PV plants performance analysis using the principal component analysis method. Energy. 2020; 207: 118315. doi: 10.1016/j.energy.2020.118315
14. Sainthiya H, Beniwal NS. Comparative analysis of electrical performance parameters under combined water cooling technique of photovoltaic module: An experimental investigation. Energy Sources, Part A: Recovery, Utilization, and Environmental Effects. 2020; 42(15): 1902–1913. doi: 10.1080/15567036.2019.1604894
15. Nabil T, Mansour TM. Augmenting the performance of photovoltaic panel by decreasing its temperature using various cooling techniques. Results in Engineering. 2022; 15: 100564. doi: 10.1016/j.rineng.2022.100564
16. Shukla A, Kant K, Sharma A, et al. Cooling methodologies of photovoltaic module for enhancing electrical efficiency: A review. Solar Energy Materials and Solar Cells. 2017; 160: 275–286. doi: 10.1016/j.solmat.2016.10.047
17. Almuwailhi A, Zeitoun O. Investigating the cooling of solar photovoltaic modules under the conditions of Riyadh. Journal of King Saud University-Engineering Sciences. 2023; 35(2): 123–136. doi: 10.1016/j.jksues.2021.03.007
18. Eid AF, Lee S, Hong SG, et al. Hybrid cooling techniques to improve the performance of solar photovoltaic modules. Solar Energy. 2022; 245: 254–264. doi: 10.1016/j.solener.2022.09.026
19. Shaker LM, Al-Amiery AA, Hanoon MM, et al. Examining the influence of thermal effects on solar cells: A comprehensive review. Sustainable Energy Research. 2024; 11. doi: 10.1186/s40807-024-00100-8

Thermal Science and Engineering 2025, 8(1), 10475.
https://doi.org/10.24294/tse10475

Article

Numerical approach determining the optimal distance separating two heat sources heated by joule effect in a square cavity

Mohammed Salah Belalem[1,*], Abdelkader Ferhah[1], Toufik Chergui[2]

[1] Energetics in Arid Zones Laboratory ENERGARID Laboratory, Bechar University, Bechar 08-000, Algeria
[2] Renewable Energy Applied Research Unit, URAER, CDER, Ghardaïa 47-133, Algeria
*** Corresponding author:** Mohammed Salah Belalem, belalemmedsalah@yahoo.com

CITATION

Belalem MS, Ferhah A, Chergui T. Numerical approach determining the optimal distance separating two heat sources heated by joule effect in a square cavity. Thermal Science and Engineering. 2025; 8(1): 10475. https://doi.org/10.24294/tse10475

ARTICLE INFO

Received: 22 November 2025
Accepted: 17 January 2025
Available online: 17 February 2025

Abstract: This study presents a comprehensive two-dimensional numerical analysis of natural laminar convection within a square cavity containing two circular heat sources, which simulate electric cables generating heat due to Joule heating. This scenario is particularly relevant in aeronautics, where excessive heating of electrical installations can lead to significant material and human safety risks. The primary objective of this research is to identify the optimal spacing between the two heat sources to mitigate the risk of overheating and ensure the safe operation of the electrical installation. To achieve this, various configurations were analyzed by adjusting the distance between the heat sources while also varying the Rayleigh number across a range from 10^3 to 10^6. The governing equations for the fluid flow and heat transfer were solved using a FORTRAN-based numerical code employing the finite volume method. The results indicate that the heat transfer characteristics within the cavity are significantly influenced by both the distance between the heat sources and the Rayleigh number. The analysis revealed that the average Nusselt number (Nu_{avg}) peaked at a value of 14.69 when the distance between the heat sources was set at 0.7 units and the Rayleigh number was at 10^6. This finding suggests that maintaining this specific spacing between the electrical cables can optimize heat dissipation and enhance the safety of the installation. In conclusion, the study recommends adopting a spacing of 0.7 units between the electrical cables to ensure optimal thermal performance and minimize the risk of overheating, thereby safeguarding both the materials and personnel involved in aeronautical operations.

Keywords: natural convection; heat source; optimal distance; finite volume; joule effect; electrical installation

1. Introduction

The importance of this work lies in the vast use of relatively simple form obstacles, square, for example in industrial applications. Many scientific works have been published to analyze the phenomenon of cooling electronic and/or electrical components using convection in its three forms. Among these published works, we quote:

Ortega and Moffat [1] performed natural convection experiments on cooling blocks simulating electronic components. The blocks are mounted on one of two parallel and vertical walls (80 blocks arranged in an arrangement of 8 columns and 10 rows).

Patnana et al. [2] numerically simulated the incompressible flows of non-Newtonian fluids around a circular cylinder in an unsteady regime, the work was established with the commercial code (Fluent), and the Reynolds number varies between $40 \leq Re \leq 140$, the power index $0.4 \leq n \leq 1.8$, the Prandtl number $1 \leq Pr \leq$

100. The results show that thinning fluids enhance the increase in heat transfer against obstacle-thickening fluids. Also, the increase in the fluid power index generates many more vortices, on the other hand, the size of the vortices decreases with the increase in the Reynolds number.

Chandra and Chhabra [3] carried out a numerical simulation study of the incompressible flow around a semi-circular and unconfined cylinder. The study touches on the hydrodynamic and thermal spirit. They determined values called Reynolds numbers, critical for the appearance of vortices behind the obstacle. In conclusion, this study suggests the evolution of the drag coefficient with respect to the variation of Reynolds numbers.

Kumar and Dhiman [4] conducted a numerical study for Reynolds numbers $1 \leq \mathrm{Re} \leq 100$, Richardson $0 \leq \mathrm{Ri} \leq 1$, and blocking rates $10\% \leq \beta \leq 50\%$, the mixed convection of a heated cylinder square arranged in a vertical channel. Air was taken as the driving fluid. The authors observed a transition from a stable flow regime to a periodic flow regime at different Richardson numbers (Ri) and Reynolds numbers (Re), (for a Ri = 0, at Re = 35, 65, 74 and 62), (Ri = −0.5, at Re = 12, 39, 48 and 54), and (Ri = −1, at Re = 9, 30, 39 and 50) for a blocking ratio β = 10%, 25%, 30% and 50%, respectively. The onset of the flow separation is also determined. Finally, the authors determined correlations for the Strouhal number, for the drag coefficient, and for the heat transfer coefficient. Laidoudi and Bouzit [5] conducted a numerical study using the commercial code ANSYS CFX to examine the effects of thermal buoyancy on the thermohydrodynamic characteristics of an incompressible Poiseuille flow around symmetrically confined and asymmetrically immersed cylinders. Numerical results were presented and discussed for the following condition ranges: $10 \leq \mathrm{Re} \leq 40$, Richardson number $0 \leq \mathrm{Ri} \leq 4$, and the eccentricity factor $0 \leq \varepsilon \leq 0.7$ for a Prandtl number Pr = 1 and a blocking rate B = 20%.

Amieur and Amieur [6] investigate the complex interactions between fluid flow and thermal dynamics when a laminar flow encounters a fixed obstacle. Using the finite element method (FEM), the research focuses on how various geometric parameters of the obstacle, specifically its height and shape (rectangular, triangular, or half-cylindrical) affect the thermo-hydrodynamic behavior of the flow. The results indicate that the flow structure is significantly influenced by the size and shape of the turbulator. Specifically, the presence of vortex structures both upstream and downstream of the turbulator can be attributed to two main factors: the presence of a heat source and the pressure drops caused by the obstruction of the flow. These pressure drops are primarily determined by the geometric parameters of the turbulator, which affect how the fluid interacts with the obstacles. This interaction leads to complex flow patterns that can enhance mixing and heat transfer in various applications.

Chiocca et al. [7] used the finite element method to evaluate the ability of different thermal methods used to simulate a gas metal arc welding process pass to reproduce the temperature distribution around the weld, which was low; the results obtained are compared to experimental measurements. The study showed that in the vicinity of the weld bead, very similar thermal behaviors can be obtained with each of the methods analyzed. A very good agreement was found when comparing the experimental measurements with the numerical simulations.

To estimate heat transfer in low-pressure cavities, Alkhalidi et al. [8] used the finite volume method to solve the governing equations as well as the temperature jump and slip flow boundary conditions for different cavity aspect ratios (H/L) and Rayleigh numbers for macro and microfluids. The results show that the heat transfer ratios become significant when the Rayleigh number is high and when the aspect ratio is less than 5.

Lan and Jiao [9] numerically simulated the quasi-critical natural convection of water in a cylindrical hydrothermal reactor. The results show that natural convection is dominated by a large high-speed vortex when the heat flux ratio is less than 1, and it is dominated by two independent weak vortices when the heat flux ratio is greater than 1. When the temperature approaches the pseudocritical. At this point, the flow structure remains qualitatively unchanged, but wall heat transfer is enhanced and fluid motion is generally weakened. The study, design, and development of algorithmic solutions for the detection of thermal peaks in the case of multiple heat sources (number of heat sources greater than "one") have been carried out.

Fathi [10] used the methodology of the GDSCAN algorithm (which is a thermal scanning algorithm based on GDS (Gradient Detection Sensor) for multiple detection of heat sources in integrated circuits). The GDSCAN algorithm provided highly accurate temperature estimates with an error margin of no more than 1.5% and an optimal sensor network architecture including minimal thermal sensors.

Faraji et al. [11] considered the natural convection caused by melting in an inclined rectangular enclosure filled with a nano-enhanced phase change material, analyzing the effect of the insertion of nanoparticles by quantifying their contribution to the transfer of global heat. The case is heated from below using a protruding heat source (microprocessor) generating heat at a constant and uniform volumetric flow rate and mounted on a substrate (motherboard). All walls are considered adiabatic. The results obtained show that the insertion of nanoparticles has a significant quantitative effect on the overall heat transfer. They also show that the insertion of metal nanoparticles of different concentrations affects the thermal behavior of the heat sink, which contributes to the efficient cooling of the heat source.

In an analysis, Hussain et al. [12] explored the stagnation point of the Jeffery liquid flow on an expandable cylinder. The Cattaneo-Christov model with double stratification, heat source and thermal relaxation was used to study heat and mass transfer. The results of the study show that higher values of the ratio parameter reduce the magnitude of the drag coefficient, while an opposite trend is noted for a higher Deborah number in terms of delay time and curvature of the drag parameter.

Vinodkumar Reddy et al. [13] carried out an exploration study of the convective flow of the MHD stagnation point of Casson nanofluid on a stretching sheet in a porous medium with higher order chemical reactions and multiple slips. Thermal transmission was examined in the presence of radiation, Joule heating, viscous dissipation and heat source. The results show that increasing the values of Joule radiation and heating parameters, as well as the Eckert number, leads to an increase in temperature.

Benouis Fatima Zohra [14] Improving the cooling of electronic components in critical environments was considered through detailed simulations. The results provided that the introduction of fins into the cooling system allows a significant improvement in heat transfer, thus contributing to better dissipation of heat generated by electronic components. Additionally, the analyses revealed that a few fin configurations, such as flat plate fins and pin fins, offer distinct advantages in terms of cooling efficiency and power consumption. Flat plate fins have been shown to be effective in optimizing heat transfer under certain conditions, while pin fins have demonstrated the ability to reduce energy consumption due to their innovative design. Paving the way for more efficient and durable cooling solutions for electronic components in modern IT environments.

Our work aims to study natural laminar convection in a square cavity containing two circular heat sources heated by the Joule effect and modeling two electrical cables. The discoveries may affect several sectors and applications, in particular the aeronautical sector (subject of the study), industrial and domestic electrical installations. The main objective will therefore be to find the optimal distance between the heat sources and which must be respected to avoid excessive heating which could damage the installation and cause material and human damage.

2. Materials and methods

2.1. Physical model and boundary conditions

The physical model studied (see **Figure 1**) is a square cavity with isothermal side walls H, containing two heat sources of circular shape and diameter D = 0.1H, the distance between the sources is to model two electrical cables in which passes an electric current producing a release of heat by the Joule effect (**Table 1**).

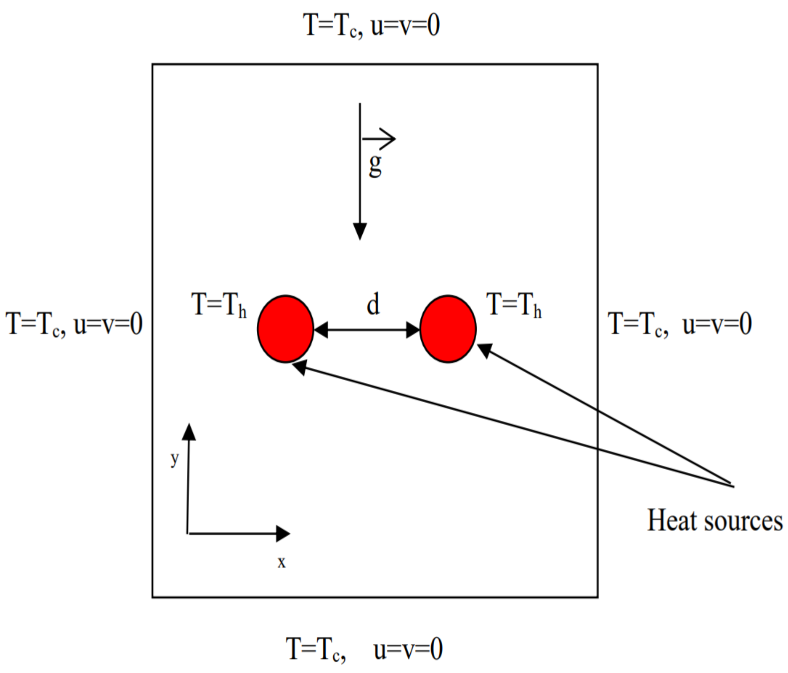

Figure 1. Physical model.

Table 1. Boundary conditions.

Wall	Speed	Temperature
All walls	$u = v = 0$	$T = T_c$

The aim is to determine the optimum distance between the two heat sources to avoid excessive heating of the installation. For this we vary the dimensionless distance between the sources *d* = 0.4H, 0.5H, 0.6H and 0.7H and this for different values of the Rayleigh number Ra = 10^3, 10^4, 10^5,10^6.

2.2. Mathematical formulation

To establish a simple mathematical model for the physical problem, we made assumptions to facilitate its solution, namely:

- The fluid is Newtonian and incompressible.
- The medium is continuous.
- The flow is two-dimensional.
- The diet is laminar.
- The viscous dissipation is negligible ($\mu_\Phi = 0$).
- The Boussinesq approximation is validated everywhere.
- The cables are not insulated.
- The magnetic field is negligible

Equation of continuity

$$\left(\frac{\partial u}{\partial x}+\frac{\partial v}{\partial y}\right)=0 \tag{1}$$

Momentum equation along the *x* axis

$$\rho\left(u\frac{\partial u}{\partial x}+\mathrm{v}\frac{\partial u}{\partial y}\right)=-\frac{\partial p}{\partial x}+\mu\left[\frac{\partial^2 u}{\partial x^2}+\frac{\partial^2 u}{\partial y^2}\right] \tag{2}$$

Momentum equation along the y axis

$$\rho\left(u\frac{\partial v}{\partial x}+\mathrm{v}\frac{\partial v}{\partial y}\right)=-\frac{\partial p}{\partial y}+\mu\left[\frac{\partial^2 v}{\partial x^2}+\frac{\partial^2 v}{\partial y^2}\right]+g\beta(T-T_0) \tag{3}$$

Energy equation

$$u\frac{\partial T}{\partial x}+v\frac{\partial T}{\partial y}=\frac{\lambda}{\rho C_P}\left[\frac{\partial^2 T}{\partial x^2}+\frac{\partial^2 T}{\partial y^2}\right] \tag{4}$$

2.2.1. Dimensional equations

The dimensionless form is used to find general solutions to physical problems independently of measurement systems. It also simplifies the resolution of equation systems and reduces physical parameters. To display the control parameters of the problem studied, it is necessary to introduce reference quantities.

Reference quantities:

$$x^*=\frac{x}{L_{\mathrm{ref}}},y^*=\frac{y}{L_{\mathrm{ref}}},t^*=\frac{tV_r}{L_{\mathrm{ref}}},u^*=\frac{u}{V_{\mathrm{ref}}},$$

$$\upsilon^*=\frac{v}{V_{\mathrm{ref}}},p^*=\frac{p}{\rho V_{\mathrm{ref}}^2},T^*=\frac{T-T_\infty}{\Delta T},t^*=\frac{t}{t_{\mathrm{ref}}},$$

with: $u_{\mathrm{ref}} = \sqrt{g\beta \Delta \mathrm{TH}}$: reference speed, $T_{\mathrm{ref}} = \frac{Th-Tc}{2}$: reference temperature, $\mathrm{p_{ref}} = \rho \mathrm{u}^2$: reference pressure, $\mathrm{t_{ref}} = \frac{\mathrm{H}}{\sqrt{\mathrm{g\beta\Delta TH}}}$: reference time

2.2.2. Dimensionless equations

Equation of continuity

$$\frac{\partial(u^*)}{\partial x^*} + \frac{\partial(v^*)}{\partial y^*} = 0 \tag{5}$$

Momentum equation along the *x* axis

$$u^*\frac{\partial u^*}{\partial x^*} + v^*\frac{\partial u^*}{\partial y^*} = -\frac{\partial p*}{\partial x^*} + \sqrt{\frac{\mathrm{Pr}}{\mathrm{Ra}}}\left[\frac{\partial^2 u^*}{\partial x^{*2}} + \frac{\partial^2 u^*}{\partial y^{*2}}\right] \tag{6}$$

Momentum equation along the *y* axis

$$u^*\frac{\partial v^*}{\partial x^*} + \mathrm{v}^*\frac{\partial v^*}{\partial y^*} = -\frac{\partial p*}{\partial y^*} + \sqrt{\frac{\mathrm{Pr}}{\mathrm{Ra}}}\left[\frac{\partial^2 v^*}{\partial x^{*2}} + \frac{\partial^2 v^*}{\partial y^{*2}}\right] + \mathrm{Pr.Ra.}\Delta\mathrm{T} \tag{7}$$

Energy equation

$$u^*\frac{\partial T^*}{\partial x^*} + v^*\frac{\partial T^*}{\partial y^*} = \frac{1}{\sqrt{\mathrm{Pr.Ra}}}\left[\frac{\partial^2 T^*}{\partial x^{*2}} + \frac{\partial^2 T^*}{\partial y^{*2}}\right] \tag{8}$$

With: Pr = $c_p\mu/\lambda_f$ Prandtl number, Ra $= \rho g\beta\Delta\mathrm{TH}^3/\mu^2$ Rayleigh number, ΔT = $T_h - T_c$: difference between hot and cold temperature.

3. Results and discussion

3.1. Hydrodynamic field

The **Figure 2a,b,e,f**, **Figure 3a,b,e,f**, **Figure 4a,b,e,f**, and **Figure 5a,b,e,f** show the appearance of the streamlines as a function of the variation of the distance between heat sources and the variation of the Rayleigh number. From the **Figure 5a,b,e,f** which shows the evolution of the stream lines as a function of the Rayleigh number for a distance between heat sources *d* = 0.7, the flow field remain symmetrical with respect to the vertical axis of the cavity for any Rayleigh value. It can be seen that for Ra = 10^6, our flow field is essentially formed by four main cells of opposite direction two by two at the top of the cavity thus favoring the convective heat transfer in the cavity. **Figure 2a,b,e,f** shows the evolution of the streamlines as a function of the Rayleigh number for *d* = 0.4 our flow field is symmetrical with respect to the diagonal of the cavity. Notice for Ra = 10^5 that the flow field starts to lose its symmetry, with the cell rise from bottom right upward, giving rise to two small fluid recirculation cells near the right source with vortex formation at the upper corner of the cavity.

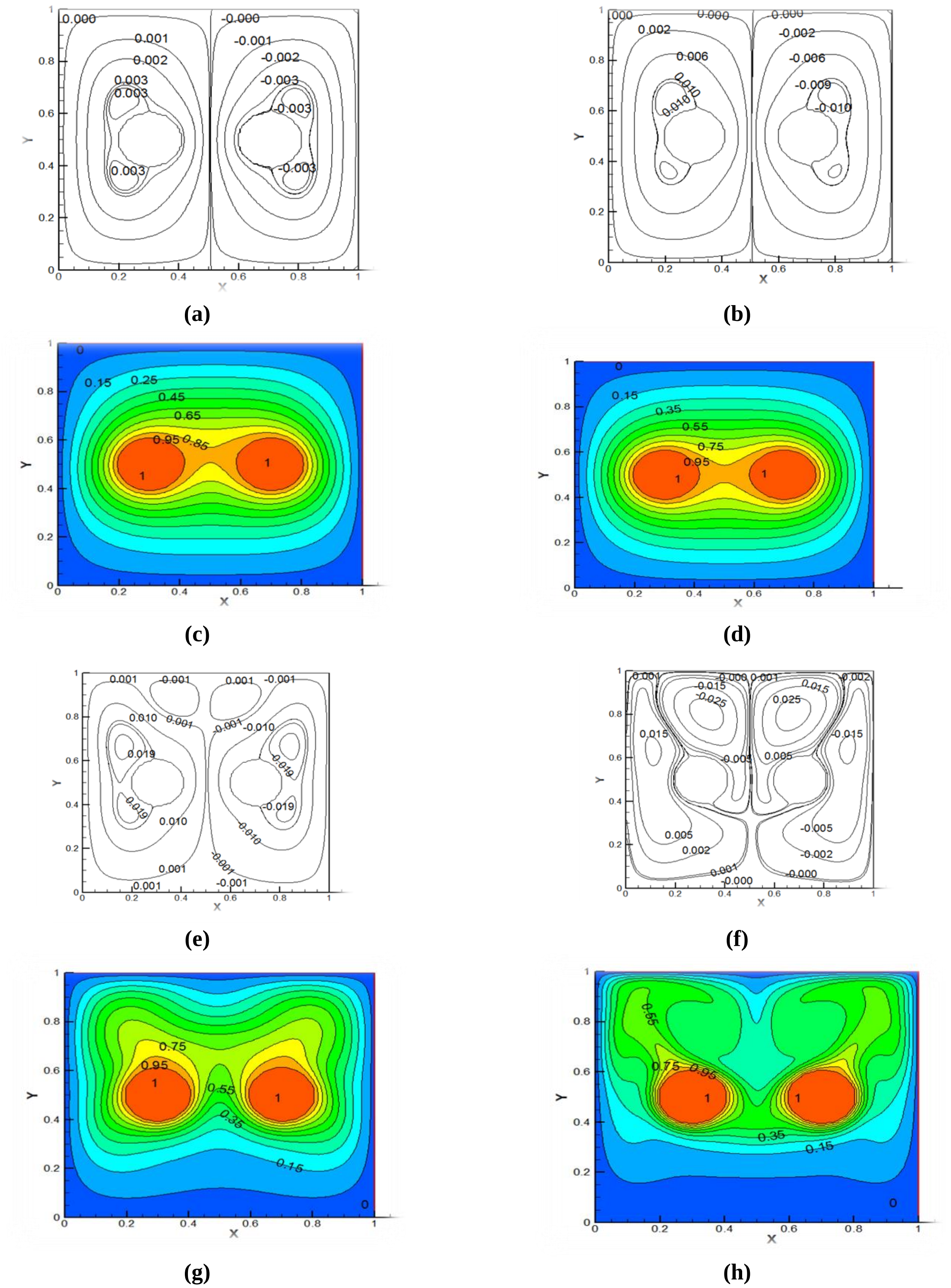

Figure 2. (a) Streamlines; **(c)** isotherms, Ra = 10^3; **(b)** Streamlines; **(d)** isotherms, Ra = 10^4; **(e)** Streamlines **(g)** isotherms, Ra = 10^5; **(f)** Streamlines; **(h)** isotherms, Ra = 10^6 (d = 0.4).

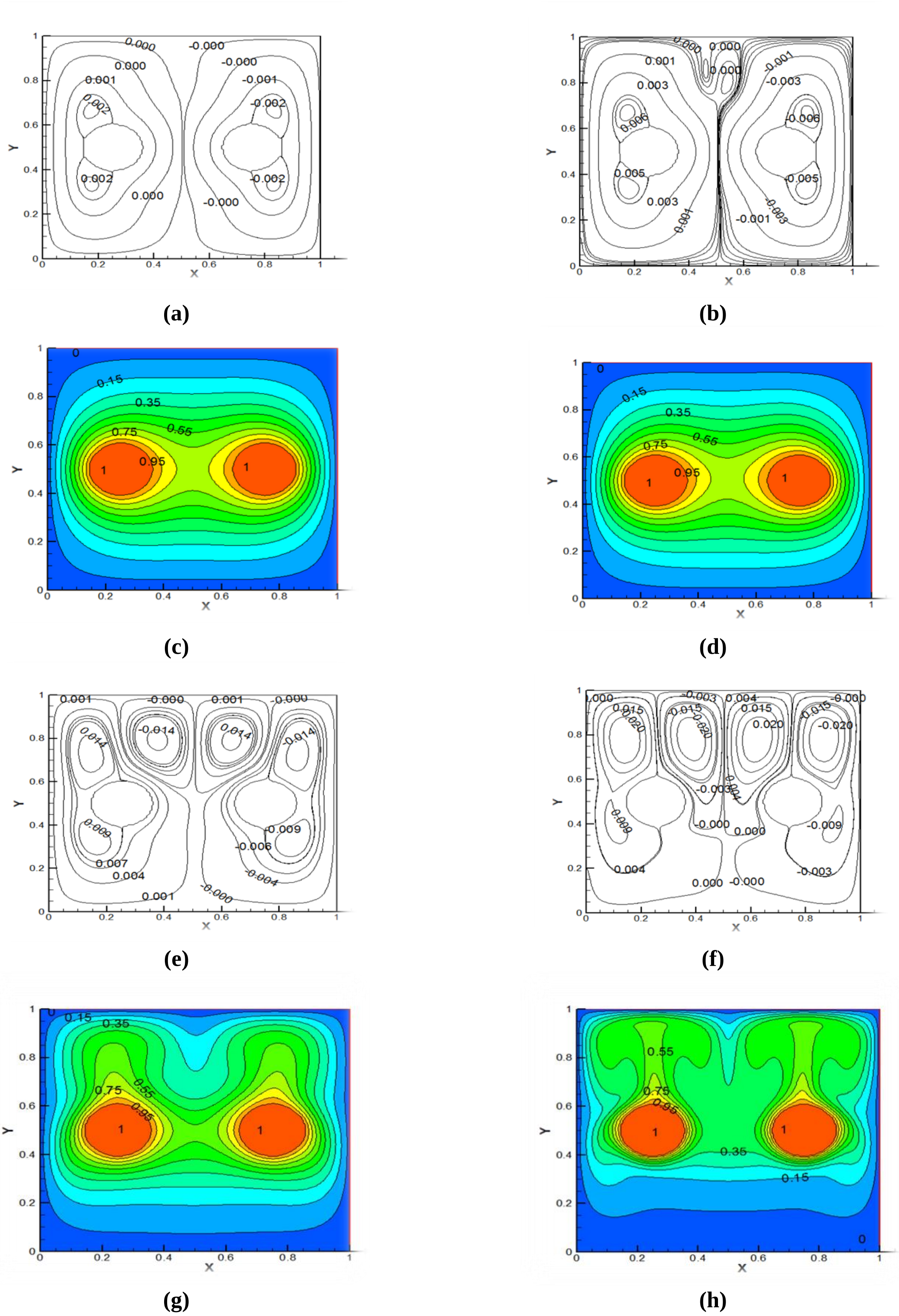

Figure 3. (a) Streamlines; **(c)** isotherms, Ra = 10^3; **(b)** Streamlines; **(d)** isotherms, Ra = 10^4; **(e)** Streamlines **(g)** isotherms, Ra = 10^5; **(f)** Streamlines; **(h)** isotherms, Ra = 10^6; (d = 0.5).

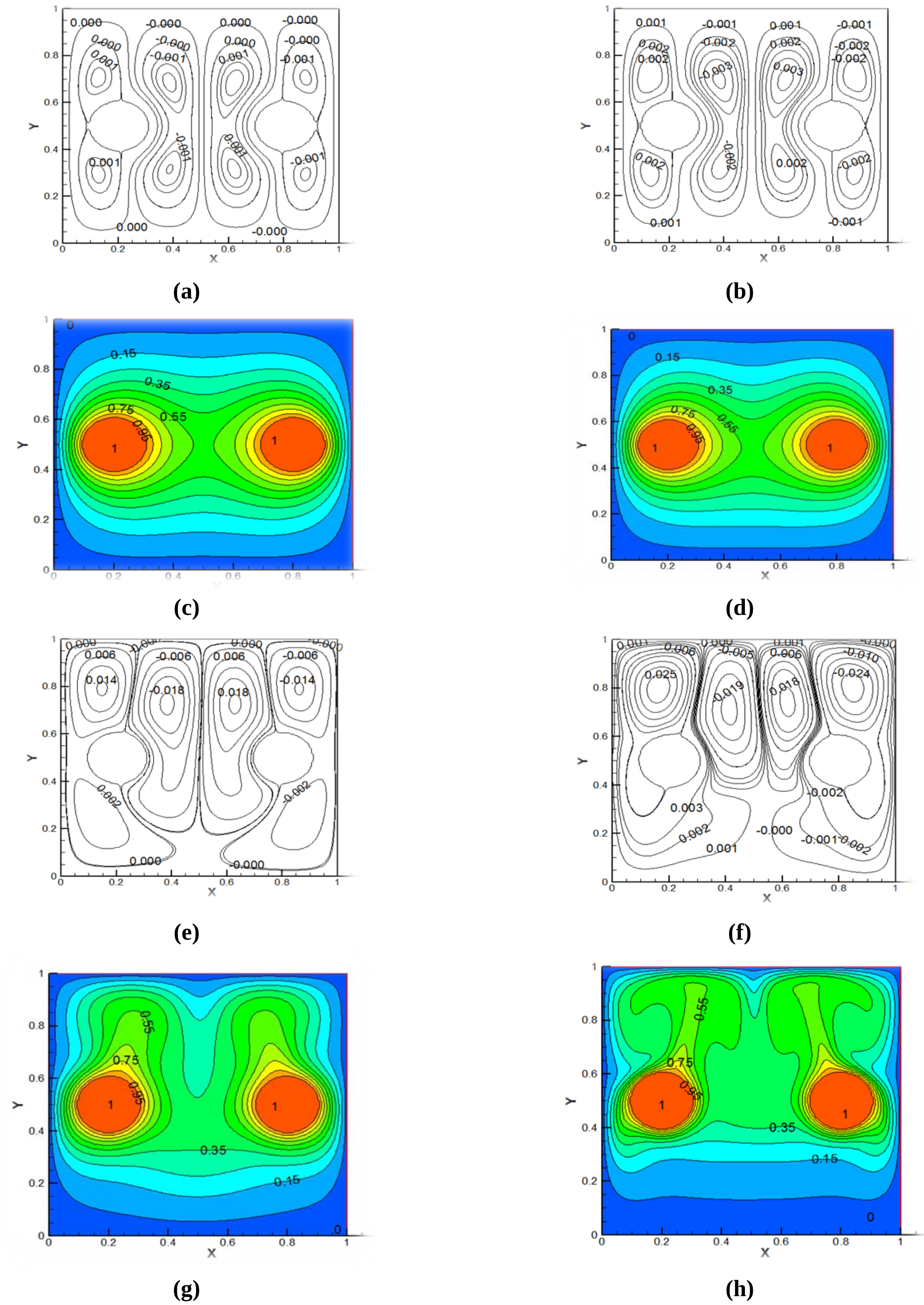

Figure 4. (a) Streamlines; **(c)** isotherms, Ra = 10^3; **(b)** Streamlines; **(d)** isotherms, Ra = 10^4; **(e)** Streamlines **(g)** isotherms, Ra = 10^5; **(f)** Streamlines; **(h)** isotherms, Ra = 10^6; (d = 0.6).

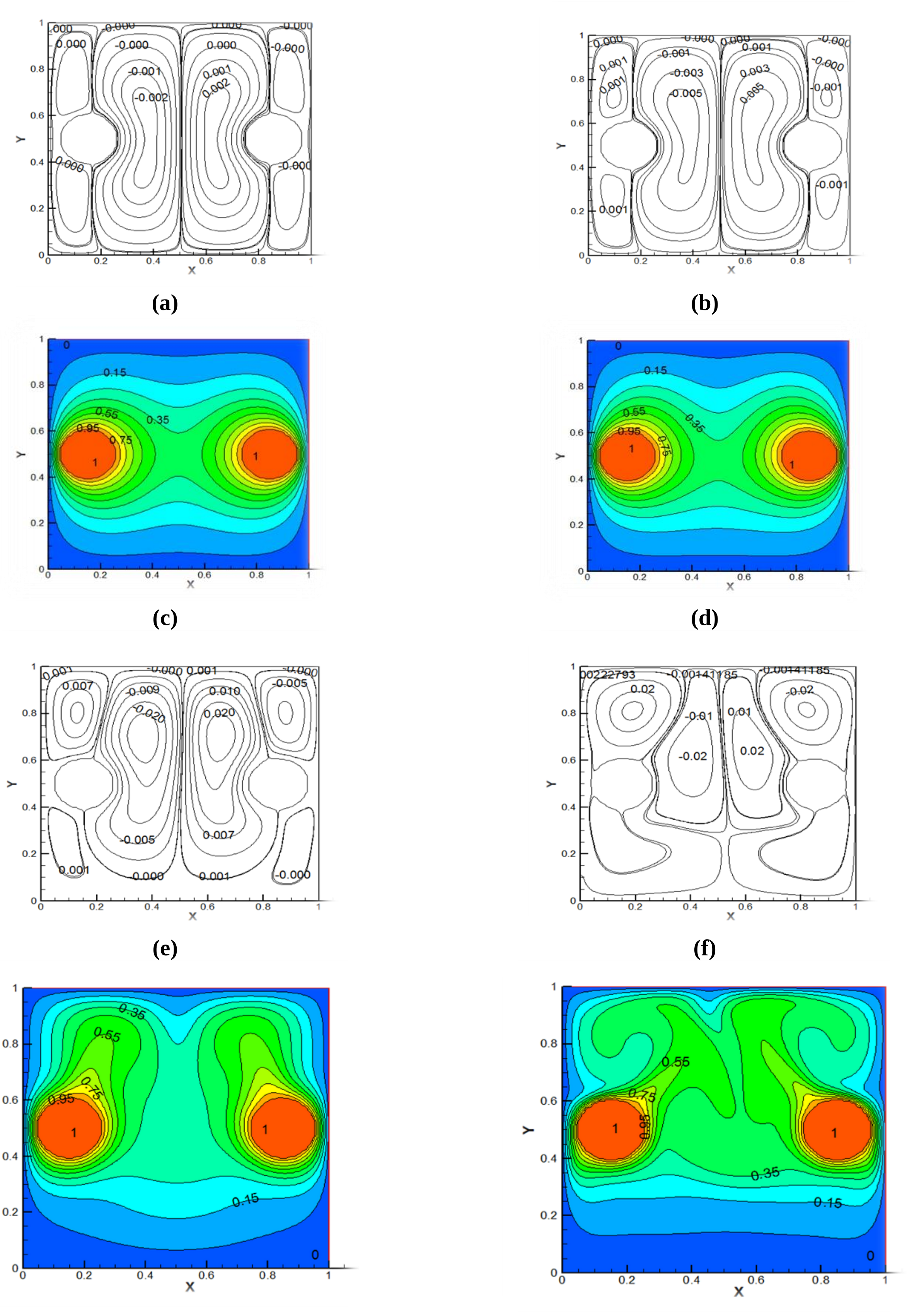

Figure 5. (a) Streamlines; **(c)** isotherms, Ra = 10^3; **(b)** Streamlines; **(d)** isotherms, Ra = 10^4; **(e)** Streamlines **(g)** isotherms, Ra = 10^5; **(f)** Streamlines; **(h)** isotherms, Ra = 10^6; (d = 0.7).

3.2. Thermal field

From **Figure 5c,d,g,h**, which shows the contours of the isotherms for a distance separating the two heat sources equal to 0.7, it can be seen that for a Rayleigh value equal to 106 that the hottest zone is located around the sources of heat. Air recirculation results in the formation of the high-temperature zones of curvilinear shape which is oriented towards the upper corners and the central part above the two sources. It is also observed that the entire area below the two heat sources is a cold or "dead" zone. It is therefore a question of an acceleration of the natural convection mechanism. The lightest layers, i.e., the least dense ones, the warmer ones are dragged upwards due to the force of gravity. These same layers cool along the walls of the enclosure which is colder than the heat sources.

Influence of the rayleigh number (Ra)

a) d = 0.4, 0.5

The **Figure 2c,d,g,h**, **Figure 3c,d,g,h**, **Figure 4c,d,g,h**, and **Figure 5c,d,g,h** shows the appearance of the isotherms as a function of the variation of the distance heat sources and the Rayleigh number. which show the contours of the isotherms for a distance separating the two heat sources equal to 0.4 and 0.5 respectively in horizontal position and for different Rayleigh values, we see that for Ra = 10^3 and Ra = 10^4 the isotherm lines are tight in the vicinity of the two sources and they move away from the walls of the cavity and this is essentially due to the fact that the highest temperatures are find heat sources nearby, which indicates the heat exchange in the cavity is in a conductive state. For Rayleigh values equal to 10^5 and 10^6 we see that the hottest zone is located around the heat sources. Air recirculations result in the formation of a high temperature zone with a curvilinear shape. We also observe that the entire area located below the two heat sources is a cold or "dead" zone. This is indeed the mechanism of natural convection. The lightest layers, i.e., the least dense, i.e., the warmest, are pulled upwards due to the force of gravity. These same layers cool along the walls of the enclosure which is lower than that of the sources, that is to say colder. As they cool, they become heavier, but they still remain a little lighter than the lower layers located below the sources which remain cold.

b) d = 0.6, 0.7

According to **Figure 4c,d,g,h** and **Figure 5c,d,g,h** which show the contours of the isotherms for a distance separating the two heat sources equal to 0.6, and 0.7 respectively in horizontal position and for different values of Rayleigh we can see that for Ra = 10^3 and Ra = 10^4 the same phenomenon as for the previous cases (d = 0.4 and 0.5). For Rayleigh values equal to 10^5 and 10^6 we see that the hottest zone is located around the heat sources. The air recirculations lead to the formation of high-temperature zones with a curvilinear shape which is oriented towards the upper corners and the central part above the two sources. We also observe that the entire area located below the two heat sources is a cold or "dead" zone. It is therefore an acceleration of the natural convection mechanism. The lightest layers, i.e., the least dense, i.e., the warmest, are pulled upwards due to the force of gravity. These same layers cool along the walls of the enclosure which is lower than that of the sources, that is to say colder. As they cool, they become heavier, but they still remain a little lighter than the lower layers located below the sources which remain cold.

4. Maximum stream function (ψ_{max})

Which describes the movement of particles according to their displacement, speed and acceleration without taking into consideration the original forces of this movement. The stream function (ψ) is calculated as follows:

$$u = \frac{\partial \psi}{\partial y}\ et\ v = -\frac{\partial \psi}{\partial x}.$$

Figure 6 illustrates the appearance of the maximum stream function as a function of the variation of the distance and the Rayleigh number. According to this figure we notice that for values of Ra between 10^3 and 10^4 the stream function takes a small and almost constant maximum value regardless of the distance between the heat sources, which indicates that the heat transfer in the cavity is more conductive than convective. While for Rayleigh greater than 10^5 and especially for the value of 10^6, Ψ_{max} takes its maximum value for a distance separating the sources equal to 0.7. We conclude that the heat transfer rate in this case is maximum.

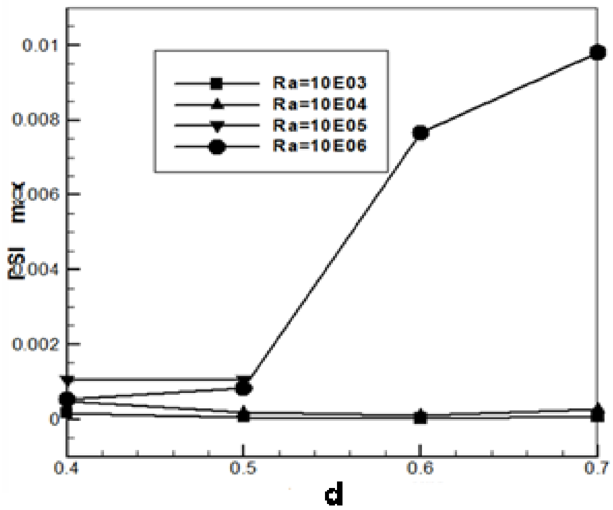

Figure 6. Variation of maximum stream function (Ψ_{max}) for different values of the distance between heat sources.

So, for low values of the Rayleigh number, we can conclude that the heat transfer to the cavity is ensured by conduction, something which does not favor the cooling of the heat sources (cables) and therefore can create a risk for our installation and consequently material and human damage. For values of the Rayleigh number greater than 10^4 and more particularly values 10^5 and 10^6, we see that the heat transfer is convective, this facilitates the flow of hot air surrounding the heat sources and consequently cools the internal environment of the cavity which avoids all risks that could damage our installation.

5. Heat transfer rate

The rate of heat transfer by convection in an enclosure is obtained from the calculation of the Nusselt number, which is a dimensionless number, it represents the ratio between the heat flow exchanged by convection to that by conduction. It is defined as follows: $Nu = \frac{hL}{\lambda}$, with:

h: heat transfer coefficient ($W \cdot m^{-2} \cdot K^{-1}$)

L: characteristic length (m)

λ: thermal conductivity ($W \cdot m^{-1} \cdot K^{-1}$)

The average Nusselt number is defined as:

$$\overline{Nu} = \frac{1}{L}\int_0^L Nudx.$$

5.1. Influence of the distance between heat sources (d)

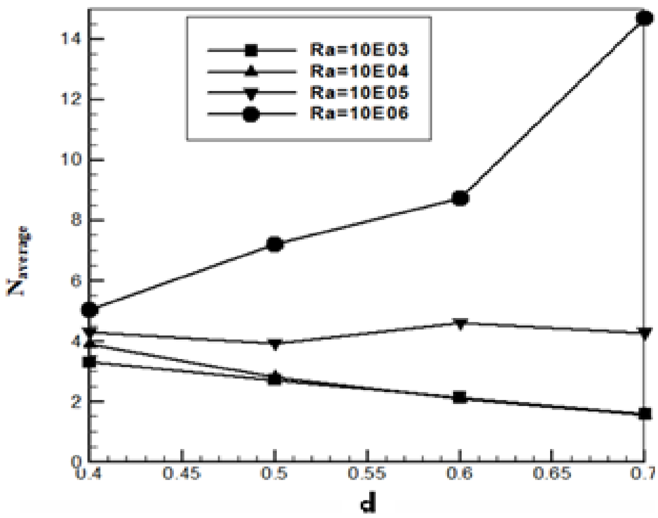

Figure 7. Variation of average nusselt number (Nu_{Avg}) for different values of the distance between heat sources.

According to the **Figure 7**, which shows the evolution of the average Nusselt number as a function of the distance between the sources in the case where the two sources are, we see that for values of *d* = 0.4 and *d* = 0.6, there is a slight increase in the average Nusselt number by increasing the Rayleigh number (from 10^3 to 10^6), this means that the heat transfer improves slightly by moving the sources away from each other and by increasing the Rayleigh value. For *d* = 0.7 we notice that the average Nusselt number reaches a maximum value for Ra = 10^6, which implies that convection is favored in this case.

5.2. Influence of the rayleigh number (Ra)

From the **Figure 8**, which shows the evolution of the average Nusselt number as a function of the Rayleigh number for each position of the two sources, we see that for Rayleigh values lower than 10^5, there is a slight decrease in the latter by increasing the distance between the sources (from 0.4 to 0.7), which implies that the heat transfer is not affected by these Rayleigh values. From Ra = 10^6 we notice a clear increase in average Nusselt as a function of the distance between the two heat sources which is favored by the increase in Ra.

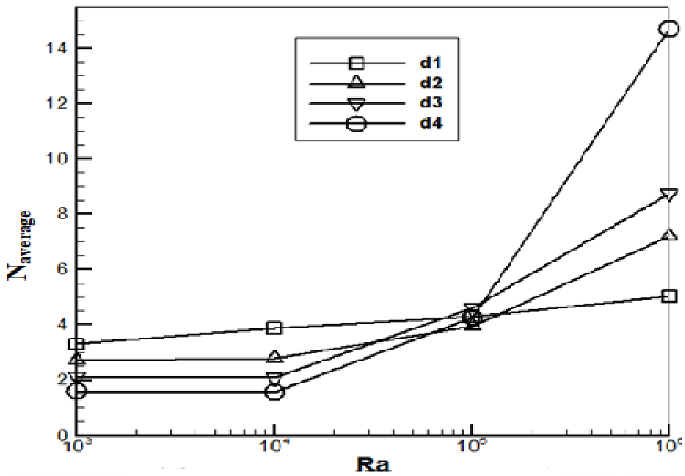

Figure 8. Variation of average nusselt number (Nu_{Avg}) versus different values of rayleigh number (Ra).

5.3. Average nusselt number (Nu_{avg})

From the **Figure 8**, which shows us the evolution of the average Nusselt number as a function of the position of the heat sources for values of the Rayleigh number from 10^3 and 10^6, we notice that the average Nusselt value increases as a function of the distance between the two heat sources, which means that the heat transfer in the cavity improves by increasing the distance between the sources, we can see that the average Nusselt number increases slightly for all distances between the two heat sources for the number Rayleigh values included between 10^3 and 10^4, this is completely normal since the heat transfer between the sources of heat and the ambient environment is mainly by conduction, we observe a clear evolution of the average Nusselt number for the values of the Rayleigh number beyond 10^4.

In the case for Ra = 10^5 and according to the **Figure 8**, we see that whatever the distance between the two heat sources, the Nusselt number takes the same value, that is to say that the heat transfer in the cavity is not influenced by the spacing between the two heat sources for this value of the Rayleigh number. For Ra = 10^6, in this case, a first observation to make is that for the distance separating the two heat sources heat equal to 0.7 the convective heat transfer in the cavity is favored by the strong air circulation due essentially to the increase in the Rayleigh number. We also notice that the average Nusselt value increases as a function of the distance between the two heat sources, which means that the heat transfer in the cavity improves by increasing the distance between the sources.

6. Conclusion

The study presented concerns the numerical simulation of two-dimensional natural convection in laminar regime, in a square cavity with isothermal walls. The cavity in question contains two circular heat sources, simulating two electric cables through which an electric current passes which produces heat release by the Joule effect.

The main objective of this work was the search for the optimal distance between the heat sources, which allows a maximum heat transfer to avoid excessive heat generation in the cavity. The finite volume method was used to discretize the equations governing our steady-state convection flow in steady state, and the SIMPLE algorithm was used to solve them. The results obtained show that the heat transfer in the cavity is affected mainly by the spacing between the two heat sources and the variation of the Rayleigh number (**Figure 6**). Indeed, for the position of heat sources in the cavity, we note the heat transfer in the cavity is maximum (Nu_{Avg} = 14.69), for a distance between the heat sources equal to 0.7 and a value of Rayleigh 10^6 (**Figure 7**).

In conclusion, we can say that the optimum distance between the two sources of heat and which has been the subject of this study is reached in the case where the distance between sources is equal to 0.7, which is the optimal distance that can keep our installation safe and far from any risk caused by joule effect.

Author contributions: Conceptualization, MSB and TC; methodology, MSB; software, AF; validation, MSB, TC and AF; formal analysis, MSB and AF; investigation, MSB; resources, MSB; data curation, MSB; writing—original draft preparation, MSB; writing—review and editing, MSB; visualization, MSB and TC; supervision, TC; project administration, MSB and AF; funding acquisition, MSB and AF. All authors have read and agreed to the published version of the manuscript.

Conflict of interest: The authors declare no conflict of interest.

References

1. Ortega A, Moffat RJ. Buoyancy induced convection in a non-uniformly heated array of cubic elements on a vertical channel wall. Stanford University; 1986.
2. Patnana VK, Bharti RP, Chhabra RP. Two-dimensional unsteady forced convection heat transfer in power-law fluids from a cylinder. International Journal of Heat and Mass Transfer. 2010; 53(19–20): 4152–4167. doi: 10.1016/j.ijheatmasstransfer.2010.05.038
3. Chandra A, Chhabra RP. Flow over and forced convection heat transfer in Newtonian fluids from a semi-circular cylinder. International Journal of Heat and Mass Transfer. 2011; 54(1–3): 225–241. doi: 10.1016/j.ijheatmasstransfer.2010.09.048
4. Kumar D, Dhiman A. Opposing buoyancy characteristics of Newtonian fluid flow around a confined square cylinder at low and moderate Reynolds numbers. Numerical Heat Transfer, Part A: Applications. 2016; 69(8): 874–897. doi: 10.1080/10407782.2015.1090838
5. Laidoudi H, Bouzit M. Mixed convection in poiseuille fluid from an asymmetrically confined heated circular cylinder. Thermal Science. 2018; 22(2): 821–834. doi: 10.2298/tsci160424172l
6. Amieur R, Amieur A. Contribution to the COMSOL simulation of the effector hydrodynamics of the presence of a turbulator in a flow [Master's thesis]. University of Ghardaia, Algeria; 2018.
7. Chiocca A, Frendo F, Bertini L. Evaluation of Heat Sources for the Simulation of the Temperature Distribution in Gas Metal Arc Welded Joints. Metals. 2019; 9(11): 1142. doi: 10.3390/met9111142
8. Alkhalidi A, Kiwan S, Al-Kouz W, et al. Rarefaction and scale effects on heat transfer characteristics for enclosed rectangular cavities heated from below. Thermal Science. 2019; 23(3 Part B): 1791–1800. doi: 10.2298/tsci170621234a
9. Lan S, Jiao F. Modeling of heat source in grinding zone and numerical simulation for grinding temperature field. Int J Adv Manuf Technol. 2019; 103: 3077–3086. doi: 10.1007/s00170-019-03662-w
10. Fathi BH. Study, design and development of a thermal peak detection algorithm for multiple heat sources in integrated circuits (French) [PhD Theis]. Université du Québec en Outaouais; 2019. p. 111.
11. Faraji M, Faraji H, El Alami M. Numerical simulation of the cooling of an electronic component: effect of the angle of inclination (French). In: Proceedings of the 28ème Congrès Français de Thermique; 2020.

12. Hussain Z, Hussain A, Anwar MS, et al. Analysis of Cattaneo–Christov heat flux in Jeffery fluid flow with heat source over a stretching cylinder. J Therm Anal Calorim. 2022; 147: 3391–3402. doi: 10.1007/s10973-021-10573-0
13. Vinodkumar Reddy M, Vajravelu K, Lakshminarayana P, Sucharitha G. Heat source and Joule heating effects on convective MHD stagnation point flow of Casson nanofluid through a porous medium with chemical reaction. Numerical Heat Transfer, Part B: Fundamentals. 2023; 85(3): 286–304. doi:10.1080/10407790
14. Benouis F. Z. Cooling analysis of heat sources placed in a ventilated cavity - application to data centers [PhD thesis]. Usthb University; 2024.

Thermal Science and Engineering 2025, 8(1), 11347.
https://doi.org/10.24294/tse11347

Article

Volume calculation and heat transfer performance simulation of a helical tube with cryogenic helium under intermittent flow condition

Wenhui Cui[1,2], Zhaoxue Zhang[1,2], Meimei Zhang[1], Han Zhou[3], Pengtong Meng[3], Qian Wang[3], Linghui Gong[1,2,*]

[1] Key Laboratory of Cryogenic Science and Technology, Technical Institute of Physics and Chemistry, Chinese Academy of Sciences, Beijing 100190, China

[2] University of Chinese Academy of Sciences, Beijing 100049, China

[3] Zhongshan Institute of Advanced Cryogenic Technology, Zhongshan 528400, China

*** Corresponding author:** Linghui Gong, lhgong@mail.ipc.ac.cn

CITATION

Cui W, Zhang Z, Zhang M, et al. Volume calculation and heat transfer performance simulation of a helical tube with cryogenic helium under intermittent flow condition. Thermal Science and Engineering. 2025; 8(1): 11347. https://doi.org/10.24294/tse11347

ARTICLE INFO

Received: 16 January 2025
Accepted: 13 February 2025
Available online: 24 February 2025

Abstract: The intermittent flow cold storage heat exchanger is one of the most important components of the pulse tube expansion refrigerator based on the reverse Brayton cycle. In the experimental system, the volume and heat transfer of the helical tube play a decisive role in the stable operation of the whole experimental system. However, there are few studies on heat transfer in a helical tube under helium working medium and intermittent flow conditions. In this paper, a process and method for calculating the volume of a helical tube are proposed based on the gas vessel dynamics model. Subsequently, a three-dimensional simulation model of the helical tube was established to analyze the heat transfer process of cryogenic helium within the tube. The simulations revealed that the temperature of helium in the tube decreases to the wall temperature and does not change when the helical angle exceeds 720°. Moreover, within the mass flow rate range of 1.6 g/s to 3.2 g/s, an increase in the mass flow rate was found to enhance the heat transfer performance of the helical tube. This study provides a reference for the selection and application of a helical tube under intermittent flow conditions and also contributes to the experimental research of inter-wall heat exchanger and pulse tube expansion refrigerators.

Keywords: helical tube; refrigeration; intermittent flow; heat transfer; helium

1. Introduction

In recent years, cryogenic technology has become more and more important in many fields, such as electronic superconductivity and large scientific devices. However, there is no corresponding refrigeration system that can provide a cooling capacity of 10-100W in the liquid helium temperature zone [1]. Because of its advantages of high reliability, low vibration, and simple structure, the pulse tube expansion refrigerator based on the reverse Brayton cycle is a new type that is expected to meet this demand [2,3]. The compressed gas is aspirated, expanded, cooled, and vented by an expander controlled by cold valves alternately opened, and then enters the heat exchanger to transfer the cold energy [2]. Among them, as one of the core components, the inter-wall heat exchanger has a non-negligible effect on the performance of the refrigerator. Jia et al. [4] and Sun et al. [5] found through calculation and experimental research that especially the efficiency of the wall heat exchanger seriously affected the minimum temperature and efficiency of the refrigerator. In the corresponding experimental equipment, the helical tube heat exchanger is an important structure to provide reliable and stable working conditions. Due to the advantages of compact structure, good heat transfer performance, strong pressure capacity, etc., it has been widely used in refrigeration, power generation, and other fields [6,7]. More broadly, such intermittent flow operating conditions are common in many refrigerators, such as Stirling refrigerators [8], but few relevant studies exist [9]. Therefore, it is very vital and universal to study the heat transfer performance of a helical tube under intermittent flow conditions.

Pan et al. [9] numerically simulated the heat transfer and pressure drop of a helical tube with a rectangular cross-section under oscillating conditions, proving that it has excellent operating performance at high frequency and high speed, so it is more suitable for Stirling-type machines. Wang et al. [10] studied the low-temperature heat transfer phenomenon of nitrogen flowing in the helical tube under the combined influence of pseudo-critical conditions, floating lift, and helical tube curvature, to design heat exchangers in liquid air energy storage. The results show that when the fluid temperature is lower than the pseudo-critical temperature, the buoyancy effect predominates, whereas the centrifugal effect caused by coil curvature predominates in the opposite condition. Cha et al. [11] studied helical tube heat exchangers used in hydrogen refueling stations and found that they had better heat transfer performance than straight tube heat exchangers due to the influence of secondary flow. And when the distance between the coils is uniform, the heat transfer will be enhanced.

However, there are few studies on heat transfer performance and parameter analysis of helium working medium in the helical tube, especially in intermittent flow conditions. Therefore, based on the experimental system of the key intermittent flow wall heat exchanger in the pulse tube refrigerator, this paper calculates the gas storage volume of the indispensable helical tube and analyzes the heat transfer simulation of the helical angle, mass flow, and other parameters to provide a reference for the application of the helical tube in helium heat exchange and intermittent flow conditions.

2. Calculation about the gas storage volume of the helical tube

The experimental system for the intermittent flow cold storage heat exchanger is shown in **Figure 1**. The gas pressure, temperature, and mass flow rate in the pipeline undergo constant fluctuations over time as a result of the alternating opening and closing of solenoid valves a and b.

During the hot half cycle, with solenoid valve a opened and solenoid valve b closed, high-pressure helium enters the end-closed helical tube via solenoid valve a, leading to a continuous increase in pressure and temperature. Conversely, in the cold half cycle, solenoid valve a is closed while solenoid valve b is opened, causing the gas pressure within the helical tube to be released, resulting in a temperature reduction as low-pressure helium flows back to the compressor for pressurization. The next cycle commences when solenoid valve a is reopened and solenoid valve b is closed, and the process repeats. Importantly, to ensure the continuous and stable operation of the cycle under various experimental conditions, the selection of the appropriate helical tube is crucial.

In the intermittent flow condition, it is necessary to calculate the gas storage volume of the helical tube. The gas container dynamics model was adopted [12,13], where the duration of the hot half cycle and the cold half cycle is divided into several phases. When the time interval is small enough, it can be regarded as a steady state in each period. In each time, the filling process and venting process are considered reversible adiabatic processes, regardless of heat transfer loss. Helium is assumed to behave as the ideal gas. The compressor supply gas pressure is denoted as P_H, and the compressor return gas pressure is denoted as P_L.

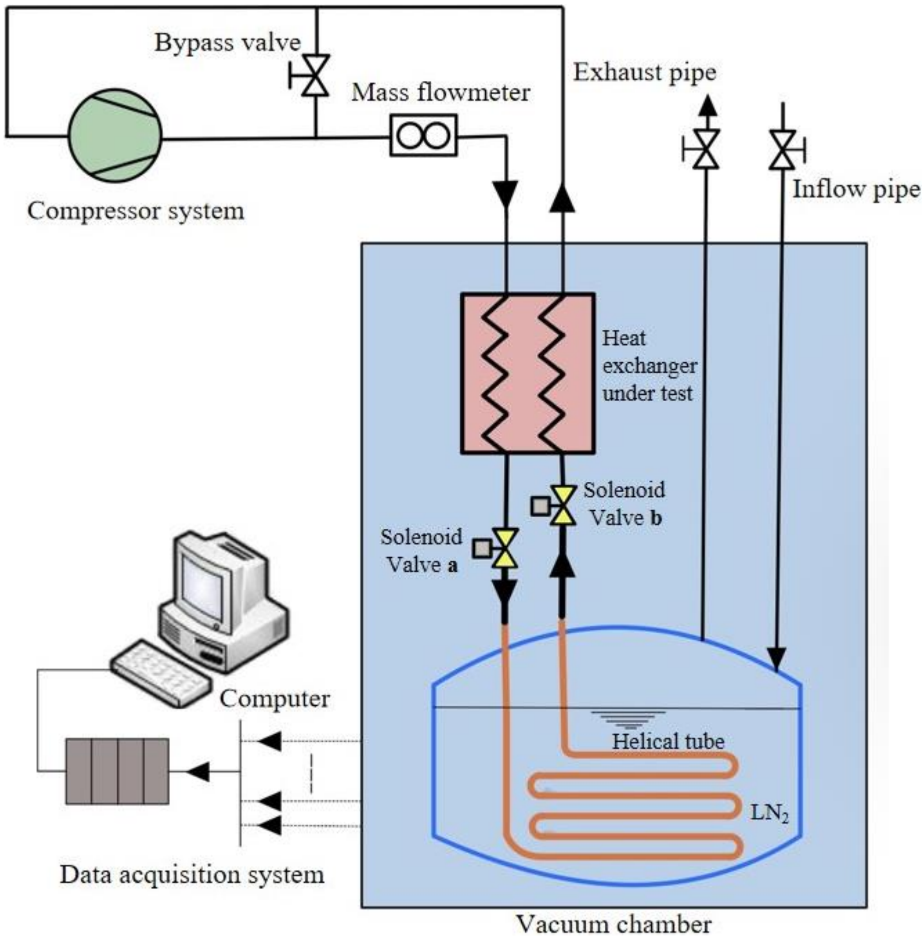

Figure 1. The flow chart of the experimental platform for intermittent flow cold storage surface heat exchanger.

2.1. Venting process

When venting, solenoid valve *b* is opened and solenoid valve a is closed. The isentropic expansion is assumed to occur during the venting process, represented by the process equation:

$$\frac{p}{\rho^{\gamma}} = \mathrm{C} \tag{1}$$

where γ is the gas-specific heat ratio, C is a constant.

Neglecting friction loss and potential energy changes, the mechanical energy conservation equation for the compressed gas can be simplified as:

$$\int vdp + \frac{u^2}{2} = 0 \tag{2}$$

In summary, the instantaneous velocity of the gas is:

$$u = \sqrt{\frac{2\gamma}{\gamma - 1}\left(p_i^{\frac{\gamma-1}{\gamma}} - p_L^{\frac{\gamma-1}{\gamma}}\right)} \tag{3}$$

where p_i is the gas pressure at time t_i, Pa.

According to the continuity equation, the mass flow rate at time t_i can be obtained:

$$q_i = A\rho_i\sqrt{\frac{2\gamma}{\gamma - 1}\left(p_i^{\frac{\gamma-1}{\gamma}} - p_L^{\frac{\gamma-1}{\gamma}}\right)} \tag{4}$$

In the process of venting, the gas density in the helical tube decreases continuously. According to the law of conservation of mass and the definition of density, the gas density in the helical tube after $\triangle t$ time can be obtained:

$$\rho_{i+1} = \rho_i - \frac{q_i}{V}\Delta t \tag{5}$$

where Δt is the time step, s; q_i is the mass flow rate of the venting process at time t_i, kg/s; ρ_{i} is the gas density at time t_i, kg/m^3; V is the gas storage volume of the helical tube, m^3.

Because venting in period is a reversible adiabatic process (Q = 0), the temperature equation in the helical tube can be derived using the first law of thermodynamics and the relationship between the internal energy and temperature of an ideal gas [14,15]:

$$\Delta U = Q - \int p dv \tag{6}$$

$$\Delta U = p\Delta v \tag{7}$$

$$\Delta U = c_v \Delta T \tag{8}$$

$$T_{i+1} = T_i - \frac{p_i}{(\rho_i^2 c_v)}(\rho_i - \rho_{i+1}) \tag{9}$$

where $\triangle U$ is the variation of gas internal energy, J/kg; Q is the exchange heat per kilogram of gas, J/kg; T_i is the gas temperature at time t_i, K; c_v is the constant volume specific heat capacity of gas, J/(kg·K).

According to the ideal gas equation of state, the gas pressure can be calculated:

$$p_{i+1} = \rho_{i+1} R_g T_{i+1} \tag{10}$$

where R_g is the gas constant of helium, J/(kg·K).

2.2. Filling process

When filling, solenoid valve a is opened and solenoid valve b is closed. Similarly, assuming the filling process is isentropic compression, the mass flow rate of inflation at time t_i:

$$q_i = A\rho_H\sqrt{\frac{2\gamma}{\gamma-1}(p_H^{\frac{\gamma-1}{\gamma}} - p_i^{\frac{\gamma-1}{\gamma}})} \tag{11}$$

The gas density in the helical tube after $\triangle t$ time:

$$\rho_{i+1} = \rho_i + \frac{q_i}{V}\Delta t \tag{12}$$

The gas temperature in the helical tube:

$$T_{i+1} = T_i + \frac{p_i}{(\rho_i^2 c_v)}(\rho_{i+1} - \rho_i) \tag{13}$$

The gas pressure in the helical tube:

$$p_{i+1} = \rho_{i+1} R_g T_{i+1} \tag{14}$$

The calculation process of the gas storage volume of the helical tube is shown in **Figure 2**. It can be seen that the gas storage volume is closely related to the physical properties of helium, mass flow rate, and changing temperature and pressure in different periods; that is to say, it is more fundamentally affected by the key parameter of operating frequency.

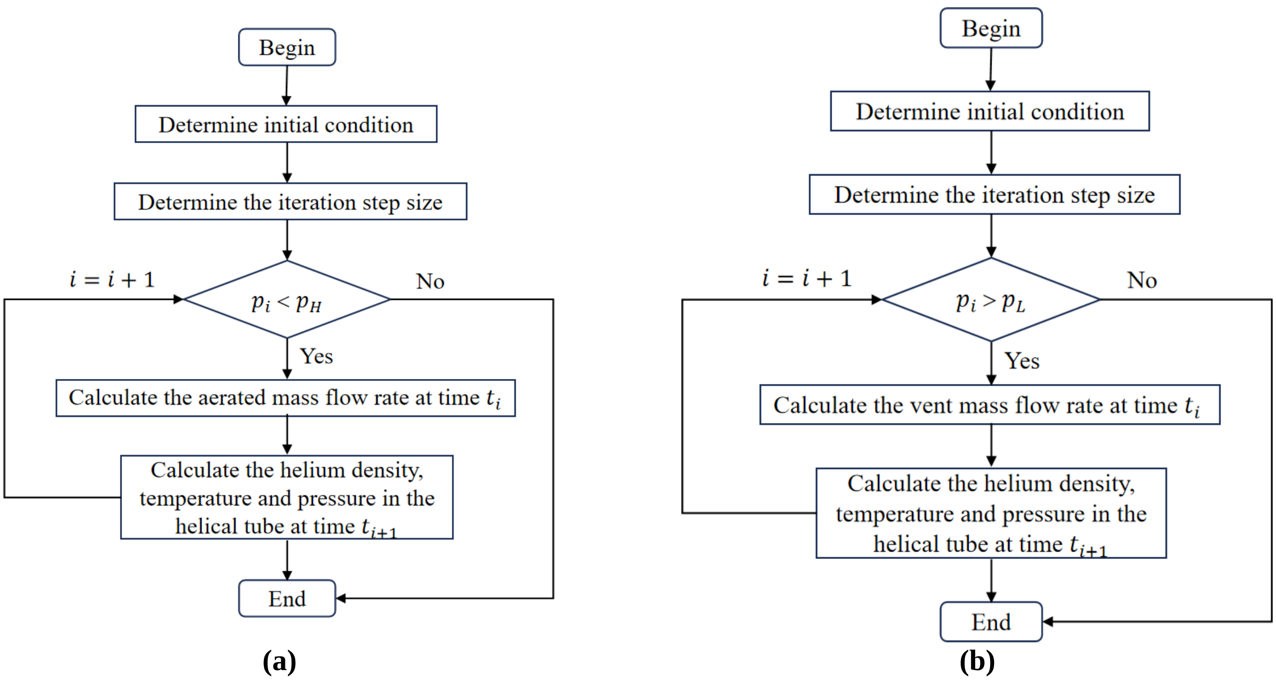

Figure 2. Helical tube gas storage volume calculation process: **(a)** Filling process; **(b)** venting process.

2.3. Calculation results

Given the supply gas pressure in the compressor of 2 MPa and return gas pressure of 0.5 MPa, ignoring the flow resistance through the heat exchanger, it is calculated that under different solenoid valve diameters, the gas storage volume of the helical tube changes with the working frequency of the solenoid valve, as shown in **Figure 3**.

As the operating frequency of the solenoid valve increases, the gas storage volume required by the helical tube becomes smaller. At the same operating frequency, the larger the diameter of the solenoid valve, the larger the gas storage volume required by the helical tube. At the same time, because the inflation process is a stable gas supply from a high-pressure gas source, and the pressure in the helical tube during the gas release process is decreasing, the average mass flow rate of the inflation process is greater than that of the gas release process, so for the helical tube with a given gas storage volume, the solenoid valve b should be larger than the valve diameter of the solenoid valve a.

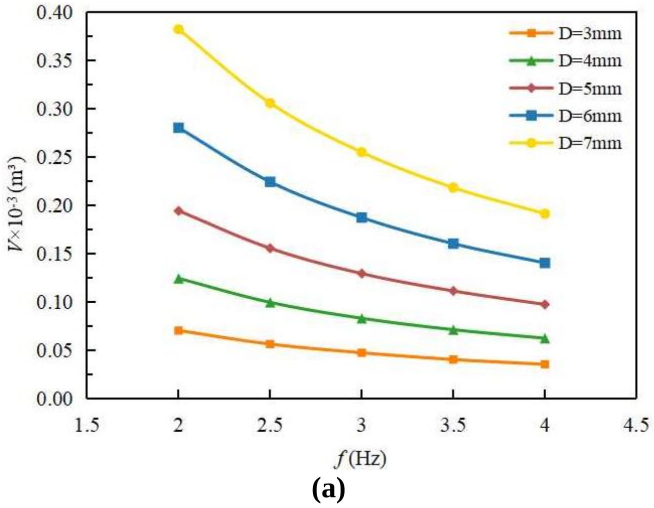

Figure 3. Under different solenoid valve diameters, the change of the gas storage volume of the helical tube with the working frequency: **(a)** Filling process; **(b)** venting process.

When the diameter of the solenoid value a is 5 mm and the frequency is 4 Hz, the gas storage volume of the helical tube is calculated to be 0.0975 L, and the diameter of the solenoid valve b is 8.23 mm.

The variation curve of helium mass flow rate and gas pressure in the helical tube with time is shown in **Figure 4**. The mass flow rate changes steadily from large to small to full, while the pressure in the tube increases rapidly and becomes stable. When the gas is discharged, the pressure in the tube decreases rapidly, which makes the mass flow rate decrease with a larger slope, unlike the high-pressure gas source when the gas is charged. Finally, the helical tube presents a dynamic cycle change condition.

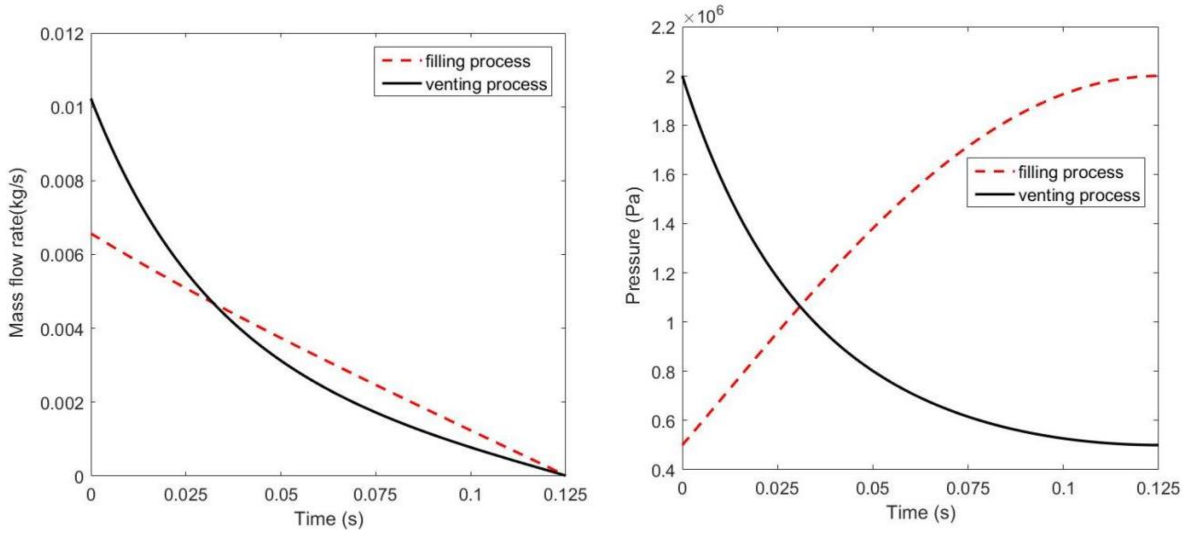

(a) **(b)**

Figure 4. Variation curves of mass flow rate and pressure with time during the filling and venting process: **(a)** mass flow rate; **(b)** pressure.

3. Simulation study on heat transfer characteristics of helical tube

3.1. Model and grid

Modeling of the helical tube was achieved using SolidWorks, based on the volume calculations outlined in Section 2.3. The schematic diagram of the helical tube, as depicted in **Figure 5a**, illustrates key dimensions for the model, including a diameter (d) of 6 mm, a pitch (H) of 15 mm, a curvature diameter (D) of 250 mm, and a total length (L) of 3142.1 mm.

The polyhedral mesh division method was utilized [16], resulting in a total of 2,272,600 grids, and the mesh independence was verified. For the flow field capture of complex geometry such as helical tubes, the polyhedral mesh partitioning method can not only generate high-quality unstructured mesh that can adapt to complex geometry and improve the calculation accuracy, but also ensure the simulation has high stability and convergence and reduce numerical errors [17].

The mesh division of the helical tube inlet is shown in **Figure 5b**.

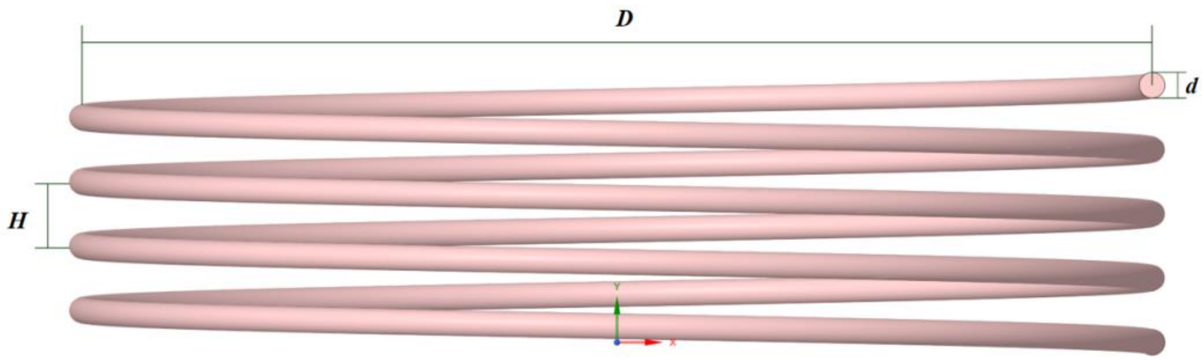

(a)

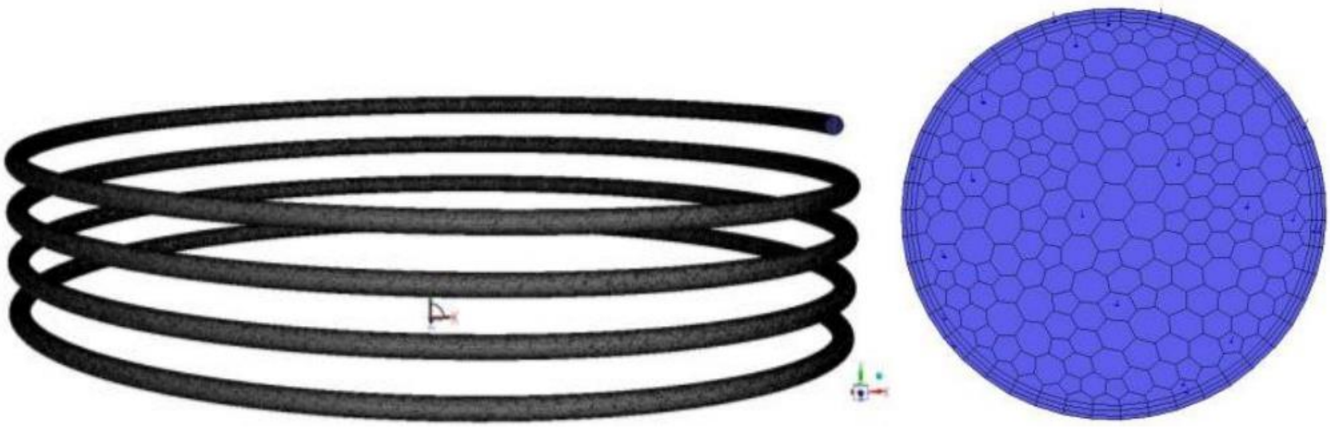

(b)

Figure 5. Geometry and mesh of the numerical model: **(a)** geometric model; **(b)** meshing of helical inlet.

3.2. Boundary conditions and solution methods

The numerical simulation of the helical tube is carried out by Fluent software with specific boundary conditions. The inlet boundary is set as a mass flow inlet with a temperature of 82 K, and the outlet boundary is defined as a pressure outlet. Additionally, the wall conditions are specified as equal wall temperature and non-slip boundary [18], with a temperature of 77 K, a wall thickness of 1 mm, and red copper as the wall material.

The simulation incorporates the helium real gas model of the NIST database for physical parameters and employs the RNG k-ε turbulence model [19–21]. RNG k-ε model takes into account turbulent anisotropy and vortex flow conditions [22,23], thus improving the accuracy of dealing with high turbulence at the end of the cavity [24], so it is widely used in the helical tube flow heat transfer model, which corresponds to the intermittent flow operating conditions in this paper [25].

The governing equations for momentum, energy, turbulent kinetic energy, and turbulent dissipation rate are solved using the second-order upwind scheme [26]. The mass flow at the inlet and outlet of the helical tube was monitored to ensure the convergence of the numerical simulation.

3.3. Results and analysis

The temperature contours of the model for various helical angles are shown in **Figure 6**, with all contours indicating the right side as the inner direction of the helical tube.

It can be seen that the fluid near the tube wall is first cooled after the helium enters the helical tube. Due to the centrifugal force, the temperature inside the helical tube decreases faster. As the helical angle escalates, the fluid temperature at different positions in the tube continues to approach, and until the section of 720°, the fluid temperature at different locations is basically the same.

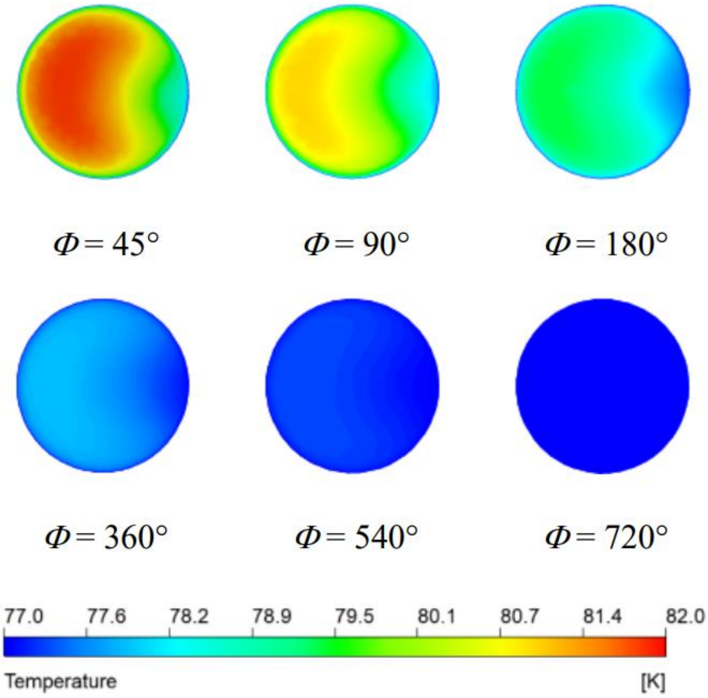

Figure 6. The contours of temperature at different helical angles.

Under different mass flow conditions, the variation curve of helium temperature with a helical angle is shown in **Figure 7**, and the variation curve of convective heat transfer coefficient with a helical angle is shown in **Figure 8**.

It can be seen that the smaller the mass flow rate, the faster the temperature reduction rate of helium, because at a lower mass flow rate, the heat exchange required to reduce the same temperature decreases so that the temperature can drop faster. When the helical angle is greater than 720°, it gradually becomes stable, and there is no significant difference in temperature among the three.

As can be seen from **Figure 8**, the heat transfer coefficient reaches its maximum at the entrance section and then decreases to stable. With the increase of mass flow rate, the heat transfer coefficient gradually increases, indicating that increasing mass flow rate within a certain range can improve the heat transfer performance of the helical tube under the condition that the outlet temperature of the helical tube is almost unchanged.

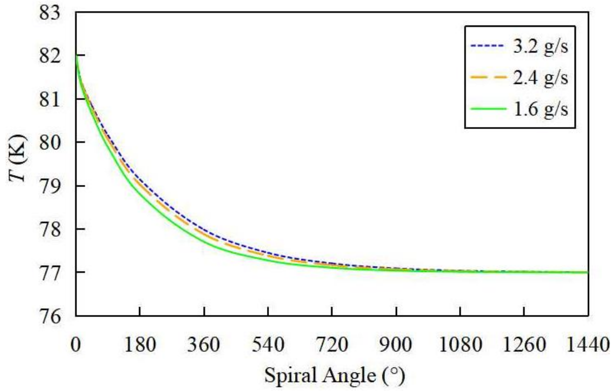

Figure 7. The variation curves of fluid temperature with helical angle at three different mass flows.

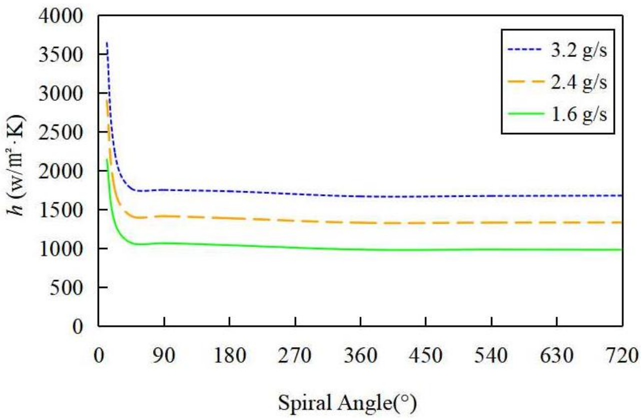

Figure 8. The variation curves of the convective heat transfer coefficient with helical angle at three different mass flows.

4. Conclusion

The volume of the helical tube in the experimental system of intermittent flow cold storage heat exchanger is calculated based on the gas container dynamics model. It is observed that the volume of the helical tube decreases as the working frequency of the solenoid valve increases. Conversely, the volume of the helical tube increases as the diameter of the solenoid valve increases. A three-dimensional numerical model was built to investigate the heat transfer characteristics of cryogenic helium in the helical tube. The study found that the flow of helium in the helical tube was influenced by centrifugal force, resulting in a temperature distribution with a radial gradient. It was observed that the temperature inside the helical tube decreased faster. When the helical angle exceeded 720°, the temperature of helium throughout the cross-section became uniform, reaching its lowest outlet temperature. The helium exhibits a faster rate of temperature reduction as the mass flow rate decreases within the range of 1.6 g/s to 3.2 g/s. Furthermore, increasing the mass flow rate can enhance the heat transfer coefficient. It provides a reference for the selection and application of a helical tube under intermittent flow conditions. Subsequently, the influence of helical tube curvature, section shape, and other parameters and the heat transfer law can be studied. Further, verification analysis will be carried out according to more practical and specific experimental results.

Author contributions: Conceptualization and methodology, WC and ZZ; software, WC; validation, MZ and LG; formal analysis, WC and HZ; investigation, PM; resources, QW; data curation, HZ; writing—original draft preparation, WC and ZZ; writing—review and editing, WC and ZZ; visualization, HZ and PM; supervision, QW, MZ and LG. All authors have read and agreed to the published version of the manuscript.

Acknowledgments: The authors would like to thank Zhongshan Advanced Cryogenic Technology Research Institute for their support in establishing the experimental platform.

Conflict of interest: The authors declare no conflict of interest.

References

1. Hu J, Luo E. Progress in regenerative cryocoolers. Science & Technology Review. 2015; (02): 99–107. doi: 10.3981/j.issn.1000-7857.2015.02.015.
2. Jia Q, Gong L, Feng G, et al. Thermodynamic analyses and the experimental validation of the Pulse Tube Expander system. Cryogenics. 2018; 91: 118–124. doi: 10.1016/j.cryogenics.2018.01.005
3. Cui W, Gong L, Jia Q, et al. Numerical study of heat transfer characteristics of intermittent flow cold storage surface heat exchanger. IOP Conference Series: Materials Science and Engineering. 2024; 1301(1): 012036. doi: 10.1088/1757-899x/1301/1/012036
4. Jia Q. Theoretical study and experimental verification of pulse tube expander and jet expander [PhD thesis]. Technical Institute of Physics and Chemistry, Chinese Academy of Sciences; 2020.
5. Sun W, Dai W, Liang J, et al. Research on pulse tube refrigerator with low temperature switch valve. Cryogenics and Superconductivity. 2000; (3): 1–9. doi:10.16711/j.1001-7100.2000.03.001
6. Zhu L, Cai T, Chen X, et al. Gas-solid flow behavior and heat transfer in a spiral-based reactor for calcium-based thermochemical energy storage. Journal of Energy Storage. 2024; 99: 113481. doi: 10.1016/j.est.2024.113481
7. Zhang Y, Wang D, Lin J, et al. Development of a computer code for thermal–hydraulic design and analysis of helically coiled tube once-through steam generator. Nuclear Engineering and Technology. 2017; 49(7): 1388–1395. doi: 10.1016/j.net.2017.06.017
8. Choudhari M, Gawali BS, Patil JD. Oscillating flow heat transfer: a comprehensive review. Energy Sources, Part A: Recovery, Utilization, and Environmental Effects. 2022; 44(3): 7598–7619. doi: 10.1080/15567036.2022.2113932
9. Pan C, Zhang T, Wang J, et al. CFD study of heat transfer and pressure drop for oscillating flow in helical rectangular channel heat exchanger. International Journal of Thermal Sciences. 2018; 129: 106–114. doi: 10.1016/j.ijthermalsci.2018.02.035
10. Wang Y, Lu T, Liu X, et al. Heat Transfer of Near Pseudocritical Nitrogen in Helically Coiled Tube for Cryogenic Energy Storage. Energies. 2022; 15(8): 2752. doi: 10.3390/en15082752
11. Cha H, Choi Y, Kim S. Heat transfer performance of a helical heat exchanger depending on coil distance and flow guide for supercritical cryo-compressed hydrogen. Progress in Superconductivity and Cryogenics. 2022; 24(3): 62–67. doi: 10.9714/PSAC.2022.24.3.062
12. Bejan A. Advanced engineering thermodynamics, 4th ed. Newark: Wiley; 2016.
13. Shen W, Tong J. Engineering thermodynamics, 5th ed. China: Higher Education Press; 2016.
14. Rahman MA. Review on heat transfer augmentation in helically coiled tube heat exchanger. International Journal of Thermofluids. 2024; 24: 100937. doi: 10.1016/j.ijft.2024.100937
15. Kaushik S, Singh S, Panwar K. Experimental study of fluid flow properties in spiral tube heat exchanger with varying insert shape over spiral tube profile. Materials Today: Proceedings. 2023; 80: 78–84. doi: 10.1016/j.matpr.2022.10.117
16. Yan F, Lu H, Feng S. Numerical Simulation of Liquified Natural Gas Boiling Heat Transfer Characteristics in Helically Coiled Tube-in-Tube Heat Exchangers. Frontiers in Heat and Mass Transfer. 2024; 22(5): 1493–1514. doi: 10.32604/fhmt.2024.055324
17. Zhao Y, Mao Q. Experimental and numerical analysis of unsteady state conditions on thermal storage performance of a conical spiral shell-tube energy storage system. Journal of Energy Storage. 2024; 88: 111579. doi: 10.1016/j.est.2024.111579
18. Kazemi-Esfe H, Shekari Y, Omidvar P. Comparison of heat transfer characteristics of a heat exchanger with straight helical tube and a heat exchanger with coiled flow reverser. Applied Thermal Engineering. 2024; 253: 123772. doi: 10.1016/j.applthermaleng.2024.123772
19. Bi H, Yang J, Chen C, et al. Heat transfer and flow characteristics of intermittent oscillating flow in tube. Applied Thermal Engineering. 2023; 225: 120233. doi: 10.1016/j.applthermaleng.2023.120233
20. Wu J, Zhao J, Sun X, et al. Design method and software development for the spiral-wound heat exchanger with bilateral phase change. Applied Thermal Engineering. 2020; 166: 114674. doi: 10.1016/j.applthermaleng.2019.114674
21. Li S, Cai W, Chen J, et al. Numerical study on the flow and heat transfer characteristics of forced convective condensation with propane in a spiral pipe. International Journal of Heat and Mass Transfer. 2018; 117: 1169–1187. doi: 10.1016/j.ijheatmasstransfer.2017.10.080
22. Dong X, Wu Y, Zhang C, et al. Experimental and numerical study on heat transfer and flow characteristics of molten salt

nanofluids in spiral-wound tube heat exchanger. International Journal of Thermal Sciences. 2023; 191: 108343. doi: 10.1016/j.ijthermalsci.2023.108343

23. Han Z, Reitz RD. Turbulence Modeling of Internal Combustion Engines Using RNG κ-ε Models. Combustion Science and Technology. 1995; 106(4–6): 267–295. doi: 10.1080/00102209508907782
24. Zhang D, Zhang G, Wang H, et al. Numerical investigation of time-dependent cloud cavitating flow around a hydrofoil. Thermal Science. 2016; 20(3): 913–920. doi: 10.2298/tsci1603913z
25. Pan C, Zhou Y, Wang J. CFD study of heat transfer for oscillating flow in helically coiled tube heat-exchanger. Computers & Chemical Engineering. 2014; 69: 59–65. doi: 10.1016/j.compchemeng.2014.07.001
26. Wu J, Lu S, Wang C, et al. Numerical study on heat transfer characteristics of helically coiled grooved elliptical tube heat exchanger. International Journal of Heat and Fluid Flow. 2024; 110: 109622. doi: 10.1016/j.ijheatfluidflow.2024.109622

Thermal Science and Engineering 2025, 8(1), 11162.
https://doi.org/10.24294/tse11162

Review

Emerging trends in manufacturing of micro and macro scale devices using metal iodide-based nanomaterials

Nazia Nusrat[1], Humaira Aslam[1], Syeda Hira Fatima[2], Asifa Naheed[2], Sohail Jahanzeb[1], Narjis Fatima[3], Amena Khaliq[4], Moazzam Ali[1], Mian Muhammad Waqas[1], Misbah Ullah Khan[1,*], Shehla Honey[1,*]

[1] Centre for Nanosciences, University of Okara, Okara 56130, Pakistan
[2] Department of Zoology, Faculty of Life Sciences, University of Okara, Okara 56130, Pakistan
[3] Department of Chemistry, Govt. College University, Faisalabad, Punjab 38000, Pakistan
[4] Department of Science Education, Kyungpook National University, Daegu 41566, South Korea
*** Corresponding authors:** Misbah Ullah Khan, misbahullahkhan143@uo.edu.pk; Shehla Honey, Shehla.honey@uo.edu.pk

CITATION

Nusrat N, Aslam H, Fatima SH, et al. Emerging trends in manufacturing of micro and macro scale devices using metal iodide-based nanomaterials. Thermal Science and Engineering. 2025; 8(1): 11162. https://doi.org/10.24294/tse11162

ARTICLE INFO

Received: 31 December 2024
Accepted: 14 February 2025
Available online: 14 March 2025

Abstract: A fresh interest has been accorded to metal iodides due to their fascinating physicochemical properties such as high ionic conductivity, variable optical properties, and high thermal stabilities in making micro and macro devices. Breakthroughs in cathodic preparation and metallization of metal iodides revealed new opportunities for using these compounds in various fields, especially in energy conversion and materials with luminescent and sensory properties. In energy storage metal iodides are being looked at due to their potential to enhance battery performance, in optoelectronics the property of the metal iodides is available to create efficient LEDs and solar cells. Further, their application in sensing devices, especially in environmental and medical monitoring has been quite mentioned due to their response towards environmental changes such as heat or light. Nevertheless, some challenges are still in question, including material stability, scale-up opportunities, and compatibility with other technologies. This work highlights the groundbreaking potential of metal iodide-based nanomaterials, emphasizing their transformative role in innovation and their promise for future advancements.

Keywords: metal iodides; ionic conductivity; optical characteristics; thermal stability; energy storage; optoelectronics

1. Introduction

The technological development of micro and macro devices has increased interest in metal iodide-based compounds since the materials have properties that fit well across multiple applications. Salts of iodide like silver iodide (AgI), copper iodide (CuI), and cesium iodide (CsI) are highly conductive ionic materials with good optical transmittance and high thermal stability that make them suitable for device applications. These materials are useful enablers of miniaturization, as shown in **Figure 1**, which means that producing devices that are smaller and more energy efficient can be done without compromising functioning. Flexible aggression and high efficiency coupled with miniaturization of components have been critical factors influencing compound adoption in microelectronic systems such as sensors, energy storage, and optoelectronic systems.

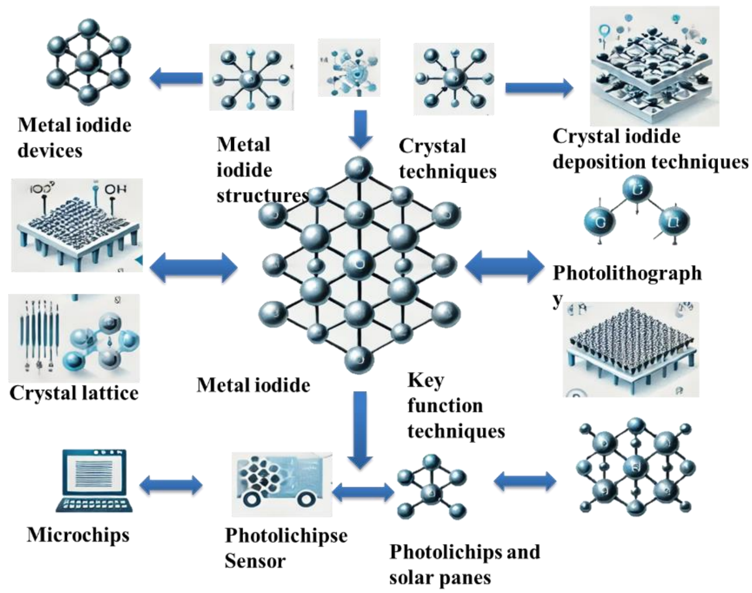

Figure 1. Represent the graphical abstract of this review.

The synthesis and processing of metal iodides have developed with improved fabrication techniques guaranteeing controlled micro- and nanoscale characteristics of the resulting materials. For instance, solution processes, Vapor deposition methods, and Chemical vapor deposition (CVD) techniques can be used, and each technique provides specific benefits depending on the goal of the metal iodide synthesis. These methods help specifically in the formation of thin films, nanoparticles, and nanowires which are compulsory for the Microfabrication of devices [1]. Furthermore, material science has given birth to hybrid forms of metal iodide which when combined with other materials such as polymers or graphene, will improve the efficiency and stability of the devices. These hybrid systems are especially advantageous in such applications as energy storage, where better charge maintenance and faster ion mobility are necessary [2].

Specifically, metal iodides are being gradually applied in energy storage, particularly in lithium-ion batteries and sodium-ion batteries due to their great potential for enhancing battery performance. It mainly concerns the improvement of the charge transport throughout the battery thanks to the high ionic conductivity of metal iodides. Also, their thermal stability makes it possible to use the batteries safely in diverse circumstances [3]. Metal iodides are also being considered for supercapacitors applications in their ability to produce electrodes with increased surface areas, and improved charge storage capabilities. These enhancements are in line with the developing demands of compact storage that harness high power density storage systems for portable electronics, electric vehicles, and portable medical equipment [4,5].

It is for these reasons that metal iodides have become invaluable their chemical structures allow them to glow, and to absorb certain kinds of light. Metal iodides are employed in light-emitting diodes (LEDs), laser diodes, and photovoltaic cells where the conversion of electrical energy to light, or its converse, is highly effective [6,7]. The ability of the metal iodides to have continual variation in the frequency range of device operation also can be beneficial in practically any frequency range making the metal iodides ideal for a diverse range of uses, anywhere from simple electronics to medical equipment. Furthermore, the cost to realize metal iodide-based optoelectronic devices is significantly less than the cost to realize traditional materials like silicon or organics [8,9].

There are however several factors that hinder the use of metal iodides in commercial devices even though their use has the following benefits: Questions concerning the stability and applicability of such materials for long-term and large-scale applications need to be answered, especially where the devices are exposed to severe environmental conditions or where the devices are to be used continually [4,10]. Moreover, the toxicity of some metal iodides is high, and in particular their use in medical and environmental concerns like silver iodide. However, the still-growing efforts to develop more stable, biocompatible, and scalable metal iodide compounds, and advancement in fabrication technology should help address these problems. Metal iodides will become key components of next-generation micro and macro devices of higher performance in the advancement of the field [11,12].

2. Fabrication techniques

Multiple techniques exist for fabricating metal iodide materials allowing experts to modify their functional properties as well as structural characteristics shown in **Figure 2**. The fabrication process requires two main methods including sol-gel methods and hydrothermal synthesis for controlling structure and morphology. The production of thin films with left and right distributions depends on the Chemical vapor deposition (CVD) and spin coating methods. Efficient production of simple bulk materials happens through solution casting in combination with co-precipitation whereas precise material composition and thickness control is achieved using electrochemical deposition processes. Distinct benefits generated by these methods decide what application methods best suit electronics as well as optics and catalysis domains. The integration of these domains supports the role of fabrication methods in enhancing today’s technological advancement.

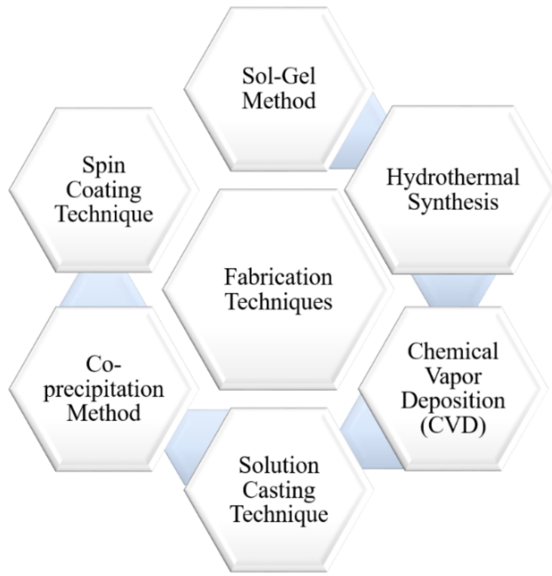

Figure 2. Represent the fabrication techniques of metal iodide-based materials.

2.1. Micro device manufacturing

Over the last few years, metal iodides have become promising candidates for integration into microdevices including sensors, photodetectors, and transistors because of their reliably turned electronic and optical attributes. The most significant benefit of metal iodides in microfabrication is that their bandgap can be tuned, and as such the electronic and optical properties of the material can be controlled. For example, CuI and AgI are preferred for high transmittance; a characteristic that is most crucial in optoelectronic applications [13]. Spin-coating and thermal evaporation are mostly used to incorporate metal iodides into micro-fabricated devices. Organometals can be created by depositing thin metal iodides and spin-coating and subsequent annealing provides the required morphology and thickness of the film [14]. Thermal evaporation, in contrast, provides a way of depositing very high-quality smooth and conformal films of metal iodides on different substrates; this is important for the optimization of the devices and scalability [15].

These fabrication techniques provide high levels of accuracy, and the devices made by these techniques are microscale and possess excellent electrical optical, and mechanical behaviors. In the course of designing sensors, it is important for the electronic properties of metal iodides to be tailored to increase sensitivity to gases, ions, or light [16]. Due to their high charge carrier mobility, metal iodides are used also in photodetectors and transistors, essential in communication systems and medical diagnostics. These microdevices have low defect densities, and by closely controlling the material's structure at the time of fabrication, their performance and reliability are enhanced. Due to the growing need for the miniaturization of electronic devices and high efficiency, the application of metal iodides will continue to be significant within microelectronics necessary for the demands of technologies of the following generations [17,18].

The micro device manufacturing industry establishes precise tiny components to work at microscale dimensions. The production process contains several vital characteristics involving minimal power consumption together with miniature product manufacturing along with superb dimensional standards and very small-sized light-weight components. Micro device technologies operate best for applications that require accurate small-scale structures thanks to their combined features. Micro device production enables the production of intricate components with precise details while using rawest materials. The production of uniform precise parts depends on a process that combines micro-milling with micro-electromechanical systems fabrication and laser machining and lithography methods. The components reach enhanced reliability and performance due to both excellent tolerance standards and high-quality surfaces they achieve. Many high-tech business operations depend on micro device manufacturing for their functioning. In electronics production semiconductor chips and microprocessors emerge from this technology while the manufacturing of small dimensional sensors also takes place. Medical implants gain useful assistance through microfabrication methods that also support precision surgical tools and lab-on-a-chip devices in healthcare applications. Aerospace companies enhance flying systems and spacecraft capabilities through weight reduction components while working with reduced sizes. Manufacturing of micro devices will increase in significance as technology advances because it allows future inventions to create performance transformations within industries through effective compact tools. **Figure 3** illustrates these key characteristics.

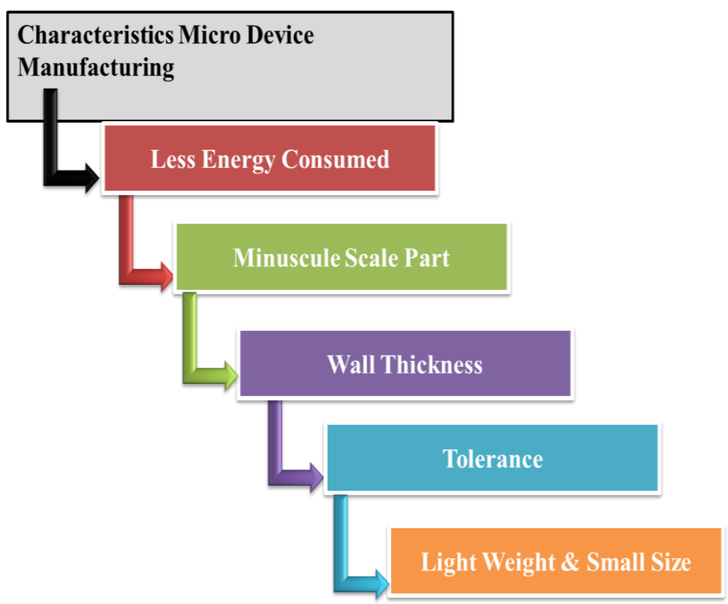

Figure 3. Characteristics of microdevices manufacturing.

2.2. Macro device manufacturing

The production of large-scale high-precision durable components relies on multiple fabrication procedures which fall under macro device fabrication. The fabrication of macro devices utilizes several techniques including machine operations (milling, turning and drilling) as well as injection molding for plastic parts quantity production and casting for complex metal form generation along with 3D printing for prototype development and specific manufacturing. According to the application different methods such as welding, forging and extrusion are employed to transform materials and make them joinable. Technical methods get chosen for production based on properties of materials and design complexity as well as production volume and cost-efficiency.

In the macro device generation, metal iodides are mainly used for their high ionic conductivity and thermal stability; they are used in solar cells and light-emitting diodes (LEDs). In the field of solar energy, the iodides based on hybrid perovskite have become more popular, especially for methyl ammonium lead iodide ($MAPbI_3$) owned to record high power conversion efficiencies [19]. These materials provide a high charge carrier mobility, meaning that efficient charge transport in photovoltaic devices enhances the energy conversion potential [20]. These perovskite iodides demonstrate high stability and have high process ability coupled with thin-film formation capability that makes them favorable as optoelectronic materials for cost-efficient, large-area photovoltaic applications [21].

In the field of LEDs, metal iodides are prized for their characteristics as they can release light in a broad area of the electromagnetic spectrum, which includes visible light and infrared. In the case of metal iodides, the high ionic conductivity is most advantageous for achieving efficient injection of charges and low energy loss in LED devices [22]. Their stability at high operational temperatures also means durability, thus suitable for commercial and industrial applications such as lighting. In addition, new hybrid iodide materials like perovskite have been well demonstrated to boost the efficiency and wavelength of light emission of LEDs. As the studies of the metals iodide-oriented materials are being extended prospects of these compounds are expected to become more profound in creating high-performance macro-devices, especially in renewable energy and optoelectronics [23].

Any design or system creation process includes diverse essential components according to **Figure 4** illustrated below. Project objectives together with boundaries get defined first in the development process. The Generic Requirements apply generic standard criteria to multiple domains yet Specific Requirements handle project-specific demands. Graphical notation represents the system through visual images which the Language Specification defines accurately while graphical notation supplies easy interpretation of these images. The modeling tools help designers create visual elements of system components which align with project objectives through design and visualization processes. System accuracy alongside functionality and external readiness receives constant refinement through successive improvements during the Refinement stage.

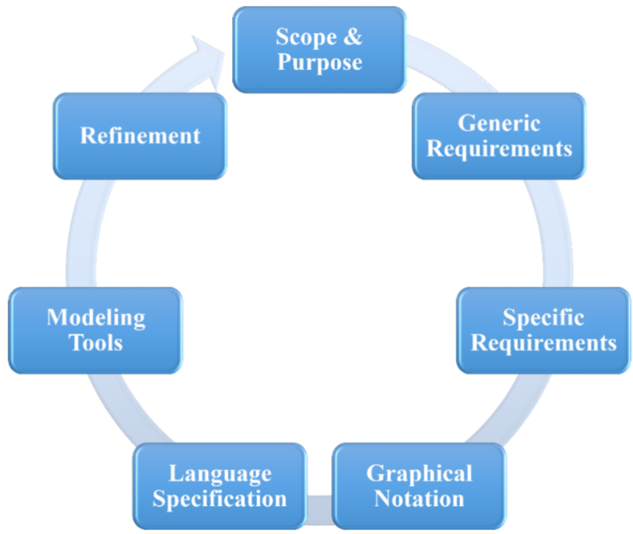

Figure 4. Represent the schematic scheme of macro manufacturing techniques.

2.3. Energy devices

Metal iodide materials as well as perovskites have shown high efficiency in energy applications, especially in solar cells and batteries. Concerning solar cells, metal iodide perovskites such as $MAPbI_3$ have offered significantly high power conversion efficiencies that have all but overshadowed traditional silicon-based photovoltaic solar cells [24]. These materials have the advantage of using easily scalable, low-cost deposition techniques such as solutions processing, which include spin coating or ink-jetting, and are hence preferred for large-scale fabrication. These perovskites have high ionic conductivity, whereby charge carrier transport is efficient for energy harvesting applications, and tunable optical characteristics for tailoring light absorption efficiency, a key factor in improving the efficiency of solar panels. Thus, metal iodide perovskites are identified as one of the top materials for future solar devices with further work dedicated to the enhancement of perovskite solar cells stability and progress towards big-scale manufacturing [14,25].

In batteries, the metal iodides are also being studied for use as solid electrolytes, because of their high ionic conductivity. Some common metal iodide salts include lithium iodide (LiI) and Sodium iodide (NaI), which are incorporated in solid-state batteries as an improvement of the use of liquid electrolytes due to the safety and stability offered in the application. These solid electrolytes also allow for overcoming several problems of lithium-ion batteries, including leakage, corrosion, and flammability. Furthermore, the solid-state electrolytes based on metal iodide show high ionic conductivity that is higher than 10 µs/cm allowing for a higher rate capability which increases the rate of charge and discharge of batteries [26]. Their application in next-generation energy storage materials is already under investigation for practical use in solid-state batteries and supercapacitors promising a new generation of batteries that may boast high energy densities, long cycle life, and improved operational safety [27].

Metal iodide nanomaterials have many uses in energy devices because of their properties such as high ionic conductivity, thermal stability, and good optoelectronic properties shown in **Figure 5**. These materials are comprehensively used in solar cells, especially in perovskite, as a solar material for in-v solar technologies; and energy conversion efficiency. They also demonstrate their importance in batteries by either being the solid electrolyte or the cathode in new-generation lithium-ion and sodium-ion systems. Moreover, metal iodide nanomaterials help to increase the efficiency of fuel cells and ion transport depending on the conditions. These components when incorporated into supercapacitors enhance the capacity of charge storage and in LED, they are crucial in developing energy-efficient illumination. All these applications support the recognition of their importance for the development of new-generation energy solutions.

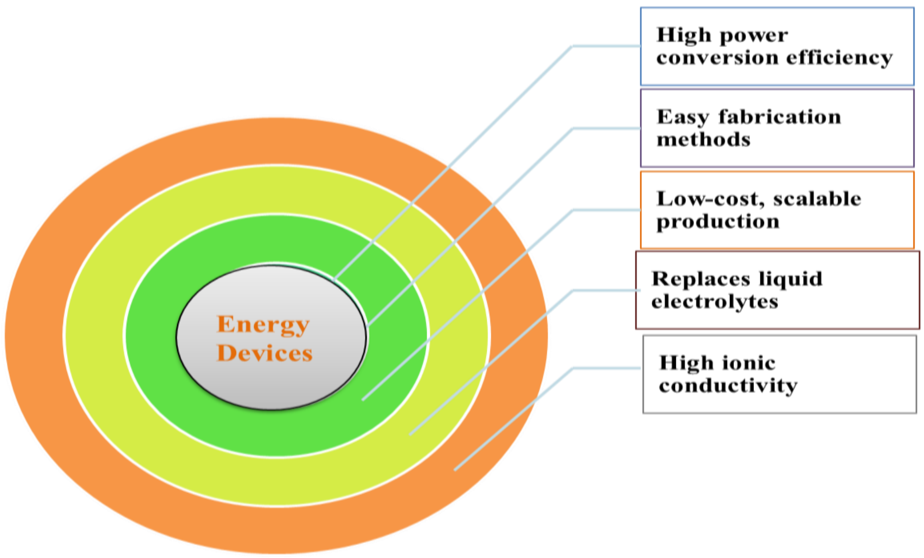

Figure 5. Some applications of metal iodide nanomaterials in energy devices.

2.4. Optoelectronics

Metal iodides are of great essence in optoelectronics because they exhibit variable optical characteristics that enhance light absorption and emission. For example, in light-emitting diodes (LEDs), metal iodides are intermediates that favor the conversion of electrical energy to light. One key advantage of metal iodides is the great control possible in the tunability of bandgap to obtain the desired emission wavelength, from [28] displays to communication systems. Besides, metal iodides play important roles in designing photodetectors that are relevant in areas such as imaging, sensing, telecommunications, and other applications. Catchability and stability, and the fact that the metal iodides are photosensitive, and can be easily precipitated have placed them among the promising materials for the new generation optoelectronic components. For example, infrared and ultraviolet photodetectors, such as AgI metal iodides also provide the best performance owing to their broad absorption spectra [29].

The electrical and optical properties of metal iodides also render this compound ideal for inclusion into other optoelectronic devices such as sunlight-catching cells, lasers, and photoelectric sensors. One of the features differentiating these materials is their ability to resonate to the various wavelengths of light which is the major reason why they will continue to be used across numerous industries including consumer electronics, environment monitoring, and even in medical fields [30]. Given the increasing demand for more energy-efficient and higher-performing optoelectronic devices, metal iodides are predicted to be the essential building block in satisfying the requirements of modern technologies within this segment [31].

Metal iodide nanomaterials have taken the optoelectronics world by storm with their ability to revolutionize new-age device-making by enhancing the performance and efficiency of the devices. Thus, they have been widely used in light-emitting diodes (LEDs), due to their high brightness, tunable wavelengths, and better energy efficiency. In photodetectors, they improve the efficiency by which light is collected and captured and the sensitivity which is important for high-speed communications and imaging devices. Metal iodides are also at the forefront of lasers with stable and coherent light sources for health, productivity, and communication. Furthermore, their incorporation into displays offers possibilities for the development of rich, high-resolution, and flexible screens in contemporary electronics. Combining scalable data with high performance, metal iodides are opening the door to efficient future solutions to optoelectronics, some of which are listed below in **Figure 6**.

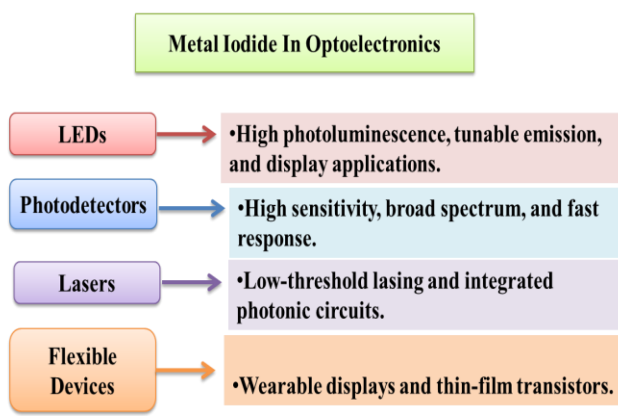

Figure 6. Application of metal iodide in optoelectronics.

2.5. Sensing technologies

There is much interest in metal iodides in the field of sensing solutions, especially for gases, ions as well as biomolecules. Metal iodides possess distinct characteristics including high ionic mobility and chemical stability, and due to these two noble characteristics, metal iodides are ideal for use in chemical and biological sensors [32]. For instance, metal iodides can be incorporated into electrochemical sensors for measuring certain ions or gases or responding selectively to CO_2, NH_3, or NO_2. The flexible nature of metal iodides makes them suitable for use within optical sensors, whereby any changes in the absorption or emission of light can be measured to determine the presence of different materials [33]. Due to this flexibility, metal iodides are especially sought after for uses in environmental sensing, clinical detection, and even for industrial uses [34].

Nanoscale metal iodide has recently become the subject of great interest due to its potential applications in sensing systems because of its ability to respond quickly, selectively, and electronically. These materials are widely employed in chemical sensors owing to their high electrical conductivity and surface activity that allows analyzing oxygen, nitrogen dioxide, and ammonia, for example. Metal iodides are involved in the analysis of biomolecules and, due to this ability, biosensors are used in medicine for the detection of glucose, DNA, and proteins. Moreover, they find use in the optical sensors for exploiting their ability of photoluminescence, which offers precise and quick response to light or alteration in the environment. They assert the potential of MI-based materials in the development of state-of-the-art sensing systems for environmental, health, and industrial monitoring, some of which are listed in **Figure 7**.

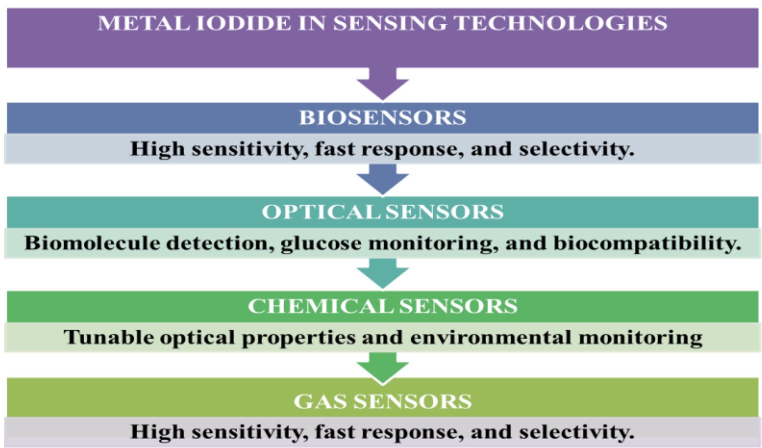

Figure 7. Application of metal iodide in sensing technologies.

Convenient and rapid methods based on metal iodide sensors were designed for the identification of biomolecules, glucose, DNA, pathogens, etc. The selective control of size and properties of metal iodides means that it is possible to engineer the affinity between the sensor and certain biomolecules which is important in point-of-care diagnostic applications [35]. Another advantage of the selected metal iodides is that they are relatively stable under different working conditions thus the sensors can work for a long time hence suitability for practical use. The development of higher demand for precise, transportable, and non-lethal sensing systems will be defined by the new use and incorporation of Metal iodides into these apps in the areas of human health and environmental control [36].

3. Challenges and future directions

The prospects for using metal iodide-based materials in devices appear solid yet the path to full practical implementation requires resolution of various vital technical obstacles. Environmental stability issues represent the primary technical challenge to adopting metal iodides in practical applications. The chemical decomposition of multiple metal iodide compounds begins immediately after they come into contact with moisture and experience both oxygen exposure and light exposure especially when lead compounds form their base. Device longevity together with operational performance decreases when targeted devices are exposed to exterior usage conditions or need strong reliability guarantees [37]. A variety of solutions are currently studied by researchers to enhance resistivity in metal iodide-based materials. Protective layers composed of metal oxides polymers and hydrophobic act as blocking elements which guard metal iodides against water and oxygen to increase operational timespan. The combination of dopants along with environmental-friendly elements in alloyed form stabilizes materials against environmental degradation. Switching lead substances with tin or bismuth produces material enhancement. The creation of nanostructured core-shell nanoparticles and layered heterostructures provides two layers of protection against destructive agents and improves mechanical strength and provides chemical stability. Thin protective layers made from graphene materials and atomic layer deposition (ALD)-grown oxides form exceptional barriers to block oxygen and moisture from entering the system.

Producing top-quality metal iodide films and nanomaterials encounters crucial challenges during the process of creating large-scale uniform products at cost-effective levels [32]. Current research involves multiple optimization methods for fabrication to address this manufacturing difficulty. The production of uniform metal iodide films on a large scale becomes feasible through continuous roll-to-roll processing since it enables creation of consistent large areas alongside high-quality devices. Flexible electronics together with extensive area solutions benefit from low-cost solution processing methods through spin coating and dip coating and inkjet printing for scalable fabrication. The film thickness control along with compositional accuracy can be achieved through vapor deposition methods which include both chemical vapor deposition (CVD) and physical vapor deposition (PVD).

When metal iodides are used for electronic applications, their environmental safety becomes challenging due to lead-containing substances that affect stability and scalability. Lead's dangerous nature poses critical challenges for waste management operations because it puts the environment at severe risk [38]. Tin-based and bismuth-based and antimony-based iodides stand as research-based material alternatives for electronic applications because they match optoelectronic properties while reducing environmental harm during application. The production process becomes environmentally beneficial by incorporating environmentally friendly solvents and reducing agents with alternative synthesis techniques. Waste device material recovery through solvent extraction methods together with mechanical recycling and thermal recovery allows researchers to minimize environmental hazards along with lower waste output. Achieving sustainable material development requires combining environmental regulations with lifecycle assessment testing to make the process possible.

Research by multiple fields of science stands as a fundamental requirement to convert metal iodide-based materials suitable for future applications while addressing their existing obstacles. The modern materials will transition from experimental materials to practical components in healthcare systems and aerospace technology and renewable energy generation when properly scaled manufacturing takes place alongside environmental improvement efforts and stability enhancements [39,40].

4. Conclusion

Due to the specific properties of metal iodide-based materials, they play a major role in the advancement of micro and macro techniques making a notable contribution to many fields. Because of their high ionic conductivity tunable optical properties and high thermal stability, researchers have employed them in energy devices, Optoelectronics, and sensing devices proving their applicability. These materials are further expected to assume even a larger role in the design of newer devices as research goes on, in areas such as renewable energy, health care, and communication. Nevertheless, the future of metal iodides depends on ongoing research and development improvements in material synthesis, integrating these materials into devices, and scaling up their production. In addition, care for environmental issues for instance through the use of environmentally friendly processing and disposal will form part of their sustainable use. The metal iodides will most undoubtedly be a significant component in the future of numerous present-day technologies as James has fully focused on overcoming all the challenges noting that efficiency with a characteristic of environmental friendliness of a material is the key focus.

Conflict of interest: The authors declare no conflict of interest.

References

1. Aslam H, Umar A, Nusrat N, et al. Nanomaterials in the treatment of degenerative intellectual and developmental disabilities. Exploration of BioMat-X. 2024. doi: 10.37349/ebmx.2024.00024
2. Patel MR, Singh PDD, Harshita, et al. Single crystal perovskites: Synthetic strategies, properties and applications in sensing, detectors, solar cells and energy storage devices. Coordination Chemistry Reviews. 2024; 519: 216105. doi: 10.1016/j.ccr.2024.216105
3. Zhang L, Guo H, Zong W, et al. Metal–iodine batteries: achievements, challenges, and future. Energy & Environmental Science. 2023; 16(11): 4872-4925. doi: 10.1039/d3ee01677c
4. Yu H, Wang Z, Zheng R, et al. Toward Sustainable Metal-Iodine Batteries: Materials, Electrochemistry and Design Strategies. Angewandte Chemie. 2023; 135(46). doi: 10.1002/ange.202308397
5. Shetty SK, Ismayil, Nayak P, et al. Sodium iodide dopant mediated enhancements in energy storage characteristics of polysaccharide polymer electrolytes. Journal of Energy Storage. 2024; 95: 112553. doi: 10.1016/j.est.2024.112553
6. Han K, Jin J, Zhou X, et al. Narrow-Band Green-Emitting Hybrid Organic–Inorganic Eu (II)-Iodides for Next-Generation Micro-LED Displays. Advanced Materials. 2024; 36(21). doi: 10.1002/adma.202313247
7. Qi JL, Wu J, Yan SF, et al. Cluster-Centered Excited-State-Induced Bright Low-Energy Emissive Hybrid Copper Iodide Constructing Stable White LEDs. Inorganic Chemistry. 2023; 62(46): 18825-18829. doi: 10.1021/acs.inorgchem.3c03608
8. Kim K, Yoo JI, Kim HB, et al. Highly efficient tandem organic light-emitting diodes using p-type metal halide copper iodide (CuI). Journal of Information Display. 2023; 25(3): 235-242. doi: 10.1080/15980316.2023.2272561

9. Meng X, Jiang J, Yang X, et al. Organic-Inorganic Hybrid Cuprous-Based Metal Halides with Unique Two-Dimensional Crystal Structure for White Light-Emitting Diodes. Angewandte Chemie International Edition. 2024. doi: 10.1002/anie.202411047
10. Zhang K, She Y, Cai X, et al. Epitaxial substitution of metal iodides for low-temperature growth of two-dimensional metal chalcogenides. Nature Nanotechnology. 2023; 18(5): 448-455. doi: 10.1038/s41565-023-01326-1
11. Uddin MA, Rana PJS, Ni Z, et al. Iodide manipulation using zinc additives for efficient perovskite solar minimodules. Nature Communications. 2024; 15(1). doi: 10.1038/s41467-024-45649-6
12. Sheng W, He J, Yang J, et al. Multifunctional Metal-Organic Frameworks Capsules Modulate Reactivity of Lead Iodide toward Efficient Perovskite Solar Cells with UV Resistance. Advanced Materials. 2023; 35(33). doi: 10.1002/adma.202301852
13. Aslam H, Nusrat N, Mansour M, et al. Photonic silver iodide nanostructures for optical biosensors. Exploration of BioMat-X. 2024: 366-379. doi: 10.37349/ebmx.2024.00025
14. Srivastava A, Satrughna JAK, Tiwari MK, et al. Lead metal halide perovskite solar cells: Fabrication, advancement strategies, alternatives, and future perspectives. Materials Today Communications. 2023; 35: 105686. doi: 10.1016/j.mtcomm.2023.105686
15. Li J, Dagar J, Shargaieva O, et al. Ink Design Enabling Slot-Die Coated Perovskite Solar Cells with >22% Power Conversion Efficiency, Micro-Modules, and 1 Year of Outdoor Performance Evaluation. Advanced Energy Materials. 2023; 13(33). doi: 10.1002/aenm.202203898
16. Khorasani A, Mohamadkhani F, Marandi M, et al. Opportunities, Challenges, and Strategies for Scalable Deposition of Metal Halide Perovskite Solar Cells and Modules. Advanced Energy and Sustainability Research. 2024; 5(7). doi: 10.1002/aesr.202470017
17. Yang M, Nie Z, Li X, et al. Advances of metal halide perovskite large-size single crystals in photodetectors: from crystal materials to growth techniques. Journal of Materials Chemistry C. 2023; 11(18): 5908-5967. doi: 10.1039/d2tc04913a
18. Gu Z, Zhang Y, Zhao Y, et al. From planar structures to curved optoelectronic devices: The advances of halide perovskite arrays. Matter. 2023; 6(9): 2666-2696. doi: 10.1016/j.matt.2023.05.007
19. Zhong Y, Liu Z, Luo X, et al. Macro–micro coordination optimization of lead iodide reactivity toward millimeter-to-centimeter-scale perovskite solar cells with minimal efficiency loss. Energy & Environmental Science. 2024; 17(15): 5500-5512. doi: 10.1039/d4ee01371a
20. Doherty TAS, Stranks SD. Multimodal Characterization of Halide Perovskites: From the Macro to the Atomic Scale. Halide Perovskite Semiconductors. 2023. doi: 10.1002/9783527829026.ch16
21. Sheng Y, Wen X, Jia B, et al. Direct laser writing on halide perovskites: from mechanisms to applications. Light: Advanced Manufacturing. 2024; 4(1): 1. doi: 10.37188/lam.2024.004
22. Palewicz M, Sikora A, Piasecki T, et al. Determination of the Electrical Parameters of Iodine-Doped Polymer Solar Cells at the Macro- and Nanoscale for Indoor Applications. Energies. 2023; 16(12): 4741. doi: 10.3390/en16124741
23. Liu T, Zhao Y, Song M, et al. Ordered Macro–Microporous Single Crystals of Covalent Organic Frameworks with Efficient Sorption of Iodine. Journal of the American Chemical Society. 2023; 145(4): 2544-2552. doi: 10.1021/jacs.2c12284
24. Hao D, Yang Z, Huang J, et al. Recent Developments of Optoelectronic Synaptic Devices Based on Metal Halide Perovskites. Advanced Functional Materials. 2022; 33(8). doi: 10.1002/adfm.202211467
25. Wei X, Bai Y, Chen Q. Fabrication and Modification Strategies of Metal Halide Perovskite Absorbers. Journal of Renewable Materials. 2023; 11(1): 61-77. doi: 10.32604/jrm.2023.022773
26. Zhu Y, Lv P, Hu M, et al. Synergetic Passivation of Metal-Halide Perovskite with Fluorinated Phenmethylammonium toward Efficient Solar Cells and Modules. Advanced Energy Materials. 2022; 13(8). doi: 10.1002/aenm.202203681
27. Chen L, He M, Gong W, et al. Robust salt-shelled metal halide for highly efficient photoluminescence and wearable real-time human motion perception. Nano Energy. 2023; 108: 108235. doi: 10.1016/j.nanoen.2023.108235
28. Dong H, Ran C, Gao W, et al. Metal Halide Perovskite for next-generation optoelectronics: progresses and prospects. eLight. 2023; 3(1). doi: 10.1186/s43593-022-00033-z
29. Darekar MS, Beekanahalli Mokshanatha P. Chemical synthesis of Lead Iodide nanoparticles for photovoltaic and optoelectronic device applications. International Journal of Nano Dimension. 2024.
30. Dey K, Ghosh D, Pilot M, et al. Substitution of lead with tin suppresses ionic transport in halide perovskite optoelectronics. Energy & Environmental Science. 2024; 17(2): 760-769. doi: 10.1039/d3ee03772j

31. Zhong J, Zhou D, Bai Q, et al. Growth of millimeter-sized 2D metal iodide crystals induced by ion-specific preference at water-air interfaces. Nature Communications. 2024; 15(1). doi: 10.1038/s41467-024-47241-4
32. Getachew G, Wibrianto A, Rasal AS, et al. Metal halide perovskite nanocrystals for biomedical engineering: Recent advances, challenges, and future perspectives. Coordination Chemistry Reviews. 2023; 482: 215073. doi: 10.1016/j.ccr.2023.215073
33. Li H, Li J, Shen N, et al. Progress and challenges of metal halide perovskites in X-ray detection and imaging. Nano Energy. 2024; 119: 109055. doi: 10.1016/j.nanoen.2023.109055
34. Salem MAS, Khan AM, Manea YK, et al. Highly efficient iodine capture and ultrafast fluorescent detection of heavy metals using PANI/LDH@CNT nanocomposite. Journal of Hazardous Materials. 2023; 447: 130732. doi: 10.1016/j.jhazmat.2023.130732
35. Liu Z, Qin X, Chen Q, et al. Metal–Halide Perovskite Nanocrystal Superlattice: Self-Assembly and Optical Fingerprints. Advanced Materials. 2023; 35(16). doi: 10.1002/adma.202209279
36. Ghosh J, Parveen S, Sellin PJ, et al. Recent Advances and Opportunities in Low-Dimensional Layered Perovskites for Emergent Applications beyond Photovoltaics. Advanced Materials Technologies. 2023; 8(17). doi: 10.1002/admt.202300400
37. Hwang I. Challenges in Controlling the Crystallization Pathways and Kinetics for Highly Reproducible Solution-Processing of Metal Halide Perovskites. The Journal of Physical Chemistry C. 2023; 127(50): 24011-24026. doi: 10.1021/acs.jpcc.3c05787
38. Shen X, Kang K, Yu Z, et al. Passivation strategies for mitigating defect challenges in halide perovskite light-emitting diodes. Joule. 2023; 7(2): 272-308. doi: 10.1016/j.joule.2023.01.008
39. Chu QQ, Sun Z, Hah J, et al. Progress, challenges, and further trends of all perovskites tandem solar cells: A comprehensive review. Materials Today. 2023; 67: 399-423. doi: 10.1016/j.mattod.2023.06.002
40. Baig N. Two-dimensional nanomaterials: A critical review of recent progress, properties, applications, and future directions. Composites Part A: Applied Science and Manufacturing. 2023; 165: 107362. doi: 10.1016/j.compositesa.2022.107362

EnPress Publisher, LLC

Add: 9650 Telstar Avenue, Unit A, Suite 121, El Monte, CA 91731, USA.
Email: contact@enpress-publisher.com
Web: https://systems.enpress-publisher.com

ISSN 2578-1782